MODELING OF BRITTLE FAILURE AND COMPARISONS TO LABORATORY EXPERIMENTS

by

DAVID AVERY LOCKNER

A.B. Geology, University of Rochester
(1972)

M.S. Geology, University of Rochester
(1973)

SUBMITTED TO THE DEPARTMENT OF EARTH, ATMOSPHERIC AND PLANETARY SCIENCES IN PARTIAL FULFILLMENT OF THE REQUIREMENTS FOR THE DEGREE OF

DOCTOR OF PHILOSOPHY

at the

MASSACHUSETTS INSTITUTE OF TECHNOLOGY

February 1990

Signature of Author .....
Department of Earth, Atmospheric and Planetary Sciences
February 1, 1990

Certified by .....
Theodore R. Madden
Professor, Department of Earth, Atmospheric and Planetary Sciences
Thesis Supervisor

Accepted by .....
Thomas H. Jordan
Department Chairman

MODELING OF BRITTLE FAILURE AND COMPARISONS TO LABORATORY EXPERIMENTS

by

DAVID AVERY LOCKNER

Submitted to the Department of Earth, Atmospheric and Planetary Sciences
on February 1, 1990 in partial fulfillment of the
requirements for the Degree of Doctor of Philosophy in Geophysics

ABSTRACT

A numerical multiple crack interaction model was developed to simulate the failure process in brittle solids containing significant populations of flaws. The model, which is 2D, allows for the growth of microcracks on a regular array of potential crack sites. Individual cracks may be oriented vertically, horizontally or at 45° to the sample axes. Quasi-static equilibrium equations are expressed in terms of finite difference approximations, and are solved by applying a Renormalization Group Theory approach. More than 5,000 potential crack sites are included in the current version of the model. We have successfully duplicated a variety of brittle fracture phenomena observed in laboratory rock mechanics studies by employing a limited number of parameters and relations in the model. Included in the model are 1) Lamé constants λ, μ for intact matrix material 2) coefficient of friction, f, for friction on cracks 3) an algorithm to allow for crack closure in response to normal stress 4) an initial crack population and 5) for time-dependent modeling, a power law sub-critical crack growth rule. A fracture mechanics approach is used to determine crack growth. Approximate stress intensity factors are computed for all cracks and when critical values are exceeded, cracks are allowed to grow in either mode I (tension) or mode II (in-plane shear). Simulations are performed by specifying a combination of stress and strain boundary conditions. The model is capable of duplicating experimentally observed features such as elastic moduli, dilatancy, acoustic velocities, peak strength, Mohr-Coulomb failure envelope and, to a limited degree, crack coalescence.

A number of supplemental laboratory experiments have also been performed, focusing primarily on low-temperature creep. In one set of experiments, cylindrical samples of granite were deformed at 26° C, constant confining pressure (600 bars) and constant pore pressure (200 bars). Axial and volumetric strain were determined from changes in the output of resistance foil strain gauges bonded to the rock surface. In addition, DC electrical resistivity was measured parallel to the sample axis. During these experiments (typically lasting from one to two weeks), the deviatoric stress σ_d applied to the sample was cycled between 70% and 90% of the short-term failure strength. The majority of the experiments were conducted in the secondary or 'steady-state' creep regime. Inelastic volumetric strain rate was found to obey the law $\log_{10}(\dot{\varepsilon}_v) = A + B\,\sigma_d + C\,\log_{10}(\varepsilon_v)$ where $B = 7.4 \pm 0.2$ kb^{-1} and $C \approx -4$. The C-coefficient represents a strain-hardening-like term. The stress-dependence is of the same form as the stress-dependence measured for mode I crack growth in double cantilever beam experiments. The observed creep behavior is analyzed in terms of stress corrosion and crack growth models.

A second set of experiments was designed to measure the development of electrical resistivity anisotropy during deformation of granite. In this series, two triaxial deformation experiments were conducted on brine-saturated (0.1 and 0.01 M_{aq} KCl) Westerly granite at effective pressures of 100 and 400 bars. Deformation histories included constant strain rate, constant stress and stress relaxation sequences. Complex resistivity, over the frequency range from 10^{-3} to 10^{5} Hz, was measured in both axial and transverse directions during the experiments. Low-frequency-limit resistivity ρ_{DC} increased with initial loading and then decreased steadily after the onset of dilatancy. The initial increase in ρ_{DC} was greatest in the transverse direction, in one experiment reaching a peak contrast $\rho_{DC\perp}/\rho_{DC\parallel} = 1.4$ at approximately 35% peak strength. With continued loading and the resultant opening of microcracks, the resistivity contrast decreased to approximately 0.8 by failure. In terms of the frequency dependence of resistivity, the general form of the real part of the resitivity varied little during deformation other than a uniform change in magnitude proportional to the changes in ρ_{DC}. Under initial hydrostatic stress, the phase angle between current and voltage ranged from 10 to 30 mrad over the frequency range 0.001 to 100 Hz. With the onset of dilatancy, notable changes occured in the phase spectra in the 0.001 to 10 Hz region. The changes differed in the axial and transverse directions and appeared to be the result of changing pore structure since they diminished upon removal of deviatoric stress. Although the variations in complex resistivity were subtle, their occurance in the Earth may be exploited as a means of identifying secular changes in stress or strain through induced polarization or magnetotelluric measurements.

Finally, a series of experiments was conducted to measure changes in electrical conductivity during densification of water-saturated quartz powders at elevated temperatures. Starting material was ultra-fine quartz powder (5-10 μm-diameter). Confining pressure ranged from 2,000 to 3,700 bars and pore pressure from 300 to 2,000 bars. All runs were conducted at 700°C and were saturated with distilled water. Initial porosity in all experiments was in excess of 40%. Experiments lasted from 10 hr to 8 days, with ending porosities from 19% to as little as 8 ± 1%. In all experiments, initial volumetric compaction rates were rapid (10^{-5} to 10^{-6} s^{-1}), decreasing quickly to rates in the range 10^{-7} to 10^{-8} s^{-1} after approximately 1 day. Electrical conductivity as well as porosity decreased monotonically during the experiments. Conductivity ranged from 10^{-2} to 10^{-4} mho/m. A model is presented in which decrease in conductivity is initially controlled by the loss of fluid filled pore volume, followed by a transition, at approximately 15% porosity, to a condition in which conductivity in controlled by constrictions in interconnecting channels.

Thesis Supervisor: Dr. Theodore R. Madden
Title: Professor of Geophysics

Co-supervisor: Dr. Brian Evans
Title: Professor of Geophysics

BIOGRAPHY

1968 - 1973: Attended University of Rochester, N.Y., received A.B. and M.S. in Geology.
1973 - 1974: Attended Stanford University, Calif. (no degree).
1974 - present: Research scientist in Office of Earthquake Studies, U.S. Geological Survey, Menlo Park, California.

Publications:

Bonham-Carter, G., Thomas, J., and Lockner, D. A., 1973, A numerical model of steady wind-driven currents in Lake Ontario and the Rochester Embayment based on shallow-lake theory, Internat. Field Year for the Great Lakes, Rochester Embayment Project, Dept. of Geol. Sci., Univ. of Rochester, New York.

Lockner, D. A., 1973, Sensitivity of a numerical circulation model for Lake Ontario to changes in lake symmetry and friction depth, and to variable wind stress, Rochester Embayment Project, Dept. of Geol. Sci., Univ. of Rochester, New York.

Byerlee, J. D. and Lockner, D. A., 1977, Acoustic emission during fluid injection in rock, Proceedings, First Conference on Acoustic Emission/Microseismic Activity in Geological Structures and Materials, Trans Tech Publications, Clausthal-Zellerfeld, W. Germany, p. 87-98.

Lockner, D. A. and Byerlee, J. D., 1977, Acoustic emission and fault formation in rocks, Proceedings, First Conference on Acoustic Emission/Microseismic Activity in Geological Structures and Materials, Trans Tech Publications, Clausthal-Zellerfeld, W. Germany, p. 99-107.

Lockner, D. A., Walsh, J. B., and Byerlee, J. D., 1977, Changes in seismic velocity and attenuation during deformation of granite, J. Geophys. Res., v. 82, n. 33, p. 5374-5378.

Solberg, P. H., Lockner, D. A., and Byerlee, J. D., 1977, Shear and tension hydraulic fractures in low permeability rocks, Pure and Applied Geophys., v. 115, p. 191-198.

Lockner, D. A. and Byerlee, J. D., 1977, Acoustic emission and creep in rock at high confining pressure and differential stress, Bull. of the Seismological Society of Amer., v. 67, no. 2, p. 247-258.

Lockner, D. A. and Byerlee, J. D., 1977, Hydrofracture in Weber sandstone at high confining pressure and differential stress, J. Geophys. Res., v. 82, no. 14, p. 2018-2026.

Lockner, D. A. and Byerlee, J. D., 1978, Velocity anomalies: an alternative explanation based on data from laboratory experiments, Pure and Applied Geophys., v. 116, p. 765-772.

Weeks, J. D., Lockner, D. A., and Byerlee, J. D., 1978, Changes in b-value during movement on cut surfaces in granite, Bull. of the Seismological Society of Amer., v. 68, no. 2, p. 333-341.

Lindh, A. G., Lockner, D. A., and Lee, W. H. K., 1978,Velocity anomalies: an alternative explanation, Bull. of the Seismological Society of Amer., v. 68, no. 3, p. 721-734.

Solberg, P., Lockner, D. A., Summers, R., Weeks, J., and Byerlee, J. D., 1978, Experimental fault creep under constant differential stress and high confining pressure, 19th U. S. Symposium of Rock Mechanics, p. 118-120.

Lockner, D. A., Weeks, J. D., and Byerlee, J. D., 1978, A laboratory control system using the PDP 11/03 Microprocessor, U.S. Geological Survey Open-File Report 78-125, 33pp.

Baker, P. A., Kastner, M., Byerlee, J. D., and Lockner, D. A., 1980, Pressure solution and hydrothermal recrystallization of carbonate sediments - an experimental study, Marine Geology, v. 38, p. 185-203.

Lockner, D. A. and Byerlee, J. D., 1980, Development of fracture planes during creep in granite, Proceedings, Second Conference on Acoustic Emission/Microseismic Activity in Geological Structures and Materials, Trans Tech Publications, Clausthal-Zellerfeld, W. Germany, p. 11-25.

Lockner, D. A. and Byerlee, J. D., 1980, Strength measurements of the Geysers reservoir rock, Transactions, Geothermal Resources Council, v. 4, p. 353-356.

Solberg, P. H., Lockner, D. A., and Byerlee, J. D., 1980, Hydraulic fracturing in granite under geothermal conditions, International J. of Rock Mech., v. 17, p. 25-33.

Morrow, C., Lockner, D., Moore, D., and Byerlee, J., 1981, Permeability of granite in a temperature gradient, J. Geophys. Res., v. 6, p. 3002-3008.

Lockner, D. A., Summers, R., Moore, D., and Byerlee, J. D., 1982, Laboratory measurements of reservoir rock from the Geysers geothermal field, California, International J. of Rock Mech., v. 19, p. 65-80.

Lockner, D. A., Okubo, P. G., and Dieterich, J. H., 1982, Containment of stick-slip failures on a simulated fault by pore fluid injection, Geophys. Res. Letters, v. 9, p. 801-804.

Lockner, D. A. and Okubo, P. G., 1983, Measurements of frictional heating in granite, J. Geophys. Res., v. 88, p. 4313-4320.

Lockner, D. A., Johnston, M. J. S., and Byerlee, J. D., 1983, A mechanism for the generation of earthquake lights, Nature, v. 302, p. 28-33.

Lockner, D. A. and Byerlee, J. D., 1985, Complex resistivity of fault gouge and its significance for earthquake lights and induced polarization, Geophys. Res. Letters, v. 12, p. 211-214.

Lockner, D. A. and Byerlee, J. D., 1985, Complex resistivity measurements of confined rocks, J. Geophys. Res., v. 90, p. 7837-7847.

Lockner, D. A. and Byerlee, J. D., 1986, Laboratory measurements of velocity-dependent frictional strength, U.S. Geological Survey Open-File Report 86-417, 50 pp.

Lockner, D. A., Summers, R., and Byerlee, J. D., 1986, Effects of temperature and sliding rate on frictional strength of granite, Pure and Appl. Geophys., v. 124, p. 445-469.

Lockner, D. A., Byerlee, J. D., Kuksenko, V. S., and Ponomarev, A. V., 1986, Stick slip, charge separation and decay, Pure and Appl. Geophys., v. 124, p. 601-608.

Lockner, D. A. and Byerlee, J. D., 1986, Changes in complex resistivity during creep in granite, Pure and Appl. Geophys., v. 124, p. 659-676.

Lockner, D. A. and Byerlee, J. D., 1990, An example of slip instability resulting from displacement-varying strength, Pure and Appl. Geophys., in press.

TABLE OF CONTENTS

CHAPTER 1

INTRODUCTION

The importance of flaws in affecting the material properties of solids has been recognized for some time. *Griffith* (1920), for example, pioneered the way in understanding how the presence of flaws significantly reduces the strength of brittle materials below the theoretical crystal strength. For silicates and ceramics at room temperature, many of the transport properties are controlled by the flaws, or pore structure, since the matrix material does not participate actively in the transport process. For example, fluid permeability and electrical conductivity are dominated by the structure of the pore volume. Indeed fluid filled cracks in granite are found to contribute to the electrical conductivity in a proportion far outweighing their volume fraction (*Madden*, 1983). Acoustic velocities and attenuation are also influenced by the presence of microcracks. In experimental studies, for example, volumetric strains of less than one percent have been observed to reduce p-wave velocities by more than 30% in granite samples loaded to failure (*Lockner et al.*, 1977; *Yukutake*, 1989).

One topic of research that has been of fundamental interest in the field of rock mechanics has been the understanding of the failure process in brittle rock. While in general terms the process which leads to failure has been well documented, our understanding of the precise mechanism by which microcracking localizes into a macroscopic shear plane is still incomplete (*Evans and Wong*, 1985). Many attempts at analyzing the failure process have been cast in terms of damage parameters (*Spetzler et al.*, 1982; *Ashby and Hallam*, 1986; *Sammis and Ashby*, 1986; *Costin*, 1987). *Madden* (1983) and *Williams and Madden* (1988) predicted rock failure in terms of a critical crack density based on renormalization group theory. Using continuum mechanics, *Rudnicki and Rice* (1975), *Rice* (1976) and *Rudnicki* (1977) analyzed conditions underwhich deformation for a dilatant, pressure-sensative material would localize in a weakened zone.

Earthquake prediction is a field of study which is intimately connected to an understanding of the changes that occur in a rock mass as it approaches failure. A variety of phenomena have been suggested as parameters that may be used for the prediction of earthquakes, including temporal changes in strain, tilt, creep, water level,

radon emission, electrical resistivity, seismic velocity, foreshocks and animal behavior. All of these phenomena can be associated directly or indirectly with changes in the microcrack geometry in some region surrounding an impending earthquake. An understanding of how the microstructure of a rock responds to changes in stress and strain is required to assess the detection threshold for any of these phenomena.

In terms of the mechanical strength of rock, measurable boundary conditions are in general some averaged stress and/or strain applied at distances large compared to individual cracks. Thus a fundamental question is how cracks grow in response to remote loads. Analytic solutions exist for single cracks (*e.g. Paris and Sih,* 1965) and periodic arrays of cracks (*Delameter et al.,* 1975), but determination of the response of more complicated crack geometries generally requires an iterative technique. *Segall and Pollard* (1980), for example, analyzed crack interactions using the Schwarz-Neumann alternating technique. In this procedure, boundary conditions are satisfied on the surface of each crack in sequence, and the process is repeated until the desired accuracy is achieved. Other multiple crack models (*Kranz*, 1979) simply superimposed the strain fields of individual cracks, essentially assuming that crack interactions were negligible. *Segall and Pollard* (1980) analyzed the stress perturbation due to a crack subjected to antiplane remote stress. They found that outside a critical radius $r_c = 2.25a$, where a is the crack half-length, the perturbing stress is less than 10% of the applied stress. *Pollard and Segall* (1987) develop the appropriate stress equations for plane strain as well as anti-plane strain. A similar analysis for plane strain gives $r_c \sim 3a$. This result can be compared to crack count data compiled by *Hadley* (1975) and reproduced in *Madden* (1983) for Westerly granite subjected to a variety of stress levels. Even in the undeformed rock, the longest crack length category (100 - 300 μm) had a crack count of 36 mm^{-2}. While the shorter length cracks would not interact, the 100 - 300 μm cracks have sufficient density that they would interact. By 65% failure stress, crack densities had increased sufficiently so that cracks longer than 30 μm would be expected to interact. Thus, throughout the loading history, crack interactions can be expected to play an important role. Of course, the final coalescence of cracks to form a macroscopic shear plane is a cooperative process as well.

With the development of more and more powerful computers, numerical simulations of multi-crack interaction problems are becoming feasible. However, at present, high accuracy simulations of even modest sample sizes remain impractical.

Accepting this limitation, we present in this paper a numerical crack interaction model in which only first order interactions are considered. We will compare the results of this model to laboratory deformation experiments. To the degree that the mechanical properties of rock deformation are controlled by these dominant interactions, we expect the simulations to capture the general features of laboratory experiments. In particular, we will examine such phenomena as peak strength, confining pressure dependence, dilatancy, critical crack density, acoustic velocity, conductivity and time-dependent creep. By examining the relative success of the model in reproducing experimental data, we hope to gain some insight into the processes controlling the physical properties of rocks.

References

Ashby, M. F. and S. D. Hallam, The failure of brittle solids containing small cracks under compressive stress states, *Acta Metall., 34,* 497-510, 1986.

Costin, L. S., Deformation and failure, in: *Fracture Mechanics of Rock,* (ed. Atkinson, B. K.), Academic Press, New York, pp. 167-215, 1987.

Delameter, W. R., G. Herrmann, and D. M. Barnett, Weakening of an elastic solid by a rectangular array of cracks, *J. Appl. Mech., 42,* 74-80, 1975.

Evans, B. and T.-f. Wong, Shear localization in rocks induced by tectonic deformation, in *Mechanics of Geomaterials,* edited by Z. Bazant, John Wiley, pp. 189-210, New York, 1985.

Griffith, A. A., The phenomena of rupture and flow in solids, *Philos. Trans. R. Soc. London Ser. A, 221,* 163-198, 1920.

Hadley, K., Dilatancy: further studies in crystalline rocks, Ph.D. Thesis, Mass. Inst. Tech., Cambridge, Ma, 1975.

Kranz, R. L., Crack-crack and crack-pore interactions in stressed granite, *Int. J. Rock Mech. Min. Sci. Geomech. Abstr., 16,* 37-47, 1979.

Lockner, D. A., J. B. Walsh and J. D. Byerlee, Changes in seismic velocity and attenuation during deformation of granite, *J. Geophys. Res., 82,* 5374-5378, 1977.

Madden, T. R., Microcrack connectivity in rocks: a renormalization group approach to the critical phenomena of conduction and failure in crystalline rocks, *J. Geophys. Res., 88,* 585-592, 1983.

Paris, P. and G. Sih, Stress analysis of cracks, in *Symposium on Fracture Toughness Testing and Applications, Spec. Tech. Publ. 381,* pp. 30-81, American Society for Testing and Materials, Philadelphia, Pa., 1965.

Pollard, D. D. and P. Segall, Theoretical displacements and stresses near fractures in rock: with applications to faults, joints, veins, dikes, and solution surfaces, in: *Fracture Mechanics of Rock,* (ed. Atkinson, B. K.), Academic Press, New York, pp. 277-349, 1987.

Rice, J. R., The localization of plastic deformation, in *Proceedings of the 14th International Congress of Theoretical and Applied Mechanics, 1,* edited by W. T.

Koiter, pp. 207-220, North-Holland, Amsterdam, 1976.

Rudnicki, J. W., The inception of faulting in a rock mass with a weakened zone, *J. Geophys. Res., 82,* 844-854, 1977.

Rudnicki, J. W. and J. R. Rice, Conditions for the localization of deformation in pressure-sensitive, dilatant materials, *J. Mech. Phys. Solids, 23,* 371-394, 1975.

Sammis, C. G. and M. F. Ashby, The failure of brittle porous solids under compressive stress states, *Acta metall., 34,* 511-526, 1986.

Segall, P. and D. Pollard, Mechanics of discontinuous faults, *J. Geophys. Res., 85,* 4337-4350, 1980.

Spetzler, H., H. Mitzutani and F. Rummel, Fracture and flow, in: *Anelasticity in the Earth*, Geodynamics series, *4*, (ed. Schreyer, W.), E. Schweizerbartische Verlagsbuchhandlung, Stuttgart, 85-93, 1982.

Williams, E. R. and T. R. Madden, Models for crack development and brittle failure and the role of crack configurations in guiding their behavior, unpublished manuscript, 1988.

Yukutake, H., Fracturing process of granite inferred from measurements of spatial and temporal variations in velocity during triaxial deformations, *J. Geophys. Res., 94,* in press.

CHAPTER 2

MULTIPLE CRACK INTERACTION MODEL

Symbols and Conventions

c	4^{th} rank stiffness tensor; also 3x3 matrix representation of 2D stiffness tensor
f	coefficient of friction for crack surfaces
$K_{I,II}$	crack tip stress intensities for modes I and II
l	crack length
l_o	length of unit cell in model; in present model, $l_o = 0.1$ mm
n	slope of K-log(v) plot for subcritical crack growth rate
P	stress tensor
P_c	critical probability for crack density at failure based on RNG calculation
(r,s)	vector components in cartesian, 2D r,s coordinate system; rotated 45° counterclockwise from (x,y) system
u	displacement vector
V_{pi}	P-wave velocity in i^{th} direction
(x,y)	vector components in 2D x,y coordinate system
ε	strain tensor
ε_v	volumetric strain
γ	shear strain
η	slip vector magnitude for crack surfaces
λ, μ	Lamé constants
ξ	non-dimensional weighting parameter; in present model, ξ represents fraction of a cell side that is uncracked

Compressive stresses and strains are negative.

Crack Model Description

In this section, the basic elements of the numerical crack model are described. Some details of the model will be expanded on, where appropriate, in subsequent sections. As we have already mentioned, a generalized crack interaction model, allowing for cracks of both random position and orientation, and including a significant sample volume, is not yet feasible. Recognizing this fact, we have chosen to adopt the following strategy. We have constructed a quasi-static crack model beginning with a simple crack geometry and the fewest possible rules and, by comparison to experimental results, determined how successful we were at reproducing the significant features of brittle rock deformation. The model was then modified by adding more complex features in an attempt to reconcile differences with laboratory data. In its present 2 dimensional form, the model successfully reproduces a variety of phenomena associated with brittle deformation of crystalline rock up to and including peak strength, for which microcrack growth is relatively homogeneous. Due to technical limitations, the model does not adequately deal with the severe large scale heterogeneity in material properties that accompanies strain localization and fault formation in the post-peak-strength region. For this reason our simulations will focus primarily on the phenomena associated with crack growth in the pre-failure region. Since we wish to duplicate laboratory experiments, we construct the model in a form that will allow for application of appropriate boundary conditions. These include uniform confining pressure on lateral surfaces and stress or displacement boundary conditions on sample ends. The model is presently 2D with simulated sample dimensions of 2.7 x 5.4 mm. Even with this modest size, up to 5,800 cracks, 0.1 mm-long, can be included. Expanding the sample dimensions by a factor of three or even nine is a simple matter. However, conducting simulations using the current sample size taxes our available computational resources. It does not seem necessary, for the present, to incease the sample size. Expanding the model to a full 3D simulation is also straightforward in principle. However, the details of the computer programming are complicated and have not been undertaken.

In the remainder of this section, we give a detailed description of the various program elements. Consequently, most readers will probably wish to proceed directly

to the next section entitled 'Summary of Model'. Based on the assumption that the overall mechanical stability of a brittle rock will be controlled by the gross geometric interactions of the crack arrays, we are primarily interested in first order crack interaction effects. As a result, we are willing to sacrifice a certain amount of accuracy in determining local stresses for the ability to augment the total crack population. The model, then, is constructed so as to include cracks which are equal in length to unit cell dimensions. To make this geometry work, we have developed a finite difference code, based on a staggered gridding scheme, which not only is efficient at computing stress components from nearest-neighbor displacements but also defines stresses where they are needed to solve for local equilibria. The technique used to compute local displacements is based on a multiple scaling procedure. In this procedure, small regions of the sample are analized to determine their average elastic properties. The local crack networks create severe anisotropy in these average elastic properties. As a result, fully anisotropic elastic tensors (represented by 21 independent coefficients in 3D and 6 coefficients in 2D) must be calculated in the model. We begin our discussion of the model formulation by considering the difference approximations for the governing equations.

Hooke's Law and Equilibrium Equations

For a linearly elastic solid, stress is related to strain through Hooke's law:

$$P_{ij} = c_{ijkl}\, \varepsilon_{kl} \,. \tag{2-1}$$

Through various energy arguments (*Nye*, 1986), it can be shown that c contains 21 independent coefficients. Eq. (2-1) can be written, in reduced form, as

$$P_i = c_{ij}\, \varepsilon_j \,. \tag{2-2a}$$

For example, in the case of plane-strain normal to the z-axis, (2-2a) becomes

$$\begin{bmatrix} P_{xx} \\ Pyy \\ P_{xy} \end{bmatrix} = \begin{vmatrix} c_1 & c_4 & c_5 \\ c_4 & c_2 & c_6 \\ c_5 & c_6 & c_3 \end{vmatrix} \begin{bmatrix} \varepsilon_{xx} \\ \varepsilon_{yy} \\ \gamma_{xy} \end{bmatrix}. \qquad (2\text{-}2b)$$

A typical stress component in the 2D finite difference approximation of (2-2) would be

$$P_{xx} = c_1 \Delta u_x/\Delta x + c_4\, \Delta u_y/\Delta y + c_5\, (\Delta u_y/\Delta x + \Delta u_x/\Delta y) \qquad (2\text{-}3)$$

where u_x and u_y are displacement components in the x- and y-directions, respectively.

In solving the quasi-static crack growth problem, we will also require that the equilibrium equations be satisfied:

$$\begin{aligned} &\partial P_{xx}/\partial x + \partial P_{xy}/\partial y = 0 \\ &\partial P_{xy}/\partial x + \partial P_{yy}/\partial y = 0 \\ &P_{xy} = P_{yx}\,. \end{aligned} \qquad (2\text{-}4)$$

Gridding Scheme

Tradeoffs must be made in choosing the most appropriate grid for solving the elasticity problem. The staggered grid is the most accurate finite-difference representation of elasticity of a continuous medium. This nodal arrangement, for the 2D case, is shown in Fig. 2.1a. In the staggered grid representation, displacements and stress components are defined on square lattices throughout the material. However, displacements and shear and normal stresses are all offset relative to each other.This representation has distinct advantages over the 'standard' grid representation shown in Fig. 2.1b. First, consider the most common elasticity applications in which the material is isotropic and c_5, $c_6 = 0$. In this case, notice that stress components are represented where their defining displacement differences (*e.g.* eq. (2-3)) can be obtained from nearest-neighbor displacements. This property accounts for the good accuracy of the staggered grid. In contrast, consider the standard grid shown in Fig. 2.1b. The advantage of this gridding scheme is that stresses and displacements are centered at the same locations. This property avoids some of the ambiguities encountered with the staggered grid at high-contrast boundaries of the material. The

main disadvantage of the standard grid is its reduced accuracy. For the standard grid, stresses cannot be defined in terms of displacement differences spanning a single unit cell. Instead, displacement differences must be averaged over two unit cell lengths. If these were the only considerations involved in choosing the gridding scheme, the staggered grid would be the obvious choice. However, three additional points need be considered. First, we will require the full 2D tensor representation (non-zero c_5 and c_6). The corresponding terms in the equations defining stress components do not have efficient representations on the staggered grid. Displacement differences spanning more than a unit cell are required to compute stress components and a corresponding loss of accuracy occurs. The second difficulty arises in representing the equilibrium equations. If a unit cell is defined as represented by the dashed lines in Fig. 2.1a, then both both P_{xx} and P_{xy} are available precisely where needed to balance forces in the x-direction. However, neither P_{yy} nor P_{xy} are known in positions needed for balancing forces in the y-direction. Thus, stresses must be averaged to represent the equilibrium equations and much of the accuracy achieved in evaluating stresses is now lost. The third consideration involves the fact that the elastic tensor elements, representing a material property, are varying with position throughout the material. In the staggered grid representation, stiffness components must be averaged across unit cell boundaries in computing some of the stress components. If the material properties are varying smoothly as a function of position, then the necessary averaging is not a serious problem. However, we wish to consider a material which is filled with cracks on the same scale as the unit cell of the differencing representation. Since the cracks represent a discontinuity in material properties (some components of $c_{ij} \rightarrow 0$ for an open crack), averaging across cracks becomes a serious difficulty.

Having said all this, the first attempt at developing the crack-interaction model did, in fact, use a staggered grid representation. After considerable effort, this approach was abandoned and a compromise representation, which will be referred to as a modified staggered grid, was adopted. This representation is shown in Fig. 2.1c. In this case, both displacements and material properties are defined at the centers of the unit cells while stress components are defined at cell edges. In addition, cracks can occur along all cell edges. Thus, stresses represent the forces transmitted between adjacent cells and are known in the proper positions to solve equilibrium equations for each cell. One compromise of this configuration is that only half of the displacement differences used

to compute stress components span a single unit cell dimension. The remaining displacement differences average over larger distances. Notice that in computing a single stress component, strains and stiffnesses of two unit cells plus an intervening crack are involved. This configuration is approximated by a column of elements in series. The exact form of this series approximation will be described below.

After implementing this modified staggered grid representation, it became clear that restrictions on the crack locations and orientations were too severe to allow for crack coalescence and mechanical failure of the sample. For example, the closest approximation to a diagonal shear failure plane would be a staircase of horizontal and vertical cracks (Fig. 2.2). A sample containing this crack geometry clearly has zero macroscopic tensile strength. For axi-symmetric compression, however, even in the case where there is zero frictional shear strength across crack surfaces, such a sample would be metastable to uniaxial compression and would be fully stable for finite lateral compression. Due to this important geometric restriction, the model was then modified to include diagonal cracks as shown in Fig. 2.3. This geometry proved to be a significant improvement over the previous model since diagonal cracks, oriented 45° to the sample axes and applied principal stresses, are subjected to the maximum shear stresses. While cracks at angles somewhat less than 45° to the maximum principal stress direction would have larger ratios of shear to normal stress, this additional refinement did not seem warranted in the initial diagonal crack model. The primary importance of including diagonal cracks is that slip on these crack surfaces tends to develop large tensile stress concentrations at the crack tips, leading to the formation of 'wing' cracks parallel to the maximum compressive stress direction. This process has been identified as an important aspect in microcrack development (*Evans and Wong,* 1985; *Ashby and Hallam,* 1986; *Sammis and Ashby,* 1986; *Horii and Nemat-Nasser,* 1986).

Up to this point, the model has been linear; at least for a given crack population. However, two non-linear features were added to enhance the model. These were crack closure effects and crack frictional strength. Crack closure properties are non-linear since an open crack has effectively zero stiffness regardless of how open the crack is, while a crack which closes in compression becomes stiffer (also as a non-linear function of closure). Thus the model, which computes displacement adjustments according to a linearized stress-strain relation, must be cycled through many steps to

allow the crack geometry to converge on a stable configuration. In terms of crack friction, a crack and the surrounding material will deform approximately linearly as long as no slip occurs on the crack face. However, once shear strength on the crack surface is exceeded, slip occurs with little change in shear stress. Thus there is an abrupt drop in apparent shear modulus to nearly zero. The behavior is further complicated since while the shear modulus for continued slip is essentially zero, any decrease in shear strain unloads the crack and the apparent shear modulus jumps to a non-zero value until the crack is driven to slip in the reverse sense. These frictional crack properties have been included in the final model through the use of a crack slip vector associated with each crack.

Of course, the crack interaction process itself is non-linear. A given crack population will produce complex stress and strain fields in the sample in response to a given applied load. Any crack which grows will alter its local stress field. For distances greater than the crack half-length, the stress perturbation due to a crack drops off as r^{-2} where r is the distance from the crack center (*Pollard and Segall*, 1987, pp. 328). As the crack density increases it becomes more and more likely that neighboring cracks will be induced to failure even though the applied boundary stresses have not changed. This process is observed in our simulations where a sample held at constant boundary stress conditions near failure will require many iterations before all crack growth ceases.

Difference Approximations

The basic procedure for solving the elasticity problem involves the following steps. 1) For a given crack population and nodal displacements, strains within each unit cell are computed. 2)From these strains, stresses are computed. 3)Equilibrium equations are solved to compute nodal displacement adjustments. 4)Stresses are recomputed and the crack population is modified according to local stress states. After any desired modifications of the boundary conditions, the entire procedure is then repeated.

Unit cell strains are obtained by first approximating displacements at cell edges using a series-average scheme involving two adjacent nodal displacements and the intervening edge crack. For example, consider the grid without diagonal cracks shown in Fig. 2.4a. To determine the average y-displacement u_y^{α} along cell side α with no

crack present, using cells A and B in series gives

$$u_y^{\alpha} = u_y^{A} + c_2^{A}/(c_2^{A} + c_2^{B})\,(u_y^{B} - u_y^{A}) \qquad (2\text{-}5a)$$

where c_2^{i} is the elastic constant c_2 of the i^{th} cell. In a similar fashion, the x-displacement u_x^{α} along side *a* is given by

$$u_x^{\alpha} = u_x^{A} + c_3^{A}/(c_3^{A} + c_3^{B})\,(u_x^{B} - u_x^{A}) \qquad (2\text{-}5b)$$

where, in this case, shear moduli c_3^{i} are used. If side α contains an open crack (Fig. 2.4b), then no stress is transmitted across the side and

$$\begin{aligned} u_j^{\alpha} &= u_j^{A} \\ u_j^{\beta} &= u_j^{B} \end{aligned} \qquad (2\text{-}6)$$

If side α contains an open crack of length l out of a total side length l_o (Fig. 2.4c), then the *average* displacements on the side are approximated by

$$\begin{aligned} u_x^{\alpha} &= \xi\,(u_x^{A} + c_3^{AB}\,(u_x^{B} - u_x^{A})) + (1 - \xi)\,u_x^{A} \\ u_x^{\beta} &= \xi\,(u_x^{A} + c_3^{AB}\,(u_x^{B} - u_x^{A})) + (1 - \xi)\,u_x^{B} \\ u_y^{\alpha} &= \xi\,(u_y^{A} + c_2^{AB}\,(u_y^{B} - u_y^{A})) + (1 - \xi)\,u_y^{A} \\ u_y^{\beta} &= \xi\,(u_y^{A} + c_2^{AB}\,(u_y^{B} - u_y^{A})) + (1 - \xi)\,u_y^{B}\,. \end{aligned} \qquad (2\text{-}7)$$

The weighting parameter for the crack length is defined as

$$\xi = 1 - l/l_o \qquad (2\text{-}8)$$

and $c_i^{AB} = c_i^{A}/(c_i^{A} + c_i^{B})$. Once the average displacements are computed for each edge, strains and then stresses are computed. For example, to compute P_{yy}, the *average* normal stress between cells A and B (Fig. 2.4d), first compute strain components in cells A and B. For example,

$$\begin{aligned}
\varepsilon_{xx}^{A} &= (u_x^{\gamma} - u_x^{\delta})/l_o \\
\varepsilon_{yy}^{A} &= 2(u_y^{\alpha} - u_y^{A})/l_o \\
\gamma_{xy}^{A} &= (u_y^{\gamma} - u_y^{\delta})/l_o + 2(u_x^{\alpha} - u_x^{A})/l_o
\end{aligned} \tag{2-9}$$

Then the average normal stress component becomes

$$\begin{aligned}
P_{yy} = \xi/2 \; (& c_4^{A} \varepsilon_{xx}^{A} + c_4^{B} \varepsilon_{xx}^{B} \\
& + c_2^{A} \varepsilon_{yy}^{A} + c_2^{B} \varepsilon_{yy}^{B} \\
& + c_6^{A} \gamma_{xy}^{A} + c_6^{B} \gamma_{xy}^{B}) .
\end{aligned} \tag{2-10}$$

The weighting function ξ assures that no stress is transmitted across a fully cracked edge. Expressions for the other stress components are constructed in a similar manner. Eq. (2-10) gives the desired result for both fully cracked edges ($P_i = 0$) and uncracked edges (where it reduces to the form shown in (2-3)).

For simplicity, the previous development has been restricted to horizontal and vertical cracks. However, the model has been augmented to include diagonal cracks. In this case, the procedure for computing strains and then stresses is essentially the same as before, with the added complexity of computing local stress and strain components along directions rotated 45° to the sample axes. The assumption that material properties at the finest level are isotropic leads, mercifully, to significant simplification of the difference equations and offsets some of the geometric complications. The isotropic stiffness tensor values, expressed in terms of the Lamé constants λ and μ, are one of the model inputs:

$$c_{iso} = \begin{vmatrix} \lambda+2\mu & \lambda & 0 \\ \lambda & \lambda+2\mu & 0 \\ 0 & 0 & \mu \end{vmatrix} = \begin{vmatrix} c_{1iso} & c_{4iso} & 0 \\ c_{4iso} & c_{2iso} & 0 \\ 0 & 0 & c_{3iso} \end{vmatrix} . \tag{2-11}$$

In this case, the series approximation for displacements at cell edges (*e.g.* eq. 2-5a) becomes

$$u_y^{\alpha} = u_y^{A} + (u_y^{B} - u_y^{A})/2 . \tag{2-12}$$

Average edge displacements for edges containing cracks become, for example (referring again to Fig. 2.4c),

$$
\begin{aligned}
u_x^{\alpha} &= \xi\,(u_x^{A} + (u_x^{B} - u_x^{A})/2\,) + (1 - \xi)\,u_x^{A} \\
u_x^{\beta} &= \xi\,(u_x^{A} + (u_x^{B} - u_x^{A})/2\,) + (1 - \xi)\,u_x^{B} \\
u_y^{\alpha} &= \xi\,(u_y^{A} + (u_y^{B} - u_y^{A})/2\,) + (1 - \xi)\,u_y^{A} \\
u_y^{\beta} &= \xi\,(u_y^{A} + (u_y^{B} - u_y^{A})/2\,) + (1 - \xi)\,u_y^{B}\,.
\end{aligned}
\qquad (2\text{-}13)
$$

Strains needed for computing P_{yy} are again given by eq. (2-9), and

$$
P_{yy} = \xi/2\;\left(c_{4iso}\,(\varepsilon_{xx}^{A} + \varepsilon_{xx}^{B}) + c_{2iso}\,(\varepsilon_{yy}^{A} + \varepsilon_{yy}^{B})\right). \qquad (2\text{-}14)
$$

To accomodate diagonal cracks, displacements are maintained in two coordinate systems; the standard (x,y) system and an (r,s) system rotated counterclockwise by 45° (Fig. 2.3). Then, displacements, strains and stresses along diagonal edges are all computed in the (r,s) system.

Crack Closure

Numerous studies have analized the closure of cracks in compression (*e.g. Brace et al.*, 1965; *Walsh*, 1965; *Walsh and Brace*, 1966; *Walsh and Grosengaugh*, 1979). Since we wish to simulate the effects of confining pressure in our model, it is desirable to have some mechanism for crack closure. As with other aspects of the model, it seemed appropriate to choose a closure algorithm that was simple while reproducing the main features of the closure process. The algorithm currently in use describes crack closure in terms of the net strain ε_{normal} between nodes across a crack. If $\varepsilon_{normal} > 0$, the crack is designated open. For $\varepsilon_{normal} < 0$, the fraction of the crack that is open is given by $A^{-b\varepsilon}$. Constants A and b have been chosen so that cracks are approximately 80% closed for a normal stress of 1 kb (100 MPa). This gives reasonable agreement with granite data (*Brace et al.*, 1965; *Bernabe*, 1986; *Morrow et al.*, 1986). A more accurate algorithm is planned for future implementation.

Crack Surface Friction

The algorithm for computing slip offsets on crack surfaces has a simple form. A slip vector is defined for each crack so that the total slip offset parallel to the crack surface is η (Fig. 2.5). We begin by assuming that an edge which in not completely cracked will have no slip offset ($\eta = 0$). This is done partly as a matter of convenience. However, the increased compliance of a partially cracked edge is taken into account in the procedure used to compute subnode displacements. The main disadvantage of neglecting slip on partially cracked edges is that it sets a threshold of a unit crack length for frictional historesis effects. For edges which are completely cracked, the total shear strain γ in the material near the crack will be reduced by slip on the crack:

$$\gamma = \gamma_0 - \eta/d \tag{2-15}$$

where γ_0 is the shear strain that would result if there were no slip on the crack and d is the distance between displacement nodes. If the crack is open, then no shear stress and therefore no shear strain can be sustained so that $\eta = \gamma_0 d$. Then, the only remaining case is for a crack which is partially or completely closed (as express by the parameter ξ). Since ξ represents the fraction of the crack that is closed and the normal stress P_{normal} as computed above represents the stress averaged over the entire edge, the average normal stress on the closed portion of the crack is really $P^c_{normal} = P_{normal}/\xi$. Then the magnitude of the shear stress that can be supported by the closed portion of the crack is

$$|P^c_{shear}| = -f P^c_{normal} = -f P_{normal} / \xi \tag{2-16}$$

where f represents the coefficient of friction. The minus sign is required since compressive stresses are negative. The corresponding range in strain is just $|\gamma| = -f P_{normal} / (\xi\mu)$. Since shear strain and therefore shear stress will be zero for $\eta = \gamma_0 d$, η must fall in the range

$$d (\gamma_0 + f P_{normal} / (\xi\mu)) \le \eta \le d (\gamma_0 - f P_{normal} / (\xi\mu)) . \tag{2-17}$$

If η from the previous program iteration falls within this range, it remains unchanged so that the crack remains locked in its previous position. If η lies outside of this range, it is reset to the nearest bound, indicating that the crack has slid at its frictional strength limit. This procedure allows the crack to slide in one direction and then, if loaded in the reverse sense, to remain locked until its shear strength is again exceeded. It also allows a crack to become stronger or weaker as the normal stress varies. In the present simulations, the coefficient of friction was $f = 0.5$. *Byerlee* (1978) found that for a wide range of silicates, the coefficient of friction ranged from $0.6 < f < 0.85$. The cracks most favorably orientated for sliding would be inclined approximately 30° to the maximum compressive stress. Since the present model is limited to 45° cracks, a coefficient of 0.5 on these cracks would allow slip at approximately the same differential stress as $f = 0.6$ on a 30° crack.

Crack Growth Criteria

Once the stress components along cell edges have been computed, a procedure must be developed to decide when cracks will grow. The algorithm adopted in this model is based on the stress intensity factors K_I (mode I tensile crack growth) and K_{II} (mode II in-plane shear crack growth) as used in fracture mechanics. In terms of the mechanical properties of a medium, a crack would be represented as a discontinuity in elastic properties. When the medium is stressed, this leads to discontinuities in both stress and displacement. In the case of the long, thin cracks that are of interest in the present study, singularities in stress and displacement develop at the crack tips which can be expressed in terms of the stress intensity factors. The fracture mechanics approach to the analysis of stressed cracks has been developed in, for example, *Lawn and Wilshaw* (1975) and *Liebowitz* (1968) and a variety of solutions to particular problems appear in *Sih* (1973) and *Paris and Sih* (1965). Applications to geologic problems appear in, for example,*Li* (1987), *Pollard and Segall* (1987), *Dmowska and Rice* (1983) and *Rudnicki* (1980). We wish to consider the conditions necessary for microcrack growth in an overall compressive stress state. It is generally accepted that cracks grow in tension when the stress singularity at a crack tip overwhelms the remotely applied stress field. A classic example is the development of wing cracks in response to slip on a crack oriented obliquely to the principal stress directions. *Lawn and Wilshaw* (1973)

analyze this situation of mixed mode loading in which both K_I and K_{II} are present. Using a maximum strain energy release rate criterion, they show that the presence of mode II stress intensity promotes out-of-plane crack growth. In fact, crack extension tends to be in the direction where local tensile stress is the greatest. We have adopted this rule as a criterion for choosing the direction of tensile crack growth. A limited number of tests were conducted to verify the performance of the model. The simplest case of an isolated crack loaded in tension gave the proper in-plane extension. An isolated diagonal crack loaded in compression also developed wing cracks in the proper orientation. Finally, a variety of right and left stepping crack pairs were loaded in shear. On a qualitative basis, the development of interconnecting cracks agreed with the predictions of *Segall and Pollard* (1980) (*e.g.* tensile cracks developed, spanning the fault jog, in the case of right-lateral slip on right stepping cracks).

In addition to choosing the direction of propagation, we must also decide at what stress level a crack will propagate. While this would be straight forward for an isolated crack, our model must deal with a variety of complicated geometries. This is a key element in the model and, unfortunately, is dealt with in only an approximate manner. Future versions would clearly benefit from an improvement of this treatment. The problem would be more tractable if stresses at crack tips were known more accurately. However, the stress components computed for each cell side are local stresses and at the same time are averaged over distances large compared to the crack tip singularity region. Before describing the precise crack growth algorithm, we will summarize the basic result. In effect, a crack will grow when a tensile strength limit on a neighboring cell edge is exceeded. This limit is $T_0 = K_{IC} l_0^{-1/2} = 1$ kb for the current model parameters (K_{IC} is the critical stress intensity factor for mode I crack growth and l_0 is the length of the unit cell in the model).

While the mode I crack growth criterion reduces to the preceeding tensile stress criterion for most cases, the actual algorithm is more complicated and approximates a maximum strain energy release rate rule for cases where crack interaction is weak. If we first consider a single crack of unit length l_0, stresses on adjacent cell sides would occur in 'region 3', using the classification of *Pollard and Segall* (1987). This encompasses the region greater than one crack width from the crack center ($r > l/2$ where l is crack length) and is characterized by a stress field perturbation, due to the crack, that drops off as $(r/l)^{-2}$. As an example, an isolated unit length crack was loaded

in tension and the normal stress on the edge just off the end of the crack was 1.3 times greater than the remotely applied stress. Using the region 3 stress approximation from Pollard and Segall, we would expect a stress amplification of 1.2. Again, for isolated cracks, this near-field calculation could be handled efficiently. The difficulty is that in the model, crack networks develop so that effective crack lengths become large and shapes become irregular. In this case there is no simple way of relating the stress computed for a cell edge to the stress intensity at a neighboring crack tip. By default, we have chosen to assume that the stress for a cell side represents 1.3 times the equivalent far-field stress for a crack tip loaded in isolation. The approximate stress intensity factor then becomes $K_I = (\pi l_o/2)^{1/2} P_{normal}/1.3$. This expression is correct for the simple case of pure mode I extension. However, we make no attempt at improving upon it in the case of more complicated geometries. When the approximate stress intensity computed in this manner exceeds a critical value K_{IC}, the crack is allowed to grow. The critical stress intensity factor K_{IC} can be considered a material property. It has been determined experimentally (*Atkinson and Meredith*, 1987b) to be 1 - 4 MPa-$m^{1/2}$ for many silicates. A value of 1 MPa-$m^{1/2}$ has been used in this study. This criterion is also applied to cell sides that are only partially cracked. In this case, the model was calibrated by loading a single partially cracked cell side in pure mode I and observing the resulting stress that was developed on the uncracked portion of the cell. An appropriate empirical function was then developed to relate the local stress to the far-field stress so that in this case, $K_I = (\pi l/2)^{1/2} P_{remote}$.

An initial series of simulations was conducted in which cracks grew only when this mode I growth criterion was met. In this case, it was found that there was no curvature to the Mohr failure envelope and that the sample strength continued to increase unbounded with increasing confining pressure. It was obvious that some additional failure mechanism was required to operate at high confining pressure. The crack growth criterion that was settled on was for mode II crack extension. It may be more appropriate to use the term 'apparent' mode II since the microscopic mechanism for in-plane shear is left unspecified. One possible mechanism would be the development and coalescence of en echelon tensile cracks. At the level of resolution of the model, however, crack growth appears to be mode II, and the term 'apparent' will not be used further. For mode II growth, we compute a stress intensity factor $K_{II} = |\tau|(\pi l_o/2)^{1/2}$ where τ is shear stress. Then, a crack is allowed to propagate in mode II for $K_{II} \geq$

K_{IIC}. *Rice* (1980) and *Wong* (1982a) examined the critical strain energy release rate G_{IIC} for mode II crack propagation. They reported that, based on laboratory measurements of poly-crystalline rock, G_{IIC} ranged from 0.5×10^4 to 7×10^4 J-m^{-2} (seismological estimates of G_{IIC} are typically 2 to 4 orders of magnitude larger). Since G_{II} is related to K_{II} by $G_{II} = \{(1-\nu^2)/E\}K_{II}^2$, these laboratory determinations suggest that for crystalline rocks, K_{IIC} ranges from approximately 10 to 50 MPa-m$^{1/2}$. A value of K_{IIC} = 15 MPa-m$^{1/2}$ has been used in all computer runs. As we will show in the simulations, at low confining pressure, tensile crack growth is dominant. However, as confining pressure is increased, tensile cracking is suppressed and an increasing number of cracks grow in shear. The ratio of the critical stress intensity factors determines the pressure where this transition occurs.

Finally, the crack growth algorithm used in the model is as follows. Each junction where potentially eight cracks can meet is evaluated individually. The approximate stress intensity factors are computed for each uncracked edge and divided by the appropriate critical stress intensity factor.The largest value is selected and, if it is greater than unity, the corresponding edge, and only that edge, is allowed to grow a crack.

Time Dependence

As presented so far, the model contains no time-dependence other that the basic assumption of causality that new cracks will grow in response to the present crack population and boundary conditions. That is, once a stable configuration is achieved, no crack growth will occur until the boundary conditions are changed. The majority of the simulations were performed in this manner. However, it is well known that rocks will creep under constant applied boundary stress conditions. To investigate these time-dependent phenomena, a limited number of simulations were conducted in which the model was extended to include subcritical crack growth. The dominant mode of subcritical crack growth rate, v, is found empirically to satisfy a power law dependence on stress intensity factor (*Atkinson and Meredith*, 1987a); *i.e.* $v = AK_I^n$, where A and n are constants. Since the present model computes an approximate stress intensity factor for each crack, it is relatively straight forward to include the subcritical crack growth rate.

Satisfying Equilibruim Conditions

Equilibrium is achieved by balancing forces and moments. Balancing moments requires that in the absence of internal torques, shear stresses in orthogonal directions at every point must be equal (*e.g.* $P_{xy} = P_{yx}$ and $P_{rs} = P_{sr}$). Forces are balanced in x- and y-directions for each element in the sample. In the square array geometry (Fig. 2.1c), elements are simply the square unit cells. In the diagonal crack geometry (Fig. 2.3), elements are the 45-45-90° triangular elements of which there are four per unit cell. In this case, shear and normal stresses acting on the diagonal sides of elements are resolved into tractions in the (x,y) reference frame. An inversion routine is used to adjust displacements to bring each cell into equilibrium. First, the sample is divided into blocks of 3x3 unit cells each. Each of these blocks is adjusted separately. For an individual block, vectors are generated for stress components, P_j, on each side, sums of forces acting on each cell, F_i, and displacement adjustments, Δu_i, of each node. For each iteration, P_j is premultiplied by a simple matrix A_{ij}, which is determined by the cell geometry, to compute the force imbalances F_i on each cell. Another matrix, relating pressure changes to displacement changes, $S_{ji} = \partial P_j/\partial u_i$, must be constructed each time the crack population or the material properties of the block are changed. The desired displacement adjustments are those needed to null the force imbalances. Then

$$S\,\Delta u = \Delta P \tag{2-18}$$

and the stress adjustments are related to the force corrections through A,

$$-F = A\,\Delta P\,. \tag{2-19}$$

Defining the matrix product G = AS gives

$$-F = AS\,\Delta u = G\,\Delta u\,. \tag{2-20}$$

Therefore, displacement adjustments are expressed as

$$\Delta u = -G^{-1}\,F\,. \tag{2-21}$$

G is a square, sparse, non-symmetric matrix.

Multiple Scaling or Renormalization Group Method

In principle, the matrix G could be constructed for the entire sample and solved in one step. However, this is problematic for any reasonably sized test sample. The current model is using a sample size of 27 x 54. With four sub-elements per unit cell and two displacement components per sub-element, this direct approach would require inverting an 11,664 x 11,664 array. In 3D, the array dimension would grow to approximately 2.8×10^6. The multiple scaling approach provides a means of avoiding dealing with the entire sample matrix at one time. By breaking the overall system into 3 x 3 blocks, matrix inversions are kept small. In the case of the square 2D array, G has dimensions of 18 x 18. For the 2D diagonal crack array, the dimension increases to 72. Even in the 3D case, the array dimension is still a managable 648. In fact, for the 2D diagonal array, more computation time is spent constructing G than in inverting it.

The basic approach in the multiple scaling procedure has been described in *Madden* (1976, 1983) and *Williams and Madden* (1988). The basic idea is taken from renormalization group theory, RNG, which was developed primarily in quantum mechanics and applied to critical phenomena. While the procedure of averaging quantities and changing scale is important in RNG, it represents only a limited aspect of the theory. We therefore prefer, in the present context, to use the term 'multiple scaling'. As an example, we will consider a three level system with the top level consisting of 27 x 27 elements. This level is divided into 81 square blocks of 3 x 3 elements each. The operators $G_{ij}^{l=3}$, where l refers to level, are individually constructed based on the location of cracks, the degree of closure of each crack, and the local elastic constants. In the present model, the material is assumed to be homogeneous (in the absence of cracks) and isotropic. This condition is not a restriction of the method, but rather, was adopted for convenience to simplify the inputs used in the starting model. Thus, the only inhomogeneity present in the model is due to the position of cracks. After the individual operators are constructed, their inverses are computed and stored for later use. For each block, a full stiffness tensor, consisting of six independent elements, is determined to represent average material properties. This is

accomplished by subjecting the block to three independent strain conditions: $\varepsilon^1 = \alpha(1,0,0)$; $\varepsilon^2 = \alpha(0,1,0)$; $\varepsilon^3 = \alpha(0,0,1)$ and finding the average stress tensors that are produced. From these nine relations between average stress and average strain, average elastic properties are determined using a least squares fit. At this stage, the original level 3 sample is represented by a 9 x 9 array of elements on level 2, comprised of averaged elastic properties. Next, the procedure is repeated, this time operating on the level 2 elements. Level 2 is divided into 9 square blocks, again consisting of 3 x 3 elements. The individual operators $G_{ij}^{l=2}$ are constructed and their inverses stored. Each block is tested to determine average elastic constants. These new elastic constants are used to represent the original sample by a set of 3 x 3 elements corresponding to level 1. The final step involves performing the same procedure on the level 1 elements to arrive at a single set of elastic constants (level 0) that represent the average properties of the entire sample.

Now that the bulk properties of the sample are known, the second half of the modeling procedure is begun. First, the desired boundary conditions are applied to the sample. Using these boundary conditions and the stored inverse operator $[G^{l=1}]^{-1}$, displacements at the nine level 1 nodes are computed. These level 1 displacements are then used as boundary conditions in conjunction with the level 2 operators $[G_{ij}^{l=2}]^{-1}$ to solve for displacements of level 2 nodes. Repeating the procedure one more time provides displacements for the level 3 nodes. From these displacements, the local stresses on the sides of individual elements are calculated. Finally, by using the local stresses in computing the stress intensity factors, the growth of new cracks is determined.

A number of comments need to be made about this basic procedure. Each change in level in the averaging scheme is accompanied by a significant reduction in the distribution of elastic properties throughout the sample. Clearly, the original sample contains the maximum contrast in properties since it can contain elements with no cracks and therefore full stiffness components as well as fully cracked sides with essentially zero stiffness. The off-diagonal average stiffness components, c_4 through c_6, for level 3 can be quite large. However, c_5 and c_6 invariably approach zero as they are averaged over larger and larger regions. For the case where there is no preferred crack orientation, the material must appear isotropic in bulk. Thus, on a scale large compared with the crack size, the elastic tensor components must assume the relations

given by eq. (2-11), although λ_{bulk} and μ_{bulk} will be less than λ and μ for the individual crystals. For simulations in which the principal stress directions of the applied stresses are oriented parallel to the x- and y-axes, the orthorhombic symmetry requires c_{5bulk}, $c_{6bulk} = 0$. This, in fact, is observed. By averaging over only three scales, c_{5bulk} and c_{6bulk} are consistantly reduced to $> 0.005\ \mu$.

Since the method for estimating average material properties is not exact, we wish to know that the estimated properties are physically meaningful. This becomes increasingly important as crack populations increase and some of the stiffness components approach zero. By considering the work needed to deform an elastic body (*Nye*, 1986), it can be shown that c_{ij} is symmetric. To be stable, any deformation from a state of zero applied stress must involve an increase in strain energy, given by $1/2\ c_{ij}\ \varepsilon_i\ \varepsilon_j$. This condition requires that c be positive definite and therefore that the three pivots of c are all positive (*e.g. Strang*, 1986). The first condition is simply

$$c_1 > 0\,. \tag{2-22a}$$

A positive second pivot requires

$$d_1 / c_1 > 0 \tag{2-22b}$$

where $d_1 = c_1c_2 - c_4c_4$. Similarly, a positive third pivot requires

$$(d_1d_2 - d_3d_3) / c_1d_1 > 0 \tag{2-22c}$$

where $d_2 = c_1c_3 - c_5c_5$ and $d_3 = c_1c_6 - c_4c_5$. Conditions (2-22a) and (2-22b) require

$$c_1 > 0 \tag{2-23a}$$
$$c_2 > 0 \tag{2-23b}$$
$$c_4^2 < c_1c_2. \tag{2-23c}$$

Condition (2-22c) places constraints on the remaining stiffness elements, requiring:

$$c_3 > 0 \tag{2-23d}$$

$$c_5^2 < c_1 c_3 \tag{2-23e}$$

$$(c_4c_5 - (d_1d_2)^{1/2})/c_1 < c_6 < (c_4c_5 + (d_1d_2)^{1/2})/c_1 \, . \tag{2-23f}$$

All stiffness tensors are evaluated according to these constraints. Occasionally, one of the restrictions will be violated, in which case, small adjustments are made to satisfy inequalities (2-23). No large adjustments are ever required.

Other than effects of crack interactions, the multiple scaling procedure described above is linear and, for a given set of boundary conditions, an equilibrium configuration can be determined in one iteration. However, there is one disadvantage of the method. As described, displacements at a given level are determined from elastic properties at that level and boundary displacements at the next lower level. Since these boundary displacements are arrived at from elastic properties averaged at the lower level, they provide an approximate boundary condition which, at best, gives only an average displacement on the boundary. Thus errors are locked into the displacement solution and are propagated along, level by level. To avoid this problem, the basic modeling scheme was modified in the following way. Rather than computing displacements at each level from the overall imposed boundary conditions, only changes in displacements, due to changes in boundary conditions and elastic constants, are computed. These changes are carried through to the finest level where they are added to the displacements from the previous iteration. Then, the entire level 3 array is re-solved, block by block, using the surrounding displacements as boundary conditions. This relaxation procedure, in which the entire sample is adjusted locally, would eventually converge on the correct solution, even without the multiple scaling procedure. However, while the procedure is efficient at removing short wavelength errors, it is very inefficient at removing long wavelength residuals. By contrast, the multiple scaling procedure ignores short wavelength information in favor of the average properties. By combining the long wavelength sensitivity of the multiple scaling technique with the short wavelength sensitivity of the relaxation procedure, we have taken advantage of the best features of each.

Computation Time

As a matter of interest, we give a brief account of the computation time involved in

the simulations. For all practical purposes, the program is completely cpu-bound. The main computational expense is in building and inverting the 72 x 72 element stiffness arrays. For a sample size of 27 x 54 unit cells, one program iteration requires approximately 30 minutes on a VAX 785. There are undoubtedly ways of improving program efficiency. However, these are not anticipated to result in dramatic improvements in computation speed.

Summary of Model

The multiple crack interaction model requires the following inputs (values used in current model are listed in brackets):

Lamé constants λ, μ for intact matrix material. [$\lambda = \mu = 400$ kb (40 GPa)]

Critical stress intensity factors, K_{IC}, K_{IIC}, for crack growth criteria. [K_{IC} = 0.01 kb-$m^{1/2}$ (1 MPa-$m^{1/2}$); $K_{IIC}/K_{IC} = 15$]

Coefficient of friction, f, for friction on cracks. [$f = 0.5$]

Parameters A, b to define crack closure characteristics. [approximately 80% crack closure for $P_{normal} = 1$ kb]

For time-dependent model, power law exponent n relating crack growth rate to stress intensity factor. [n = 20]

Initial crack population.

Stress/strain boundary conditions (and time history if desired).

General assumptions and features of the model are:

Matrix material is elastic and, in present model, isotropic.

Cracks grow unstably according to fracture mechanics critical stress intensity rules in either mode I (tension) or mode II (in-plane shear). As used in the model, in-plane shear crack growth may be more appropriately referred to as an apparent mode II phenomena, since the microscopic mechanism, whether tensile or shear, is left unspecified.

For time-dependent modeling, crack growth rate is assumed to obey subcritical crack growth power law.

Cracks can only grow along vertical and horizontal boundaries and diagonals of unit cells.

Cracks close in response to normal stress.

Closed portions of cracks can support shear stress up to their frictional strength limit. Fricitonal strength is represented by a single coefficient of friction f. For time-independent modeling, f is constant. In some

time-dependent simulations, subcritical crack slip rate is a function of f.

A slip vector is assigned to each crack to keep track of slip offset.

In the present application, a uniform stress boundary condition is designated for the sides of the sample to simulate laboratory triaxial experiments in which confining pressure is applied.

Top and bottom boundary conditions are given as vertical displacements and zero average shear stress.

Material in contact with top and bottom of sample is assumed to have the same average elastic properties as the sample and changes properties as the average sample properties change.

Model Results and Comparisons to Laboratory Experiments

The main series of computer runs has been designed to simulate laboratory experiments performed on a triaxial testing apparatus. In a typical triaxial experiment, a cylindrical sample is placed in a pressure vessel which is then pressurized with an appropriate confining fluid (Fig. 2.6). A thin, impermeable jacket is used to separate the sample from the confining fluid. Deviatoric stress is achieved by advancing a piston against the end of the sample column. Thus, the boundary conditions become: On the sides of the sample, uniform normal stress ($\sigma_2 = \sigma_3 = P_{conf}$) and zero shear stress. A displacement boundary condition is commonly prescribed at the ends of the sample, so that the maximum compressive stress σ_1 is oriented parallel to the sample axis. Due to the mismatch in moduli between the sample and steel end caps, the ends of the sample are generally constrained laterally. This effect leads to a distortion of the stress field near the ends of the sample. As a result, a length-to-diameter ratio of 2.5 is commonly used to provide a sufficient working volume, which is free of end effects, in the center of the sample (*Jaeger and Cook,* 1984).

Results of a laboratory test on Westerly granite are shown in Fig. 2.7. Sample dimensions were 25.4 mm-diameter by 63.5 mm-length. The sample was deformed at a confining pressure of 400 bars (10 bars = 1 MPa) and an axial strain rate of -10^{-5} s^{-1}. Differential stress ($\sigma_{dif} = \sigma_1 - \sigma_3$), circumferential strain and volumetric strain are plotted as functions of axial strain in Fig. 2.7. Features that are typical of this type of deformation experiment of brittle rock include peak strength σ_{max}, Young's modulus (E = slope of stress-strain curve), and onset of dilatancy ($\partial\varepsilon_V/\partial\varepsilon_{11} > 0$) which generally occurs between 1/3 and 2/3 of the total strain (*Brace et al.*, 1966).

To simulate this type of experiment, the 2D computer model includes a stress boundary condition applied at the sides of the sample: $P_{xx} = P_{conf}$, $P_{xy} = 0$ (Fig. 2.8). Mixed boundary conditions are applied at the top and bottom of the sample. Vertical displacements at y = 0 and y = 2L are chosen to provide an average desired vertical strain ε_{yy}. Rather than simulating the steel end caps used in laboratory experiments, the computer sample is assumed to be in contact with rock of the same average elastic properties. Since the elastic properties of the sample change during the experiment, the adjacent rock also changes. In this way, the most severe of the end effects are removed and a sample length-to-diameter ratio of 2 is used. The final

boundary condition is that the y = 0 and y = 2L surfaces are translated laterally to maintain zero average shear tractions.

A computer simulation for P_{conf} = 1 kb is shown in Fig. 2.9. Notice that the sample 'fails', although no discrete fault plane develops. This point will be discussed more fully. Also, as was the case with the laboratory sample, the model sample becomes dilatant before failure. (For plane-strain, $\varepsilon_{zz} = 0$ so $\varepsilon_v = \varepsilon_{xx} + \varepsilon_{yy}$.) The unevenness in this and subsequent stress-strain curves comes from two sources. As discussed earlier, the model is nonlinear both through crack interactions and through the frictional properties of the cracks. Following an increment of axial strain, a set of new cracks will be formed. By redistributing stresses locally, these cracks may induce the formation of a secondary set of cracks, even though the boundary conditions are not changed. With an additional iteration of the model, a tertiary set of new cracks may be formed, and so on. This crack interaction becomes increasingly important as the sample approaches peak strength and, in fact, is the primary motivation for undertaking this study. Each of these sequences shows up as a vertical drop in differential stress in Fig. 2.9. Note that time is not a parameter in this simulation and each of these relaxation sequences is seeking a stable crack geometry for the given applied boundary conditions. In this sense, the equilibrium stress-strain curve would be represented by the locus of points connecting the minimum differential stress at each strain increment. In the post-failure region, a point was reached where the production of new cracks increased each iteration, even though the applied axial strain was held constant. Apparently, the stored internal elastic strain energy was sufficient to drive the sample into mechanical instability. This material would be termed class II by *Wawersik and Fairhurst* (1970), who distinguished between failure which was driven by the elastic energy stored in the loading system and failure which would proceed catastrophically even if the loading system has infinite stiffness, as is the case for these simulations.

The nonlinearity due to crack friction comes into play as soon as shear stresses are large enough to cause slip on cracks. This happens when the slope of the stress-strain curve begins to decrease. As with the creation of new cracks, slip on existing cracks alters the local stress field so that in the next model iteration, slip may be induced on nearby cracks. This process requires many iterations to converge and proved to be the most costly in terms of computation time. Constraints in available computer time required that in this and subsequent simulations, the model was never allowed to relax

fully. To evaluate the severity of this problem, a run was conducted using smaller strain steps so that the model remained much closer to equilibrium. While the peak strength was about 12% lower, the sequence of crack development was essentially the same as that shown in Fig. 2.9. It was therefore decided that the general features of the crack interaction process could be studied even though the sytem was being driven away from equilibrium throughout the simulations.

Model parameters used in this simulation are listed in Table 2.1. The starting crack population, which will be refered to as M1, is shown in Fig. 2.10a. Crack sites were filled randomly so that 20% of the possible crack sites were fully cracked. This is less than the critical probability for crack connectivity in 2D (28%), so that no connected path exists from top to bottom or from side to side. The largest cluster of connected cracks contains 73 cracks and is shown in Fig. 2.10c. As new cracks grow in the stressed sample, the largest clusters gradually grow by accreting smaller clusters. Since new cracks are only allowed to appear on cell edges, the resolution of the model is determined by the length scale of the unit cell. At the same time, the model is capable of dealing with partially cracked cell edges, so it was decided to emplace partial cracks on all cell edges that were not fully cracked (Fig. 2.10b). This provides only partial compensation for the limited resolution that is inherent in the model, since it restricts the locations of small cracks to cell sides and therefore cannot provide for the densities of smaller cracks which would be appropriate for a real rock. The small-scale cracks would be more appropriately simulated by reducing the material properties of the matrix material from single crystal stiffnesses to stiffnesses appropriate to a multi-crystalline aggregate containing the appropriate flaw densities. No attempt was made, however, to include these features in the present model, so that we expect strength and stiffness values in the simulation to be a bit high. In addition, restricting inclined cracks to 45° will also tend to make the sample stronger. By including partially cracked edges in the starting model, we do provide seed cracks in regions which happen to lack full cracks and therefore would otherwise be unrealistically strong. If l_0 is the length of a cell side, then the distribution of normalized crack lengths l/l_0 for starting model M1 is shown in Fig. 2.10d. This seed crack size distribution was chosen arbitrarily as a simple starting model. Also shown in Fig. 2.10d is the distribution of cluster sizes for clusters of connected cracks.

Confining Pressure Dependence

Stress-strain curves for a suite of runs at selected confining pressures are plotted in Fig. 2.11. Simulations are then plotted individually in Figs. 2.12 through 2.19. All of these runs used the parameter values listed in Table 2.1 and starting crack population M1. With the exception of the unconfined run, all of the stress-strain curves have the same initial slopes. The crack closure algorithm used in the model was chosen so that cracks would close by approximately 1 kb normal stress. Thus, the unconfined run has a reduced initial slope since it is the only case where significant closure of horizontal cracks could occur during axial loading. In all examples, the slope of the stress-strain curve (Young's modulus) first began to decrease when shear stress was sufficiently large to cause slip on existing diagonal cracks. Slip on these cracks results in the concentration of stress at the crack tips. At low confining pressure, the local tensile stresses that develop at the crack tips eventually overcome the overall compressive stress state imposed by the confining pressure, resulting in the growth of axial wing cracks. As discussed earlier, this process leads to the opening of microcracks in the rock and the onset of dilatancy. However, as confining pressure is increased, the differential stress needed to produce tensile stresses at crack tips also increases. One reason for this is that the ambient stress field at the crack tips becomes more compressive with increased confining pressure, creating a larger stress difference which must be overcome to achieve a tensile stress state. The other reason is that increased confining pressure increases the frictional strength of the cracks so that higher shear stresses are needed before cracks begin to slip. Thus, as confining pressure is increased, shear stress at the crack tips also increases. A point will be reached where it becomes easier for diagonal cracks to extend in mode II shear than in tension. This transition is shown in Figs. 2.12 through 2.19 where cumulative crack growth is plotted *vs* axial strain. Horizontal (y-normal) cracks are, for the most part, closed by the axial load and contribute little to the kinematics of the problem. For this reason, they are not plotted. Crack populations that are important are the vertical (x-normal) and diagonal cracks. As discussed earlier, cracks are allowed to grow in either tension (mode I) or shear (mode II), when the appropriate critical stress intensity factor is exceeded. In the present simulations, in which there is no time-dependent crack growth, we assume that once the critical stress intensity is exceeded on a partially

cracked edge, the crack will grow unstably in a single program iteration, cracking the entire edge and creating a 'new' crack. In this context, a 'new' crack is said to occur each time a potential crack site becomes fully cracked. The cumulative number of cracks which grew in each of these four categories is plotted in the figures. Referring to Fig. 2.14, for example, mode I axial cracks begin to grow at the onset of dilatancy, and are the dominant mode of cracking. This development of axial cracks as open voids in the rock has been well documented in laboratory experiments and is responsible for most of the anisotropy in material properties that develops as rocks approach failure. The onset of dilatancy corresponds to the ambient stress level where locally the confining pressure is overcome and tensile stresses are developed. The primary mechanism for this is slip on diagonal cracks, producing tensile stresses at the crack tips and the development of vertical 'wing' cracks. The onset of failure at 1.05% axial strain is accompanied by the abrupt production of diagonal cracks in tension. Since the overall stress field for cracks of this orientation is compressive, development of tensile cracks indicates that locally the stress field is being rotated. A frequently cited mechanism for the coalescence of axial cracks into a shear zone is the buckling of closely spaced slender columns (*Wong*, 1982a; *Nemat-Nasser and Horii*, 1982; *Ashby and Hallam*, 1986; *Sammis and Ashby*, 1986). While our computer model does not contain a direct analog to buckling, the large rotations of the local stress fields represent the development of a similar geometric instability. The other significant crack growth that occurs is the development of diagonal cracks in mode II. These cracks grow at a nearly continuous rate throughout the loading cycle and represent failure of partially cracked sites. To understand this, remember that the initial crack population (Fig. 2.10b) consisted of 20% fully cracked sites and 80% partially cracked sites. Thus some sites were broken nearly through and developed large K_{II} stress intensity factors when loaded. At quite modest differential stress levels, some of these cracks were driven to link up with neighboring cracks. Especially at low confining pressure, this mode II crack growth is an artifact of the model since cracks are restricted to cell edges. In a real rock the majority of these cracks would be expected to grow wing cracks rather than extending in-plane.

For the run at zero confining pressure (Fig. 2.12) axial tension cracks are the dominant mode of crack growth. Only ten cracks grow in mode II throughout the entire simulation. At 0.5, 1 and 2 kb confining pressure, the pattern of tensile crack growth

remains much the same as for the unconfined sample. The most dramatic change to occur with increasing confining pressure is the systematic increase in the rate of diagonal mode II crack growth. By 4 kb (Fig. 2.16), diagonal mode II crack growth dominates the tensile crack growth throughout the run. By 8 kb, tensile crack growth is completely suppressed and the material behaves ductily. Note that there is little strength loss after failure as well as a significant reduction in total dilatancy. Up to about three percent axial strain, approximately 800 new diagonal cracks are formed, resulting in 47% of the possible diagonal crack sites being cracked. At this point crack growth diminishes and the entire sample deforms in distributed shear remeniscent of cataclastic flow. By 12 kb, the transition is complete and the material would be classified as elastic-plastic.

Mohr Diagram

The peak strength data shown in Fig. 2.11 are replotted in terms of shear *vs* normal stress in Fig. 2.20. The Mohr failure envelope is constructed by connecting tangents to the failure stress circles. The failure envelope is concave downwards as is commonly observed for brittle rock (*Jaeger and Cook,* 1984). When a suite of simulations was performed in which cracks were allowed to grow only in tension, according to the K_{IC} growth criterion, a linear failure envelope resulted. For this reason, we suggest that the curvature of the failure envelope is due to the activation, with increasing confining pressure, of mode II crack growth. *Wong* (1982b) reported a similar trend for Westerly granite.

The maximum shear strength that can be sustained by a single, unflawed crystal can readily be calculated by estimating the stress needed to break an entire lattice plane of bonds in unison. It is generally assumed that this ultimate shear strength is given by $\mu/10$ (*Dieter*, 1961). By limiting the maximum shear stress that could be sustained by the rock, this ultimate shear strength would force the failure envelope to become horizontal at high normal stress. However, before this could happen, dislocations would be activated and lead to plastic deformation. This behavior is observed in minerals such as halite and calcite (*Fredrich et al.,* 1989) which become ductile at room temperature and modest confining pressure. However, there is no evidence for the mobilization of defects in quartz or feldspar at room temperature and pressures as high

as 15 kb (*Tullis and Yund,* 1977). In the present model, this ultimate shear strength would be approximately 40 kb and is too large by at least a factor of two to have any direct effect in the simulations. Instead, as described in the previous section, we have included a mode II critical stress intensity factor of 0.15 kb-$m^{1/2}$ (15 MPa-$m^{1/2}$) to produce the desired Mohr envelope curvature. *Rice* (1980) and *Wong*(1982a) have used the post-failure response of laboratory samples to calculate critical energy release rates G_{IIC} for mode II crack growth. Although their determinations were not for single crystals, they should provide a good estimate of the appropriate values to use in our simulations. In fact, their findings suggest that for typical crystalline rocks, K_{IIC} should range from 10 to 40 MPa-$m^{1/2}$. The inclusion of K_{IIC} in the model limits the peak shear stress to approximately 15 kb and causes a transition, with increasing confining pressure, from axial crack growth to distributed shear throughout the sample. A similar behavior was reported by *Tullis and Yund* (1977) for low-temperature deformation of granite. A possible physical mechanism would be the development of en echelon tensile cracks in front of the advancing shear plane. At lower confining pressure, the tensile cracks would grow into wing cracks and deflect the main shear crack. However, at high confining pressure, the tensile cracks cannot grow and instead collapse to form a cohesionless damage zone. Such a mechanism is suggested in biaxial PMMA experiments (*Petit and Barquins*, 1988).

On a Mohr diagram, the transition should occur when the brittle failure envelope and frictional strength curve converge. As the brittle-ductile transition is approached, the strength contrast between intact material and fractured material vanishes. Consequently, the driving force for concentrating shear along discrete fracture planes also vanishes. *Byerlee* (1967) suggested such a brittle-ductile transition for Westerly granite. He measured peak strength and frictional sliding strength as a function of confining pressure and noted that the two were converging at approximately 12 kb confining pressure (Fig. 2.21). Samples that were fractured at this pressure and then forced to deformed further, did so by stick-slip, although the peak intact strength and peak fricitional strength were the same, and stick-slip stress drops were less than at lower confining pressures. These observations are consistant with the present interpretation.

A brittle-ductile transition has been suggested to operate in the lower crust (*e.g. Kirby*, 1980; *Sibson,* 1982) where it was was used to explain the lower limit of the

zone of crustal seismicity. This transition depends on thermally activated processes such as dislocation creep mechanisms and represents a transition to truly plastic deformation. *Tse and Rice* (1986) have appealed to a variation in the velocity dependence of friction with temperature to explain the depth limit of the seismogenic zone of the San Andreas fault. This mechanism is also based on thermally activated processes. The high pressure-low temperature behavior shown in Figs. 2.12 through 2.19 would be included in the semi-brittle field classification, *e.g. Tullis and Yund* (1977) and *Kirby* (1980). It is, however, distict from the semi-brittle processes which they described as being a combination of brittle microfracturing and thermally activated plastic deformation.

Acoustic Velocity

The acoustic velocity for body waves in a homogeneous medium with orthorhombic symmetry can be expressed as

$$V_i = (m_i / \rho)^{1/2} \tag{2-24}$$

where ρ is density and m_i is an appropriate modulus of the medium. m_i is given by

$$m_i = \partial P_i / \partial \varepsilon_i \tag{2-25}$$

and is composed of the diagonal elements of the reduced elastic tensor. Thus, in the principal directions,

$$\begin{bmatrix} V_{px} \\ V_{py} \\ V_s \end{bmatrix} = (1/\rho)^{1/2} \begin{bmatrix} c_1^{1/2} \\ c_2^{1/2} \\ c_3^{1/2} \end{bmatrix} . \tag{2-26}$$

Since the bulk elastic tensor is calculated as a byproduct of the modeling procedure, it is a simple matter to compute acoustic velocities for the simulation. Using a density of 2.7 g/cm^3, the P-wave velocities are plotted in Fig. 2.22a. Axial velocity increases initially due to closure of horizontal cracks and then gradually decreases. Transverse velocity

decreases monotonically as vertical cracks open, dropping approximately 20% by peak strength. The same data are replotted in Fig. 2.22b *vs* normalized differential stress. Included in the plot is transverse P-wave velocity for Westerly granite at 500 bars confining pressure (from *Lockner et al.*, 1977) and for Aji granite at 810 bars confining pressure (from *Yukutake*, 1989). The Westerly data show a 35% drop in transverse P-wave velocity by peak strength while the Aji velocity drops by 20%. The difference in confining pressures is responsible for the variation in velocities between the two granite samples (Yukutake reported a 30% drop in velocity for a 540 bar experiment). The 2D simulation is in good agreement with the velocity changes observed in the 810 bar experiment. At this point it is not clear what improvement would be gained from a full 3D simulation. For the properties examined so far, the fact that the simulation is only 2D has had remarkably little effect when results are compared to actual laboratory data. However, some aspects of 3D samples are clearly not properly modeled in 2D. For example, cracks in virgin rock samples invariably form through-going connected pathways, since rocks have finite fluid and electrical conductivities (*Madden*, 1983). The beginning crack population for the 2D simulation, however, is not fully connected. Thus, proper modeling of these properties may require a full 3D formulation.

Porous Rock

In the previous set of simulations, a crack closure algorithm was included in the model which was designed to close all cracks at approximately 1 kb normal stress. Such a closure criterion is appropriate for a crystalline rock, such as granite, that has large aspect ratio cracks. However, for a rock such as sandstone, which has more equi-dimensional pores, the pores are more resistant to closure by pressure. One way of simulating this behavior is to modify the closure algorithm so as to be less sensitive to pressure. Fig. 2.23a shows a set of stress-strain curves for runs in which cracks would not close until approximately 100 kb. The main difference in response is a gradual increase in Young's modulus in the elastic loading portions of the loading histories. As confining pressure is increased, the cracks (pores) gradually close, increasing the elastic moduli of the material. This pressure dependence has been noted for sandstones. For example, in Fig. 2.23b, Young's modulus is plotted *vs* confining pressure for Berea sandstone (18% porosity).

Microcrack Development and Critical Crack Density

In this section, we will examine the development of the crack population in response to loading. Since horizontal cracks are closed by the application of axial stress, they contribute little to the kinematics of the failure process. Consequently, we will only consider vertical and diagonal crack populations in this section. Figs. 2.24 through 2.28 show the evolution of the crack population throughout the 1 kb run. Note that near the peak stress (Fig. 2.25) the largest connected cluster is still rather limited in extent, although, just after peak strength (Fig. 2.26) the largest cluster has jumped in size by joining to another large cluster. It is not until well into the post-failure region (Fig. 2.27) that the sample boundaries become fully connected. Intuitively, one might expect the sample to become fully connected very close to peak strength. However, these two properties are not closely related. For example, in 3D, undeformed rocks typically contain a fully connected pore structure since they have finite fluid and electrical conductivity. In the 1 kb simulation, peak strength is achieved when 22% of the possible sites have become fully cracked. This is an increase of only 10% relative to the original crack population (and a two percent increase in the number of possible sites that are cracked). Complete loss of mechanical strength does not occur until approximately 28% of the potential sites are fully cracked, or a 40% increase over the initial crack population. In a second simulation, in which a starting crack population of 11% was used, peak strength occured after only 16% of the possible sites were cracked. We must point out here an important shortcoming of the model. For reasons that will be discussed in a later section, the model tends to suppress the development of a through-going failure plane. Thus the microcrack growth in the post-peak-strength region, where strain localization is expected (*Rudnicki and Rice,* 1975), at best places an upper bound on the amount of uniform cracking that could be expected from a more accurate model. As a result, we will concentrate on the crack growth leading up to peak strength. Fig. 2.28 shows the development of the crack population. Notice that the small cracks are essentially passive throughout the failure process. Stress intensities for these cracks are never large enough for them to grow on their own. Instead, small cracks are consumed uniformly as cracks extend from the network of fully cracked edges. *Wong et al.* (1989) point out the importance of the interconnected pore structure

in controlling material properties. Other studies (*e.g. Tapponnier and Brace,* 1976; *Hadley,* 1975) have recognized that cracks tend not to grow in isolation, but rather are spawned from pre-existing cracks. This characteristic also plays an inportant role in the crack development in the present model.

Madden (1983) applied renormalization group theory to the problem of evaluating critical crack densities for both failure and electrical conduction in rock. Most of his 3D calculations were based on a 2x2x2 unit cube with cracks on bounding surfaces. The critical parameter for both failure and conductivity was Nl^2/S where N is number of cracks, l is crack length and S is the area used in the crack count. Critical values for failure and conductivity were, respectively, 0.79 and 0.21. We wish to apply this same approach to crack densities in our model, in this case based on a 3x3 unit square to conform to the RNG grouping used to calculate bulk material properties. Since our model is 2D and we have included diagonal cracks, our critical densities will be different. For 2D, and assuming unit length cracks, the critical parameter is simply N/S. The calculation is actually performed in two steps. Remember that in the calculation of elastic properties, cracks were only included at the finest scale. At all other scales, each unit cell was considered homogeneous. To calculate the critical density needed for failure, we use the same approach. Starting one level above the finest scale, we assume that each unit cell is either failed or intact. We then wish to know, for a given probability of failure for each unit cell, what is the probability that the entire sample will be failed. There are in fact three fixed points, at probabilities of 0, 1 and the critical probability P*. For any probability below P*, an infinite sample will be intact while for probabilities greater than P*, the sample will have failed. Examples of the failure criterion are shown in Fig. 2.29. A 3x3 block is considered failed for vertical maximum compressive stress when the the top and bottom sides are completely separated by failed cells. Failed cells are considered connected if they touch on either corners or edges. A Monte Carlo method was used to determine the critical probability of P* = 0.38 for all levels above the finest level. The finest level is treated separately since it is the only one in the model that contains cracks explicitly; in the other levels, cracks are represented by their effects on the average elastic moduli. Then, all that remains is to determine the critical crack density at the finest level needed to give the critical probability of 0.38 appropriate for the coarser levels. For vertical loading, horizontal cracks are ignored since, in general, they will be immobilized by friction.

Once again, a block is considered failed if the top and bottom are completely separated by a connected set of cracks. The critical probability for a crack site being cracked on the finest level is found to be $P^*_{crack} = 0.29 \pm 0.01$. The crack densities at peak strength are significantly less than this value. However, the samples are still stable in the post-peak-strength region, where they can still support significant load. For the 1 kb simulation, the runaway condition of uncontrolled crack growth that is indicative of a critical phenomenon occured when $P^*_{crack} = 0.28$. Thus the RNG calculation predicts the point of mechanical instability quite well. Peak strength crack densities are plotted in Fig. 2.30 as a function of confining pressure. Notice that a 1 kb run using model M2, in which starting crack probability was 11%, reach peak strength at a much lower density than the runs using an initial crack probability of 20%. This may reflect the fact that new crack populations are anisotropic and non-random. This result indicates that models which predict failure based on a damage parameter may have varying degrees of success depending on the initial crack densities of the test samples. Also shown in Fig. 2.30 are crack densities at the onset of tertiary creep in time-dependent creep runs. These crack densities are systematically higher than the crack densities for non-time-dependent peak strength using the same starting models. This is an interesting feature for which we have no explanation at present.

The critical crack density for electrical conduction, representing the point at which the sample becomes fully connected, can also be calculated. In determining the critical probability on the coarser scales, the connectedness criterion must be changed. Now, cells that touch at corners are no longer considered connected. Instead, only cells sharing a common side are connected. This condition give a critical probability $P^* = 0.62$. At the finest level, horizontal cracks must be included since, even though they are held closed mechanically, they will still have finite conductivity. We find that the critical crack probability for electrical conduction is $P^*_{crack} = 0.28 \pm 0.01$. This is in good agreement with the crack density for which the 1 kb run became fully connected. It turns out that for the 2D crack geometry used in our simulations, critical crack densities for failure and conductivity are essentially the same.

Time Dependence and Creep Simulations

In the simulations presented so far, there has been no explicit time-dependence

other than the progressive development of new cracks in response to the stress field created by existing cracks. Once an equilibrium crack geometry has been achieved, no new cracks will grow without further modification of the boundary conditions. However, it is well known that in actual experiments as well as in the earth, time-dependent crack growth and creep occur whenever sufficient deviatoric stress is present. Static fatigue is one of the most important low-temperature time-dependent phenomena in rock. It refers to a process by which materials are observed to fail at stresses below their short term failure strength when subjected to corrosive environments. Since water, which is ubiquitous in the earth's crust, actively attacks the Si-O bond, silicates in general exhibit this phenomenon. Considerable attention has been paid to the study of stable tensile crack growth in glass (*Charles,* 1958) and more recently in rock (*Atkinson,* 1987). The typical relationship between crack extension rate and stress intensity is shown in Fig. 2.31. Over most of the range of stress intensity achieved in laboratory tests, crack growth rate can be fit by a power law dependence on stress intensity:

$$v = AK_I^n . \tag{2-27}$$

For many silicates at room temperature, the exponent n falls in the range of 10 to 30 (*Atkinson,* 1987). As K_{IC} is approached, a region often occurs, especially in glass, in which stress dependence first decreases and then increases super-exponentially until the crack grows unstably at K_{IC}. Since an approximate value of K_I is already computed in the model to determine the point where unstable crack growth will occur, it is a simple matter to include subcritical time-dependent crack growth. For simplicity, we assume a strict power law relation for subcritical crack growth, adopting an exponent of 20.

Time-dependent shear has also been observed for faults oriented obliquely to the principal stress directions (*Rutter and Mainprice,* 1978; *Solberg et al.,* 1978; *Higgs,* 1981). This phenomenon has been studied extensively in terms of rate- and history-dependent friction models (*e.g. Dieterich,* 1981; *Rice,* 1983; *Ruina,* 1983). While some fault materials have been found to develop negative velocity dependence of steady-state shear strength after sliding for some distance, initial velocity dependence seems to be consistantly positive (*Lockner and Byerlee,* 1986). In general, we expect some degree of time-dependent relaxation of stress on microcracks that have been

loaded close to their shear strength limit. Secondary creep rate from *Solberg et al.* (1978) is plotted as a function of coefficient of friction f/f_C in Fig. 2.32. f_C (= 0.7 for the Solberg data) is the value of f where unstable slip occurs. In these studies of time-dependent fault creep, the faults contained gouge layers of finite thickness. Since complex structures develop and evolve in the gouge layer with continued slip (*Moore, et al.*, 1989; *Yund et al.*, 1989), the details of how slip is accomodated may be quite different in experiments containing thick gouge layers than in the case of slip on microcracks with little or no gouge. As a first attempt, we have used

$$\log_{10} v \text{ [mm/s]} = 7.56 \, (f/f_C) - 15.26 \, . \qquad (2\text{-}28)$$

This relation is plotted as the straight line in Fig. 2.32.

To study how these time-dependent effects influence the model, we have conducted a series of creep test simulations using the subcritical crack growth and shear slip rate algorithms individually and then combined. In a creep test, the sample is loaded to a desired deviatoric stress state which is then held constant as the sample deforms. The time history for a creep simulation using both subcritical crack growth and time-dependent shear slip and run at P_C = 1 kb and P_{dif} = 5.5 kb is shown in Fig. 2.33. The starting crack population referred to as M2 is show in Fig. 2.34. In this case, only 11% of the possible crack sites were fully cracked. The simulation exhibited the classic creep response of exponentially decaying primary creep rate followed by secondary (constant rate) creep and finally accelerating tertiary creep. In Fig. 2.35, two creep tests, at differential stresses of 5.0 and 5.8 kb are compared to a constant strain rate simulation which included no time-dependent algorithm. All three simulations used the same confining pressure and starting crack population. This comparison is similar to a technique employed by *Wawersik and Fairhurst* (1970) and *Wong* (1982b) to evaluate the post-failure stress envelope. By connecting the points on the various curves where the samples failed, we find that the post-failure envelope has positive slope, indicating a class II material according to Wawesik's terminology. We have already mentioned in an earlier section that in non-time-dependent simulations, a runaway condition is reached in the post-failure region in which the number of new cracks generated during each program iteration continued to increase. This feature is another characteristic of a class II material.

An important assumption implicit in reconstructing the post-failure envelope from creep curves is that the crack population at a point on the stress-strain curve is path-independent. While the validity of this assumption cannot be tested with real samples, we have the ability to deform identical samples under different conditions. The development of new cracks during the three simulations is shown in Fig. 2.36. While the growth of cracks as a function of axial strain is quite different in the three examples, the relative changes in the various crack populations shows good correspondence from one experiment to the next. At the time of failure, total crack counts are quite similar. By the end of the constant strain rate run, differential stress had dropped to the same level as the upper creep run (5.8 kb). Mode I vertical crack counts in both cases had reached approximately 200. The 5.0 kb differential stress run, which should intersect the failure envelope at a more advanced stage in the failure process, reached a runaway condition at a mode I vertical crack count of approximately 300. Thus, in terms of cumulative crack damage, this reconstruction technique seems valid.

A more rigorous test is to compare the locations of individual cracks. In Fig. 2.37, the crack population occuring at peak strength in the constant creep rate run is compared to the crack populations occuring near the end of secondary creep and in the early stages of tertiary creep for the P_{dif} = 5.8 kb run. In all plots, the background (dotted) cracks are common to both data sets. In plots (a) and (b), the solid lines represent cracks present in the creep run but not in the strain rate run. Solid lines in (c) and (d) represent cracks present in the strain rate run but not in the creep run. Notice that in the secondary creep plots (a and c), most of the cracks that are not common to both data sets are mode I axial cracks. The few diagonal cracks that are exclusive to the creep run appear in what will become the overall damage zone responsible for accelerating tertiary creep. Notably fewer axial cracks, exclusive to the strain rate run, appear in plot (d) than in plot (c). This would indicate that the creep run is preferentially developing many of the same axial cracks that grow in the non-time-dependent run. Since there is only about a 500 bar difference in stress level between these two runs, we would not expect large differences in crack populations. However, a similar comparison between the constant strain rate run and the 5.0 kb differential stress creep run is shown in Fig. 2.38. The development of crack patterns is quite similar to that described for the 5.8 kb run. In this case, the stress difference between the constant strain rate run and the creep

run is approximately 1.3 kb. The close similarity between the crack growth patterns in these two runs supports the use of creep curves to reconstruct post-failure curves.

In the non-time-dependent simulations it was found that small cracks were not actively involved in the development of fracture patterns. Instead, most new cracks were spawned from existing crack arrays. This is also found to be true for the time-dependent simulations. This process is similar to the suggestions of *Kranz* (1979) and *Batzle et al.* (1980) that surface irregularities on existing cracks may act as sites for initiation of new microcracks. In terms of the time-dependent modeling, crack growth rate is so strongly stress dependent that small cracks have essentially no chance to grow. Consider two isolated cracks under the same ambient stress conditions where one crack is twice as long as the other. To extend an increment δ, will require nearly 200 times longer for the small crack. Thus, under creep conditions, we can expect the largest cracks to quickly grow to near their stable lengths, followed by progressively smaller cracks achieving significant growth. This process will continue until either crack growth ceases or a critical crack density is achieved which leads to tertiary creep and failure.

The static-fatigue response of rock is commonly evaluated by measuring the time-to-failure, t_f, of creep experiments. Time-to-failure generally has an exponential dependence on differential stress (*Kranz* , 1980). Results from 1 kb simulations are shown in Fig. 2.39 along with 1 kb data from *Kranz* (1980) for Barre granite. The simulations all show an exponential stress dependence. The surprising result, however, is the close agreement between the slopes of the simulated and laboratory data sets. Given the latitude in choosing the stress-dependence of crack growth rate from laboratory experiments (*Atkinson* (1987) reports $10 < n < 30$ for silicates at room temperature), there is no difficulty in matching laboratory results. Apparently, subcritical crack growth of axial cracks, and alternatively time-dependent slip on diagonal cracks, is sufficient to explain the observed time-to-failure behavior of crystalline rock.

A series of room temperature laboratory creep runs are described in Chapter 3. In those experiments the relationship between stress and volumetric strain rate was examined for wet Westerly granite under secondary creep conditions. It was found that the stress sensitivity satisfied

$$\log_{10}(\dot{\varepsilon}_v) = A + BP_{dif} + f(\varepsilon_v) \qquad (2\text{-}29)$$

where A and B are constants. B was found experimentally to be 7.4 ± 0.2 kb^{-1}. A similar stress sensitivity was found for unconfined Westerly granite (*Wawersik,* 1973), Barre granite (*Kranz,* 1980) and Tennessee sandstone (*Rutter and Mainprice,* 1978). The creep simulations shown in Fig. 2.38 give B = 5.2 ± 1 kb^{-1} for the simulations using only subcritical crack growth, and 2.5 ± 0.5 kb^{-1} for the simulations using both subcritical crack growth and time-dependent crack friction. Although we have not yet performed the necessary simulations, we expect to be able to match the laboratory values using a different choice of subcritical growth rate and slip rate parameters. The agreement between model and experimental data suggests that subcritical crack growth of the largest members of the crack population dominates the time-dependent behavior in these rock types.

Acoustic Emission

The monitoring of acoustic emission, AE, has proven to be a useful non-destructive technique for studying the development of microcracks in samples in both pre- and post-failure conditions. AE in rock is generally assumed to be the result of unstable microcrack growth. This assumption is supported by the close correlation between AE rate and inelastic strain rate, AE frequency content (0.5 to 10 MHz), and the correspondence of AE source locations and damage zones in laboratory samples (*e.g. Lockner and Byerlee,* 1977, 1980). In the computer simulation, crack extension occurs when the critical stress intensity factor is exceeded and therefore represents unstable crack growth. Consequently, each crack extension should represent an AE event. With this in mind, we have conducted a creep simulation at 500 bars confining pressure and a differential stress of 3.5 kb. The time histories of axial strain, acoustic emission rate (new crack growth rate) and transverse P-wave velocity are plotted in Fig. 2.40. For comparison, data from a 500 bar creep experiment on Westerly granite (from *Lockner and Byerlee,* 1980) are reproduced in Fig. 2.41. Once again, the computer model reproduces all of the significant features of the laboratory experiment. To achieve a comparable time-to-failure, the simulation was conducted at a lower differential stress level than the actual experiment. This was necessary since both subcritical crack growth

and time-dependent slip were included in the simulation. As shown in the previous section (Fig. 2.39), this results in an early time-to-failure when compared to granite. The three creep stages are reproduced in the simulation, as well as the correlation of AE rate and creep rate. The increase in AE rate in the tertiary creep phase in the simulation is more abrupt than in the actual experiment (note that log(AE rate) is plotted in Fig. 2.40). This may be due in part to the small sample size used in the simulation (3 mm as compared to 76 mm for the laboratory sample). Transverse P-wave velocity drops steadily to approximately 60% of the hydrostatic value in the simulation. This velocity change agrees reasonably well with the experimental data as well as with results from *Yukutake* (1989); especially considering that the simulation is 2D.

Shear Localization

In the preceeding sections, we have focused primarily on the processes and changes in material properties that occur in the dilatant pre-failure region. It was found that as the sample was loaded,the first cracks to grow were quite efficient at redistributing local stress concentrations over larger regions. Since the initial stress concentrators were distributed randomly throughout the sample, the new crack growth was relatively homogeneous. The growth of individual cracks in an overall compressive stress field tends to be bounded by the action of frictional forces acting across the crack faces. Properties of diagonal cracks,for example, are discussed further in Chapter 3. Numerous studies have shown that cracks have little tendency to link up (*e.g. Horii and Nemat-Nasser,* 1985; *Segall and Pollard,* 1980). This effect coupled with the fact that cracks tend to grow parallel to the direction of maximum compressive stress makes brittle materials suprisingly resistant to failure in compression. The process by which cracks coalesce and form a macroscopic shear plane has been a subject of great interest in rock mechanics. *Rudnicki and Rice* (1975) suggested that, at least for the case of axisymmetric compression, shear localization could be expected to occur late in the post-peak strength region. *Hadley's* (1975) data showed that granite samples which failed in compression had achieved critical crack density everywhere by the time failure occurred (*Madden,* 1983). By locating acoustic emissions in a creep experiment, *Lockner and Byerlee* (1980) (Fig. 2.42) monitored the development of the fracture plane. They found that in a 2.5 day experiment, localization of AE into a narrow region

on the eventual failure plane did not begin until 2.5 hr before failure. By two seconds before failure, this zone had elongated in the plane of the fault to only 30 mm (the eventual fault length was 200 mm). Since crystalline rock generally weakens rapidly in the post-failure region, there are significant technical difficulties in retrieving samples after only partial failure. *Wawersik and Fairhurst* (1970) and *Wong* (1982b), however, have accomplished this task to study microstructural changes in the post-failure region.

One of the primary reasons for undertaking the present modeling effort was to investigate the microcrack localization process in brittle materials. It was therefore a great disappointment to find that the numerical model, in its present form, has limitations which become significant in the post-peak-strength region. As described in the section on model description, there are two main elements in the model which operate in parallel. First, displacements for the entire sample are adjusted each program cycle to attempt to bring local elements into equilibrium. This relaxation procedure operates on 3x3 blocks of the sample, using the surrounding displacements as boundary conditions. The process is very efficient at removing short wavelength residuals but has a prohibitively slow convergence rate for wavelengths longer than three unit cell lengths. To correct the longer wavelength errors, the model depends on the multiple scale RNG procedure. For a linear problem, the multiple scaling would correct long wavelength errors in one iteration. However, the crack interaction problem is highly non-linear. As a result, we have chosen to apply significant damping to the multiple scaling adjustments. In this way, we avoid the possibility of over-driving the system and causing regions to fail artificially. The penalty that is paid for this performance stability is that regions which strain-weaken require many program iterations to transmit load to surrounding regions. And in fact, this problem becomes worse as the regions grow in size. Since the entire sample is near the critical crack density when the localization process begins, the effect is to artificially strengthen weak regions and inhibit their growth. Through trial and error, we have found that creep experiments consistantly develop more localized failure regions. We suspect that this occurs because, in the creep runs, the model iterates many times with little change in boundary conditions, allowing significant slip to occur before new cracks are formed. The fact that the creep simulations also allow time-dependent slip to occur at friction levels below f_C should aid this process. Because of this limitation of the model, the stress-strain curves in the post-failure region should be regarded as upper bounds of the

true equilibrium stress-strain curves.

We conclude this section with two examples of limited fracture localization during creep simulations. The first example (Fig. 2.43) is for the tertiary creep phase of a run using starting model M2, at confining pressure of 1 kb and differential stress of 5.8 kb. Here we have plotted the crack density N/S for vertical and diagonal cracks. Recall that the critical crack density for failure should be 0.9 and a fully cracked region would have N/S = 3. The second example (Fig. 2.44) was run at 1 kb confining pressure and 5 kb differential stress. In this case, starting model M3 was used in which the probability of vertical and diagonal cracks was 15% and the probability of horizontal cracks was 60%. Note that, as in the case of the acoustic emission density plot for granite (Fig. 2.42), crack density was relatively homogeneous through secondary creep, localizing with the onset of tertiary creep and developing into a large damage zone as tertiary creep progressed.

Conclusions

The numerical simulations presented in this section have been suprisingly sucessful at duplicating a variety of features observed in laboratory rock deformation experiments. By including in the model crack friction, crack closure, fracture toughness and subcritical crack growth, a rich assortment of behavior is observed. The model, in its present form, has notable limitations. These include modest sample size, limited accuracy in calculating stress, restriction of cracks to a periodic array, and the fact that the model is a 2D simulation. Even so, the model is able to duplicate dilatancy, pressure dependent strength, acoustic velocities, creep behavior, including time-to-failure, acoustic emission rate and to a limited extent, crack localization. In particular, the success at relating subcritical crack growth to bulk deformation properties is an unexpected result. For the most part, experimental studies of subcritical crack growth have concentrated on single cracks loaded in pure mode I. The numerical model appears to have properly combined this process with the complicated cooperative crack effects that develop large local stress heterogeneity in the sample. Numerical model results also indicate that similar crack patterns develop in creep simulations conducted at different stress levels. This result provides support for the technique of using creep experiments to examine post-failure behavior in laboratory samples. As in low confining pressure laboratory experiments, pre-failure microcrack growth in the numerical simulations is primarily parallel to the maximum compressive stress direction. Both peak strength in the non-time-dependent simulations and the onset of tertiary creep in simulations with time-dependent crack growth, are coincident with an abrupt increase in the number of diagonal cracks that extend in tension. This transition in crack growth orientation can only occur as the result of a rotation of local stresses due to crack interactions. Such behavior argues for the existance of a critical crack density which corresponds to the onset of mechanical instability of the sample. By including a mode II critical stress intensity factor in the model, a curved Mohr failure envelope was generated which approximated the failure envelope for Westerly granite. In addition, a low-temperature brittle-ductile transition was observed which involved a number of features that have been identified in low-temperature high-pressure granite experiments. While many aspects of the model can readily be improved upon to provide closer agreement with

experimental results, the basic performance has been demonstrated and should not change appreciably. Extensions of the model to larger sample size and to 3D would be interesting exercises to persue.

TABLE 2.1 - MODEL PARAMETERS

λ [kb]	μ [kb]	K_{IC} [kb-$m^{1/2}$] (MPa-$m^{1/2}$)	K_{IIC} [kb-$m^{1/2}$] (MPa-$m^{1/2}$)	f
400	400	0.01 (1)	0.15 (15)	0.5

References

Ashby, M. F. and S. D. Hallam, The failure of brittle solids containing small cracks under compressive stress states, *Acta Metall., 34,* 497-510, 1986.

Atkinson, B. K., *Fracture Mechanics of Rocks,* Academic Press, New York, 534 pp., 1987.

Atkinson, B. K. and P. G. Meredith, The theory of subcritical crack growth with applications to minerals and rocks, in: *Fracture Mechanics of Rock,* (ed. Atkinson, B. K.), Academic Press, New York, pp. 111-166, 1987a.

Atkinson, B. K. and P. G. Meredith, Experimental fracture mechanics data for rocks and minerals, in: *Fracture Mechanics of Rock,* (ed. Atkinson, B. K.), Academic Press, New York, pp. 477-525, 1987b.

Batzle, M., G. Simmons and R. W. Siegfried, Microcrack closure in rocks under stress, *J. Geophys. Res., 85,* 7072-7090, 1980.

Bernabe, Y., The effective pressure law for permeability in Chelmsford granite and Barre granite, *Int. J. Rock Mech. Min. Sci. & Geomech. Abstr., 23,* 267-275, 1986.

Brace, W. F., A. S. Orange and T. R. Madden, The effect of pressure on the electrical resistivity of water-saturated crystalline rocks, *J. Geophys. Res., 70,* 5669-5678, 1965.

Brace, W. F., B. W. Paulding and C. Scholtz, Dilatancy in the fracture of crystalline rocks, *J. Geophys. Res., 77,* 3939, 1966.

Byerlee, J. D., Frictional characteristics of granite under high confining pressure, *J. Geophys. Res., 72,* 3639-3648, 1967.

Byerlee, J. D., Friction of rocks, *Pure and Appl. Geophys., 116,* 615-626, 1978.

Charles, R. J., *J. Appl. Phys., 29,* 1549-1560, 1958.

Dieter, G. E., *Mechanical Metallurgy,* McGraw-Hill, New York, 615 pp., 1961.

Dieterich, J. H., Constitutive properties of faults with simulated gouge, in *Mechanical Behavior of Crustal Rocks, Am. Geophys. Union Monograph, 24,* 103-120, 1981.

Dmowska, R. and J. R. Rice, Fracture theory and its seismological applications, in: *Continuum Theories in Solid Earth Physics,* ed. Teisseyre, R., Volume III of series 'Physics and Evolution of the Earth's Interior', Elsevier Publ. Co./ Polish

Scientific Publishers, 1983.

Evans, B. and T.-f. Wong, Shear localization in rocks induced by tectonic deformation, in *Mechanics of Geomaterials,* edited by Z. Bazant, John Wiley, pp. 189-210, New York, 1985.

Fredrich, J., B. Evans and T.-f. Wong, Micromechanics of the brittle to plastic transition in Carrara marble, *J. Geophys. Res., 94,* 4129-4145,1989.

Hadley, K., Dilatancy: further studies in crystalline rocks, Ph.D. Thesis, Mass. Inst. Tech., Cambridge, Ma, 1975.

Higgs, N. G., Mechanical properties of ultrafine quartz, chlorite and bentonite in environments appropriate to upper-crustal earthquakes, Ph.D. Thesis, Texas A&M Univ., 267 pp., 1981.

Horii, H. and S. Nemat-Nasser, Compression-induced microcrack growth in brittle solids: axial splitting and shear failure, *J. Geophys. Res., 90,* 3105-3125, 1985.

Horii, H. and S. Nemat-Nasser, Brittle failure in compression: splitting, faulting and brittle-ductile transition, *Philos. Trans. R. Soc. London,* ser. A, *319,* 337-374, 1986.

Jaeger, J. C. and N. G. W. Cook, *Fundamentals of Rock Mechanics,* third ed.,Chapman and Hall, New York, 593 pp., 1984.

Kirby, S. H., Tectonic stresses in the lithosphere: constraints provided by the experimental deformation of rocks, *J. Geophys. Res., 85,* 6353-6363, 1980.

Kranz, R. L., Crack growth and development during creep in Westerly granite, *Int. J. Rock Mech. Min. Sci., 16,* 23-36, 1979.

Kranz, R. L., The effects of confining pressure and stress difference on static fatigue of granite, *J. Geophys. Res., 85,* 1854-1866, 1980.

Lawn, B. R. and T. R. Wilshaw, *Fracture of Brittle Solids,* Cambridge Univ. Press, New York, 204 pp., 1975.

Li, V. C., Mechanics of shear rupture applied to earthquake zones, in: *Fracture Mechanics of Rock,* (ed. Atkinson, B. K.), Academic Press, New York, pp. 351-428, 1987.

Liebowitz, H., ed., *Fracture: An Advanced Treatise,* Volumes I-VII, Academic Press, New York, 1968.

Lockner, D. A. and J. D. Byerlee, Hydrofracture in Weber sandstone at high confining pressure and differential stress, *J. Geophys. Res, 82,* 2018-2026, 1977.

Lockner, D. A. and J. D. Byerlee, Development of fracture planes during creep in granite, 2nd Conf. on Acoustic Emission/Microseismic Activity in Geol. Structures and Materials, Trans-Tech. Publications, Clausthal-Zellerfeld, W. Germany, 1980.

Lockner, D. A. and J. D. Byerlee, Laboratory measurements of velocity dependent frictional strength, Open File Rep. 86-417, U.S. Geol. Surv., 68pp., 1986.

Lockner, D. A., J. B. Walsh and J. D. Byerlee, Changes in seismic velocity and attenuation during deformation of granite, *J. Geophys. Res., 82,* 5374-5378, 1977.

Madden, T. R., Random networks and mixing laws, *Geophys., 41,* 1104-1125, 1976.

Madden, T. R., Microcrack connectivity in rocks: a renormalization group approach to the critical phenomena of conduction and failure in crystalline rocks, *J. Geophys. Res., 88,* 585-592, 1983.

Moore, D. E., R. Summers and J. D. Byerlee, Sliding behavior and deformation textures of heated illite gouge, *J. Struct. Geol., 11,* 329-342, 1989.

Morrow, C. A., Z. Bo-Chong and J. D. Byerlee, Effective pressure law for permeability of Westerly granite under cyclic loading, *J. Geophys. Res., 91,* 3870-3876, 1986.

Nye, J. F., *Physical Properties of Crystals,* Clarendon Press, Oxford, 329 pp., 1986.

Paris, P. and G. Sih, Stress analysis of cracks, in *Symposium on Fracture Toughness Testing and Applications, Spec. Tech. Publ. 381,* pp. 30-81, American Society for Testing and Materials, Philadelphia, Pa., 1965.

Petit, J. P. and M. Barquins, Can natural faults propagate under mode II conditions, *Tectonics, 7,* 1243-1256, 1988.

Pollard, D. D. and P. Segall, Theoretical displacements and stresses near fractures in rock: with applications to faults, joints, veins, dikes, and solution surfaces, in: *Fracture Mechanics of Rock,* (ed. Atkinson, B. K.), Academic Press, New York, pp. 277-349, 1987.

Rice, J. R., The mechanics of earthquake rupture, in *Physics of the Earth's Interior,* edited by A. M. Dziewonski and E. Boschi, p. 555-649, Italian Physical Soc., Bologna, Italy, 1980.

Rice, J. R., Constitutive relations for fault slip and earthquake instabilities, *Pure and Appl. Geophys., 121,* 443-475, 1983.

Rudnicki, J. W., Fracture mechanics applied to the earth's crust, *Ann. Rev. Earth*

Planet. Sci., 8, 489-525, 1980.

Rudnicki, J. W. and J. R. Rice, Conditions for the localization of deformation in pressure-sensitive, dilatant materials, *J. Mech. Phys. Solids, 23,* 371-394, 1975.

Ruina, A. L., Slip instability and state variable friction laws, *J. Geophys. Res., 88,* 10359-10370, 1983.

Rutter, E. H. and D. H. Mainprice, The effects of water on stress relaxation of faulted and unfaulted sandstone, *Pure and Appl. Geohpys., 116,* 634-654, 1978.

Sammis, C. G. and M. F. Ashby, The failure of brittle porous solids under compressive stress states, *Acta metall., 34,* 511-526, 1986.

Segall, P. and D. Pollard, Mechanics of discontinuous faults, *J. Geophys. Res., 85,* 4337-4350, 1980.

Sih, G. C., *Handbook of Stress Intensity Factors*, Institute of Fracture and Solid Mechanics, Lehigh University, Bethlehem, Penn., 1973.

Sibson, R. H., Fault zone models, heat flow, and the depth distribution of earthquakes in the continental crust of the United States, *Bull. Seis. Soc. Am., 72,* 151-163, 1982.

Solberg, P., D. A. Lockner, R. Summers, J. Weeks and J. D. Byerlee, Experimental fault creep under constant differential stress and high confining pressure, 19th Symposium of Rock Mechanics, 118-120, 1978.

Strang, G., *Introduction to Applied Mathematics,* Wellesley-Cambridge Press, Wellesley, Mass., 758 pp., 1986.

Tapponnier, P. and W. F. Brace, Development of stress-induced microcracks in Westerly granite, *Int. J. Rock Mech. Min. Sci., 13,* 103-113, 1976.

Tse, S. T. and J. R. Rice, Crustal earthquake instability in relation to the depth variation for frictional slip properties, *J. Geophys. Res., 91,* 9452-9472, 1986.

Tullis, J. and R. A. Yund, Experimental deformation of dry Westerly granite, *J. Geophys. Res., 82,* 5705-5718, 1977.

Walsh, J. B., The effect of cracks on the compressibility of rock, *J. Geophys. Res., 70,* 381-389, 1965.

Walsh, J. B. and W. F. Brace, Elasticity of rock: a review of some recent theoretical studies, *Rock Mech. and Eng. Geol., 4,* 283-297, 1966.

Walsh, J. B. and M. A. Grosenbaugh, A new model for analyzing the effect of fractures on compressibility, *J. Geophys. Res., 84,* 3532-3536, 1979.

Wawersik, W. R., Time-dependent behavior of rock in uniaxial compression, Proc., 14th Sympo. Rock Mech., 85-106, 1973.

Wawersik, W. R. and C. Fairhurst, A study of brittle rock fracture in laboratory compression experiments, *Int. J. Rock Mech. Min. Sci., 7,* 561-575, 1970.

Williams, E. R. and T. R. Madden, Models for crack development and brittle failure and the role of crack configurations in guiding their behavior, unpublished manuscript, 1988.

Wong, T.-f., Shear fracture energy of Westerly granite from post-failure behavior, *J. Geophys. Res., 87,* 990-1000, 1982a.

Wong, T.-f., Effects of temperature and pressure on failure and post-failure behavior of Westerly granite, *Mechanics of Materials, 1,* 3-17, 1982b.

Wong, T.-f., J. Fredrich and G. D. Gwanmesia, Crack aperture statistics and pore space fractal geometry of Westerly granite and Rutland quartzite: implications on elastic contact models of rock compressibility, *J. Geophys. Res., 94,* in press.

Yukutake, H., Fracturing process of granite inferred from measurements of spatial and temporal variations in velocity during triaxial deformations, *J. Geophys. Res., 94,* in press.

Yund, R. A., M. L. Blanpied, T. E. Tullis and J. D. Weeks, Amorphous material in high strain experimental fault gouges, *J. Geophys. Res., 94,* in press.

Figure Captions

Figure 2.1 Examples of 2D finite-difference gridding schemes. Unit cell is shown by dashed line. Modified staggered grid was used in present model formulation.

Figure 2.2 Diagonal fault can only be approximated by staircase assemblage of cracks if only vertical and horizontal cracks are allowed. Unlike a diagonal fault, this geometry is stable to axial compression. In addition, model displacements on the crack set require opening of voids. This would not be the case for deformation on a diagonal fault.

Figure 2.3 The basic 3 x 3 block, including diagonal cracks, which is solved in the 2D simulation. Each side of each triangular element is a potential crack site. Shear and normal stress components are computed on the sides of each element from adjacent displacements. The 72 displacement compononts are determined that will bring each triangular element into equilibrium, using surrounding displacements as boundary conditions.

Figure 2.4 Examples of series averaging scheme based on two cells and intervening crack site. Interim use is to interpolate displacements of cell sides. Ultimately, these displacements are used to compute local strains and stresses.

Figure 2.5 Representation of slip vector η along crack surfaces.

Figure 2.6 Schematic view of triaxial test geometry modeled by computer simulation.

Figure 2.7 Triaxial deformation of Westerly granite showing differential stress, transverse and volumetric strains plotted *vs* axial strain.

Figure 2.8 Boundary conditions applied in 2D simulation.

Figure 2.9 Stress and strain plots for 1 kb confining pressure simulation.

Figure 2.10 Starting crack model M1 in which 20% of potential crack sites are fully cracked. a) Fully cracked edges b) fully cracked and partially cracked edges c) largest cluster of connected cracks d) distribution of crack lengths and cluster sizes.

Figure 2.11 Summary of stress-strain curves for suite of runs at different confining pressures; brittle-ductile transition occurs with increasing confining pressure. Model parameters are listed in Table 2.1. All simulations used initial crack population M1.

Figure 2.12 Results of unconfined simulation plotted *vs* axial strain: a) differential stress b) transverse and volumetric strain c) and d) cumulative crack count for vertical and diagonal cracks in modes I and II. A new crack is said to occur in the program iteration in which a partially cracked site becomes fully cracked.

Figure 2.13 0.5 kb confining pressure simulation.

Figure 2.14 1 kb confining pressure simulation.

Figure 2.15 2 kb confining pressure simulation.

Figure 2.16 4 kb confining pressure simulation.

Figure 2.17 8 kb confining pressure simulation.

Figure 2.18 12 kb confining pressure simulation.

Figure 2.19 16 kb confining pressure simulation.

Figure 2.20 Mohr construction for simulations shown in Fig. 2.11

Figure 2.21 Fracture shear strength and frictional shear strength *vs* normal stress for Westerly granite, after *Byerlee* (1967).

Figure 2.22 Axial and transverse P-wave velocity from 1 kb confining pressure simulation. a) Plotted *vs* axial strain, b) plotted *vs* relative differential stress; includes experimental data from *Lockner et al.* (1978) (P_C = 0.5 kb) and *Yukutake* (1989) (P_C = 0.81 kb).

Figure 2.23 a) Stress-strain curves for simulations at confining pressures upto 8 kb. Crack closure algorithm was modified to simulate pressure-resistant pores (see text). b) Young's modulus *vs* confining pressure for Berea sandstone (unpublished data).

Figure 2.24 Crack plots at ε_{yy} = -0.0073 (see Fig. 2.9); P_C = 1 kb; a) all fully cracked edges (dotted lines represent cracks present in undeformed sample, solid lines represent new cracks), b) largest crack cluster.

Figure 2.25 Crack plots at ε_{yy} = -0.0096; a) all fully cracked edges (dotted lines represent cracks present in previous plot, solid lines represent new cracks), b) largest crack cluster.

Figure 2.26 Crack plots at ε_{yy} = -0.0114; a) all fully cracked edges (dotted lines represent cracks present in previous plot, solid lines represent new cracks), b) largest crack cluster.

Figure 2.27 Crack plots at ε_{yy} = -0.0124; a) all fully cracked edges (dotted lines represent cracks present in previous plot, solid lines represent new cracks), b) largest crack cluster.

Figure 2.28 Crack length/cluster size distributions for P_c = 1 kb simulation (Fig 2.9); a) ε_{yy} = -0.0073; b) ε_{yy} = -0.0096; c) ε_{yy} = -0.0114; d) ε_{yy} = -0.0124.

Figure 2.29 Examples of cell geometries used in RNG calculations for critical failure probability and critical connectivity probability.

Figure 2.30 Probabilities of crack sites being fully cracked plotted *vs* confining pressure for peak strength in non-time-dependent simulations and for onset of tertiary creep in time-dependent simulations. Critical crack probability for failure is 0.29.

Figure 2.31 Schematic view of crack growth rate *vs* stress intensity for mode I subcritical crack growth.

Figure 2.32 Log (slip rate) *vs* relative coefficient of friction for Westerly granite gouge at P_c = 4 kb (from *Solberg et al.*, 1978).

Figure 2.33 Creep simulation using starting crack model M2. P_c = 1 kb, P_{dif} = 5.5 kb.

Figure 2.34 Initial crack population model M2; 11% probability of crack site being fully cracked. a) Fully cracked sites, b) partially and fully cracked sites, c) crack length/cluster size distribution.

Figure 2.35 Non-time-dependent simulation using starting model M2 (top), creep simulations using subcritical crack growth and time-dependent crack slip (middle and bottom); P_c = 1 kb.

Figure 2.36 Cumulative crack growth data for simulations shown in Fig. 2.35.

Figure 2.37 Comparative crack distributions for non-time-dependent simulation and 5.8 kb creep simulation show in Fig. 2.35. Non-time-dependent peak strength crack distribution is used in all plots. Late secondary creep crack

distributions are used in a) and c); early tertiary creep crack distributions are used in b) and d). Dotted lines represent cracks common to both data sets. Solid lines represent: a) and b) cracks in creep sample but not in non-time-dependent sample, c) and d) cracks in non-time-dependent sample but not in creep sample.

Figure 2.38 Comparative crack distributions for non-time-dependent simulation and 5.0 kb creep simulation show in Fig. 2.35. Non-time-dependent peak strength crack distribution is used in all plots. Late secondary creep crack distributions are used in a) and c); early tertiary creep crack distributions are used in b) and d). Dotted lines represent cracks common to both data sets. Solid lines represent: a) and b) cracks in creep sample but not in non-time-dependent sample, c) and d) cracks in non-time-dependent sample but not in creep sample.

Figure 2.39 Time-to-failure plots for P_c = 1 kb creep simulations using subcritical crack growth alone, time-dependent friction alone and subcritical crack growth and time-dependent friction together. Also plotted is 1 kb time-to-failure data for Barre granite from *Kranz* (1980).

Figure 2.40 P_c = 0.5 kb creep simulation data. a) axial strain, b) acoustic emission rate and c) transverse P-wave velocity relative to hydrostatic velocity.

Figure 2.41 P_c = 0.5 kb Westerly granite creep data from *Lockner and Byerlee* (1980). a) axial strain, b) acoustic emission rate and c) relative transverse P-wave velocity.

Figure 2.42 Plot of density of acoustic emission source locations from *Lockner and Byerlee* (1980). a) Primary creep, b) secondary creep, c) initial 133 minutes of tertiary creep and d) final 18 minutes of tertiary creep.

Figure 2.43 Density of vertical and diagonal cracks in creep simulation at P_c = 1 kb and P_{dif} = 5.8 kb. a) starting model M2 crack density and b) mid-tertiary

creep crack density. Note localization of crack damage in upper part of sample. Critical density for failure = 0.9, density for fully cracked region = 3.0.

Figure 2.44 Density of vertical and diagonal cracks in creep simulation at P_c = 1 kb and P_{dif} = 5 kb. a) Starting model M3 crack density, b) late secondary creep crack density, c) early tertiary creep crack density and d) late tertiary creep crack density. Note similarity to granite sample in Fig. 2.42.

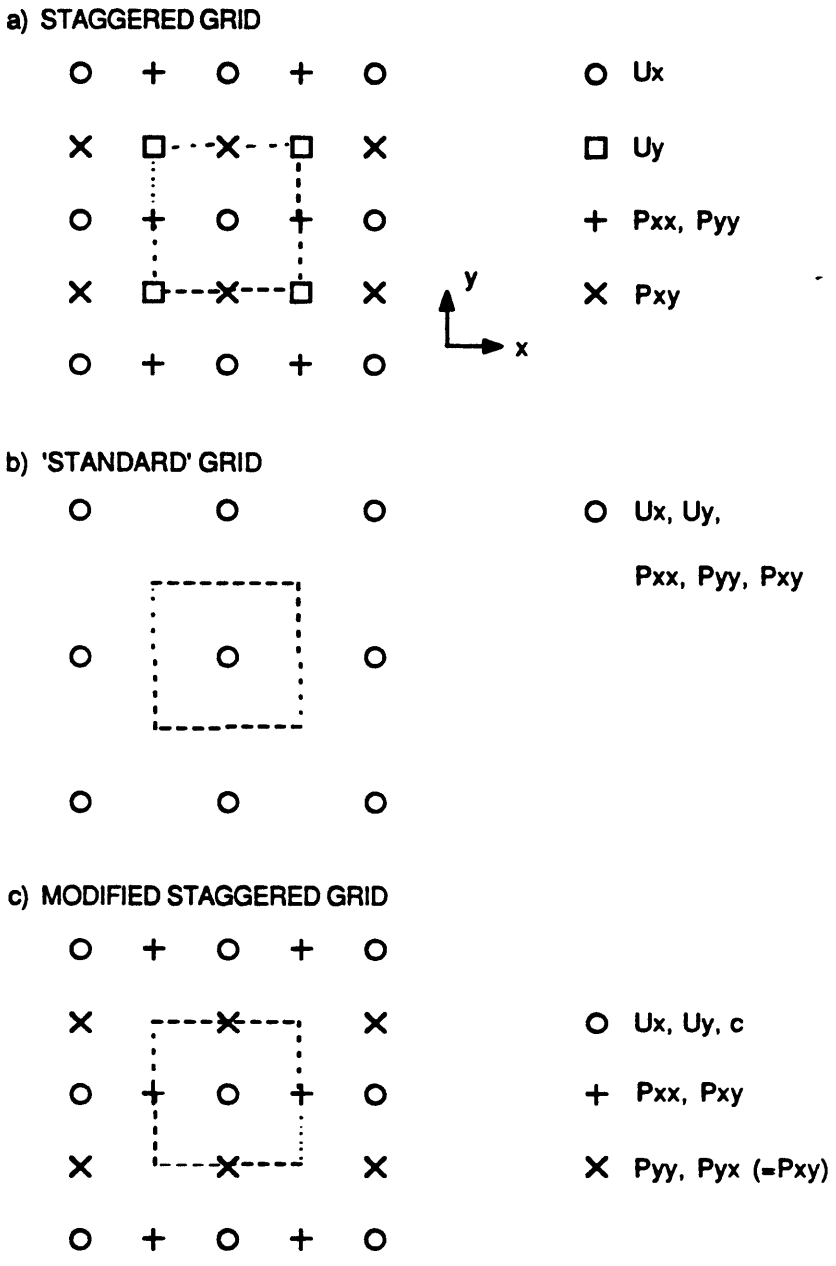
a) STAGGERED GRID
Ux
Uy
Pxx, Pyy
Pxy
y
x
b) 'STANDARD' GRID
Ux, Uy,
Pxx, Pyy, Pxy
c) MODIFIED STAGGERED GRID
Ux, Uy, c
Pxx, Pxy
Pyy, Pyx (=Pxy)

Figure 2.1

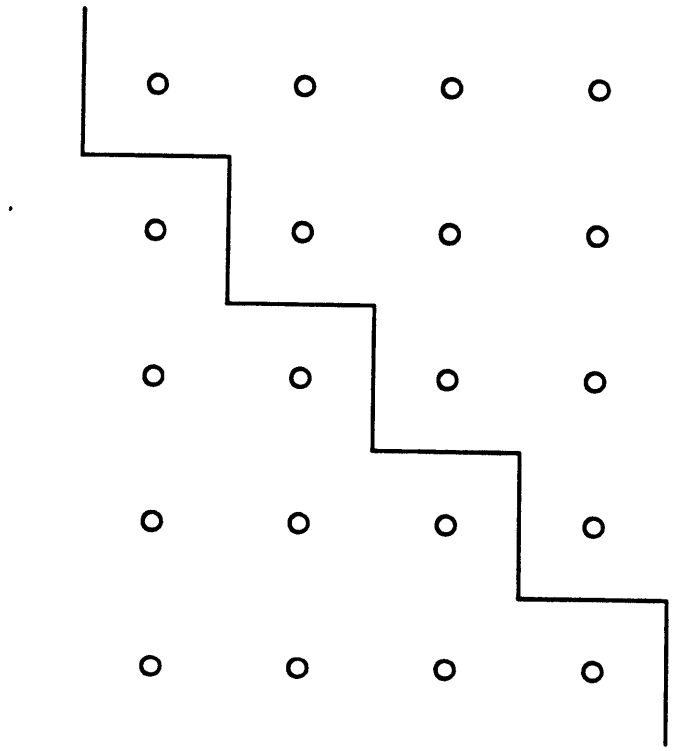

Figure 2.2

MODIFIED STAGGERED GRID WITH DIAGONAL CRACKS

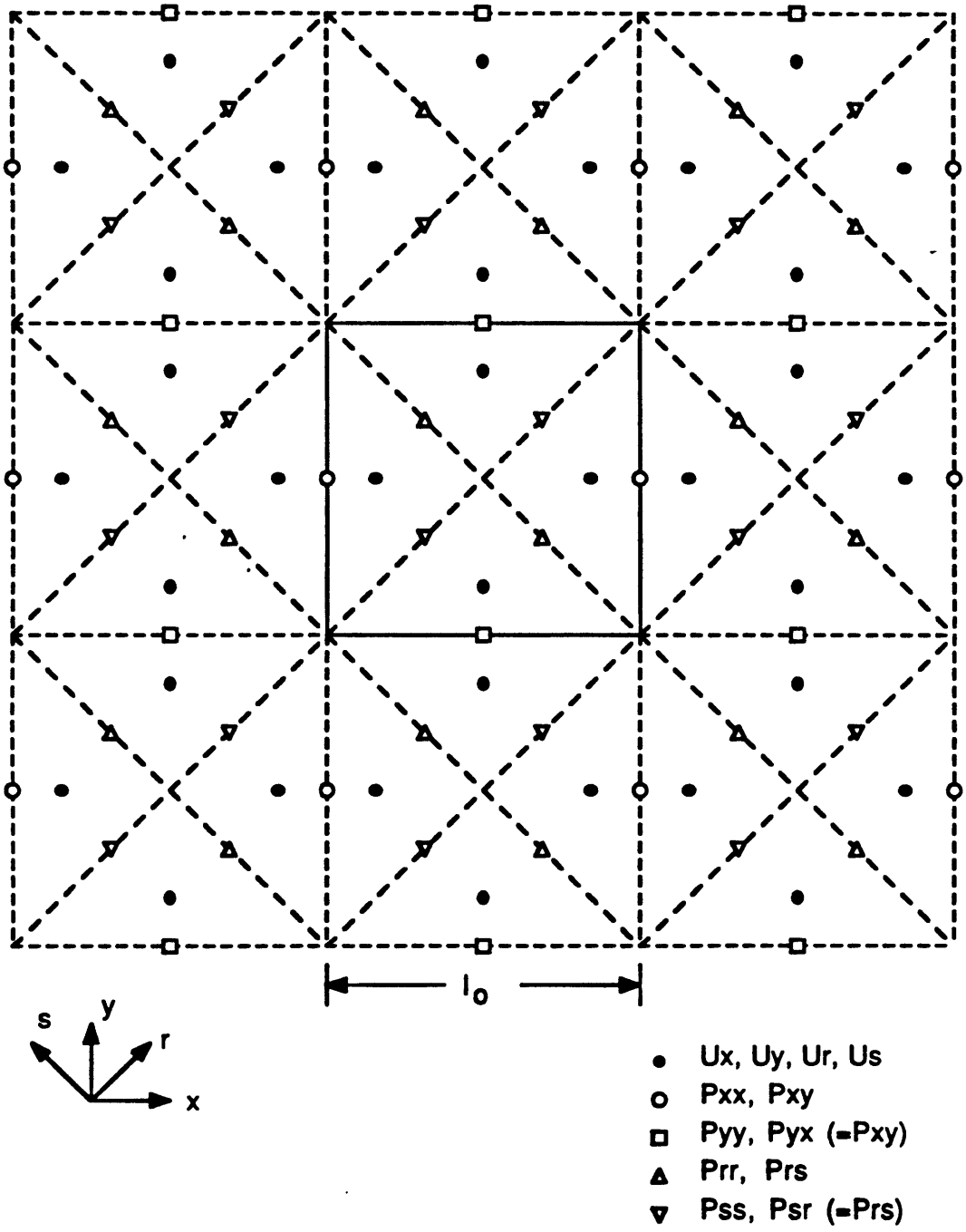

Figure 2.3

a) NO CRACK ON EDGE

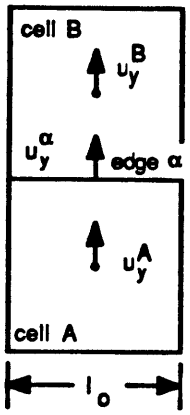

b) OPEN CRACK ON EDGE

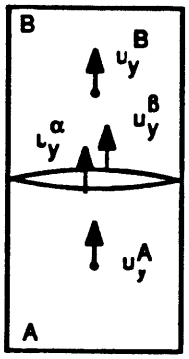

c) PARTIALLY CRACKED EDGE

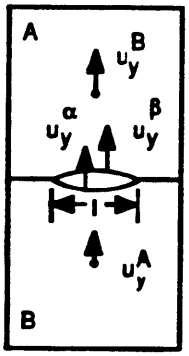

d) DISPLACEMENTS USED TO COMPUTE STRESS

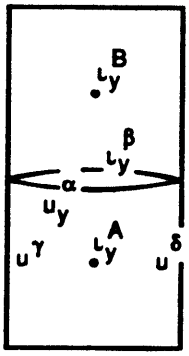

Figure 2.4

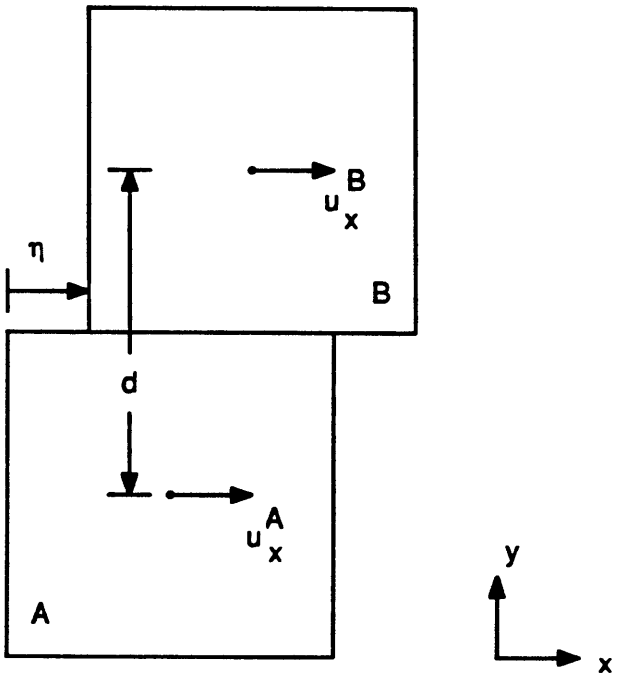

Figure 2.5

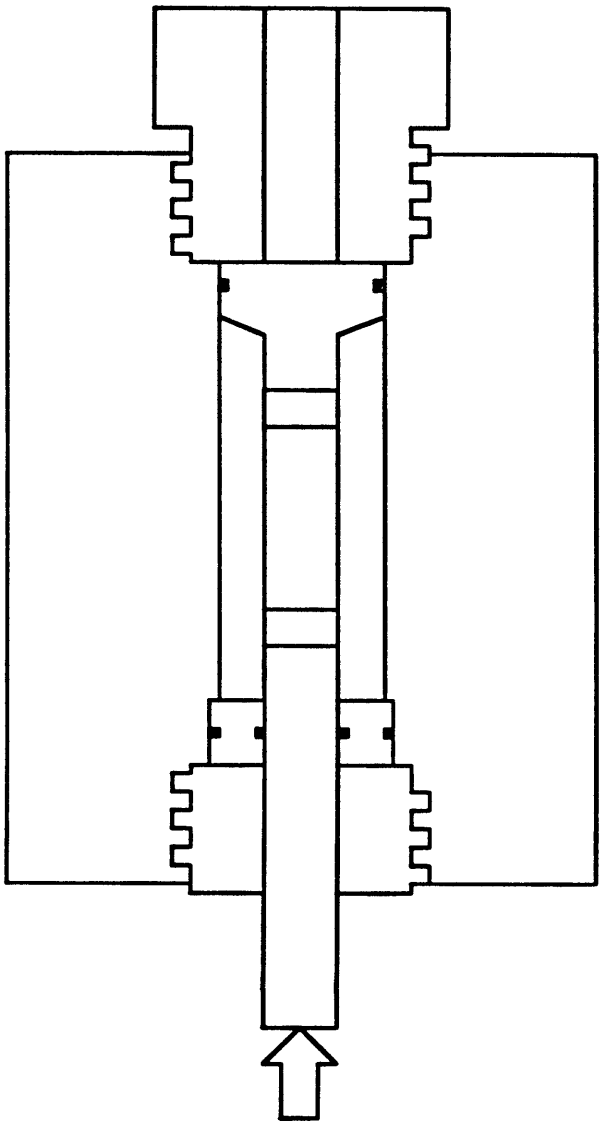

Figure 2.6

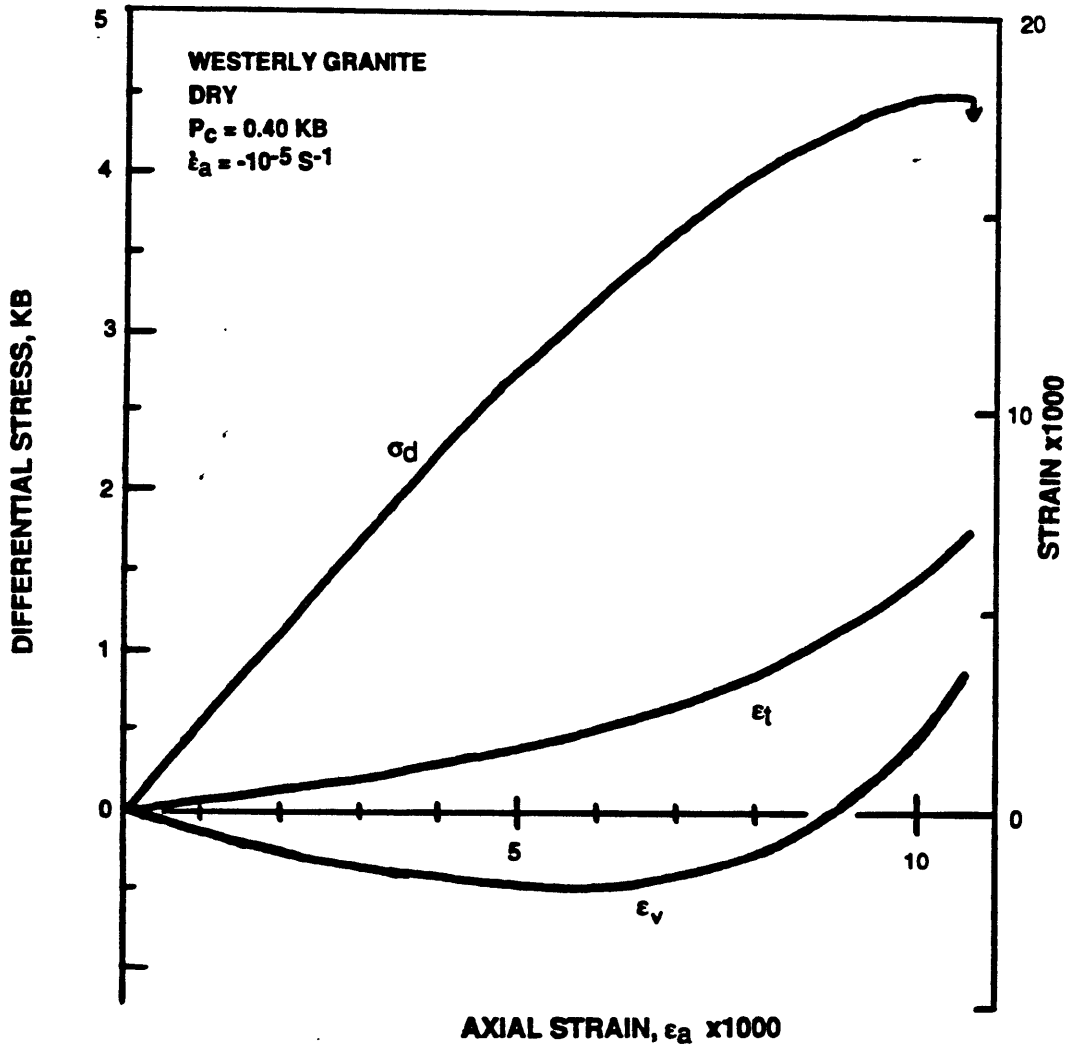
WESTERLY GRANITE
DRY
P_c = 0.40 KB
$\dot{\varepsilon}_a = -10^{-5}\ S^{-1}$
σ_d
ε_t
ε_v
DIFFERENTIAL STRESS, KB
STRAIN x1000
AXIAL STRAIN, ε_a x1000
0
1
2
3
4
5
10
20
5
10

Figure 2.7

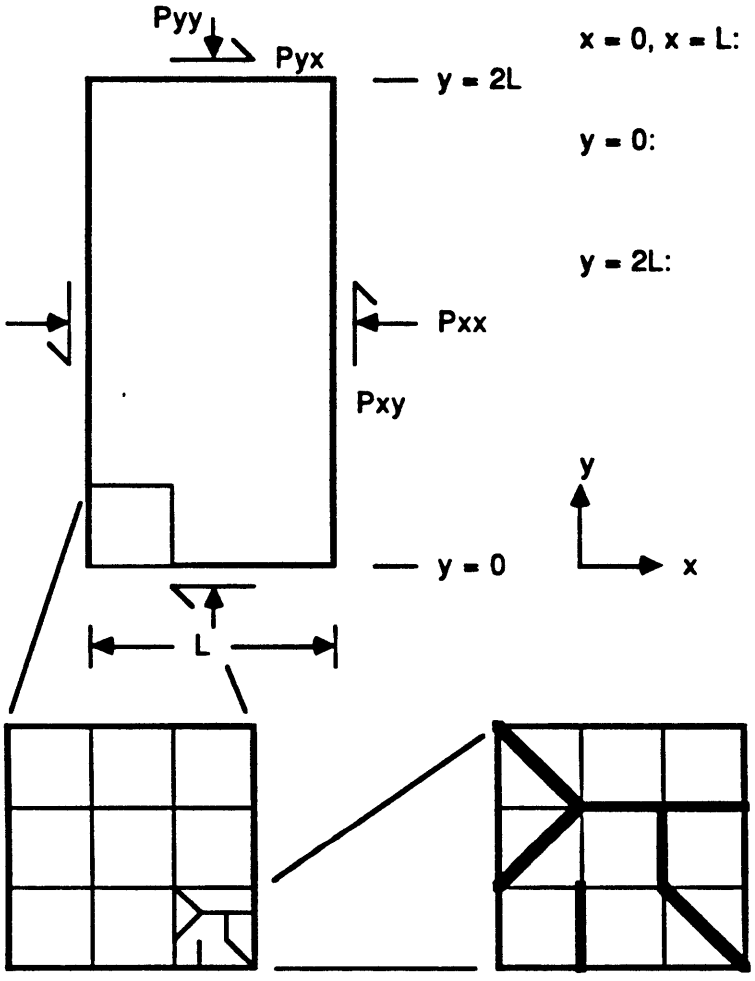

BOUNDARY CONDITIONS

x = 0, x = L:	Pxx = Pconf
	Pxy = 0
y = 0:	<Pyx> = 0
	Ux = x exx
	Uy = 0
y = 2L:	<Pyx> = 0
	Ux = x exx + c
	Uy = 2L eyy

Figure 2.8

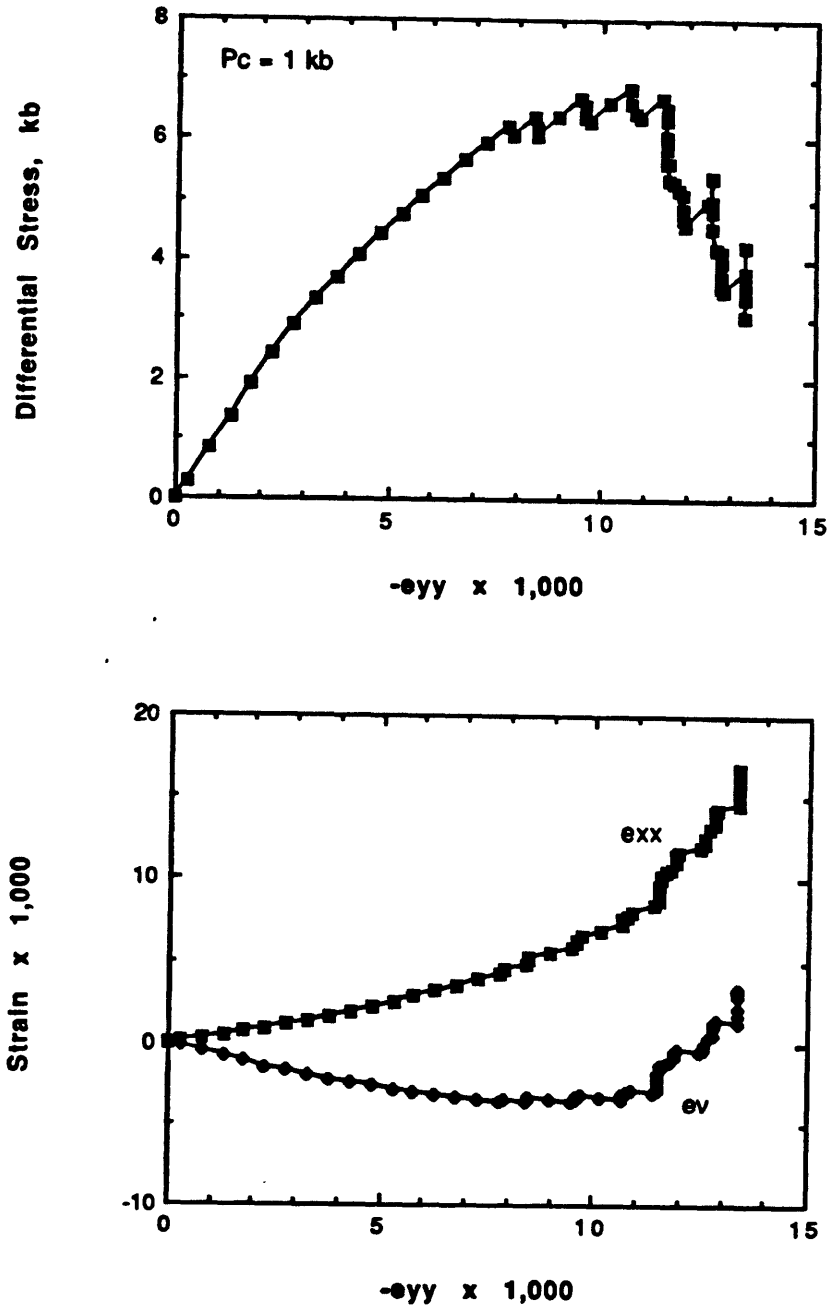
Pc = 1 kb
Differential Stress, kb
8
6
4
2
0
0
5
10
15
-eyy x 1,000
Strain x 1,000
20
10
0
-10
exx
ev
0
5
10
15
-eyy x 1,000

Figure 2.9

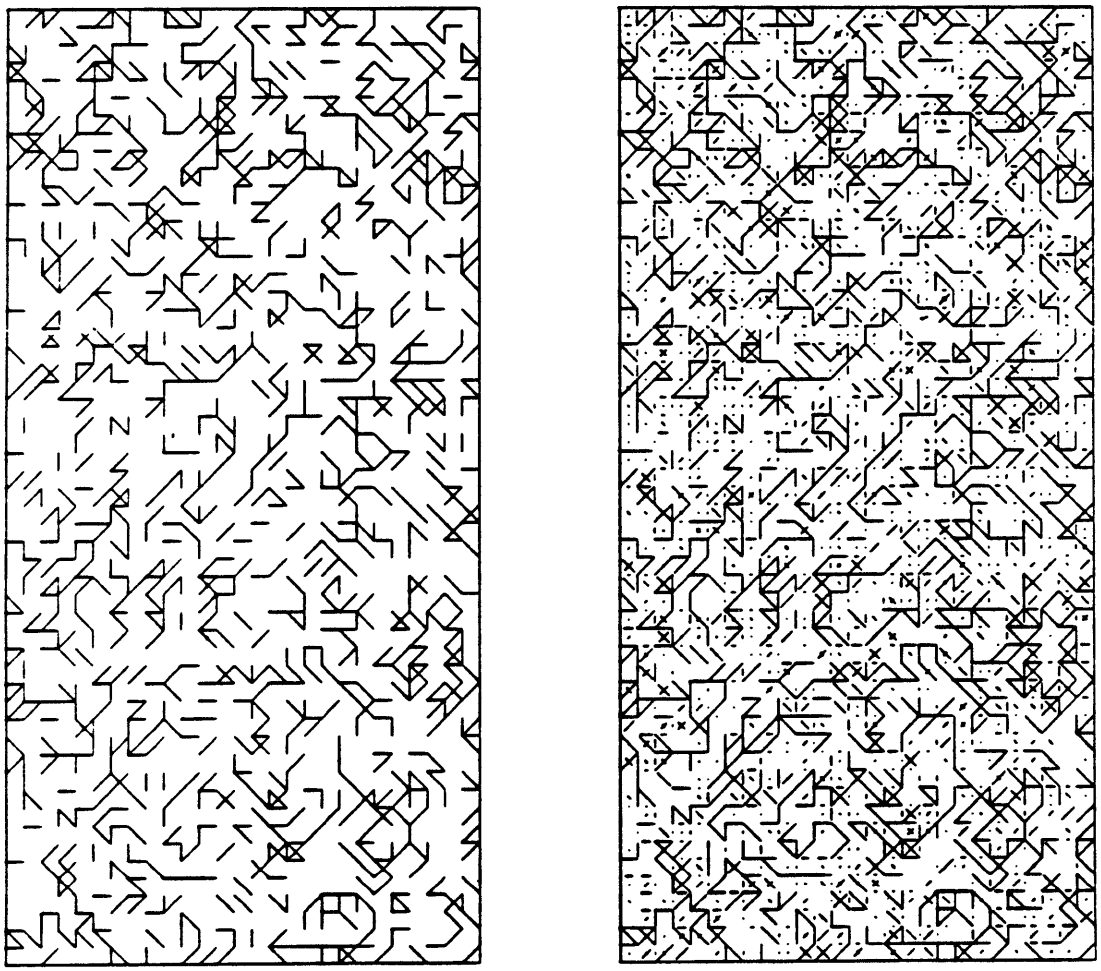

Figure 2.10

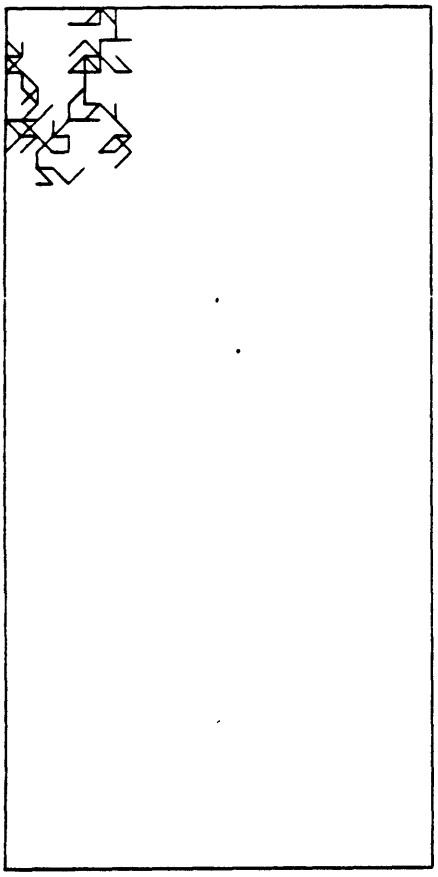

(c)

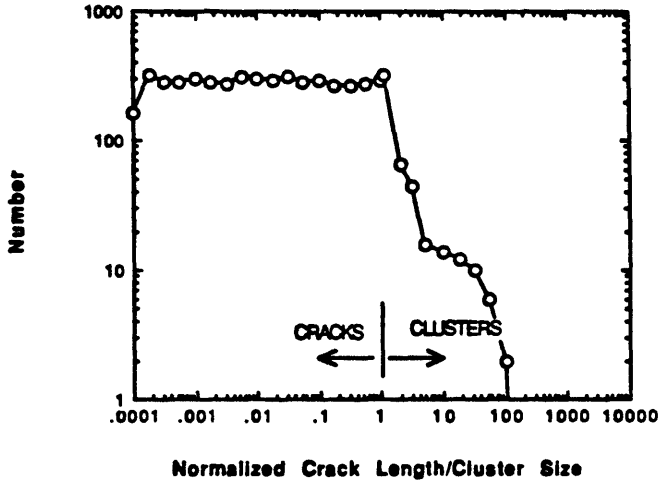

(d)

Figure 2.10 (continued)

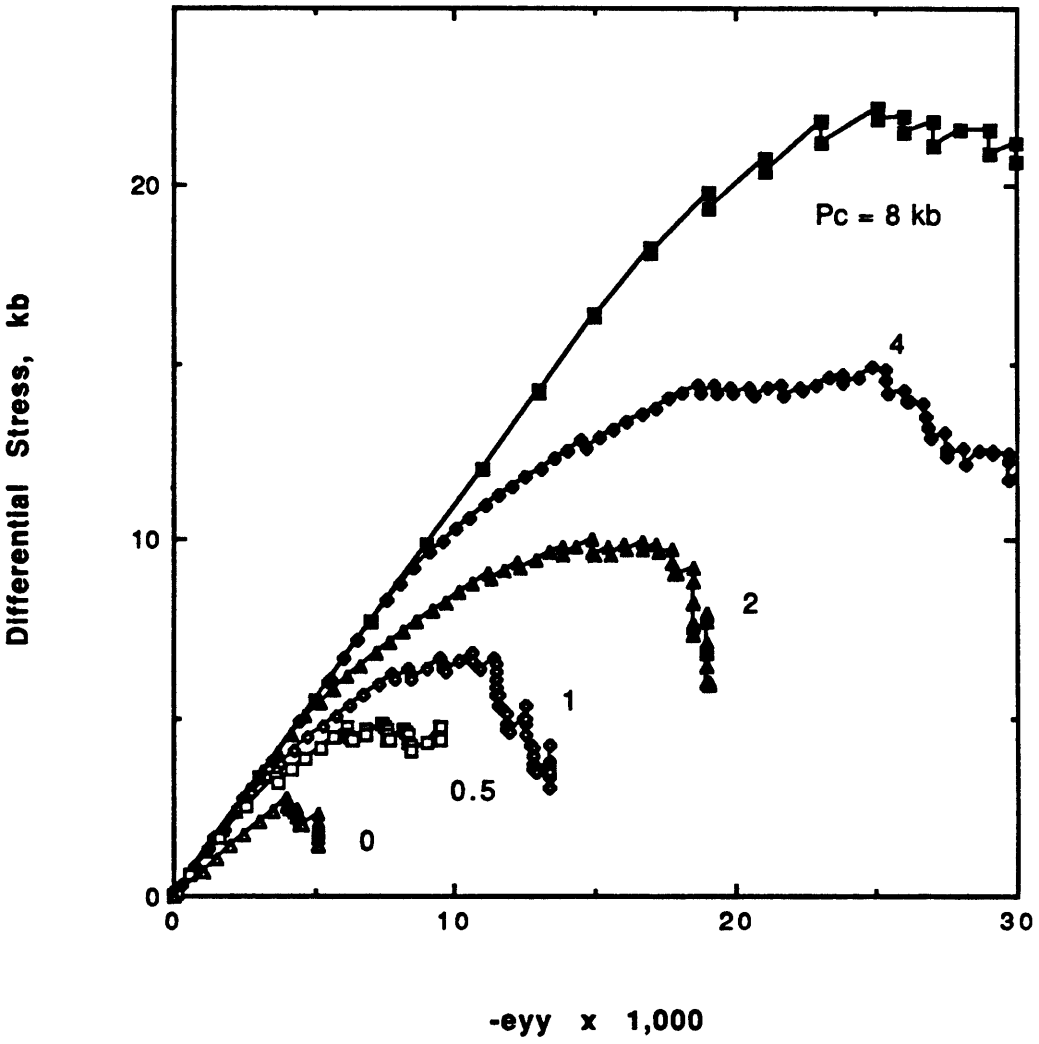
Differential Stress, kb
20
10
0
0
10
20
30
Pc = 8 kb
4
2
1
0.5
0
-eyy x 1,000

Figure 2.11

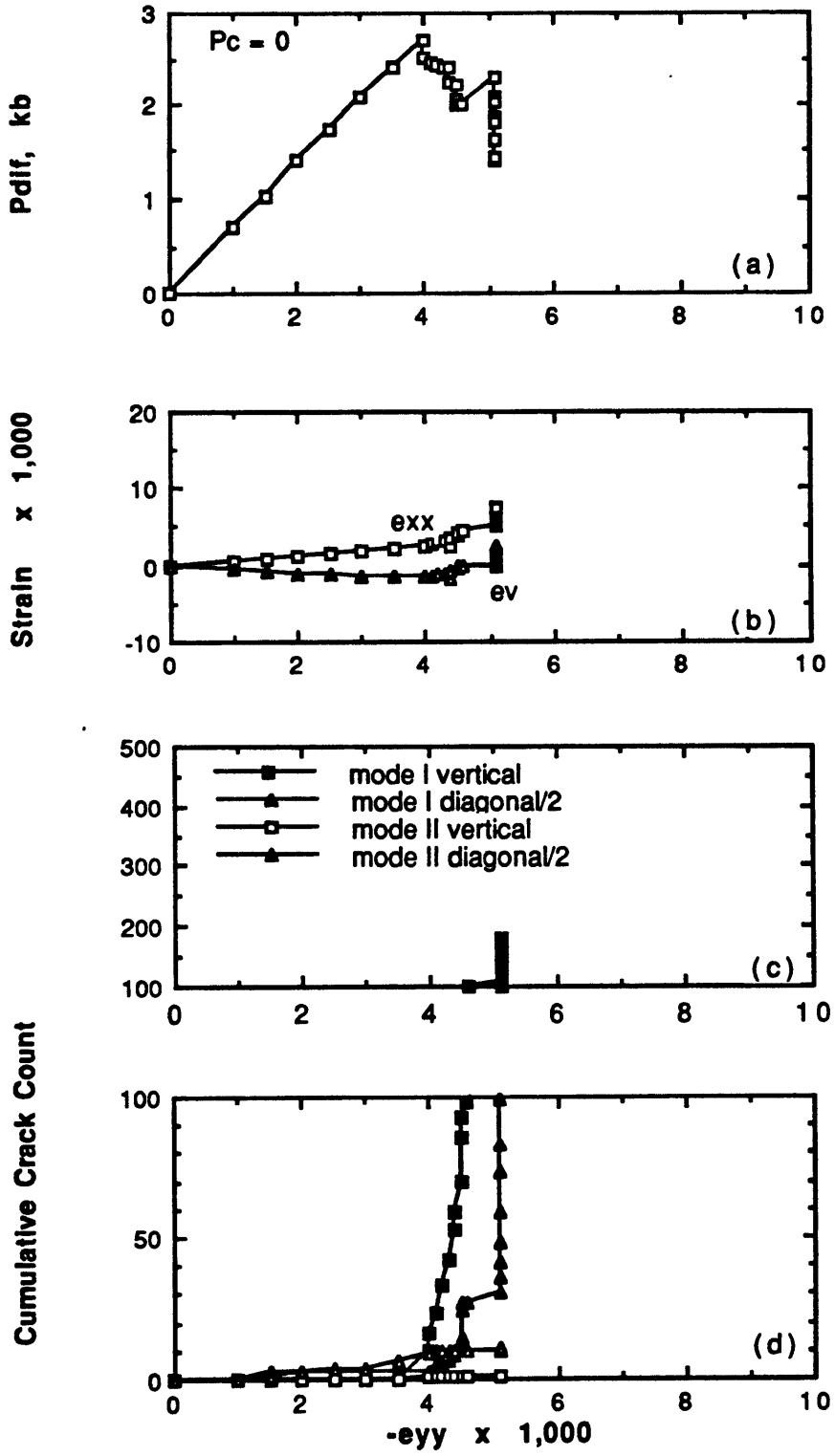
Pdif, kb
Pc = 0
(a)
Strain x 1,000
exx
ev
(b)
mode I vertical
mode I diagonal/2
mode II vertical
mode II diagonal/2
(c)
Cumulative Crack Count
(d)
-eyy x 1,000

Figure 2.12

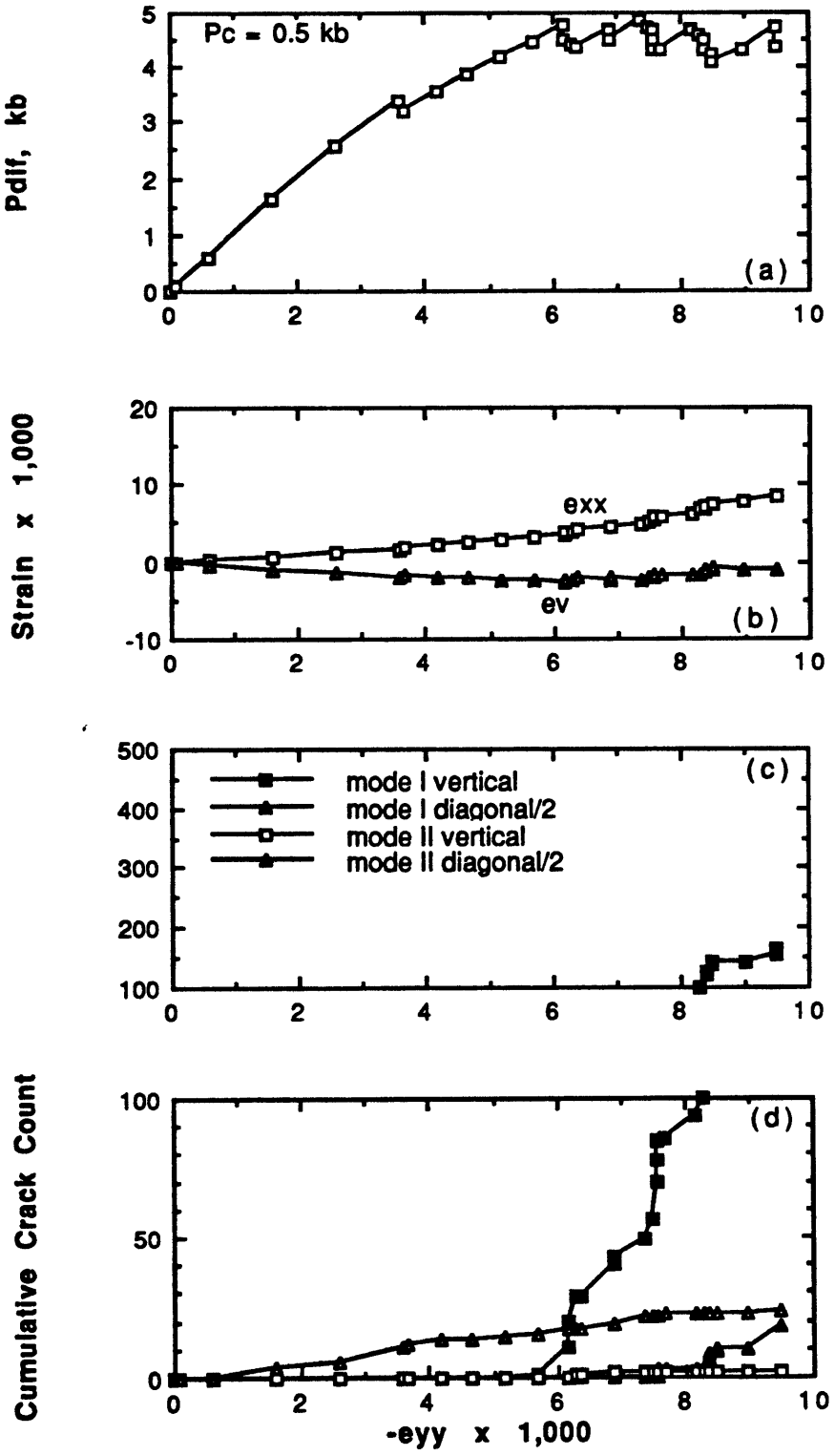
Pc = 0.5 kb
Pdif, kb
(a)
Strain x 1,000
exx
ev
(b)
mode I vertical
mode I diagonal/2
mode II vertical
mode II diagonal/2
(c)
Cumulative Crack Count
(d)
-eyy x 1,000

Figure 2.13

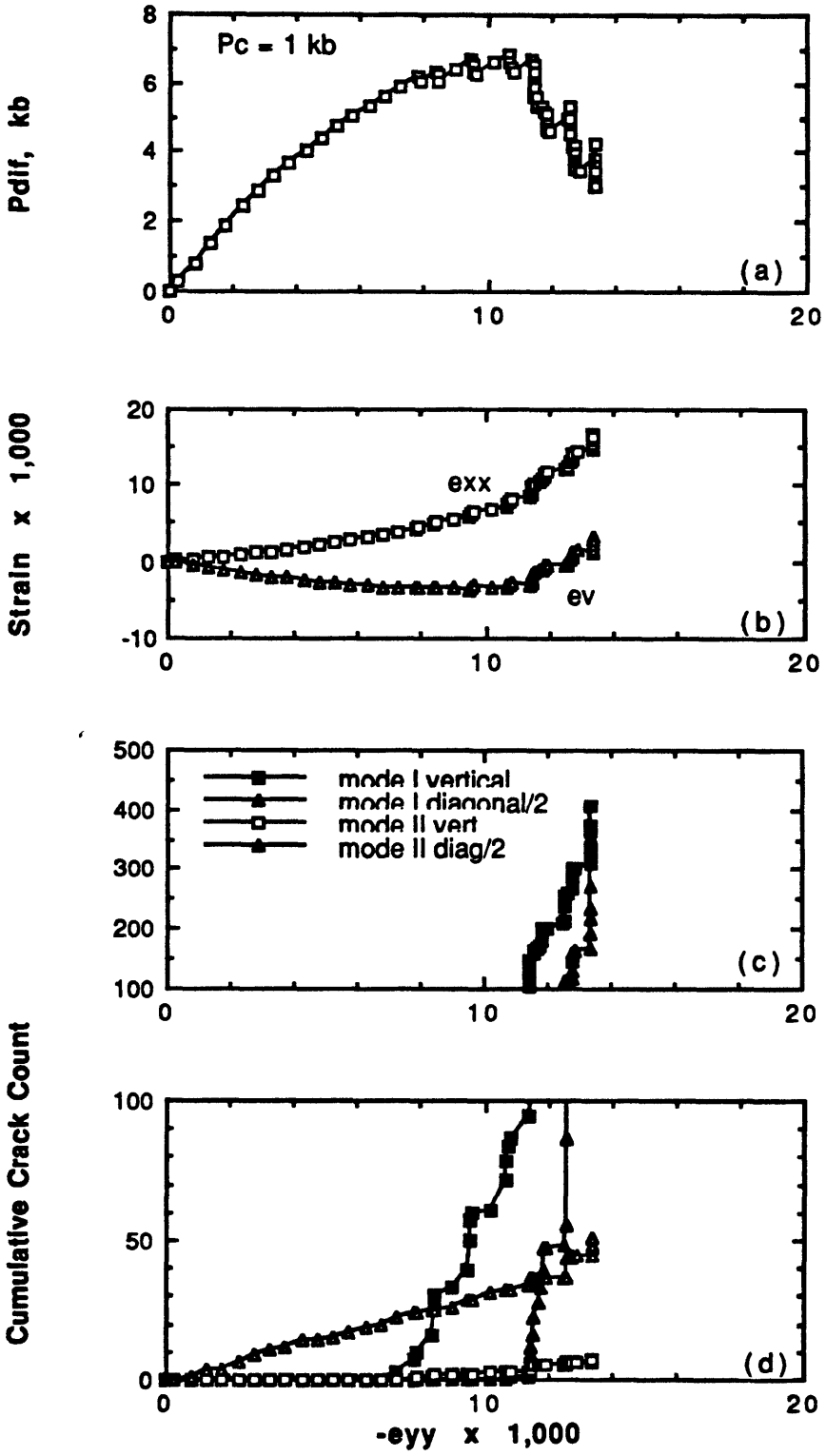
Pdif, kb
Pc = 1 kb
(a)
Strain x 1,000
exx
ev
(b)
mode I vertical
mode I diagonal/2
mode II vert
mode II diag/2
(c)
Cumulative Crack Count
(d)
-eyy x 1,000

Figure 2.14

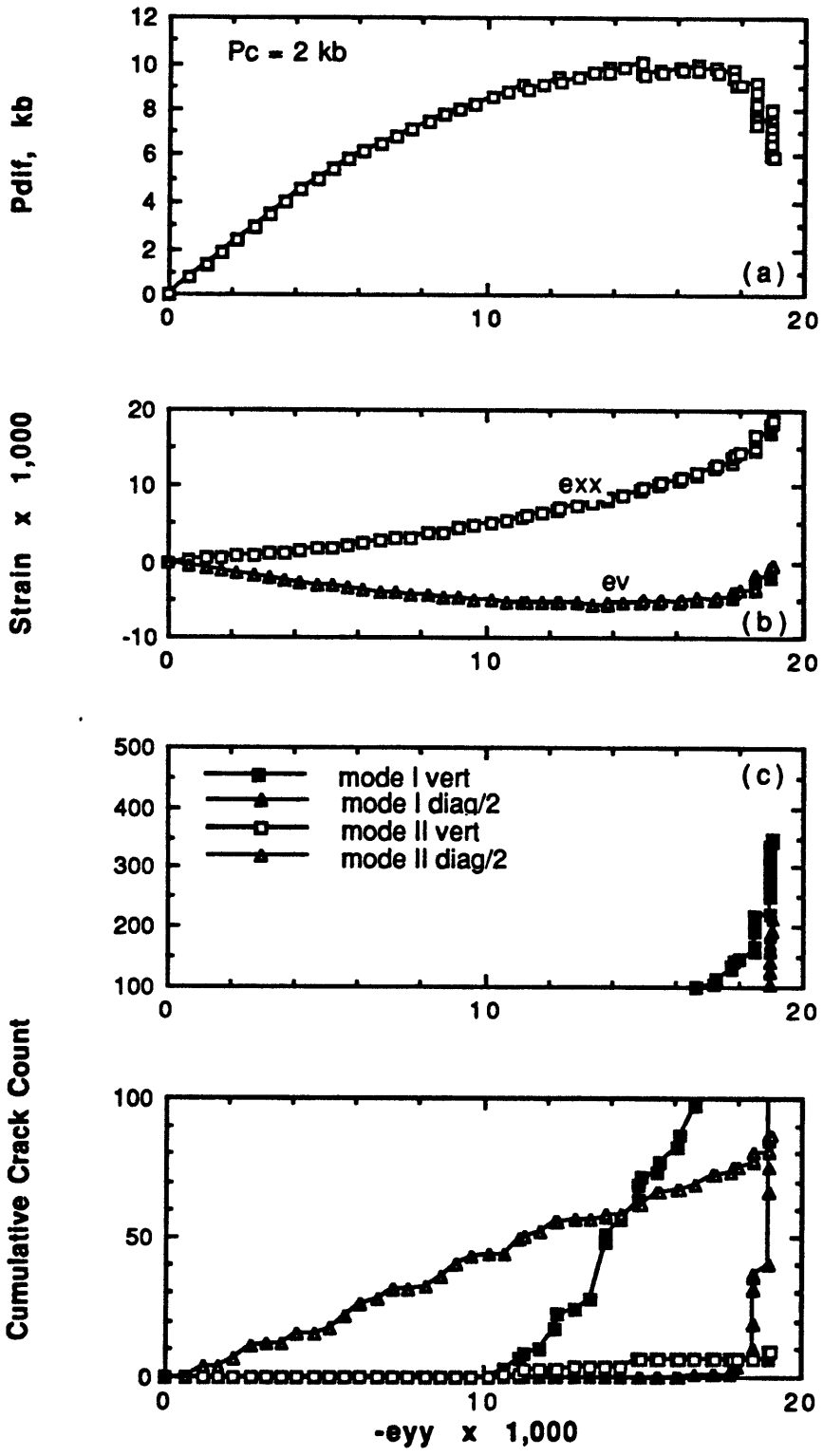
Pdif, kb
Pc = 2 kb
(a)
Strain x 1,000
exx
ev
(b)
mode I vert
mode I diag/2
mode II vert
mode II diag/2
(c)
Cumulative Crack Count
-eyy x 1,000

Figure 2.15

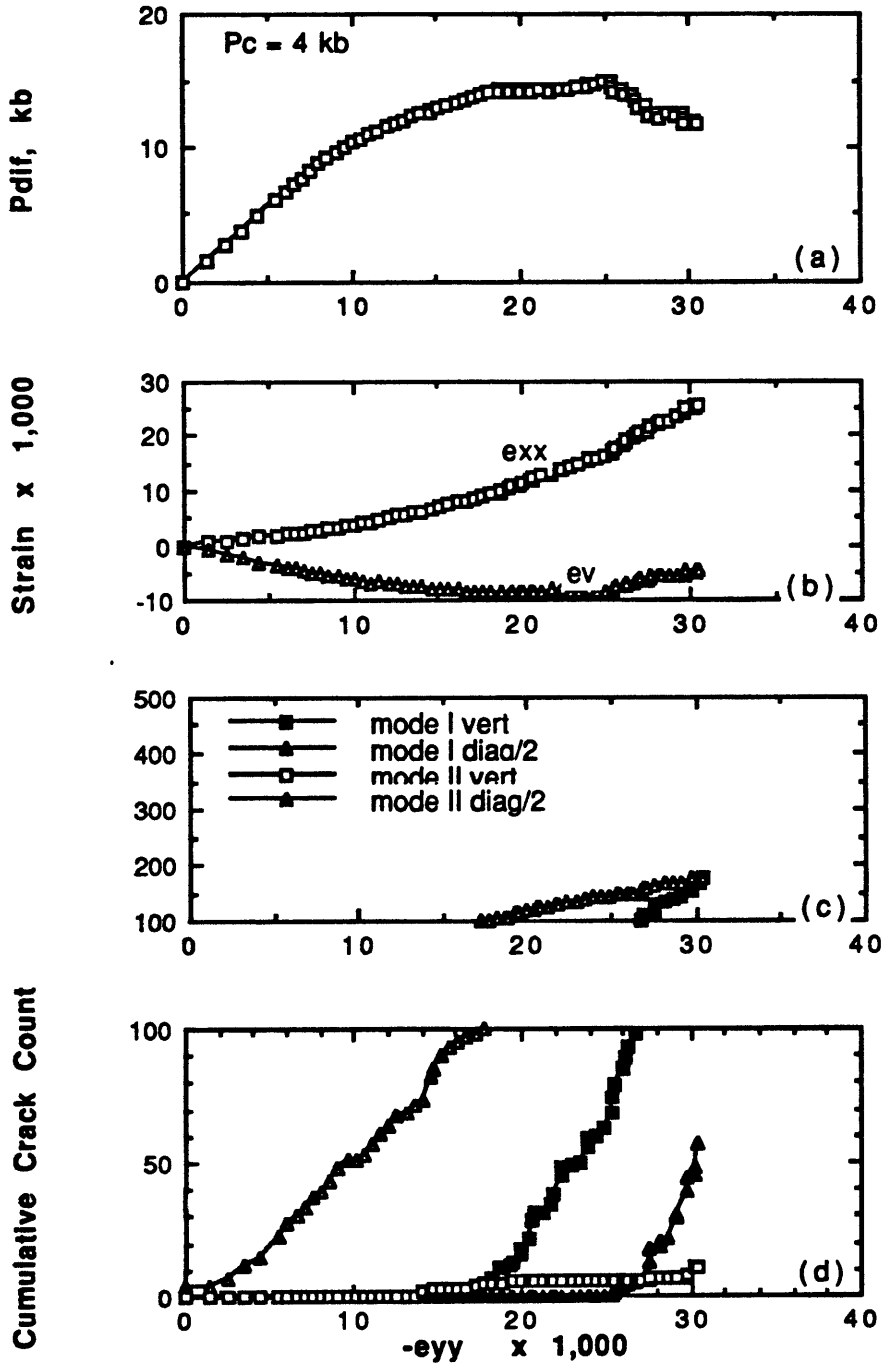
Pc = 4 kb
Pdif, kb
(a)
exx
ev
Strain x 1,000
(b)
mode I vert
mode I diag/2
mode II vert
mode II diag/2
(c)
Cumulative Crack Count
(d)
-eyy x 1,000

Figure 2.16

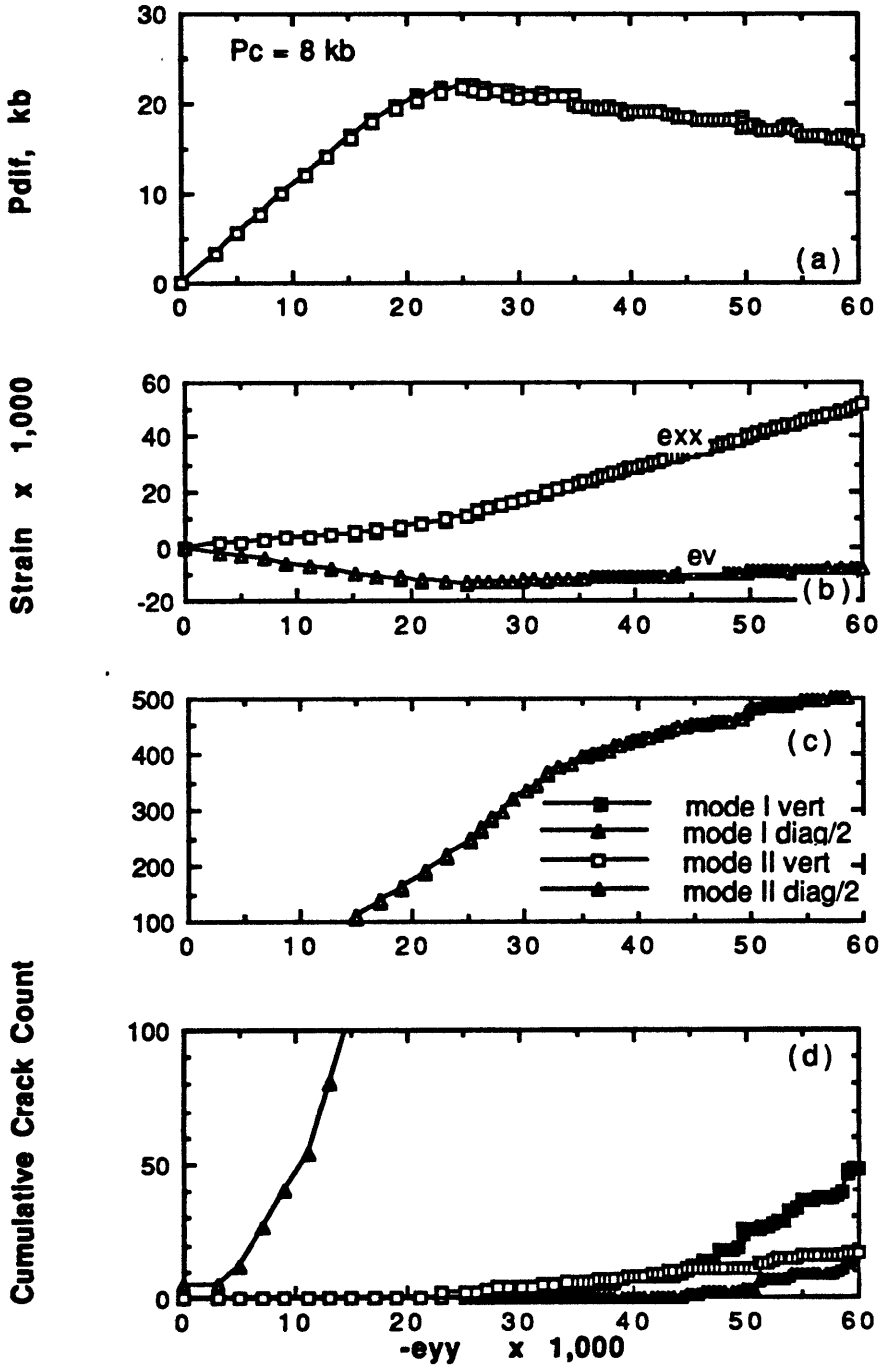
Pc = 8 kb
Pdif, kb
(a)
Strain x 1,000
exx
ev
(b)
(c)
mode I vert
mode I diag/2
mode II vert
mode II diag/2
Cumulative Crack Count
(d)
-eyy x 1,000

Figure 2.17

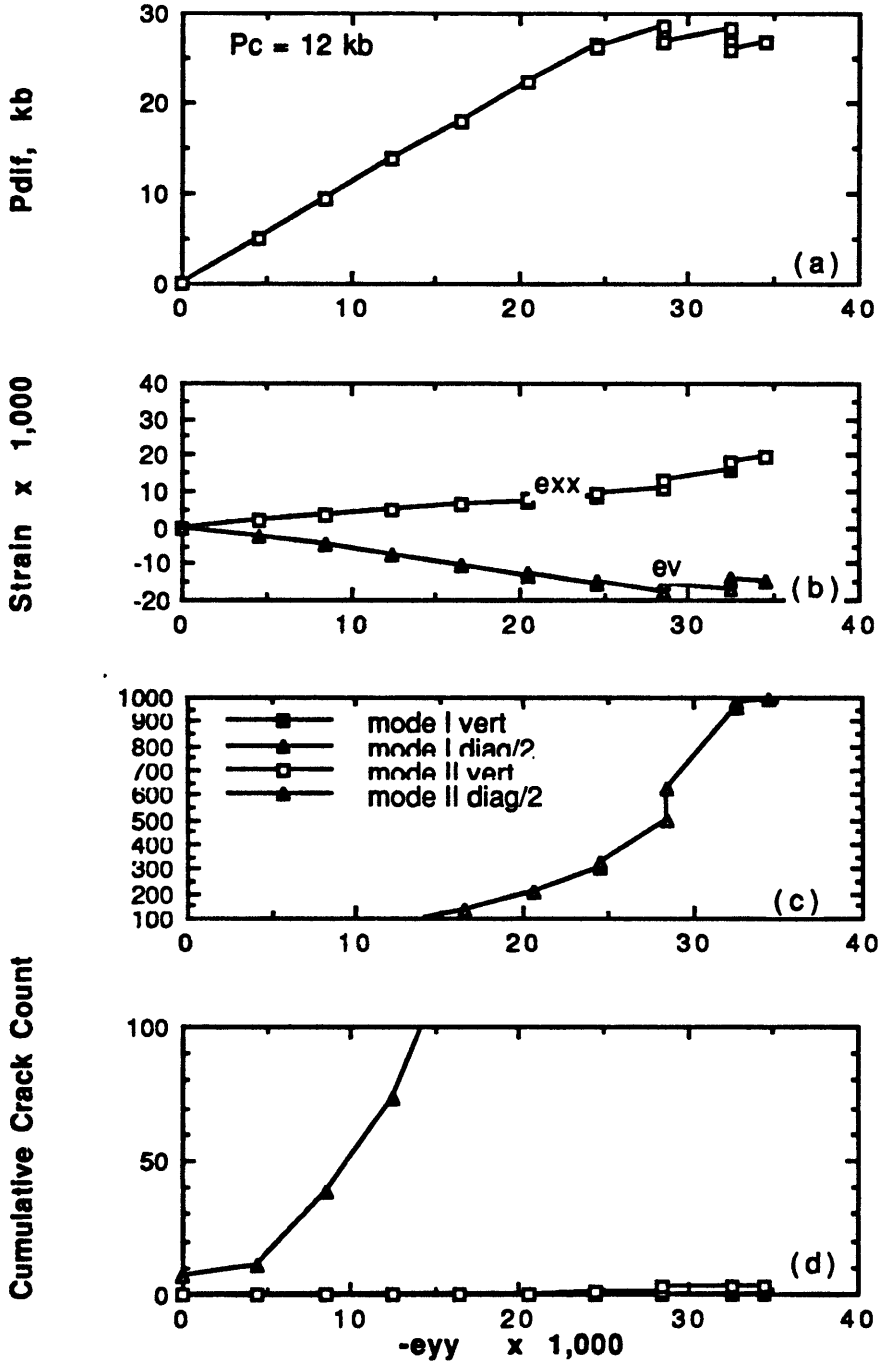
Pc = 12 kb
Pdif, kb
(a)
exx
ev
(b)
Strain x 1,000
mode I vert
mode I diag/2
mode II vert
mode II diag/2
(c)
Cumulative Crack Count
(d)
-eyy x 1,000

Figure 2.18

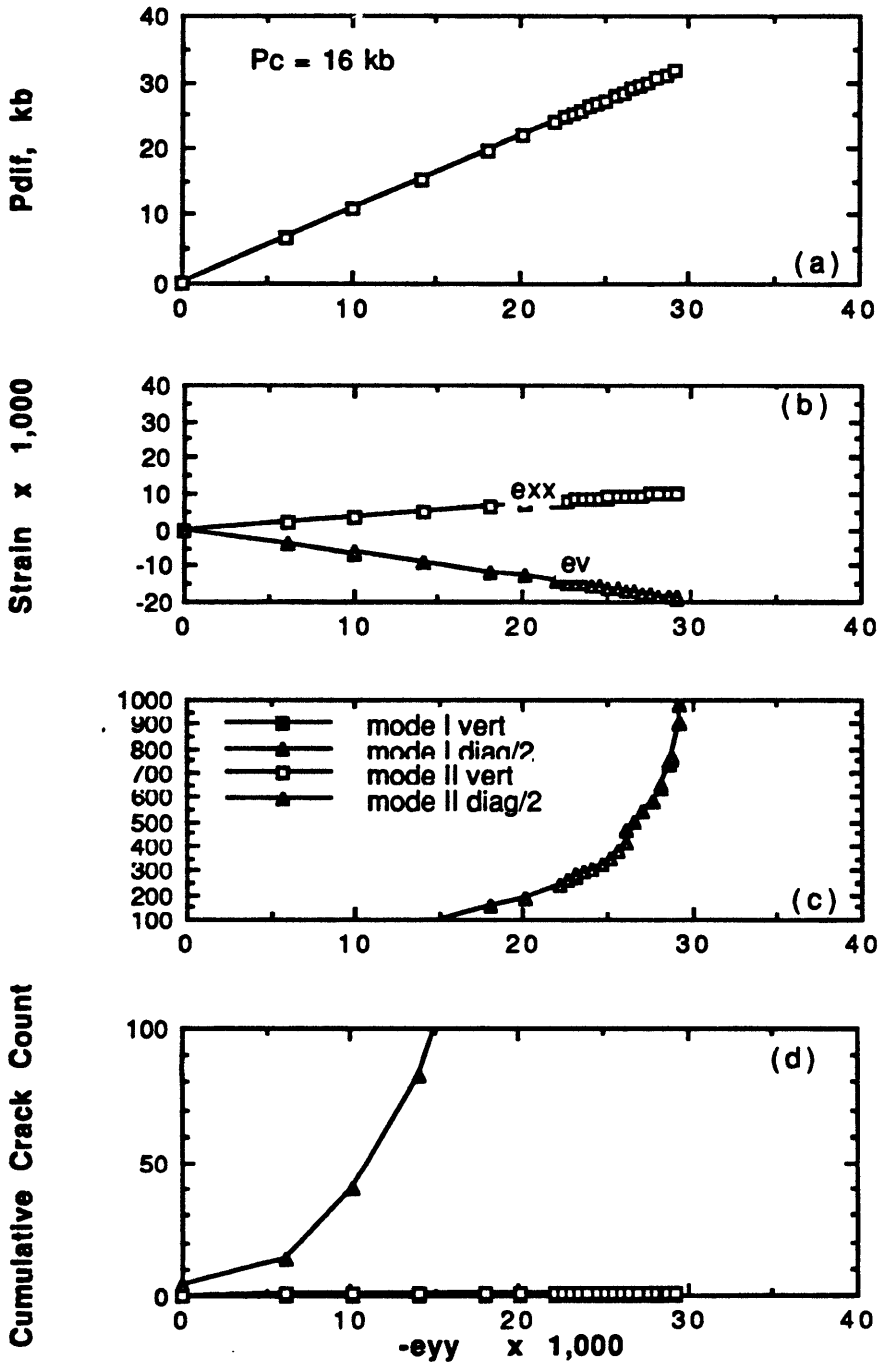
Pdif, kb
Pc = 16 kb
(a)
Strain x 1,000
(b)
exx
ev
mode I vert
mode I diag/2
mode II vert
mode II diag/2
(c)
Cumulative Crack Count
(d)
-eyy x 1,000

Figure 2.19

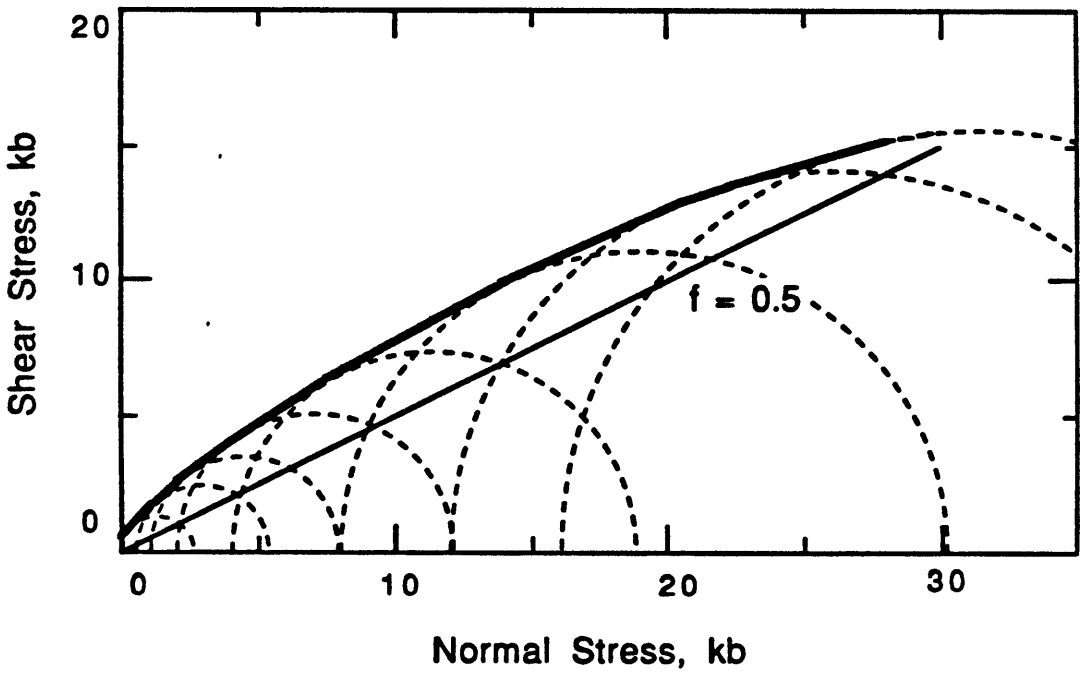

Figure 2.20

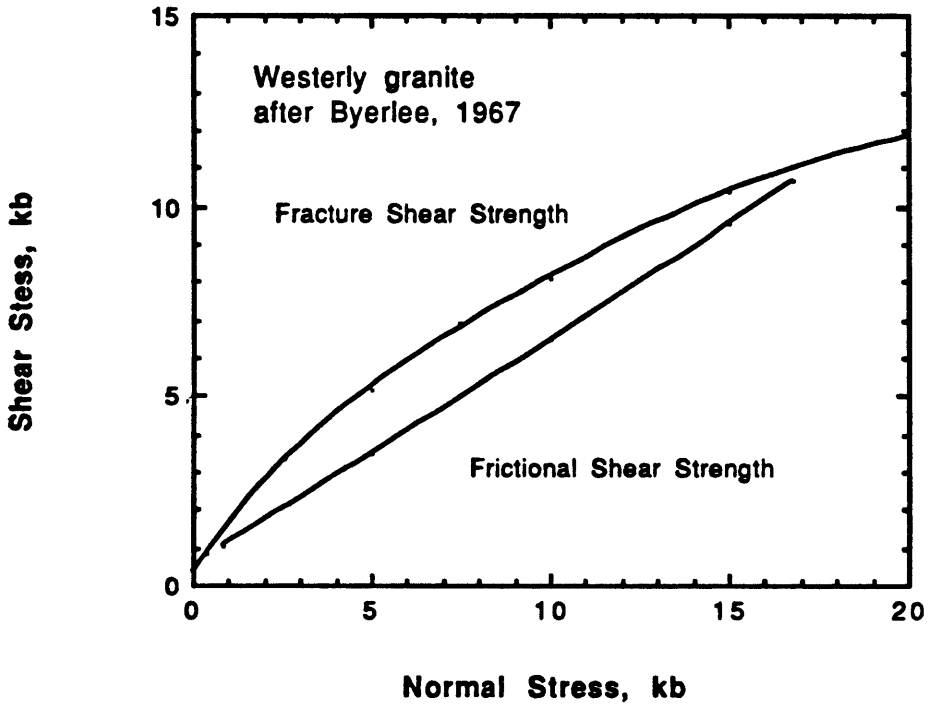
Westerly granite
after Byerlee, 1967
Fracture Shear Strength
Frictional Shear Strength
Shear Stess, kb
Normal Stress, kb
0
5
10
15
20

Figure 2.21

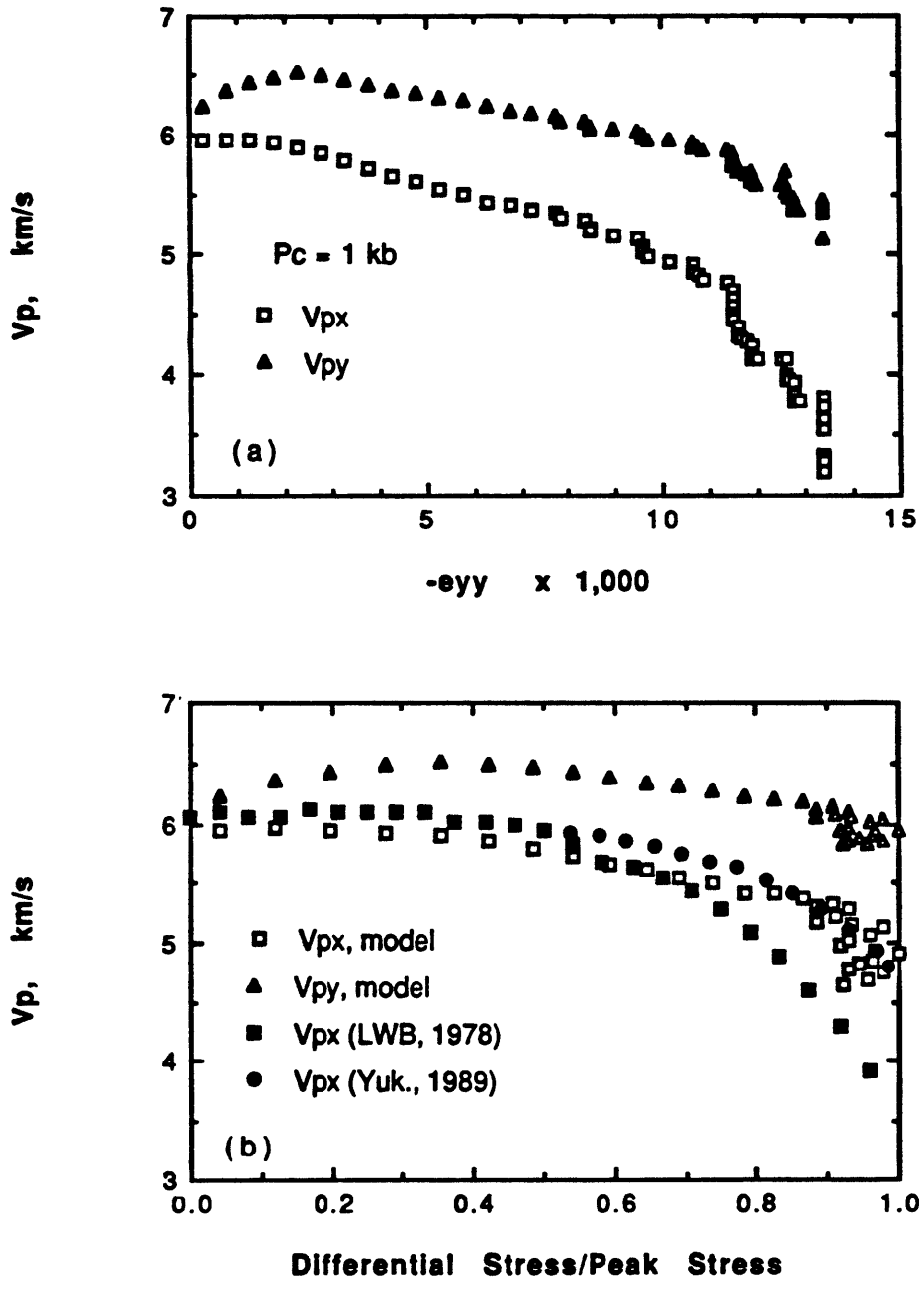
Vp, km/s
Pc = 1 kb
Vpx
Vpy
(a)
-eyy x 1,000
Vp, km/s
Vpx, model
Vpy, model
Vpx (LWB, 1978)
Vpx (Yuk., 1989)
(b)
Differential Stress/Peak Stress

Figure 2.22

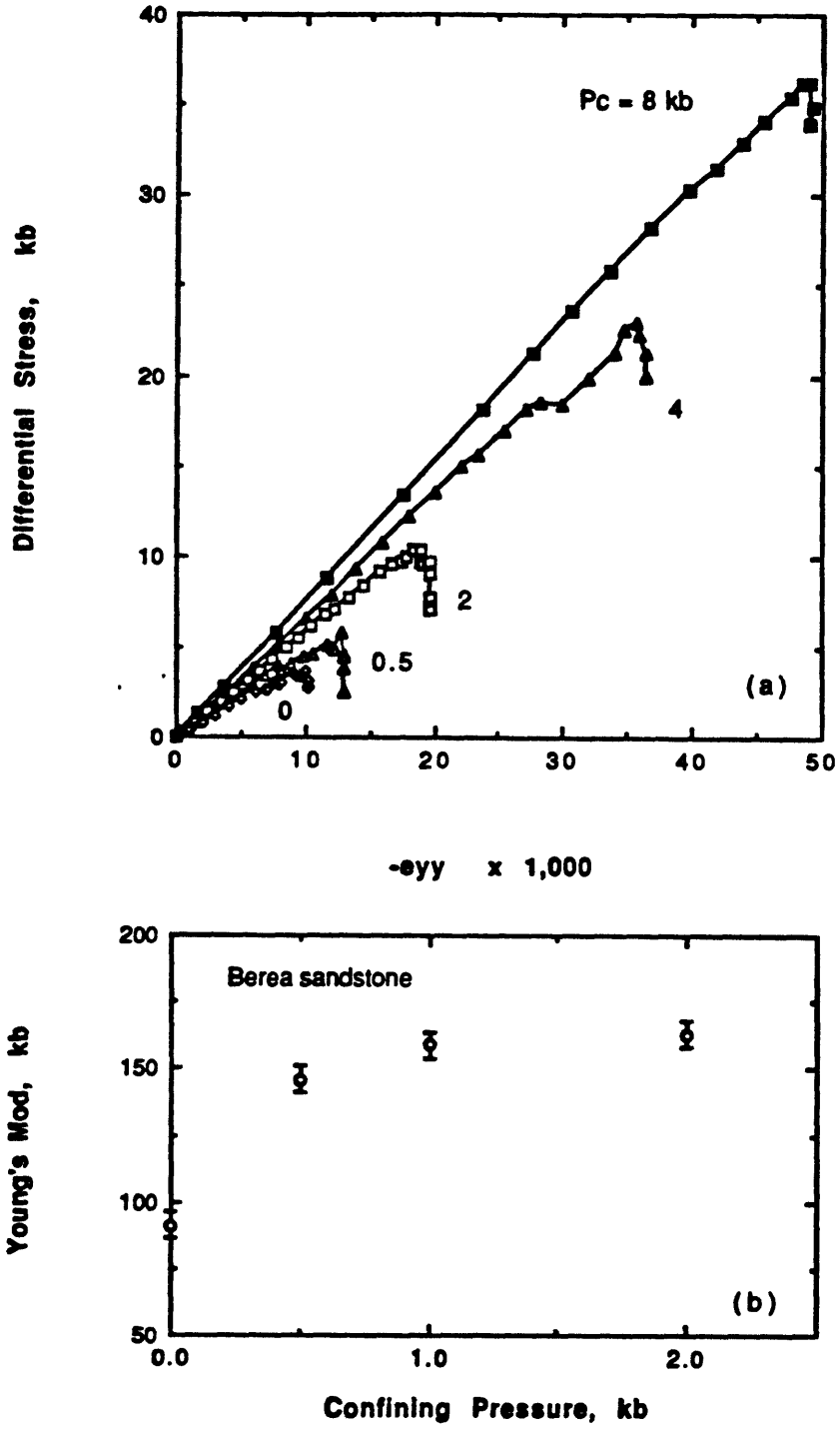
Differential Stress, kb
Pc = 8 kb
0
0.5
2
4
(a)
-eyy x 1,000
Young's Mod, kb
Berea sandstone
(b)
Confining Pressure, kb

Figure 2.23

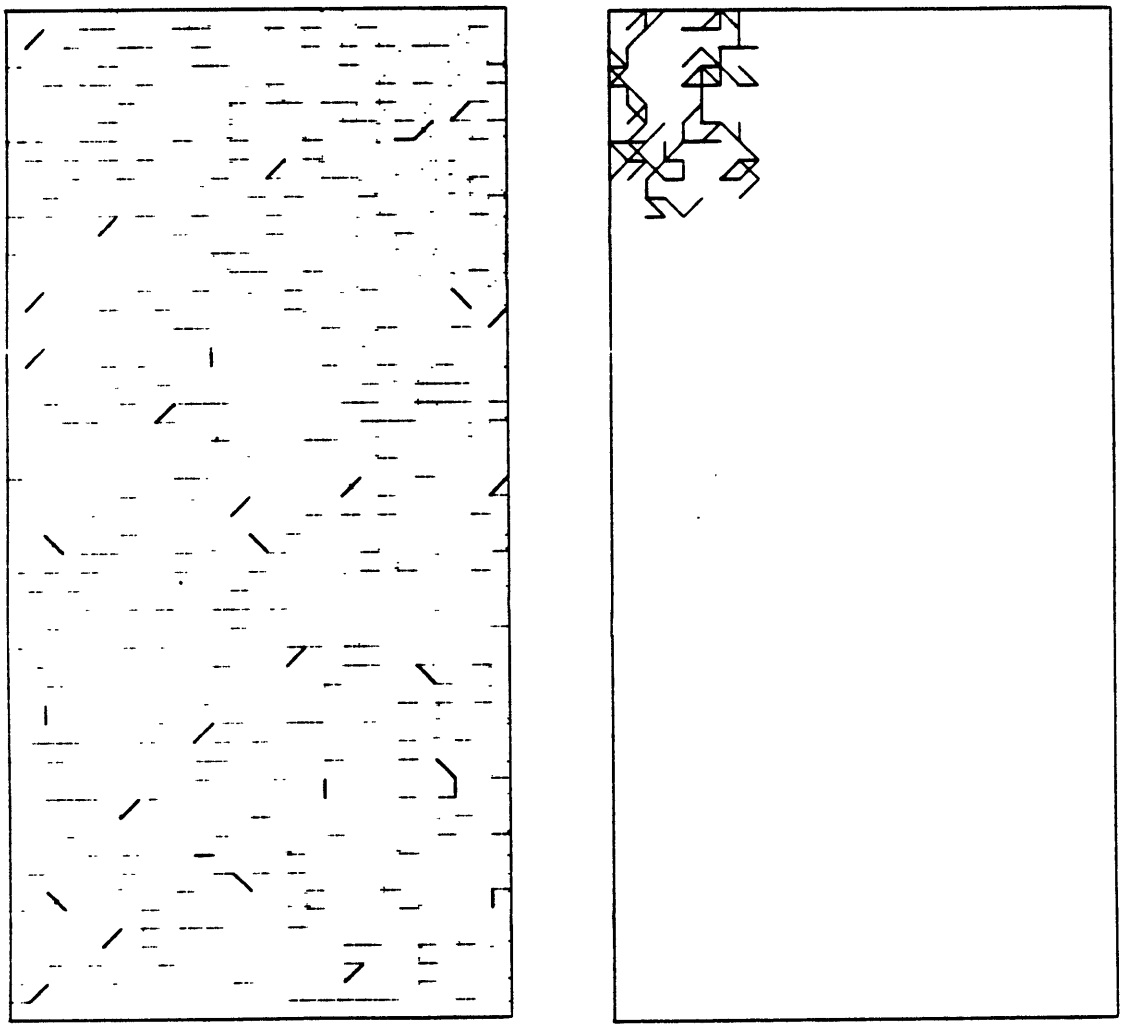

Figure 2.24

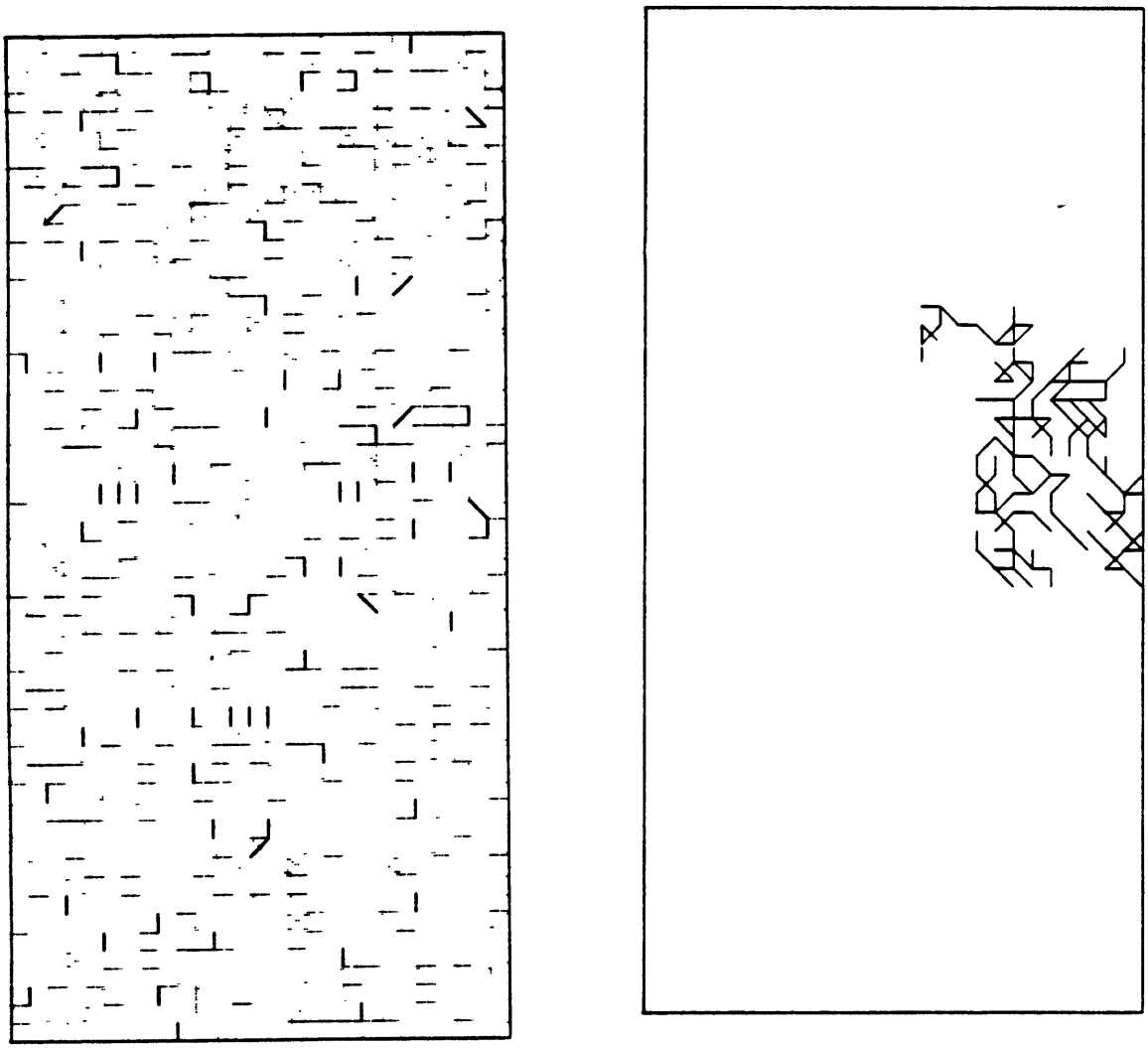

Figure 2.25

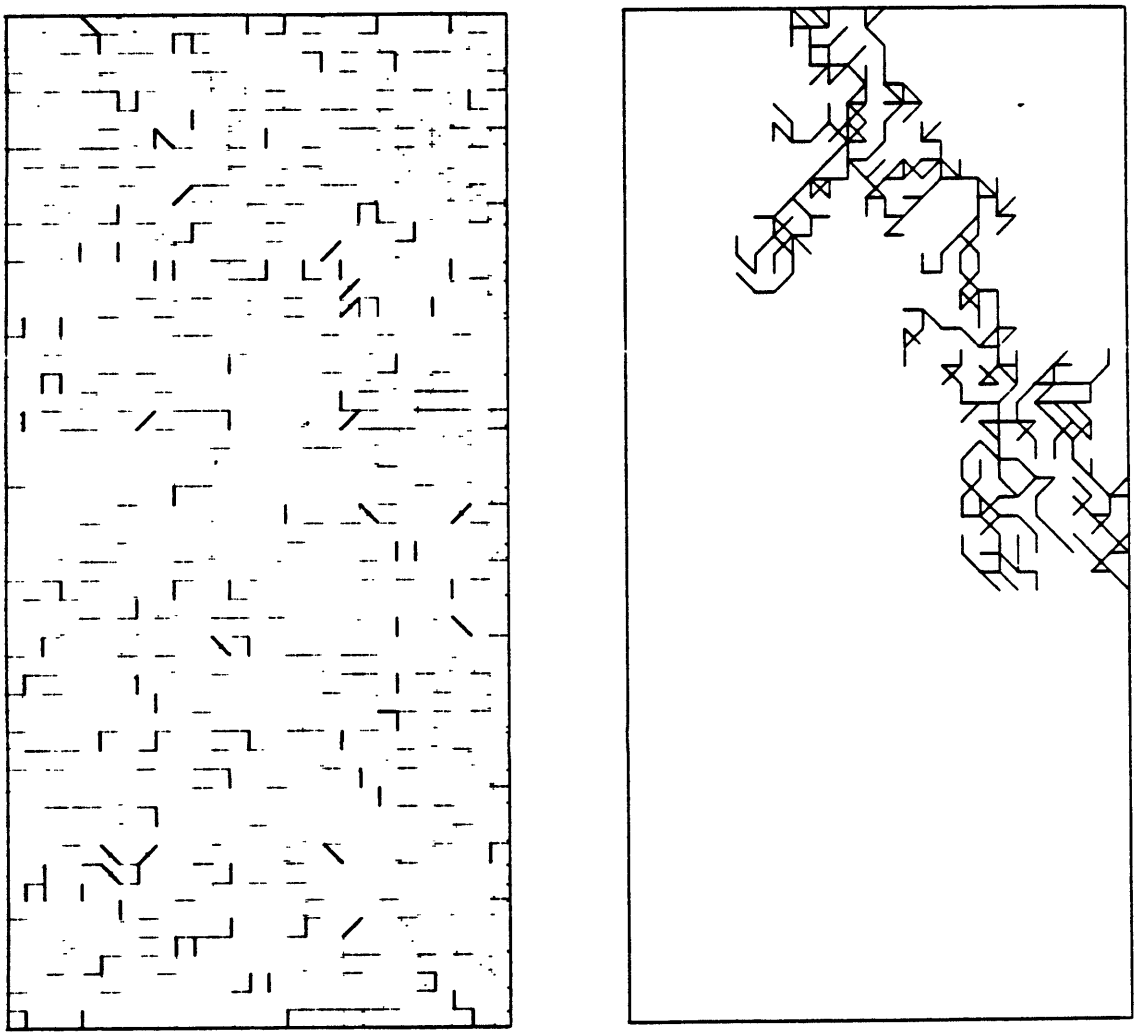

Figure 2.26

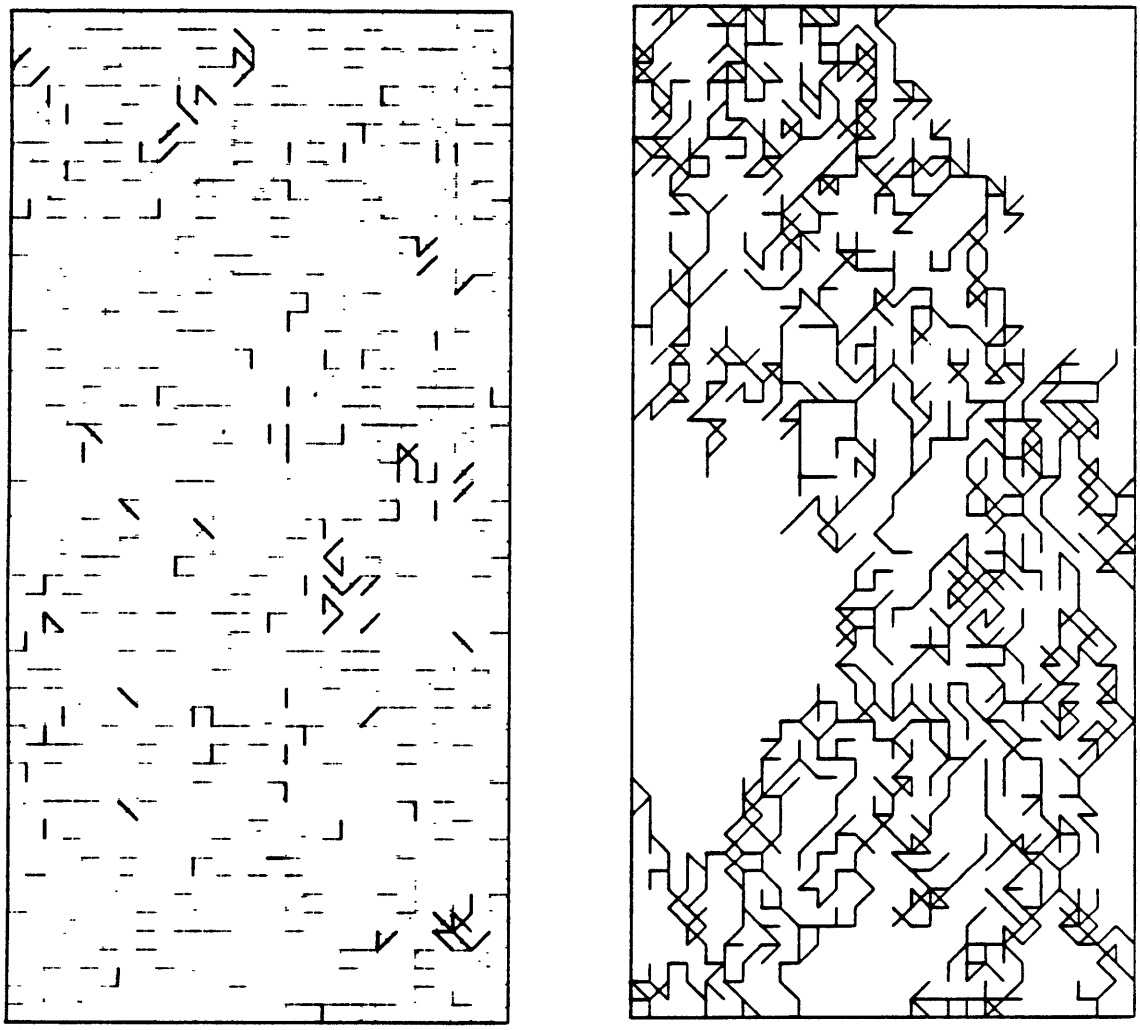

Figure 2.27

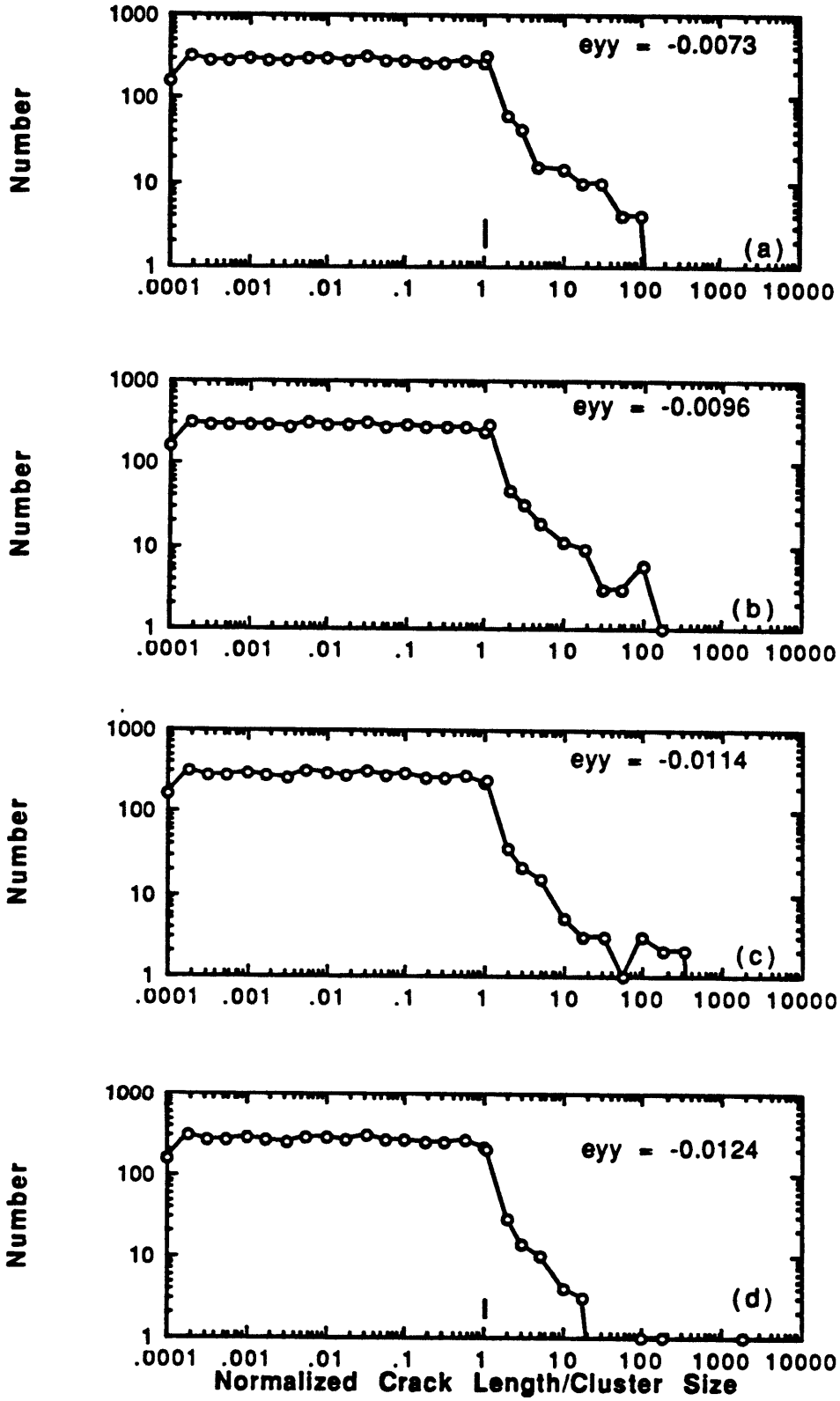
Number
1000
100
10
1
eyy = -0.0073
(a)
.0001 .001 .01 .1 1 10 100 1000 10000
Number
1000
100
10
1
eyy = -0.0096
(b)
.0001 .001 .01 .1 1 10 100 1000 10000
Number
1000
100
10
1
eyy = -0.0114
(c)
.0001 .001 .01 .1 1 10 100 1000 10000
Number
1000
100
10
1
eyy = -0.0124
(d)
.0001 .001 .01 .1 1 10 100 1000 10000
Normalized Crack Length/Cluster Size
Figure 2.28

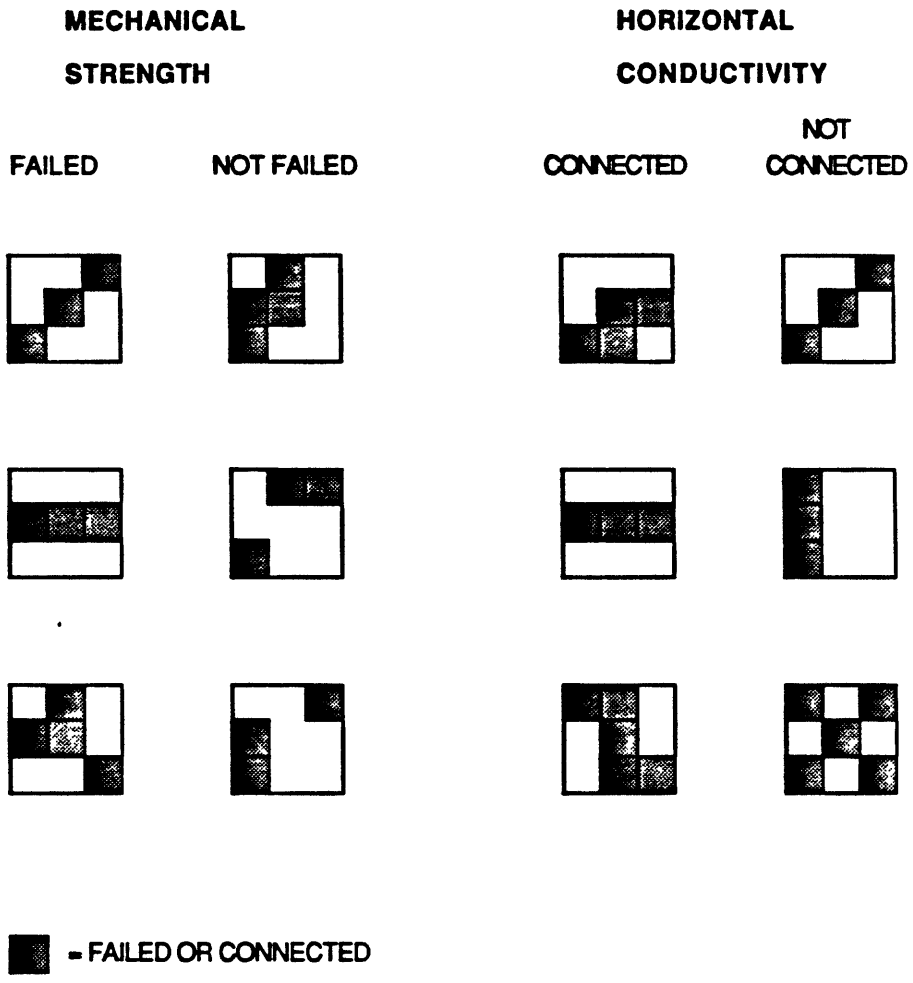
MECHANICAL
STRENGTH
HORIZONTAL
CONDUCTIVITY
FAILED
NOT FAILED
CONNECTED
NOT
CONNECTED
= FAILED OR CONNECTED

Figure 2.29

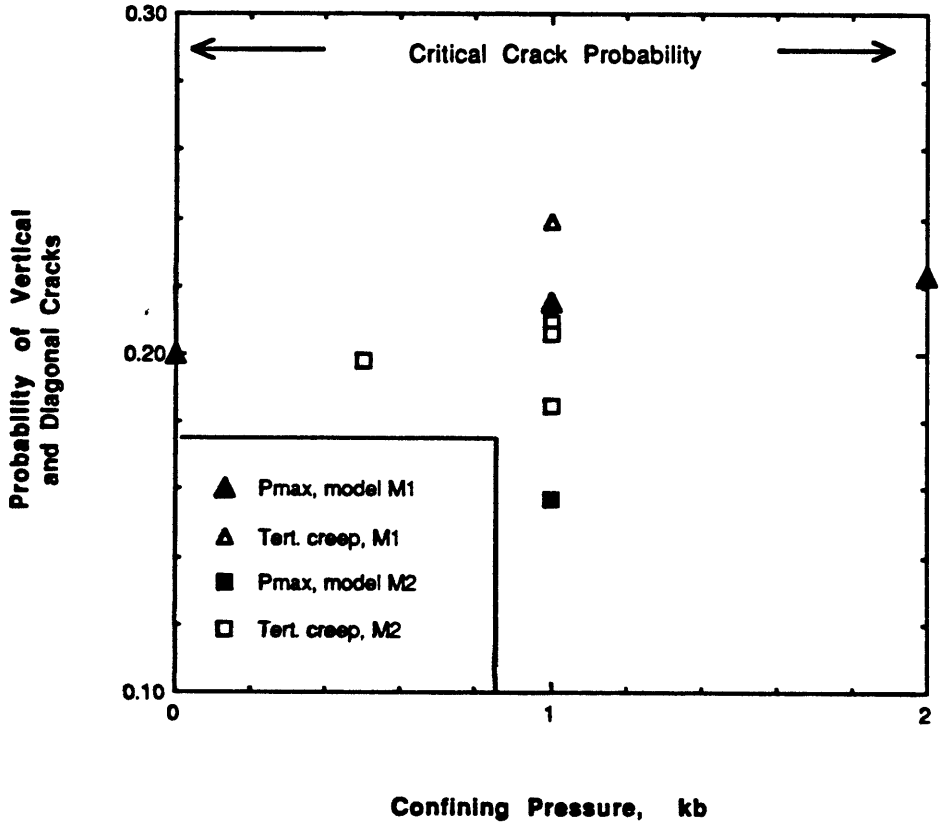
0.30
0.20
0.10
0
1
2
Critical Crack Probability
Probability of Vertical and Diagonal Cracks
Pmax, model M1
Tert. creep, M1
Pmax, model M2
Tert. creep, M2
Confining Pressure, kb

Figure 2.30

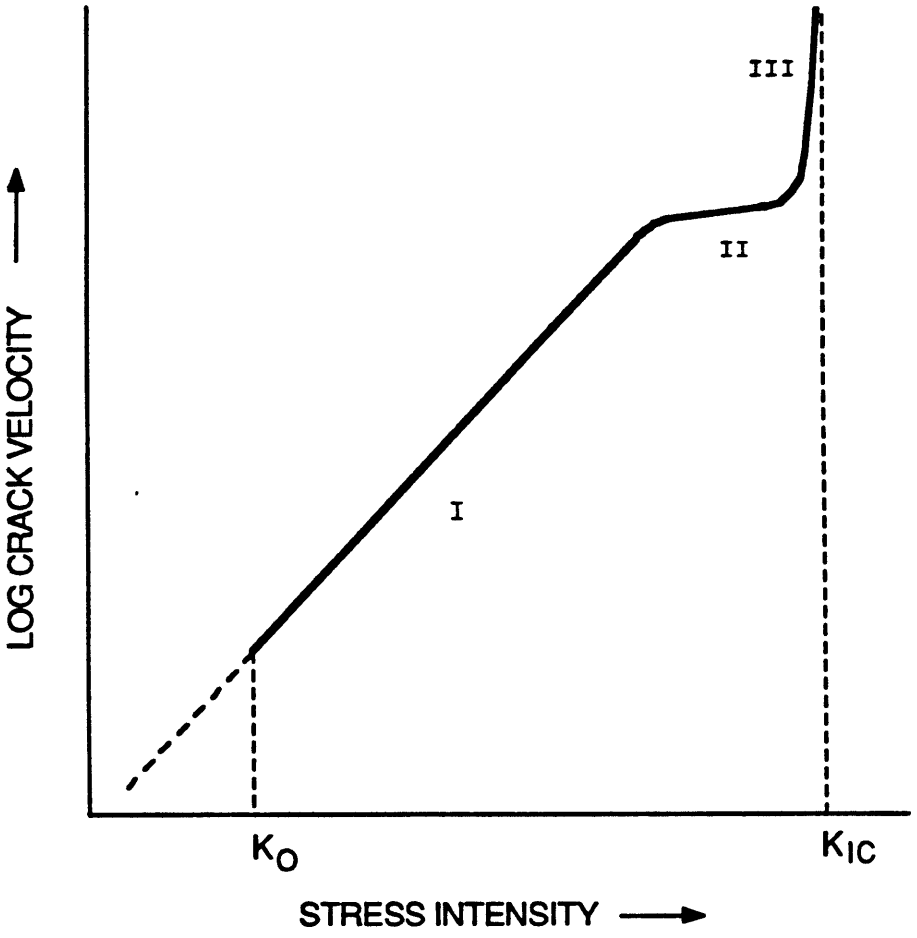

Figure 2.31

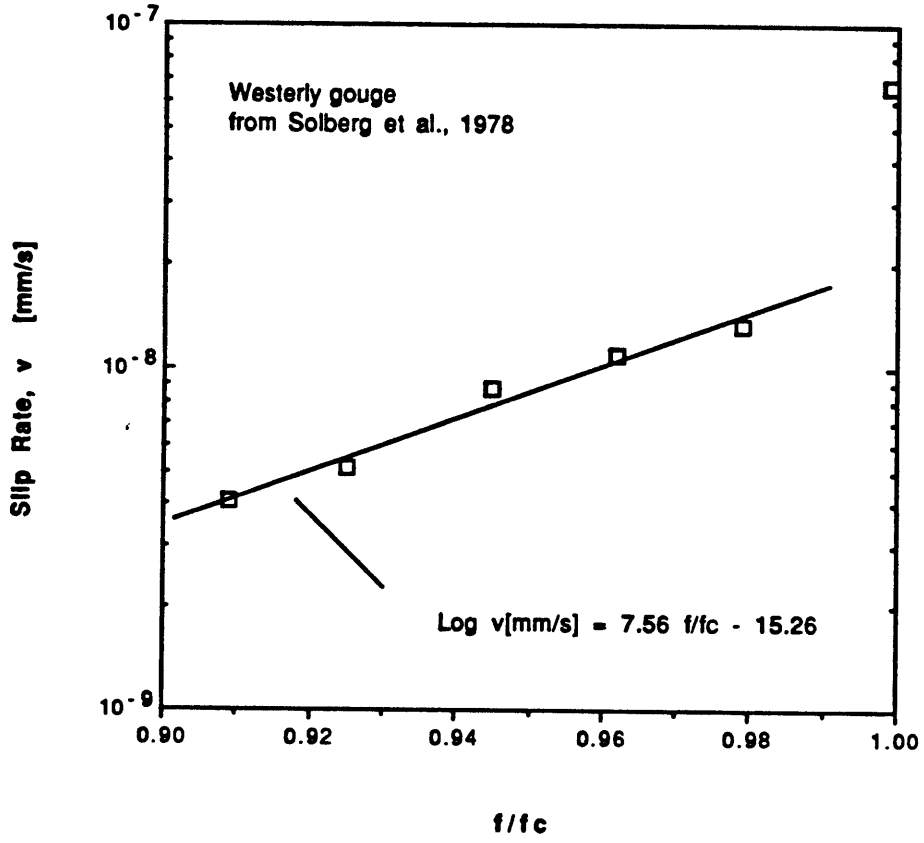
Westerly gouge
from Solberg et al., 1978
Log v[mm/s] = 7.56 f/fc - 15.26
Slip Rate, v [mm/s]
10-7
10-8
10-9
0.90
0.92
0.94
0.96
0.98
1.00
f/fc

Figure 2.32

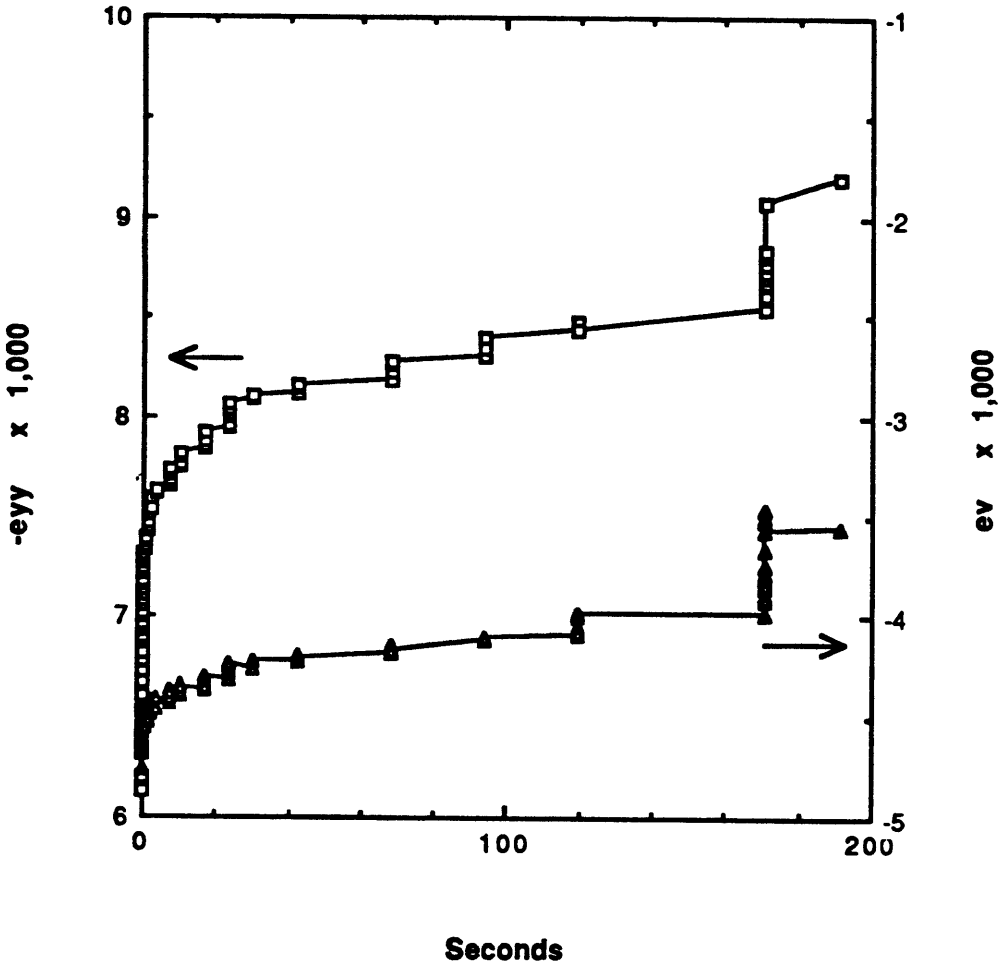

Figure 2.33

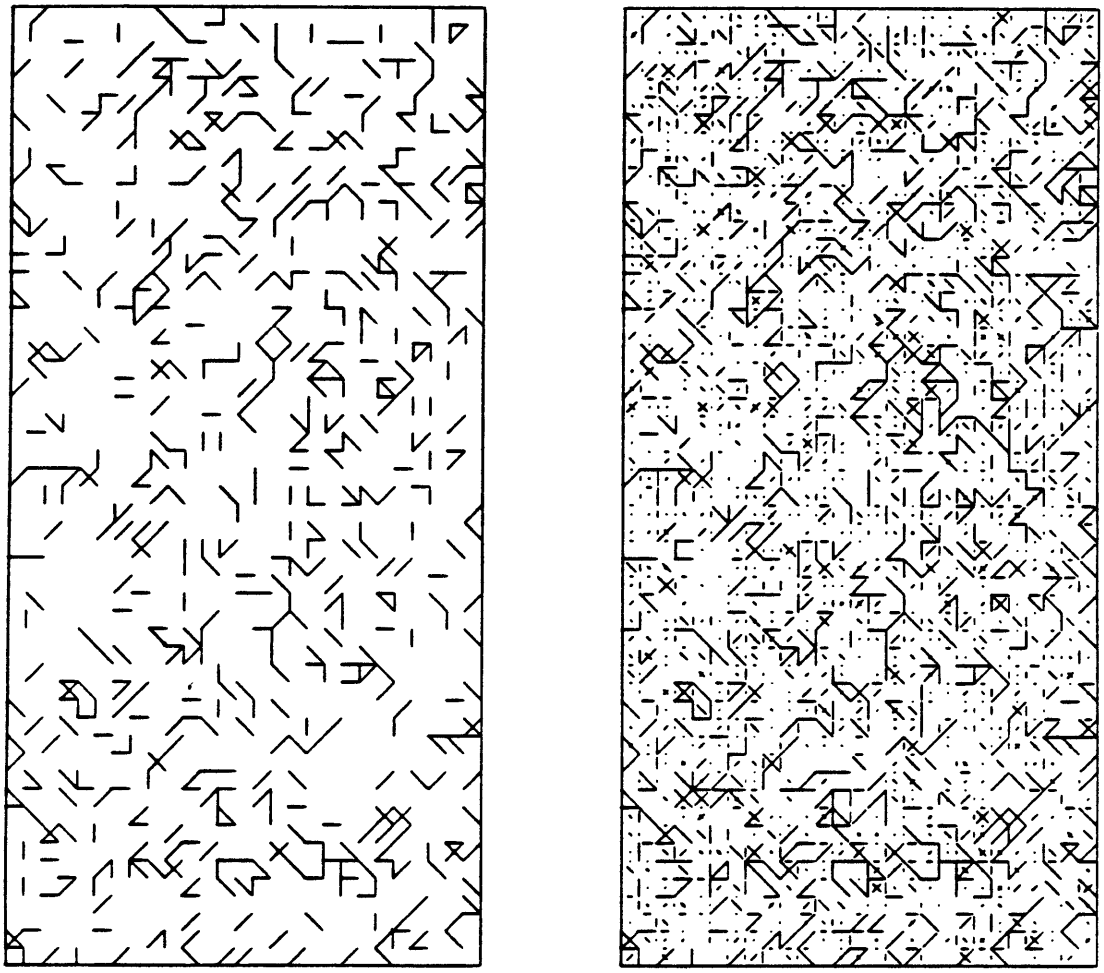

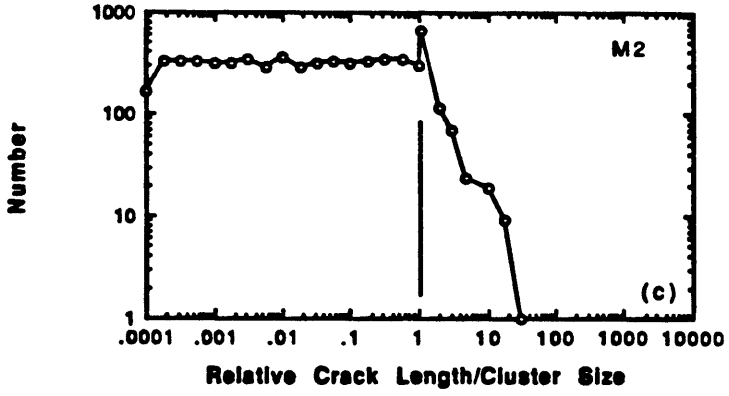
1000
100
10
1
Number
M2
(c)
.0001
.001
.01
.1
1
10
100
1000
10000
Relative Crack Length/Cluster Size

Figure 2.34

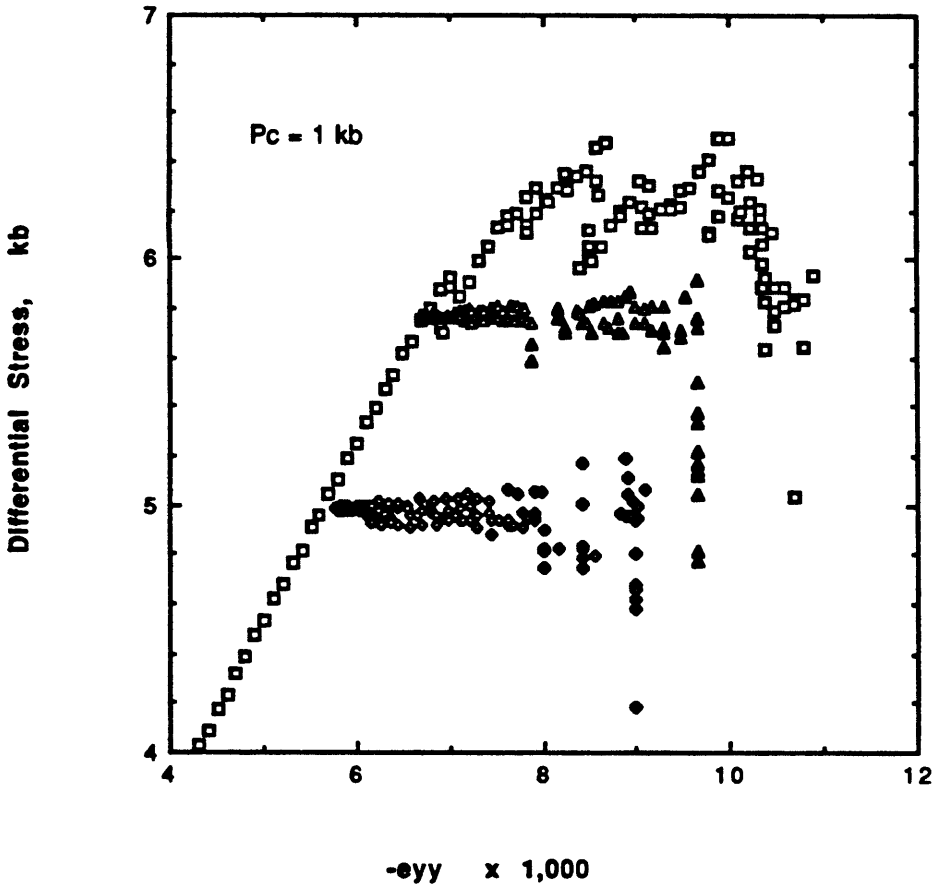

Figure 2.35

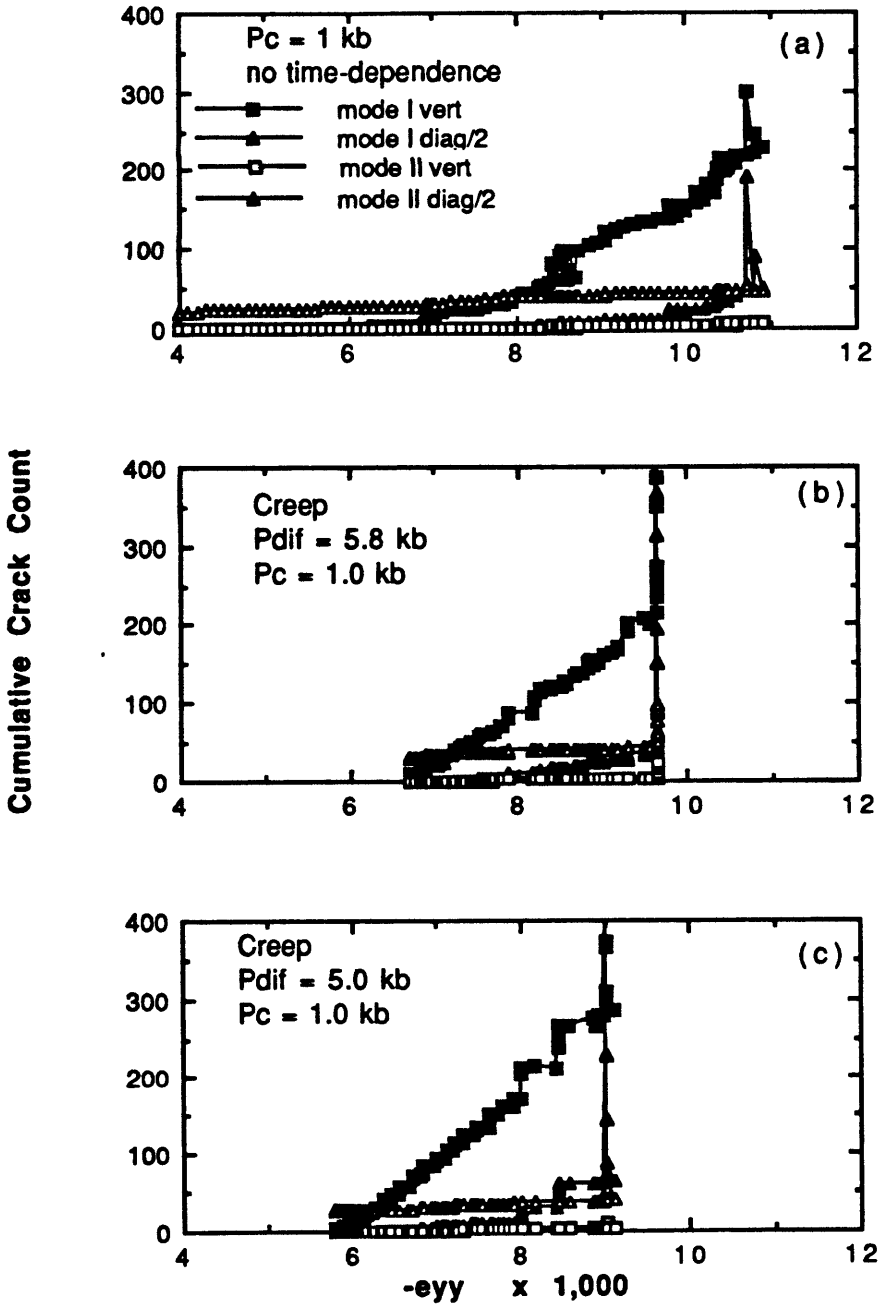
Pc = 1 kb
no time-dependence
mode I vert
mode I diag/2
mode II vert
mode II diag/2
(a)
Creep
Pdif = 5.8 kb
Pc = 1.0 kb
(b)
Creep
Pdif = 5.0 kb
Pc = 1.0 kb
(c)
Cumulative Crack Count
-eyy x 1,000
0
100
200
300
400
4
6
8
10
12

Figure 2.36

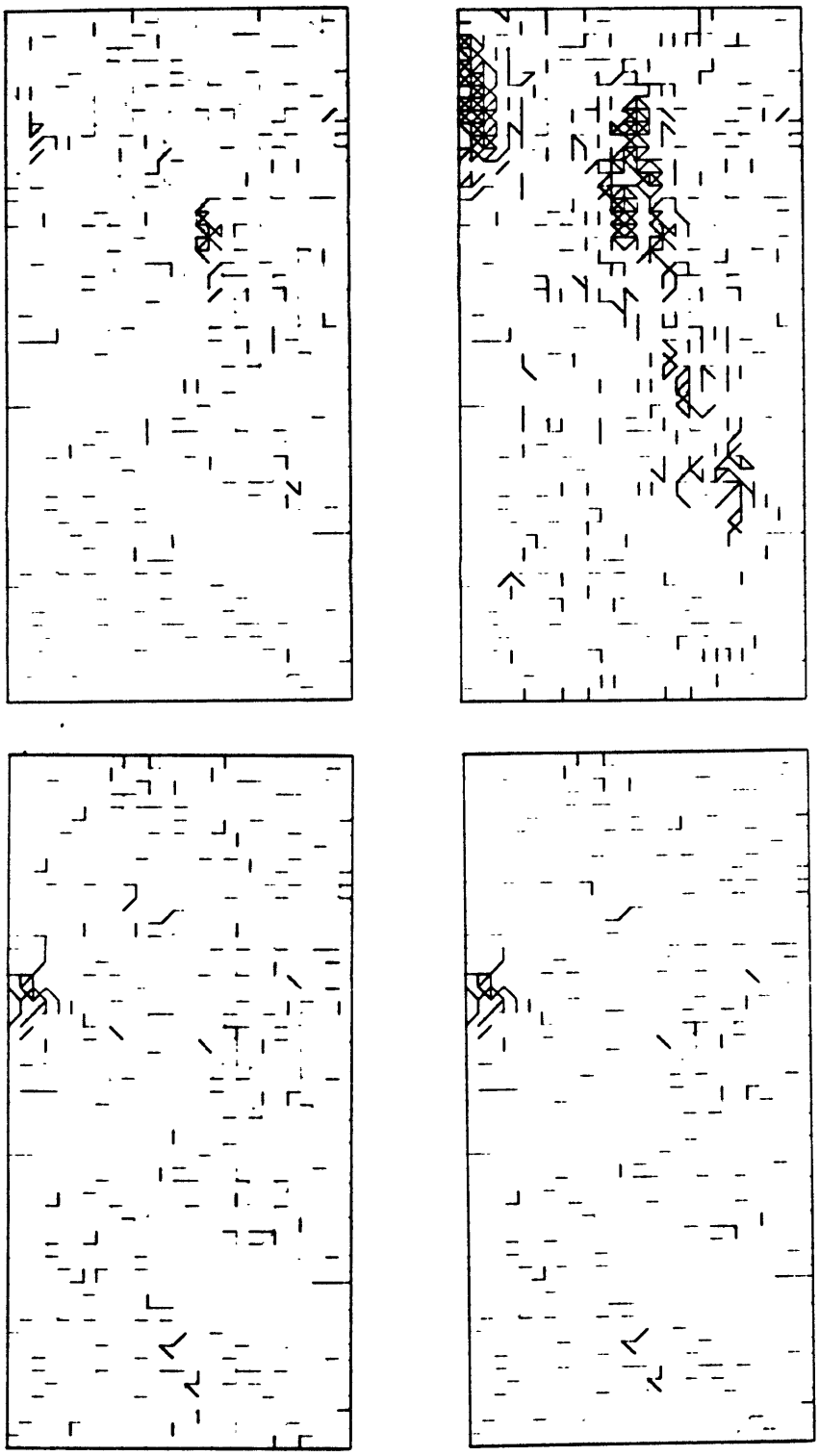

Figure 2.37

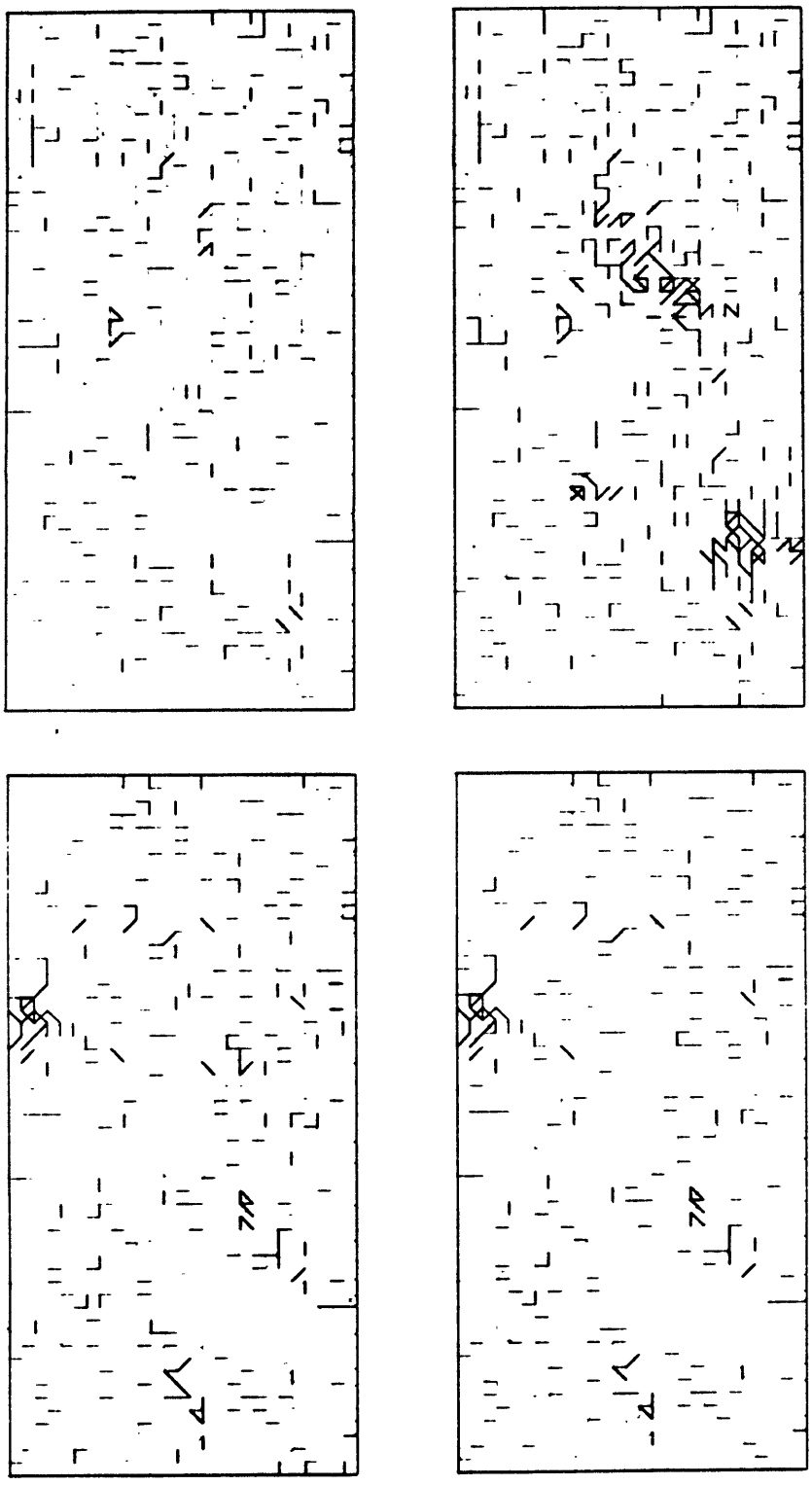

Figure 2.38

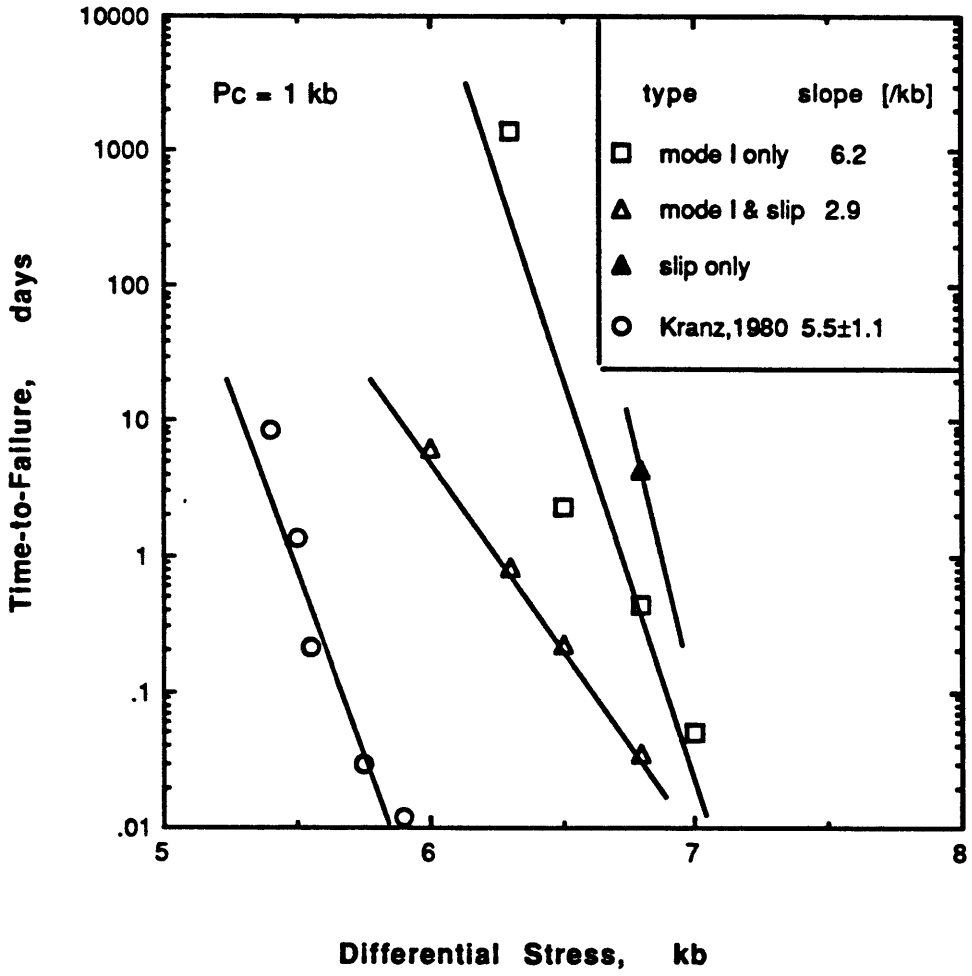
Pc = 1 kb
type slope [/kb]
mode I only 6.2
mode I & slip 2.9
slip only
Kranz,1980 5.5±1.1
Time-to-Failure, days
10000
1000
100
10
1
.1
.01
5
6
7
8
Differential Stress, kb

Figure 2.39

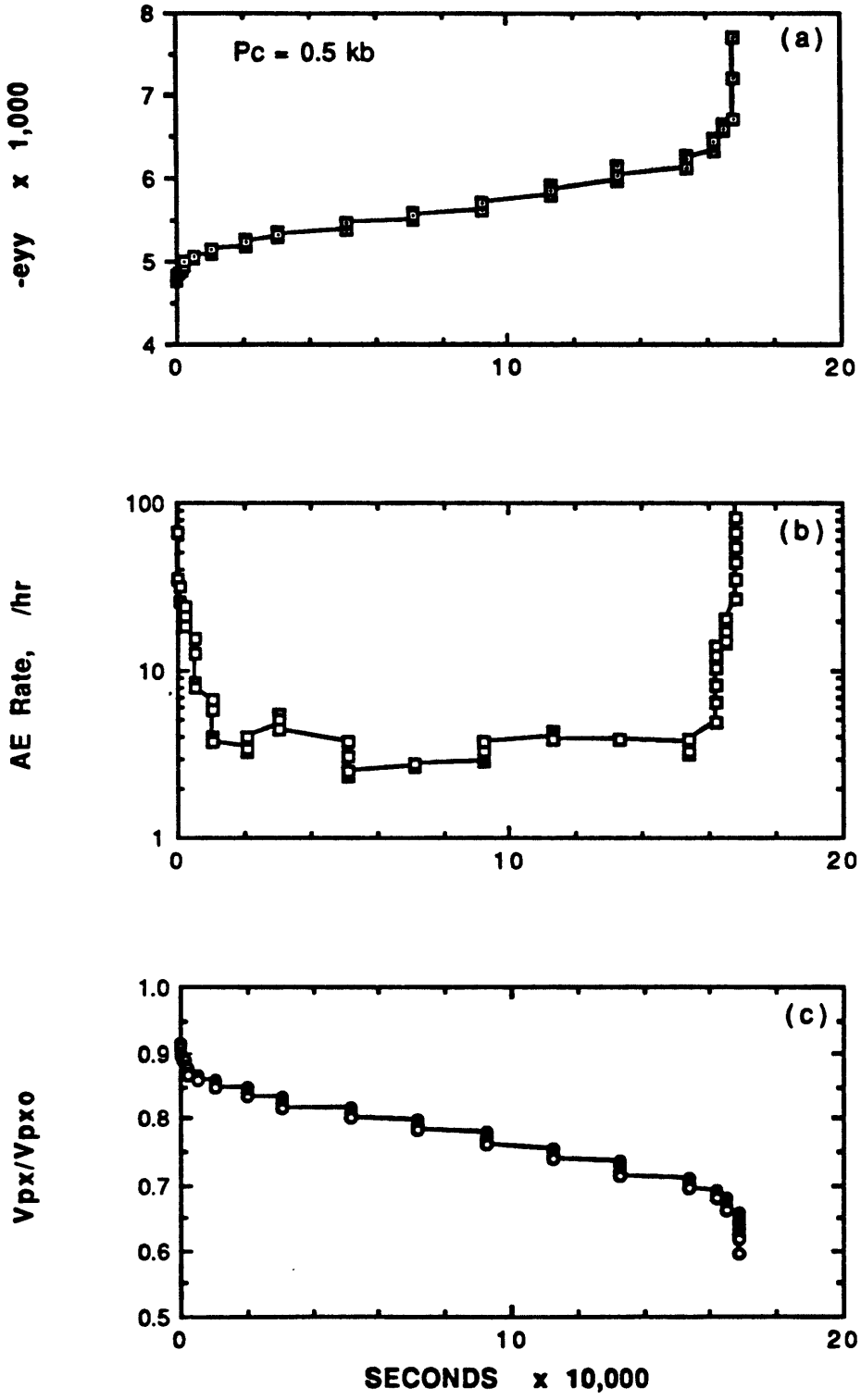
Pc = 0.5 kb
(a)
-eyy x 1,000
8
7
6
5
4
0
10
20
(b)
AE Rate, /hr
100
10
1
0
10
20
(c)
Vpx/Vpxo
1.0
0.9
0.8
0.7
0.6
0.5
0
10
20
SECONDS x 10,000

Figure 2.40

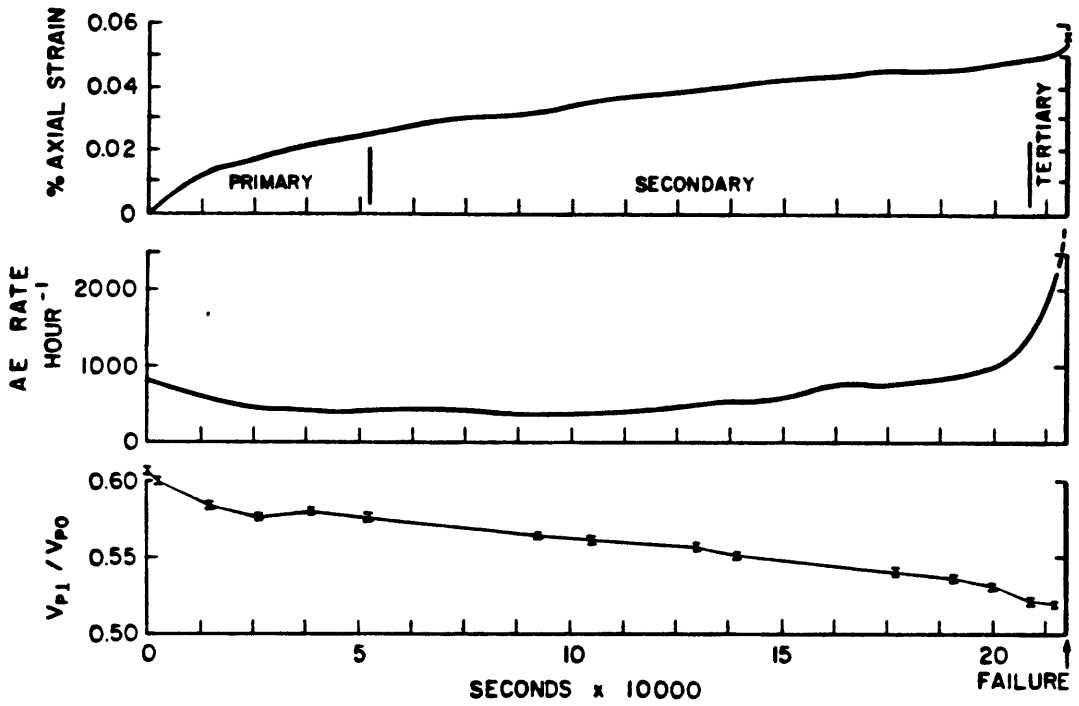
% AXIAL STRAIN
0.06
0.04
0.02
0
PRIMARY
SECONDARY
TERTIARY
AE RATE
HOUR⁻¹
2000
1000
0
V_{P1} / V_{P0}
0.60
0.55
0.50
0
5
10
15
20
FAILURE
SECONDS x 10000

Figure 2.41

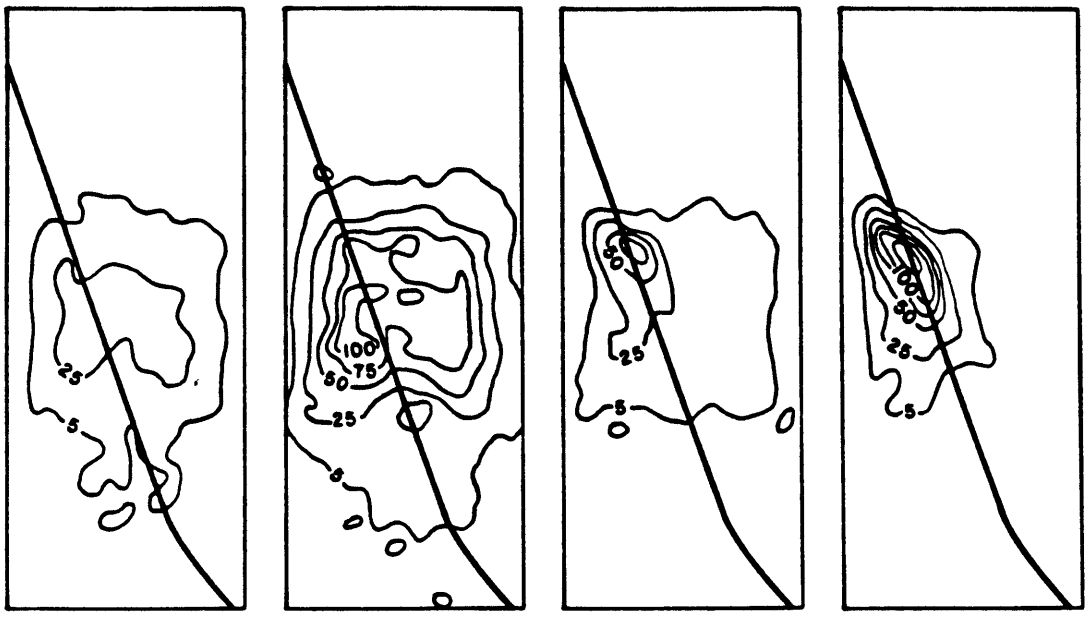
25
5
100
75
50
25
0
50
25
5
100
50
25
5
a PRIMARY
N = 7749
T = 0 to
51500 sec
b SECONDARY
N = 24975
T = 51500 to
208500 sec
c TERTIARY
N = 6687
T = 208500 to
216500 sec
d TERTIARY
N = 7710
T = 216500 to
217600 sec

Figure 2.42

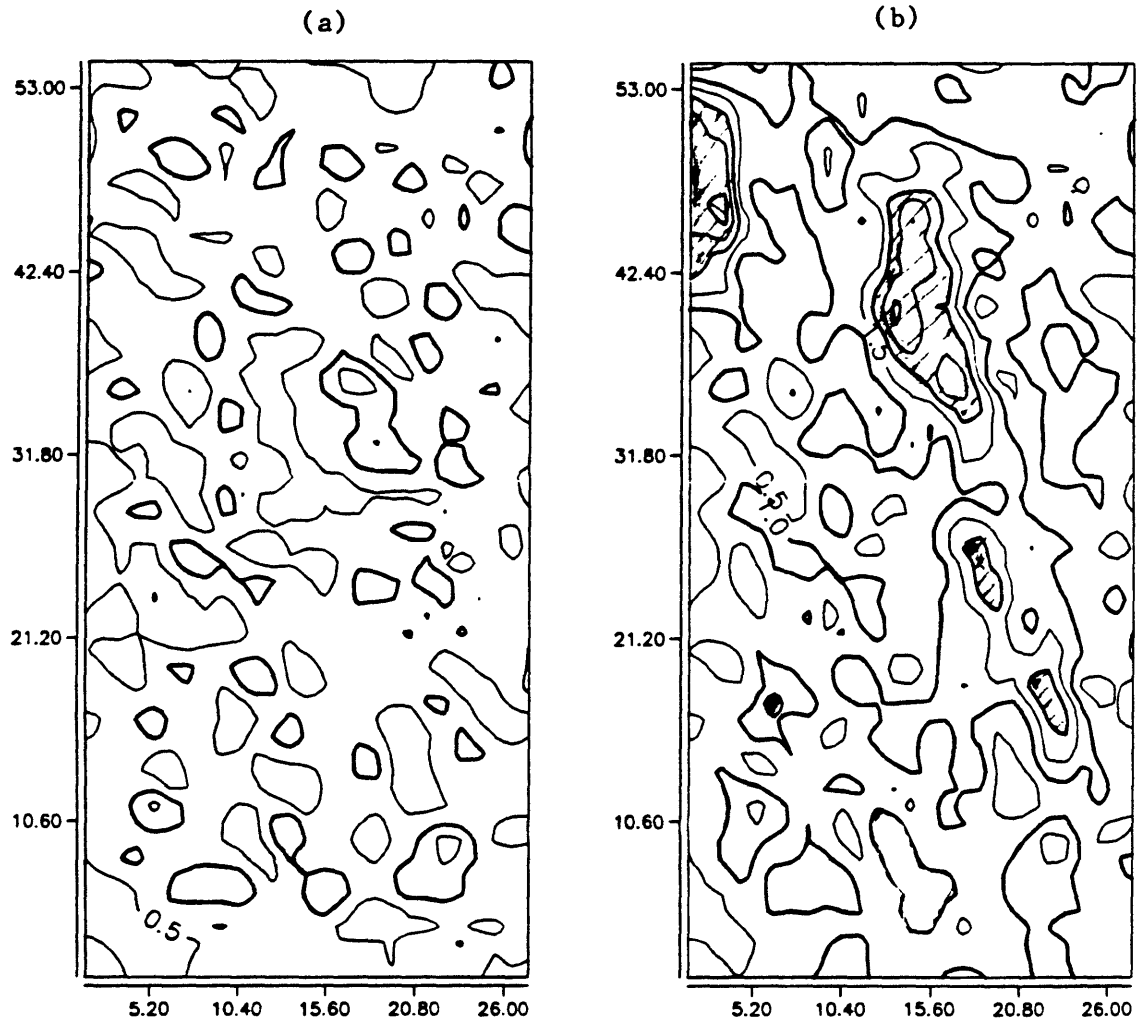

Figure 2.43

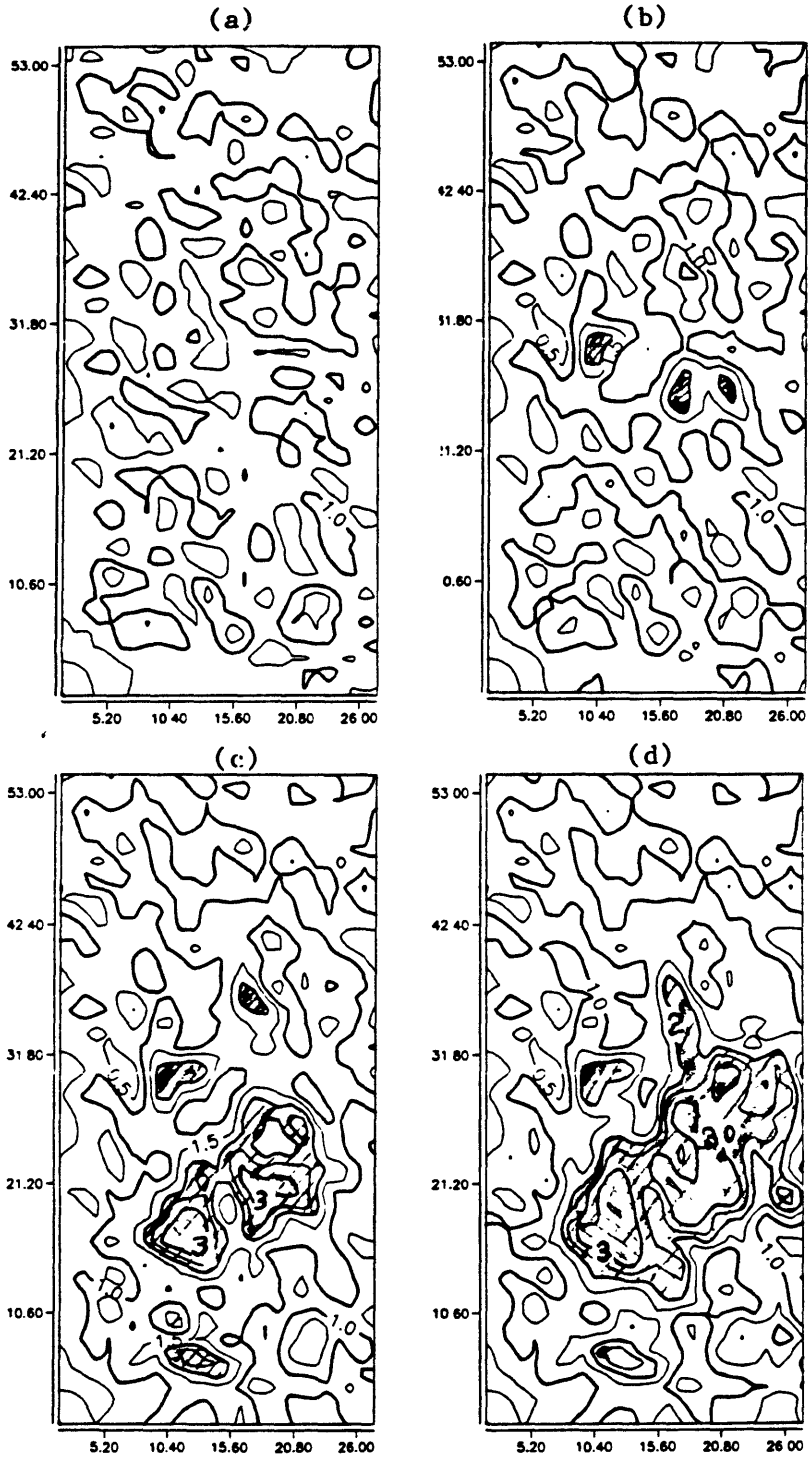

Figure 2.44

CHAPTER 3

LOW TEMPERATURE CREEP IN SATURATED GRANITE

abstract. Cylindrical samples of granite were deformed at 26°C, constant confining pressure (600 bars) and constant pore pressure (200 bars). Axial and volumetric strain were determined from changes in the output of resistance foil strain gauges bonded to the rock surface. In addition, dc electrical resistivity was measured parallel to the sample axis. During each experiment (typically lasting from one to two weeks), the deviatoric stress σ_d applied to the sample was cycled between 70% and 90% of the short-term failure strength. The bulk of the experiments were conducted in the secondary or 'steady-state' creep regime. Inelastic volumetric strain rate was found to obey the law $\log_{10}(\dot{\varepsilon}_v) = A + B\,\sigma_d + C \log_{10}(\varepsilon_v)$ where $B = 7.4 \pm 0.2$ kb^{-1} and $C \approx -4$. The C-coefficient represents a strain-hardening-like term. The stress-dependence is of the same form as the stress-dependence measured for mode I crack growth in double cantilever beam experiments. The observed creep behavior is analyzed in terms of stress corrosion and crack growth models.

Introduction

The understanding and description of the failure process in brittle rock has been a long-standing goal in the field of rock mechanics. Brittle failure is important in, for example, the stability of structures, mines and tunnels, and on a larger scale, faulting, earthquakes, tectonic processes and crustal plate bending. It has been known for a long time that when rocks are loaded below their short term failure strength they will undergo permanent, time-dependent deformation, especially when subjected to corrosive environments such as water. Under proper conditions, rock will fail after being loaded below failure strength for extended periods of time. This phenomenon, referred to as static fatigue, was first studied in glass (*Baker and Preston*, 1946; *Charles*, 1958; *Mould and Southwick*, 1959; *Adams and McMillan*, 1977) and later in rock and single crystal quartz (*Griggs*,1940; *Martin*, 1972; *Scholz*, 1972; *Wawersik*, 1973; *Wawersik and Brown*, 1973; *Cruden*, 1974; *Martin and Durham*, 1975; *Kranz*, 1980; *Lajtai et al.*, 1987) where it is important from an engineering standpoint in the

delayed failure of mine pillars and in rock bursts. Because of the practical interest in predicting failure, studies of static fatigue have been primarily interested in impirical and semi-impirical relations of time-to-failure, t_f. Constant-stress creep tests have been conducted which lead to laws of the form

$$t_f = t_o \, f(\text{stress}) \, . \tag{3-1}$$

Kranz (1980), for example, lists the common power law and exponential forms:

$$t_f = t_o \, \sigma^{-m} \tag{3-2}$$

and

$$t_f = t_o \, e^{-2.303b\sigma} \, . \tag{3-3}$$

Scholz (1968a) proposed a slightly different form:

$$t_f = t_o \exp[-E/kT + b(S^* - \sigma)] \tag{3-4}$$

where E is activation energy of the corrosion reaction, k is Boltzmann's constant, T is absolute temperature and S* is the 'instantaneous' strength.

While knowledge of time-to-failure has practical applications, understanding of the failure process requires studying the different stages of creep. When a brittle rock is held at constant stress, it will typically creep in a manner as shown in Fig. 3.1. Initial loading leads to primary or transient creep in which strain rate monotonically decays. A period of stead-state or secondary creep follows in which strain rate is approximately constant. The final tertiary creep phase involves a constantly increasing strain rate and terminates in failure of the rock. During primary and secondary creep, the nucleation and growth of microcracks occurs uniformly throughout the rock (*Kranz*, 1979, 1980). Studies of crack growth in glass and plastic plates (*e.g. Horii and Nemat-Nasser*, 1985) have shown that in compression, cracks have little tendency to link and instead, interact in such a way as to eliminate regions of high local stress (*Madden*, 1983; *Sammis and Ashby*, 1986; *Williams and Madden*, 1989). Thus during the first two

stages of creep, the growth of flaws in rock has the paradoxical effect of stabilizing the internal structure; an effect which contributes to strain-hardening. Once the crack density reaches a critical level, further crack growth leads to a local weakening of the rock and microcracking accelerates. Eventually, one such weakened region grows rapidly, microcracks coalesce, and a macroscopic fault is formed. *Lockner and Byerlee* (1980) demonstrated this process by locating the acoustic emissions generated during microcracking. They observed a diffuse distribution of acoustic emission events throughout the primary and secondary creep stages. The onset of tertiary creep was accompanied by a sudden localization of microcracking in a small region located on what eventually became the fracture surface. A similar process has been observed in the fracture of plates containing preexisting cracks (*e.g. Horii and Nemat-Nasser*, 1985).

Since tertiary creep represents rapid, unstable growth, the characterization of the critical crack density attained at the start of tertiary creep and the crack growth processes leading up to this stage should provide insight into the failure process. Early attempts at describing this process used a statistical approach (*Scholz*, 1968a), assuming a distribution $f(\sigma, \sigma_m)$ of local stresses about the mean applied stress σ_m. When the stress in any small region exceeded some local strength, that region was assumed to fail, redistributing the load over the remainder of the sample. All regions were assumed to weaken by a stress corrosion mechanism, according to eq. (3-4). *Spetzler et al.* (1982) used a different approach in which they assumed that the external stress is supported by unfractured material between microcracks. In their model, the normalized area that supported the external load was given by

$$A_n = 1 + q\,(c_o^2 - c^2) \qquad (3\text{-}5)$$

where q is a constant and c and c_o are the current and initial crack lengths. *Costin* (1987) described how damage theory can be used to model the failure process. In this approach, a damage parameter, related to the internal structure of the rock, will evolve with time and/or strain, allowing the material properties of the rock to be modelled. *Madden* (1983) and *Williams and Madden* (1989) described a different approach, based on renormalization group theory, in which the microscopic crack growth, macroscopically applied loads and bulk material properties could all be modeled.

At high homologous temperatures, rocks can deform plastically, for example, by

dislocation mechanisms (*Poirier*, 1985), or through other mechanisms such as pressure solution. This is especially true at the slow strain rates ($<10^{-12}$ s^{-1}) common to geologic processes. At low temperature, however, dislocations become pinned and other thermally activated processes that can contribute significantly to high temperature plasticity are arrested. Thus, quartz-bearing rocks tend to deform brittly at low temperature, even at slow strain rates. The principal low-temperature, time-dependent deformation mechanism in crystalline rocks appears to be a process known as stress corrosion. This process was first reported in metals when work-hardened brass bullet casings cracked after being stored in high humidity. A great deal of work has been done on glass and ceramics where it was found that cracks could be caused to grow stably from surface flaws when samples were loaded at levels below the critical stress intensity. This phenomenon is referred to as subcritical crack growth.

Stress corrosion provides a mechanism whereby a crack can grow under an applied load which would normally be too small to break bonds at the crack tip. By introducing a chemically corrosive agent (e.g. water in the case of silicates) to the crack tip, the bond energy is reduced and bonds can be broken at a reduced stress level. The rate at which a crack will grow is then controlled by the slowest in a series of steps including the reaction kinetics and the rate at which the corrosive agent can be supplied to the crack tip (generally a diffusion process (*Martin*, 1972 and *Martin and Durham*, 1975)). A wealth of data has been collected related to the rate of crack growth in glass and ceramics and more recently rocks. Reviews are given by *Anderson and Grew* (1977) and *Atkinson* (1984, 1987). A prototypical growth rate curve is shown in Fig. 3.2. Log (v) is plotted as a function of K_I (the fracture mechanics stress intensity factor for mode I crack growth). K_{IC} is the critical stress intensity factor representing the stress at which the crack will grow unstably. K-v plots are generally divided into three regions. In region I, crack velocity is very sensitive to stress while in rigion II, there is little stress sensitivity. These regions are presumably controlled by reaction kinetics (region I) and diffusion of corrosive agent to the crack tip (region II). The mechanism controlling region III, as stress intensity approaches criticality, is less clearly understood. A lower limit to the stress at which cracks will grow, K_0, has been discussed, for example, by *Rice* (1978). Expressions for describing the region I behavior were put forth by *Charles* (1958)

$$v = v_o \exp[-H/RT]\, \sigma^n \qquad (3\text{-}6)$$

and *Wiederhorn and Bolz* (1970)

$$v = v_o' \exp[(-E + b'K)/RT] \qquad (3\text{-}7)$$

where v_o, v_o', n and b' are constants, H is enthalpy, and E includes the stress-free activation energy. n typically falls in the range $20 < n < 50$ for stress corrosion in ceramics (region I) and in the range $2 < n < 10$ for diffusion controlled growth (region II). While theoretical work has been conducted on the microscopic mechanisms responsible for the crack growth behavior shown in Fig. 3.2 (reviewed in *Atkinson*, 1987), much remains to be done. Both eqs. (3-6) and (3-7) remain in use as semi-impirical expressions. In fact, there are good theoretical reasons (*Rice*, 1978) to relate crack growth rate to a*G rather than b'K in eq. (3-7), where a* is activation area and G is the strain energy release rate. This approach will be examined further in the discussion.

K-v measurements are performed almost exclusively on single cracks in tension. This is because the test apparatus used (*e.g.* double cantilevered beam and double torsion) allows for the determination of K_I. For a brittle rock loaded compressively in a creep test, time-dependent strain is primarily the result of microcrack growth (*Hadley*, 1975; *Tapponnier and Brace*, 1976; *Kranz*, 1979,1980). Acoustic emission measurements also support this assertion (*Scholz*, 1968b; *Evans and Linzer*, 1973; *Lockner and Byerlee*, 1977, 1980). The impulsive energy radiated in acoustic waves is the result of discrete microfracturing events within the sample (*e.g. Evans*, 1978). This could result either from cracks extending unstably in tension (at K_{IC}) or unstable shear failure (stick-slip) of existing cracks whose walls are in contact. The fact that acoustic emissions and strain continue with time indicates that microcracks must be initiating and growing stably (aseismically) throughout the experiment. The macroscopic strain is then the summation of the strain increments contributed by cracks of different orientations and in different stages of growth throughout the rock. Since cracks at low stress intensity are growing slowly, they will contribute very little to the macroscopic strain rate. Thus the strain rate will be controlled only by those cracks at or near K_C. This explains the strong correlation between acoustic emission and strain. By the same

token, the residence time for cracks in the near-K_C region is short. Thus the microcracking process can be viewed in terms of reaction kinetics in which the rate-limiting step is either crack nucleation or crack growth. By varying temperature, stress and other parameters, it should be possible to learn about these processes.

In the present experiments, we have measured the stress-strain rate dependence for granite in the secondary creep regime. While many static fatigue studies have been conducted on rock, these have generally been concerned with time-to-failure. As a result, relatively few data exist regarding the σ-$\dot{\varepsilon}$ dependence for rock in compression during secondary creep; the mode in which a rock in nature will spend the greatest length of time before failure. *Wawersik* (1973) conducted uniaxial creep tests on saturated Westerly granite and was able to determine stress-strain rate dependence. *Rutter and Mainprice* (1978), hereafter referred to as *RM* , performed stress relaxation experiments on confined Tennessee sandstone at room temperature and 300°C. This relaxation method has the advantage of sweeping out a range of stress in a single experiment. We have undertaken a series of experiments on Westerly granite which are, in fact, similar to those of *RM* . The bulk of our experiments were performed at constant stress steps. This procedure has yielded useful information that is not available in the stress relaxation experiments. Our experiments are exploratory in nature and as yet have only been conducted at room temperature and a single effective confining pressure. Our motivation is two-fold. We wish to examine the effect that confining pressure has on creep processes. In addition, we wish to search for a low-stress-sensitivity creep mechanism which might be dominant at low temperature and low stress. Such a mechanism could be important for geologic processes occuring at shallow- and mid-crustal conditions in that it would allow deformation to occur at lower stresses than are predicted by extrapolation of current laboratory measurements.

Experimental

All rock samples used in this study were cored from a single block of Westerly granite. Samples were 25.4 mm-diameter cylinders with nominal lengths of 63 mm. A hardened steel sample was also prepared for calibration purposes. Orthogonal pairs of resistance foil strain gauges were used to measure axial and transverse strain. Gauges were bonded to the rock surface with epoxy and then encapsulated with sealant to isolate them from the pore water. 3.2 mm-walled vinyl tubing was use to jacket the samples. Strain gauge leads were passed through the tubing and sealed with vinyl cement. This system proved effective in sealing the sample and maintaining electrical isolation ($> 10^7$ ohm) of the strain gauges. Since the gauges were in direct contact with the sample and pressed against the sample surface by the confining pressure, strains of 10^{-6} could be resolved and were stable for extended periods of time. Calibration measurements on a steel sample indicated that strain measurement variations due to temperature fluctuations determined the long term and therefore minimum strain rate resolution of the experiments.

Electrical resistivity was measured periodically during each experiment. Two Ag/AgCl electrodes were prepared by first pressing flat 25.4 mm-diameter circles of silver screen and then plating them with AgCl. Electrodes were separated from the sample by 0.25 mm wafers of porous alumina. Sample impedance was measured at 10, 30 and 100 Hz using a system described in *Lockner and Byerlee* (1985). This system is capable of measuring complex resistivity over a range of 10^{-4} to 10^6 Hz and will be utilized more fully in future experiments. In the present experiments, however, we were interested in measuring secular variations in only near-dc resistivity. A 1-volt peak-to-peak sine wave was applied to the sample in series with a known precision resistor. The complex resistivity of the sample was then computed from knowledge of the amplitude and phase relation between the voltage drops across the sample and the precision resistor.

The jacketed sample assembly was placed in a pressure vessel and confining pressure was applied. Silicone oil was used as confining fluid. A series of dry experiments were performed at 400 bars confining pressure and axial strain rates of 10^{-5} to 10^{-7} s^{-1} to test the system and confirm the dry breaking strength of Westerly

granite. Wet experiments were performed at constant confining pressure of 600 bars and pore pressure of 200 bars, using 0.01 molar KCl saturated with AgCl to protect the Ag/AgCl electrodes. Solution resistivity was 6.3 ohm-m. To remove possible soluble salts that might have been in the rock pores, 0.8 cm^3 of electrolyte was forced through these samples before each experiment. Each sample was then allowed to sit for approximately 20 h to allow fluid pressures to equilibrate. A piston was then advanced against the end of the sample, raising the differential stress at a rate of approximately 1 bar/s, to 3.45 kb which is 77% of the instantaneous dry strength. A period of approximately 20 h ensued during which stress was held constant and the sample underwent primary creep. Stress levels were then changed periodically to values ranging from 65 to 90% ultimate strength, and creep response and resistivity were monitored. Axial load was measured by means of an internal load cell situated on the end of the piston. In one experiment, a stress relaxation sequence was conducted to allow comparison to *RM's* data. In this relaxation technique, the sample was loaded to some stress close to the short-term failure strength and then maintained at constant strain. The sample then deformed internally, converting elastic strain to permanent, inelastic strain, monotonically lowering the stress as it did so. By knowing the elastic constants of the sample and loading system, the stress time derivative was converted to an inelastic strain rate.

Long term resolution of both strain and resistivity was limited by temperature fluctuations of the sample, recording amplifiers and other electronic components. To minimize the temperature-related effects, the pressure vessel and sensitive electronics were housed in a controlled temperature chamber. The vessel was maintained at a temperature of 26.50 ± 0.05 °C.

Results

A 'room-dry' experiment, in which the sample was pre-dried in vacuum for 24 h, is presented in Fig. 3.3. The sample was deformed at confining pressure of p_c = 400 bars and axial strain rate $\dot{\varepsilon}_a = -10^{-5}$ s^{-1}. Differential stress ($\sigma_d = \sigma_1 - p_c$), tangential strain ($\varepsilon_t$) and volumetric strain ($\varepsilon_v = \varepsilon_a + 2\varepsilon_t$) are plotted as functions of axial strain. (Note that we use the somewhat ackward convention that compressive stresses are positive while extensional strains are also positive.) Peak dry strength, which we will here after refer to as 'instantaneous strength', σ_i, occurs at 4.51 kb. The average value from our dry experiments of $\langle\sigma_i\rangle$ = 4.5 kb, at 400 bars confining pressure, will be used as a reference peak strength in this paper. As is characteristic for brittle rock, volumetric strain initially decreases as thin, low-aspect-ratio cracks are closed. Then, at approximately half the instantaneous strength, continued loading leads to an increase in volume, or dilatancy, as new cracks are formed and existing cracks grow in the rock. This process has been well documented for Westerly granite and other brittle rocks(*e.g. Hadley*, 1975; *Tapponnier and Brace*, 1976; *Kranz*, 1980).

The initial loading and primary creep phase for a saturated sample are shown in Fig. 3.4. Differential stress was gradually raised to 3.45 kb (at approximately 1 bar/s), resulting in an axial strain of -0.0070. This modest loading rate was used to prevent excessive pore pressure transients during the loading cycle. The volumetric strain record during this period indicates that the sample had progressed well into the dilatant stage during this initial loading. The sample was then held at constant stress for 8.6 h as it underwent characteristic transient creep.

After the transient creep phase had passed, the main part of the experiment was begun. The sample was cycled through a series of stress steps and allowed to creep at each level so that strain rates could be determined. A typical sequence of stress steps and resulting volumetric strain and strain rate are plotted as a function of time in Fig. 3.5. Note that following each increase in stress, the sample underwent a period of initially high strain rate, gradually decaying to an approximately constant rate. This transient response, remeniscent of primary creep, was consistently observed, even during repeated loading cycles. A 'stress relaxation' experiment was also performed to allow comparison to the constant stress measurements. In the relaxation experiment

(Fig. 3.6), stress was initially raised to 3.92 kb, at which point control was switched to maintain constant axial strain of the sample. This procedure required a controlled backing off of the ram applying load to the sample and a consequent reduction in stress. Even though the axial strain was constant, the sample continued to dilate as elastic strain was converted to inelastic strain.

We next examine the strain rates attained at the end of each stress step (as shown in Fig. 3.5). In some cases, we clearly did not wait long enough for the transient response to pass, but this problem can be corrected in future experiments. For the present, we recognize that some steady-state strain rates will be picked too high. We should mention at this point that the term 'steady-state' may well be a misnomer. The microcrack growth mechanisms that occur in brittle rock in compression tend to reduce stress intensity and therefore growth rate with time. Thus, the secondary creep phase identified in many experiments may either be the tail of a decaying creep curve or the region of inflection between decaying homogeneous creep and accelerating localized creep that occurs as the sample approaches failure. The results from two creep experiments are plotted in Fig. 3.7 as $\log_{10}(\dot{\varepsilon}_v)$ *vs* differential stress. Data points are connected according to the sequence in which the measurements were made. Data for the two points in brackets were too noisy to determine accurate strain rates and represent rates occuring at those stresses as predicted by the model. As expected, a strong correlation exists between stress and strain rate, but superimposed on a gradual migration to the right of the plot with increased strain. Least squares fits of the form

$$\log_{10}(\dot{\varepsilon}_v) = A + B\,\sigma_d + C\log_{10}(\varepsilon_{v,i}) \qquad (3\text{-}8)$$

and

$$\log_{10}(\dot{\varepsilon}_v) = A' + n\log_{10}(\sigma_d) + C'\log_{10}(\varepsilon_{v,i}) \qquad (3\text{-}9)$$

were performed on the data where $\varepsilon_{v,i}$ is inelastic strain. Results are given in Table 3.1. A test of how well eq. (3-8) describes the observed data is shown in Fig. 3.8. Here the data shown in Fig. 3.7a have been de-trended by plotting $\log_{10}(\dot{\varepsilon}_v)$ - C $\log_{10}(\varepsilon_{v,i})$ *vs* σ_d. This operation brings the data back to a single straight line. Thus, on an empirical basis, the quasi-steady-state creep rate of granite in the secondary creep

phase can be adequately fit by either an exponential stress dependence or power law stress dependence superimposed on what is essentially a strain-hardening process.

The conductivity measurements which were taken during these experiments confirm the continual growth of microcracks during the secondary creep phase. As dilatancy progresses, the number of paths available for conduction through the pore fluid, as well as conductance of existing paths, should increase. This effect is shown in Fig. 3.9 where conductivity (at 10 Hz) is plotted *vs.* volumetric strain. Time progresses from left to right. The initial three measurements were taken during transient creep while the remainder correspond to the entire experiment shown in Fig. 3.7a. Conductivity increased approximately three-fold over the hydrostatic value. These results are in good agreement with similar measurements taken during creep (*Lockner and Byerlee,* 1986). The observed conductivity changes are also comparable to changes reported for constant-strain-rate experiments (*Brace and Orange*, 1968; *Brace*, 1975).

Discussion

One motivation for conducting these experiments was to explore the possibility of detecting a low-stress-sensitivity creep mechanism. Such a mechanism would be masked by the commonly observed stress corrosion mechanism at room temperature and loads above 80% instantaneous strength, but could become dominant at lower stress levels (and strain rates). Extrapolation of the present data to a strain rate of 10^{-14} s^{-1} would reduce the rock strength to approximately 70% of its short term strength. If a low-sensitivity mechanism became dominant at low stress, it would further reduce the long-term strength. Such a mechanism would appear as a break in slope of the σ - $\dot{\varepsilon}_v$ plot. There is, however, no indication in our present data of a new low-stress mechanism. A practical lower limit for obtaining meaningful data through this method is approximately 10^{-11} s^{-1} and makes the prospects for isolating such a mechanism at room temperature unlikely.

Rutter and Mainprice (1978) conducted similar experiments on Tennessee sandstone at room temperature and at 300°C. Selected results from their intact sample experiments are reproduced in Fig. 3.10. They observed a dramatic decrease in stress sensitivity at 300°C, which they attributed to a change in the dominant creep mechanism from stress corrosion (low temperature and high strain rate) to pressure solution. If the stress corrosion mechanism is thermally activated according to

$$\dot{\varepsilon} = \dot{\varepsilon}_0 \exp(\beta\sigma_d / kT) \qquad (3\text{-}10)$$

where k is Boltzmann's constant, then the 20°C slope should be approximately twice the 300°C slope. Thus the first few data points in the 300°C plot would represent the stress corrosion branch. Whether or not the low-stress-dependent branch is due to pressure solution, it is operating in the proper temperature range for mid-crustal conditions; especially at low strain rates. These phenomena obviously need further investigation. For example, it is important to know if *RM's* low-stress-dependence mechanism would be operative in a low porosity rock such as granite.

Table 3.1 summarizes the strain rate data. It is interesting that at room temperature the stress sensitivity parameter B is nearly identical for our data and those of both

Wawersik and *RM*, even though effective pressure varied from zero to 1.5 kb and two different rock types were studied. If stress dependence is thermally activated, as in eq. (3-10), then

$$\beta = 2.303\ kTB\ . \qquad (3\text{-}11)$$

Then, as mentioned, *RM's* 300°C stress corrosion data also give the same stress sensitivity, although that value has a large uncertainty.

Also shown in Table 3.1 are data from room temperature time-to-failure experiments. The time-to-failure data can be related to the secondary creep rate data in the following manner. First, note that in a creep test, the transient primary and tertiary creep phases are generally short in duration when compared to the secondary creep phase. Then, if the total inelastic volumetric strain that a sample undergoes in secondary creep is denoted as $\varepsilon_{v,i}^{tot}$, the volumetric strain rate for secondary creep is approximately $\dot{\varepsilon}_v = \varepsilon_{v,i}^{tot} / t_f$. If we further assume that $\varepsilon_{v,i}^{tot}$ is approximately independent of stress level as suggested by *Griggs* (1940) and *Kranz and Scholz* (1977), especially for a given confining pressure, then substituting into (3-3) leads to

$$\dot{\varepsilon}_v = (\varepsilon_{v,i}^{tot} / t_o)\, e^{2.303b\sigma}\ . \qquad (3\text{-}12)$$

Comparison to (8) shows that $b \approx B$. Given the stated uncertainties in Kranz's values of b (eq. 3-3), his data is in agreement with our determinations of B and approximately independent of confining pressure (Fig. 3.11). On the other hand, Scholz's single-crystal quartz measurements of b (Table 3.1) are significantly smaller. This may reflect a tendency for single crystals to have smaller stress-concentrators than polycrystalline rocks. As we discuss in the next section, fracture toughness G is a more fundamental parameter for controlling crack growth rate than either σ or K. We will attempt to relate the empirical constants b and B to G in that section.

The dependence of strain rate on strain (eqs. (3-8) and (3-9)) is not suprising and is undoubtedly present in the *RM* data as well. Constant strain rate experiments on brittle rocks in compression always strain harden in the region before failure where inelastic strain occurs. As discussed earlier, this hardening represents, in part, the ability of rocks to relieve stress concentrations through microcracking. In our experiments,

failure to account for the strain hardening effect would have resulted in a 20% overestimate of the stress coefficient in a relaxation experiment.

Model

Early approaches to understanding static fatigue in glass were based on reaction rate theory. *Charles and Hillig* (1962) considered the case where chemical reactions at the crack tip were rate limiting. Such reactions are expected to be both thermally activated and stress sensitive. By stretching the bonds at the crack tip, the energy barrier to the forward reaction is reduced while the energy of the reverse reaction is increased. Using a modification of Charles and Hillig, we write for the forward rate

$$v^+ = v_0 \exp[-(E_0 + a_0^3\Gamma/r_c - \beta'\sigma)/kT] \qquad (3\text{-}13)$$

where v_0 represents the rate of jump attempts, E_0 is the stress free activation energy, a_0 is the molecular dimension, r_c is the crack tip curvature and Γ is the interfacial free energy between the crystal and reaction products. β' has units of volume and expresses the stress sensitivity. The rate of the reverse reaction is

$$v^- = v_0 \exp[-(E_0 + a_0^3\Gamma/r_c + \beta'\sigma)/kT] \qquad (3\text{-}14)$$

Combining E_0 and the surface energy into an apparent activation energy E^*, the net reaction rate becomes

$$v = v^+ - v^- = v_0 \exp(-E^*/kT) \sinh(\beta'\sigma/kT) \qquad (3\text{-}15)$$

For large stress, $v^+ >> v^-$ and eq. (3-13) approximates the net rate.

Eqs. (3-13) through (3-15) have been included because of their similarity to the empirical eq. (3-10). However, eq. (3-15) refers to conditions at the crack tip, which, for a brittle rock, will contain a stress singularity. Thus it is more appropriate (*Rice*, 1978) to express the stress-related driving force in terms of the strain energy release

$$G = -(\partial U_E/\partial c)_u \, . \qquad (3\text{-}16)$$

For $v^+ >> v^-$, (3-16) becomes

$$v = v_o \exp[-(E^* - a_o^2 G)/kT] . \quad (3\text{-}17)$$

It is well known that for rocks loaded in compression, the dominant mode of microcrack growth is tensile and is in a direction subparallel to the maximum compressive stress. The development of tensile stresses in an overall compressive stress field requires an inhomogeneity in elastic properties. *Tapponier and Brace* (1976), for example, noted the frequent occurance of axial cracks emmanating from brittle grains in contact with biotite. Of course, the largest contrasts in material properties will occur at the surface of pores or cracks; especially when open. We will use for a model a set of non-interacting cracks oriented obliquely to the applied principal stress directions (Fig. 3.12). *Nemat-Nasser and Horii* (1982) have analized the response of a single such crack in a homogeneous medium. Their analysis includes a generalized stress field and crack orientation as well as crack friction. This crack geometry has also been analized by *Ashby and Hallam* (1986). They developed a convenient result (*Sammis and Ashby,* 1986) for uniaxial compression which relates the far-field axial stress to crack length for long 'wing' cracks:

$$\sigma_1(\pi c/L)^{1/2} = 4.3K_{IC}/(1-f) \quad (3\text{-}18)$$

where K_{IC} is critical stress intensity factor for mode I (tension) and f is coefficient of friction on the crack. c is the diagonal crack half length and L in non-dimensional wing crack length; L = l/c where l is wing crack length. Eq. (18) represents the condition for stable crack growth so that at the crack tip, $K_I = K_{IC}$. Then, for axial stress ≤ stress needed to extend the crack, stress intensity at the crack tip is given by

$$K_I = \sigma_1(\pi c/L)^{1/2}(1-f)/4.3 . \quad (3\text{-}19)$$

The strain energy release rate can be written (*e.g. Rudnicki*, 1980)

$$G = K_I^2(1-\eta)/2\mu \quad (3\text{-}20)$$

where η and μ are respectively Poisson ratio and shear modulus. Inserting (3-19) and

(3-20) into (3-18) gives

$$\nu = \nu_0 \exp[-(E^* - \xi\sigma_1^2/L)/kT] \qquad (3\text{-}21)$$

with $\xi = \pi c a_o^2((1-\eta)/2\mu)((1-f)/4.3)^2$. Notice that in contrast to (3-16) we have now expressed the reaction rate in terms of the remote stress, which appears raised to the second power since it is expressing the strain energy release rate. Also, as the crack grows in creep (increasing L, constant σ_1), the driving force decreases. This represents strain-hardening of the sample.

Relating Crack Growth to Volumetric Strain

We next attempt to relate the atomistic rate theory result (3-21) to the observed macroscopic strain rates. If a crack tip advances through the chemical corrosion of bonds, then the number of reaction sites per unit volume can be expressed as

$$N = 2N_C w/a_o \qquad (3\text{-}22)$$

where N_C is the crack density (per unit volume) and w is average crack tip width. Now assume that each reaction represented by (3-21) contributes an increment of volume change

$$V_i = \alpha\, a_o^3 \qquad (3\text{-}23)$$

where α is a geometric factor. α can be interpreted by considering the change in crack volume that results from the advance of a crack tip by a distance a_o. This change in crack volume is

$$V_i w/a_o = \alpha w a_o^2 . \qquad (3\text{-}24)$$

By combining (3-21) and (3-23), volumetric strain rate becomes

$$\dot{\varepsilon}_V = V_i N \nu = \dot{\varepsilon}_{vo} \exp[-(E^* - \xi\sigma_1^2/L)/kT] \qquad (3\text{-}25)$$

where $\dot{\varepsilon}_{vo} = (2\alpha\, a_o^2\, N_c w\, \nu_o)$.

In a creep test, the initial application of axial stress will force the dominant cracks to grow to a pre-determined length according to (3-18) since the crack tip stress intensity is at the critical value. Once the sample is at stress, however, the cracks will continue to grow, gradually lowering the crack tip stress intensity due to the crack length dependence in (3-25). This relation predicts a monotonically decreasing strain rate. Accelerating tertiary creep can be interpreted as the result of a gradual increase in the intensity of crack interactions as the sample approaches failure. Since (3-25) assumes no crack interactions, it cannot predict tertiary creep. Interpreted in this manner, secondary creep is either the nearly constant strain rate tail of the exponential decay predicted by (3-25) or the region of inflection representing the transition from negative curvature primary creep to positive curvature tertiary creep. Notice, also, that a modified form of (3-25) can be used to describe the region I subcritical crack growth rate (Fig. 3.2). In this case, log(crack velocity) $\propto K_I^2$ and not $\propto K_I$ as is normally assumed. Due to the limited range of stress over which the relevant measurements are made, these forms cannot be distinguished from available data.

The validity of (3-25) can be tested by using crack density values obtained from laboratory experiments. Since many of the parameter in the pre-exponential term (especially α) have not been measured directly, only an approximate comparison to experimental data can be made. We will use crack density data measured by *Hadley* (1975) and reported in *Madden* (1983). For Westerly granite at 65% failure stress, Hadley reported an axial crack count of 51 mm^{-2} for 10 - 30 micron lengths, increasing to 208 mm^{-2} at failure. 30 - 100 micron axial crack densities increased from 58 to 121 mm^{-2} at failure. Assuming that crack widths and lengths were approximately equal, this gives $N_{c,10\text{-}30\mu m} \sim 2 - 10 \times 10^3\ mm^{-3}$ and $N_{c,30\text{-}100\mu m} \sim 1 - 2 \times 10^3\ mm^{-3}$. The least constrained parameter is α. It can be estimated by noting that for a characteristic crack, an increase dl in crack length can be related to the resulting volumetric strain by

$$\alpha\, a_o w N_c dl = d\varepsilon_v\ . \qquad (3\text{-}26)$$

Using $a_o = 10^{-3}$ μm and w = 40 μm, the crack geometry coefficient estimated from Hadley's data is $\alpha = 1.2 \pm 0.6 \times 10^3$. Finally, we use the Debye frequency, $\nu_o \sim 10^{13}$

Hz. Since (3-25) applies to uniaxial compression, we use *Wawersik's* 1973 unconfined Westerly granite data (Fig. 3.13) with an ultimate strength of 2.5 kb. At 80% failure strength, using $\dot{\varepsilon}_v = 10^{-9}\ s^{-1}$, eq. (3-25) predicts that the energy barrier, $E^* - \xi\sigma^2/L = 0.96 \pm 0.05$ eV (21 kcal/mole). At 90% failure strength, the barrier height would drop to 0.84 eV. Given the uncertainties in the calculation, these are in remarkable agreement with the value reported by *RM* (0.9 eV) for sandstone and the range given by *Scholz* (1972) (0.9 to 1.1 eV) for time-to-failure in quartz. The same relation applied to data from the present study yields energy barriers at 80 and 90% failure stress that agree with Wawersik's results to within 20%. This consistancy may indicate that all of these room temperature creep experiments are controlled by the same stress corrosion sub-critical crack growth process.

Finally, we attempt to modify (3-25) by relating the crack length parameter L in the stress sensitivity term to volumetric strain. If α is approximately independent of crack length, integrating (3-26) yields $L = \kappa\varepsilon_v$ where $\kappa = (\alpha a_o c w N_c)^{-1}$. Here we have set $\varepsilon_v = 0$ when $L = 0$. Then, (3-25) becomes

$$\dot{\varepsilon}_v = \dot{\varepsilon}_{vo} \exp[-(E^* - \xi\sigma_1^2/\kappa\varepsilon_v)/kT \qquad (3\text{-}27)$$

giving stress and strain sensitivities of

$$\partial \ln\dot{\varepsilon}_v/\partial\sigma_1 = 2\xi\sigma_1/\kappa\varepsilon_v kT \qquad (3\text{-}28)$$

and

$$\partial \ln\dot{\varepsilon}_v/\partial\varepsilon_v = -\xi\sigma_1^2/\kappa\varepsilon_v^2 kT\,. \qquad (3\text{-}29)$$

Unfortunately, the ratio ξ/κ which appears in both partial derivatives is proportional to c^2 (c is the diagonal crack half-length). Since c is not well determined experimentally, we are not able to test these relations adequately. The predicted stress sensitivity, using $c = 20\ \mu m$, is plotted along with unconfined granite data in Fig. 3.13. The same calculation gives an apparent activation energy $E^* = 1.3 \pm 0.1$ eV (1 eV = 23.1 kcal/mole). A suite of synthetic creep curves using (3-27) is plotted in Fig. 3.14. Finally, a synthetic creep experiment, stepping through a series of stress levels, is

shown in Fig. 3.15. This duplicates many of the features observed in Fig. 3.5, although it does not adequately predict secondary features such as the strain rate transients that occur after each stress increase.

Eq. (3-27) has been developed for uniaxial stress. Application of confining pressure increases the normal stress on oblique cracks, thereby increasing their frictional strength. In addition, wing cracks must do work against the confining pressure as they open. Thus, confining pressure has a first order effect on creep rates. We can include this effect by incorporating the confining pressure dependence of G in (3-17). From *Ashby and Hallam* (1986), assuming long wing cracks, (3-18) becomes

$$\sigma_1 = \frac{4.3\, K_{IC}\left(\frac{L}{\pi c}\right)^{1/2}}{1 - \lambda - f(1+\lambda) - 4.3\, L} \qquad (3\text{-}30)$$

where $\lambda = \sigma_3/\sigma_1$. Then, substituting $\sigma_d = \sigma_1 - \sigma_3$, and repeating the above analysis leads to

$$G = \frac{\frac{(1-\eta)\pi c}{2\mu}(1-f)^2 \sigma_d^{\,2} K_{IC}^{\,2}}{\left[4.3\,(\pi c)^{1/2}\sigma_3 L + 4.3\, K_{IC} L^{1/2} + 2\, f\,(\pi c)^{1/2}\sigma_3\right]^2} \qquad (3\text{-}31)$$

The σ_d^2 dependence comes from the assumption that $K_I \propto \sigma_d$. Confining pressure appears in the denominator and, as expected, inhibits crack growth. For large confining pressure, the strain hardening becomes more severe ($G \propto 1/L^2$ instead of $1/L$).

One other interesting calculation can be made based on the stress sensitivity. Since $\dot{\varepsilon}_v \propto v$, differentiating eq. (3-17) gives

$$\partial \ln \dot{\varepsilon}_v / \partial G = (\partial \ln \dot{\varepsilon}_v / \partial \ln v)(\partial \ln v / \partial G) = a_0^2/kT \qquad (3\text{-}32)$$

and from (3-31)

$$\partial G/\partial \ln \sigma_d = 2G\,. \tag{3-33}$$

Then

$$n = (\partial \ln \dot{\varepsilon}_v/\partial \ln \sigma_d)_{\text{const. } \sigma 3,L} = 2a_o^2 G/kT \tag{3-34}$$

where n appears in eq. (3-9) and is tabulated in Table 3.1. Eq. (3-34) predicts that n is independent of confining pressure which appears to agree with the experimental data. For $n = 60 \pm 5$, we have $G = 0.12 \pm 0.01$ Jm^{-2}. Experimentally determined critical energy release rates for quartz-bearing rocks (*Atkinson*, 1987) fall in the range $G_c \sim 50 - 400$ Jm^{-2}. However, these rocks are observed to develop a damage zone ahead of the advancing crack. For single crystal quartz, which is more appropriate for the atomistic analysis developed in this section, experimental results give $G_c \sim 0.4 - 10$ Jm^{-2}. This suggests that for steady-state creep, microcrack tips are advancing at G/G_c of approximately 0.01 to 0.4 or relative stress intensity $K_I/K_{IC} \sim 0.1$ to 0.6.

Conclusions

The main result of this study is the determination of the $\log_{10}$(strain rate) sensitivity to stress of 0.7 kb^{-1} for secondary creep in Westerly granite at room temperature. This value is in remarkable agreement with results from other studies on dry Westerly, Barre granite and Tennessee sandstone. Application of reaction rate theory to subcritical crack growth is successful in predicting both the stress and strain sensitivity of strain rate. This same reaction rate theory can provide a framework for understanding the exponential stress dependence of region I subcritical crack growth. A stress corrosion reaction, presumably involving the Si-O bond, with an apparent activation energy of approximately 1.3 ± 0.1 eV (30 kcal/mole) appears to control room temperature time-dependent creep in common silicate rocks above 80% failure strength. The various parameters affecting low-temperature creep require further investigation. Temperature is clearly of central importance, not only in determining activation enthalpies, but also in making the processes occuring at low stress accessable at reasonable strain rates. The effects of confining pressure and pore pressure should be determined. Fluid composition, including pH, may affect crack growth rates. Finally, crack morphology is important. How cracks grow and interact will ultimately determine the rock strength and will dominate or greatly influence permeability, acoustic velocities, electrical resistivity and other rock properties.

TABLE 3.1 - Parameters from Creep Data

Sample	Temp	P_{eff}	B	C	n	β
	[°C]	[kb]	[kb^{-1}]			[eV/kb]
		eq.:	(3-8)	(3-8)	(3-9)	(3-10)
WG5, Westerly (this study)	26	0.4	7.2	-4 to -6	59	0.43
WG6, Westerly (this study)	26	0.4	7.5	-3 to -5	64	0.44
Westerly (*Wawersik*, 1973)	25	0	7.5			0.44
TS13, Tenn. sandst. (*RM*)	20	1.5	7.6		70	0.44
TS12, Tenn. sandst. (*RM*) stress cor. branch, Fig. 3.10	300	1.5	3.7		28	0.42
TS12, Tenn. sandst., (*RM*) press. solution branch, Fig. 3.10	300	1.5	0.88		5	0.10
Time-to-Failure Experiments			b		n	
		eq.:	(3-3)		(3-2)	
Barre granite (*Kranz*, 1980)	25	0	10.8±2.8		46±12	0.64
" " "	25	0.53	5.2±1.7		51±17	0.31
" " "	25	1.0	5.5±1.1		72±32	0.33
" " "	25	2.0	8.0±2		143±84	0.47
Single crystal quartz (c axis) (*Scholz*, 1972)	25	0	0.54			0.032
Single crystal quartz (a axis) (*Scholz*, 1972)	25	0	1.7			0.10

References

Adams, R. and P. W. McMillan, Static fatigue in glass, review, *J. Mat. Sci., 12,* 643-657, 1977.

Anderson, O. L. and P. C. Grew, Stress corrosion theory of crack propagation with applications to geophysics, *Rev. Geophys. Space Phys., 15,* 77-104, 1977.

Ashby, M. F. and S. D. Hallam, The failure of brittle solids containing small cracks under compressive stress states, *Acta Metall., 34,* 497-510, 1986.

Atkinson, B. K., Subcritical crack growth in geological materials, *J. Geophys. Res., 89,* 4077-4114, 1984.

Atkinson, B. K., *Fracture Mechanics of Rocks,* Academic Press, New York, 534 pp., 1987.

Baker, T.C. and F. W. Preston, *J. Appl. Phys., 17,* 170, 1946.

Brace, W. F., Dilatancy related electrical restivity changes in rocks, *Pure Appl. Geophy., 113,* 207-217, 1975.

Brace, W. F. and A. S. Orange, Electrical resistivity changes in saturated rocks during fracture and frictional sliding, *J. Geophys. Res., 73,* 1433-1445, 1968.

Charles, R. J., *J. Appl. Phys., 29,* 1549-1560, 1958.

Charles, R. J. and W. B. Hillig, in "Symp. Mech. Strength of Glass and Ways of Improving It", Florence, Italy, Union Scientifique, Continentale du Verre, Charleroi, Belgium, 511-527, 1962.

Costin, L. S., Deformation and failure, in: *Fracture Mechanics of Rock,* (ed. Atkinson, B. K.), Academic Press, New York, pp. 167-215, 1987.

Cruden, D. M., The static fatigue of brittle rock under uniaxial compression, *Int. J. Rock Mech. Min. Sci., 11,* 67-73, 1974.

Evans, A. G., Acoustic emission sources in brittle solids, Chap. 8, in *Fundamentals of Acoustic Emission,* edited by K. Ono, presented at the Joint Meeting of Acoustical Societies of America and Japan, Honolulu, Hawaii, 209-227, 1978.

Evans, A. G. and M. Linzer, Failure prediction in structural mechanics using acoustic emission, *J. Amer. Ceram. Soc., 56,* 575-581, 1973.

Griggs, D. T., Experimental flow of rocks under conditions favoring recrystallization, *Bull. Geol. Soc. Amer., 51,* 1001-1022, 1940.

Hadley, K., Dilatancy: further studies in crystalline rocks, Ph.D. Thesis, Mass. Inst.

Tech., Cambridge, Ma, 1975.

Horii, H. and S. Nemat-Nasser, Compression-induced microcrack growth in brittle solids: axial splitting and shear failure, *J. Geophys. Res., 90,* 3105-3125, 1985.

Kranz, R. L., Crack growth and development during creep in Westerly granite, *Int. J. Rock Mech. Min. Sci., 16,* 23-36, 1979.

Kranz, R. L., The effects of confining pressure and stress difference on static fatigue of granite, *J. Geophys. Res., 85,* 1854-1866, 1980.

Kranz, R. L. and C. H. Scholz, Critical dilatant volume of rocks at the onset of tertiary creep, *J. Geophys. Res., 82,* 4893, 1977.

Lajtai, E., R. Schmidtke and L. Bielus, The effect of water on the time-dependent deformation and fracture of a granite, *Int. J. Rock MEch. Min. Sci., 24,* 247-255, 1987.

Lockner, D. A. and J. D. Byerlee, Acoustic emission and creep in rock at high confining pressure and differential stress, *Bull. Seis. Soc. Amer., 67,* 247-258, 1977.

Lockner, D. A. and J. D. Byerlee, Development of fracture planes during creep in granite, 2nd Conf. on Acoustic Emission/Microseismic Activity in Geol. Structures and Materials, Trans-Tech. Publications, Clausthal-Zellerfeld, W. Germany, 1980.

Lockner, D. A. and J. D. Byerlee, Complex resistivity measurements of confined rock, *J. Geophys. Res., 90,* 7837-7847, 1985.

Lockner, D. A. and J. D. Byerlee, Changes in complex resistivity during creep in granite, *Pure Appl. Geophys., 124,* 659-676, 1986.

Madden, T. R., Microcrack connectivity in rocks: a renormalization group approach to the critical phenomena of conduction and failure in crystalline rocks, *J. Geophys. Res., 88,* 585-592, 1983.

Martin, R. J., Time-dependent crack growth in quartz and its application to the creep of rocks, *J. Geophys. Res., 77,* 1406-1419, 1972.

Martin, R. J. and W. Durham, Mechanisms of crack growth in quartz, *J. Geophys. Res., 80,* 4837-4844, 1975.

Mould, R. E. and R. D. Southwick, *J. Amer. Ceram. Soc., 42,* 542, 1959.

Nemat-Nasser, S. and H. Horii, Compression-induced nonplanar crack extension with application to splitting, exfoliation, and rockbursts, *J. Geopys. Res., 87,* 6805-6821, 1982.

Poirier, J. P., *Creep of Crystals, High Temperature Deformation Processes in Metals, Ceramics, and Minerals,* Cambridge University Press, Cambridge, 260 pp., 1985.

Rice, J. R., Thermodynamics of the quasi-static growth of Griffith cracks, *J. Mech. Phys. Solids, 26,* 61-78, 1978.

Rudnicki, J. W., Fracture mechanics applied to the earth's crust, *Ann. Rev. Earth Planet. Sci., 8,* 489-525, 1980.

Rutter, E. H. and D. H. Mainprice, The effects of water on stress relaxation of faulted and unfaulted sandstone, *Pure and Appl. Geohpys., 116,* 634-654, 1978.

Sammis, C. G. and M. F. Ashby, The failure of brittle porous solids under compressive stress states, *Acta metall., 34,* 511-526, 1986.

Scholz, C. H., Mechanism of creep in brittle rock, *J. Geophys. Res., 73,* 3295-3302, 1968a.

Scholz, C. H., Microfracturing and the inelastic deformation of rock in compression, *J. Geophys. Res., 73,* 1417-1432, 1968b.

Scholz, C. H., Static fatigue in quartz, *J. Geophys. Res., 77,* 2104-2114, 1972.

Spetzler, H., H. Mitzutani and F. Rummel, Fracture and flow, in: *Anelasticity in the Earth,* Geodynamics series, *4,* (ed. Schreyer, W.), E. Schweizerbartische Verlagsbuchhandlung, Stuttgart, 85-93, 1982.

Tapponnier, P. and W. F. Brace, Development of stress-induced microcracks in Westerly granite, *Int. J. Rock Mech. Min. Sci., 13,* 103-113, 1976.

Wawersik, W. R., Time-dependent behavior of rock in uniaxial compression, Proc., 14th Sympo. Rock Mech., 85-106, 1973.

Wawersik, W. R. and W. S. Brown, Creep fracture of rock, Tech. Rep. UTEC ME 73-197, pp. 1-40, Eng. Dept., Univ. of Utah, Salt Lake City, 1973.

Wiederhorn, S. M. and L. H. Bolz, *J. Amer. Ceram. Soc., 53,* 543-548, 1970.

Williams, E. R. and T. R. Madden, Models for crack development and brittle failure and the role of crack configurations in guiding their behavior, unpublished manuscript, 1988.

Figure Captions

Figure 3.1 Characteristic strain response for constant-stress experiment.

Figure 3.2 Idealized K-v plot for subcritical crack growth.

Figure 3.3 Room-dry Westerly granite strength test response of stress σ_d, tangential strain ε_t, and volumetric strain ε_v.

Figure 3.4 Initial loading and transient creep response for Westerly granite at effective pressure of 0.4 kb.

Figure 3.5 Volumetric strain rate response to stress steps in secondary creep regime. Sample is Westerly granite at effective pressure of 0.4 kb.

Figure 3.6 Stress relaxation experiment (axial strain held constant) for Westerly granite at 0.4 kb effective pressure.

Figure 3.7 Stress-strain rate plot for two Westerly granite samples at 0.4 kb effective pressure in secondary creep regime. Arrows indicate sequence of measurements. Values in brackets are estimated since data was too noisy to obtain reliable measurement. Sample in (b) underwent transition to tertiary creep at end of experiment. Solid symbols are relaxation data.

Figure 3.8 Same data as Fig. 3.7a with strain hardening trend removed.

Figure 3.9 Conductivity change for same sample as Fig. 3.7a showing linear increase with volumetric strain.

Figure 3.10 Selected stress-strain rate data for Tennessee sandstone at 20 and 300°C (*Rutter and Mainprice,* 1978). By their interpretation, high temp. data changed from stress corrosion mechanism at high stress to pressure

solution mechanism at lower stress.

Figure 3.11 Summary of stress sensitivity of secondary creep volumetric strain rate. Run conditions are listed in Table 3.1.

Figure 3.12 Diagonal crack and wing cracks that grow in response to remotely applied compression.

Figure 3.13 Secondary creep rate for unconfined Westerly granite, after *Wawersik* (1973). Curve is theoretical fit using (3-27).

Figure 3.14 Synthetic creep curves for various axial stress levels from (3-27).

Figure 3.15 Modeled creep response to a sequence of stress steps. Note the strain hardening effect similar to that shown in Fig. 3.5.

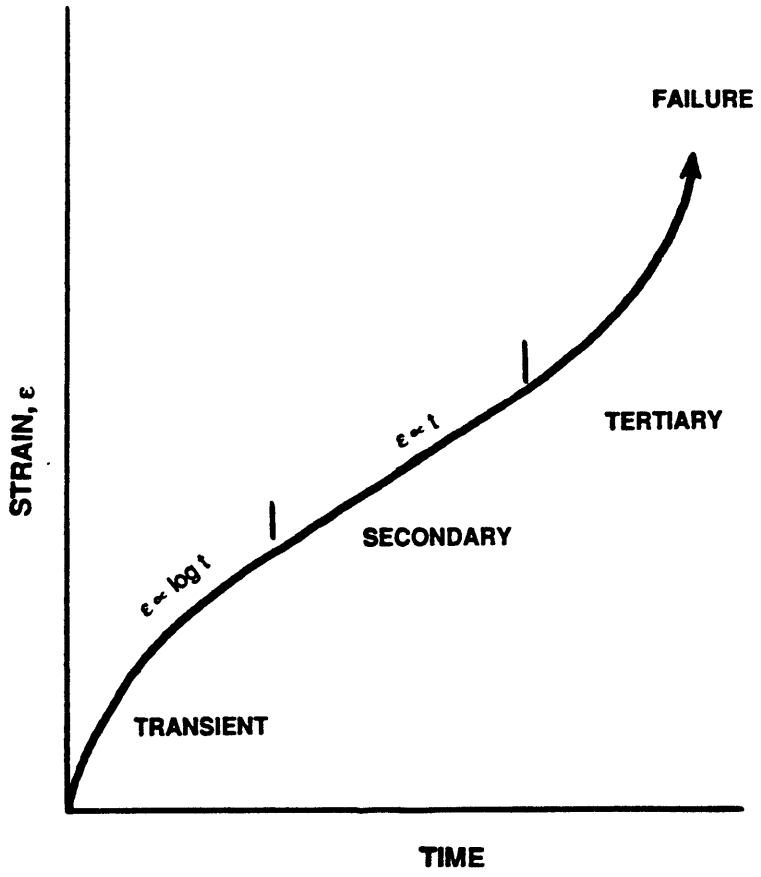
FAILURE
STRAIN, ε
ε ∝ t
TERTIARY
SECONDARY
ε ∝ log t
TRANSIENT
TIME

Figure 3.1

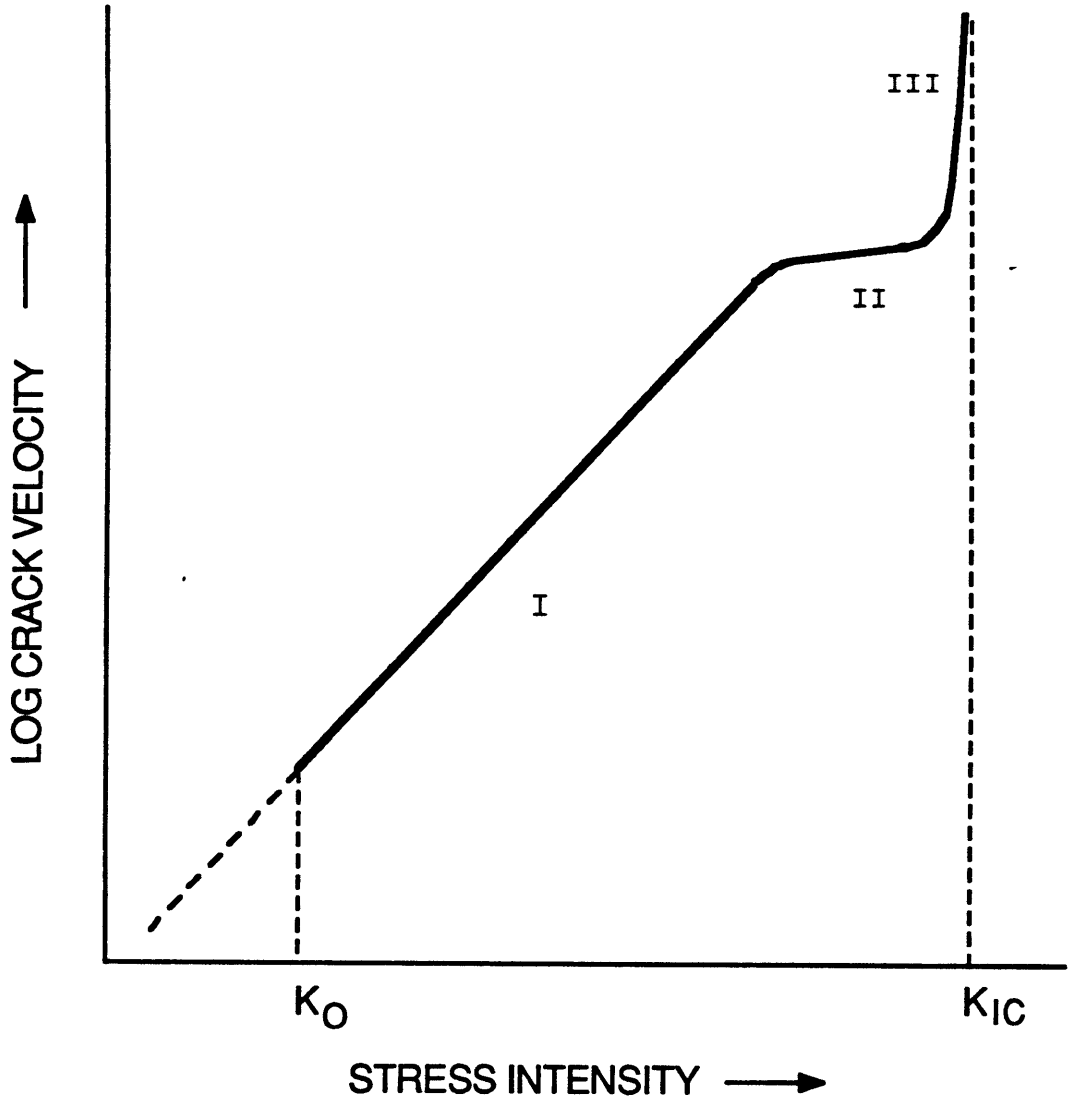

Figure 3.2

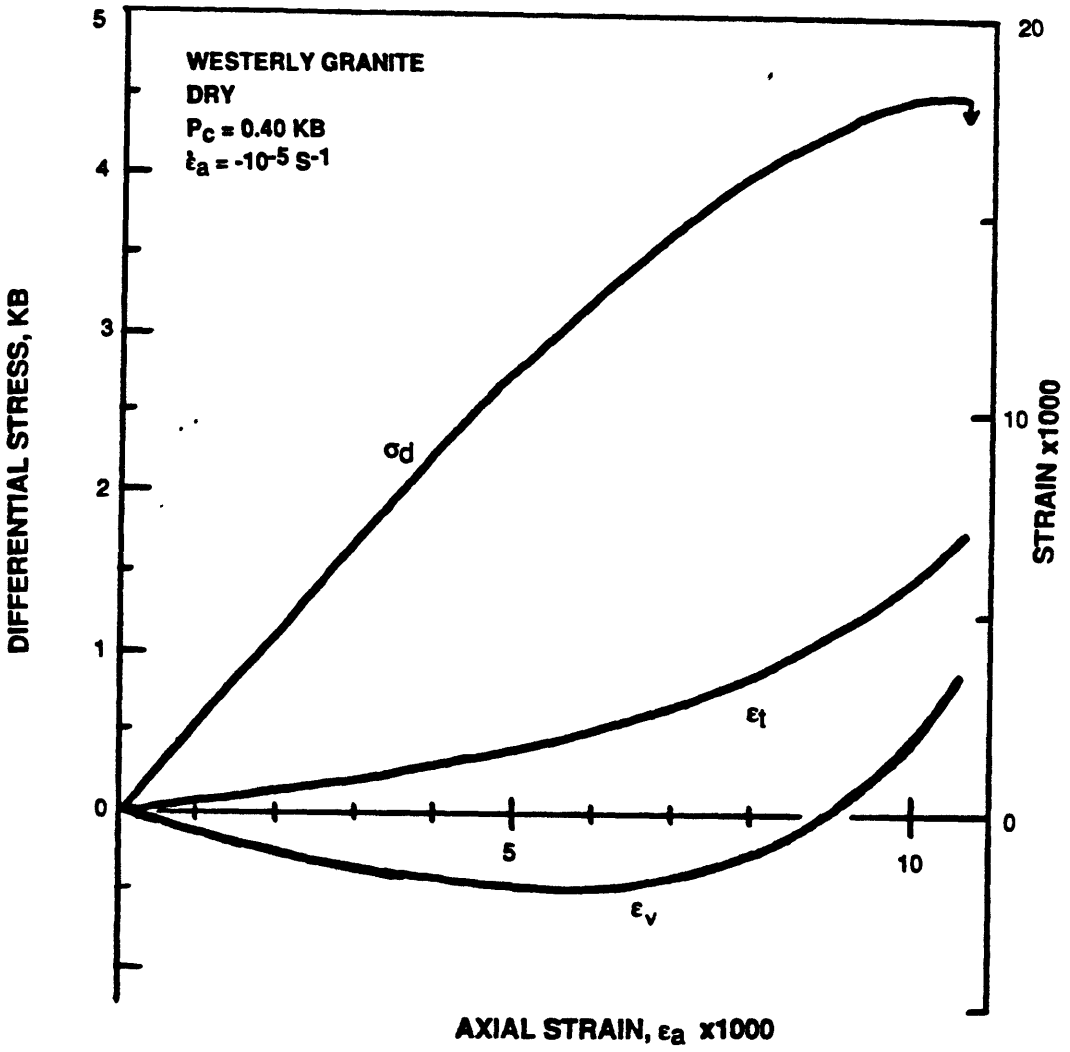
WESTERLY GRANITE
DRY
P_C = 0.40 KB
$\dot{\varepsilon}_a$ = -10^{-5} S^{-1}
σ_d
ε_t
ε_v
DIFFERENTIAL STRESS, KB
STRAIN x1000
AXIAL STRAIN, ε_a x1000
0
1
2
3
4
5
10
20
5
10

Figure 3.3

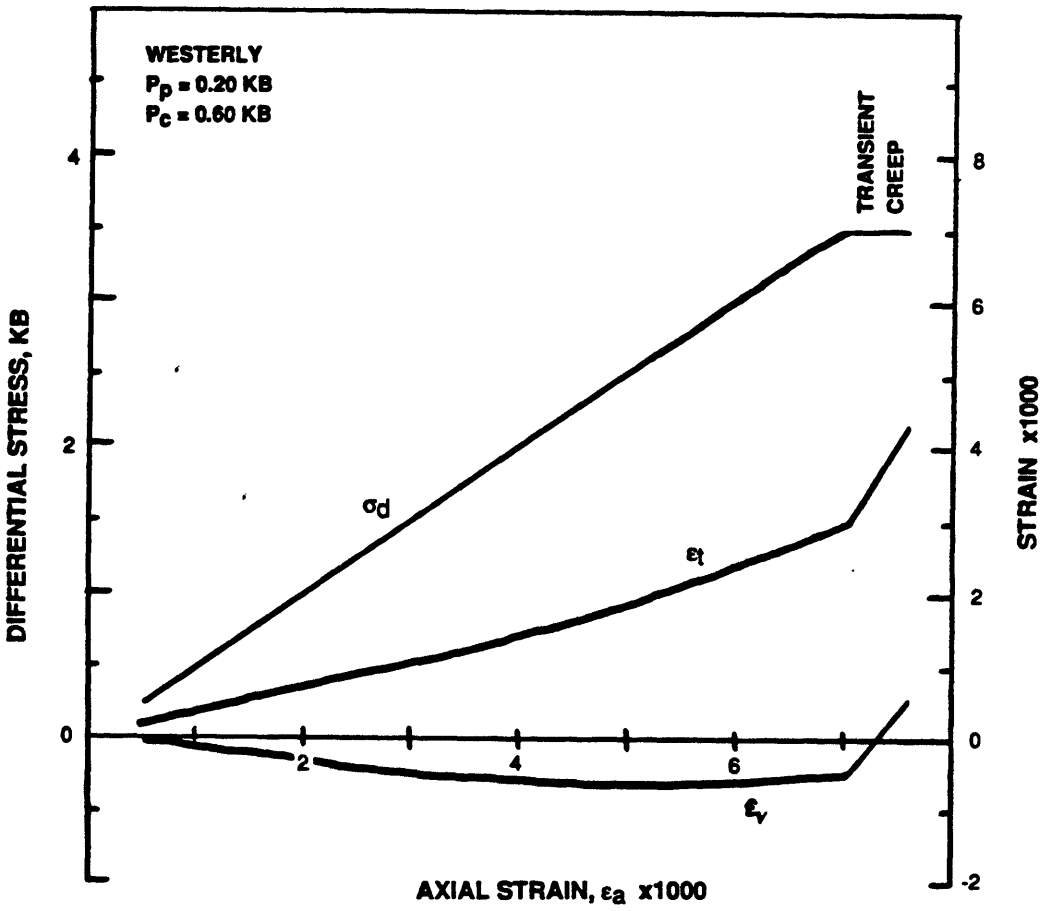
WESTERLY
P_p = 0.20 KB
P_c = 0.60 KB
TRANSIENT CREEP
σ_d
ε_t
ε_v
DIFFERENTIAL STRESS, KB
STRAIN x1000
AXIAL STRAIN, ε_a x1000
0
2
4
6
8
-2

Figure 3.4

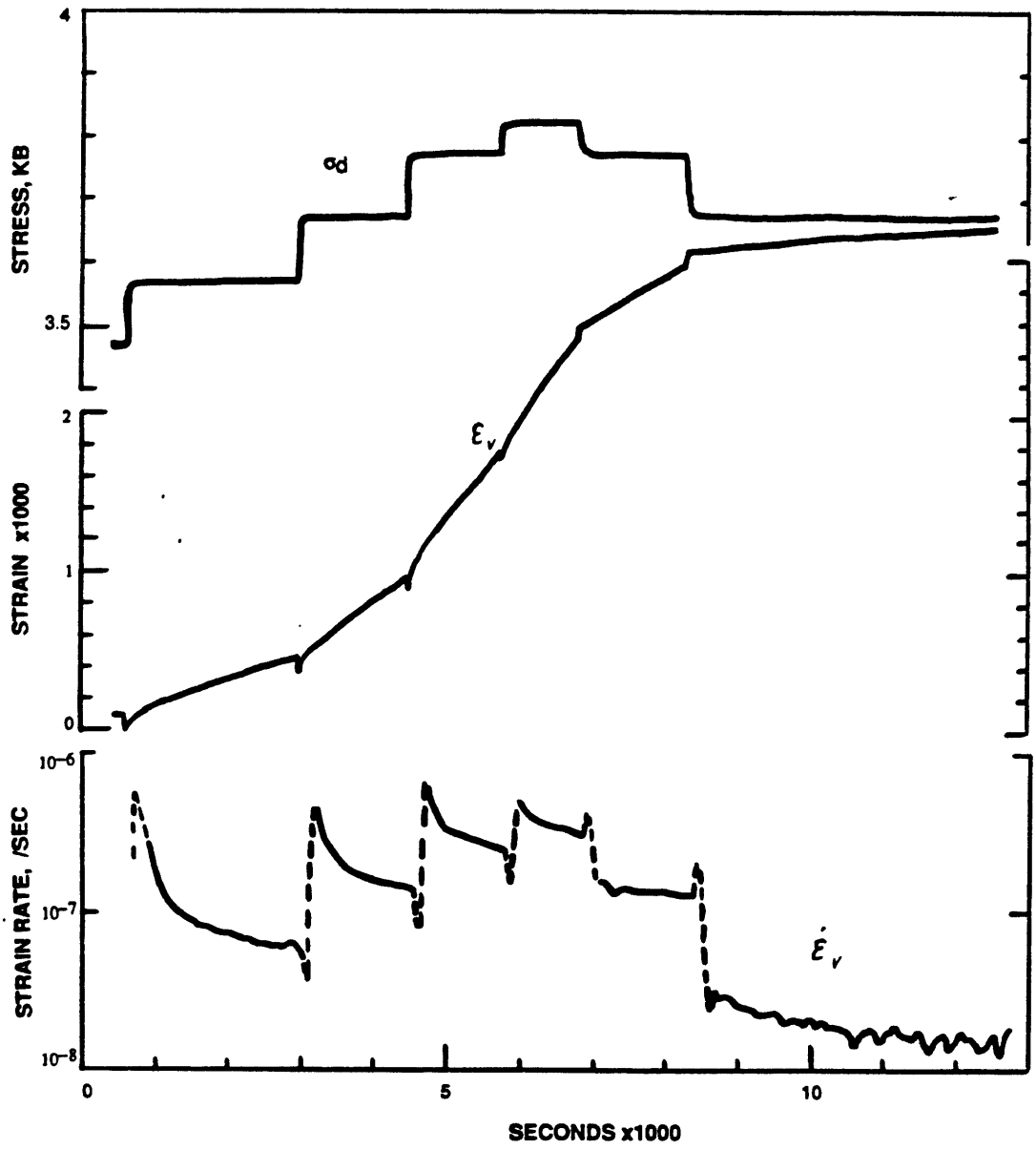
STRESS, KB
4
3.5
σ_d
STRAIN x1000
2
1
0
ε_v
STRAIN RATE, /SEC
10^{-6}
10^{-7}
10^{-8}
$\dot{\varepsilon}_v$
0
5
10
SECONDS x1000

Figure 3.5

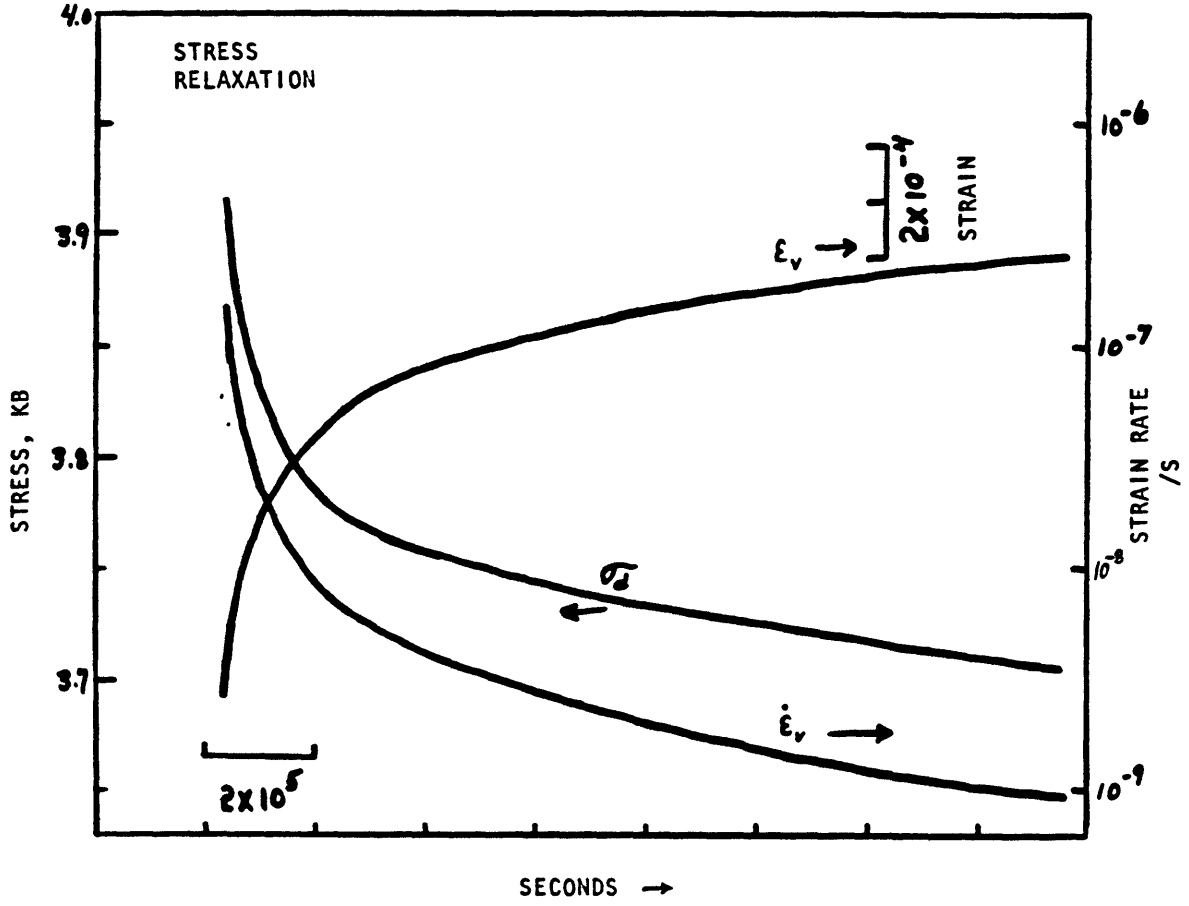
STRESS
RELAXATION
4.0
3.9
3.8
3.7
STRESS, KB
10^{-6}
10^{-7}
10^{-8}
10^{-9}
STRAIN RATE /S
2×10^{-4}
STRAIN
ε_v
σ_d
$\dot{\varepsilon}_v$
2×10^{5}
SECONDS

Figure 3.6

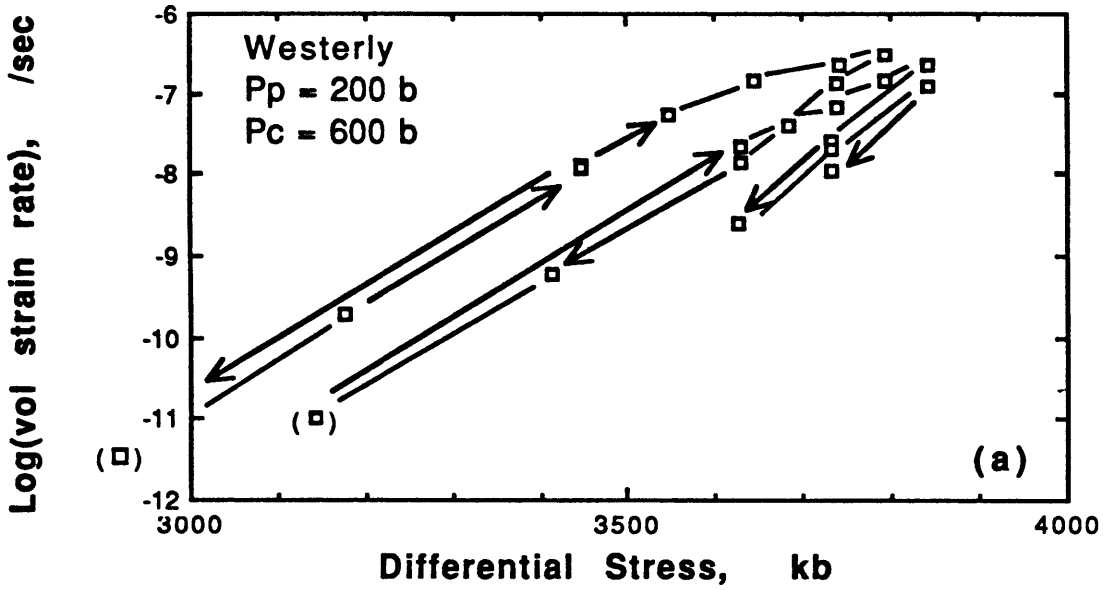
Westerly
Pp = 200 b
Pc = 600 b
(a)
Log(vol strain rate), /sec
Differential Stress, kb
-6
-7
-8
-9
-10
-11
-12
3000
3500
4000

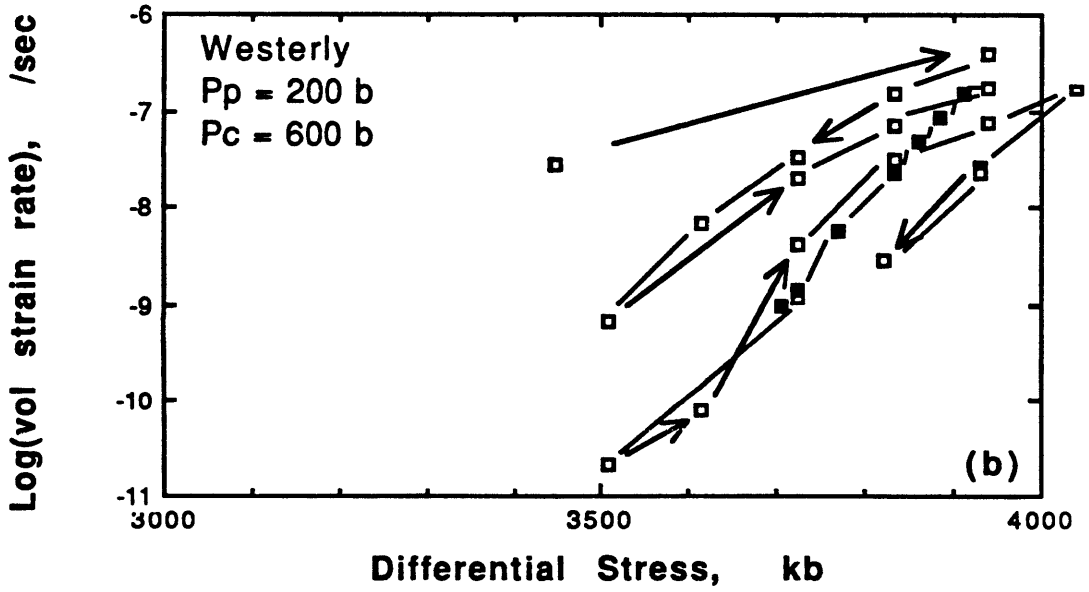
Westerly
Pp = 200 b
Pc = 600 b
(b)
Log(vol strain rate), /sec
Differential Stress, kb
-6
-7
-8
-9
-10
-11
3000
3500
4000

Figure 3.7

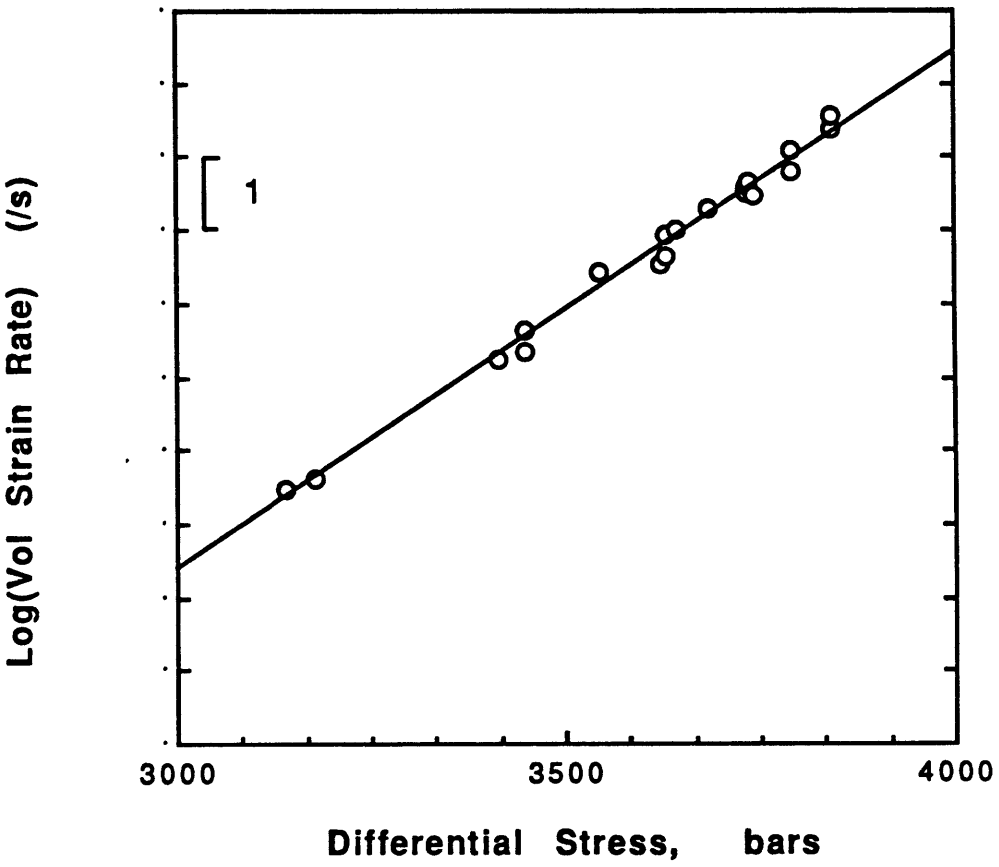
Log(Vol Strain Rate) (/s)
1
3000
3500
4000
Differential Stress, bars

Figure 3.8

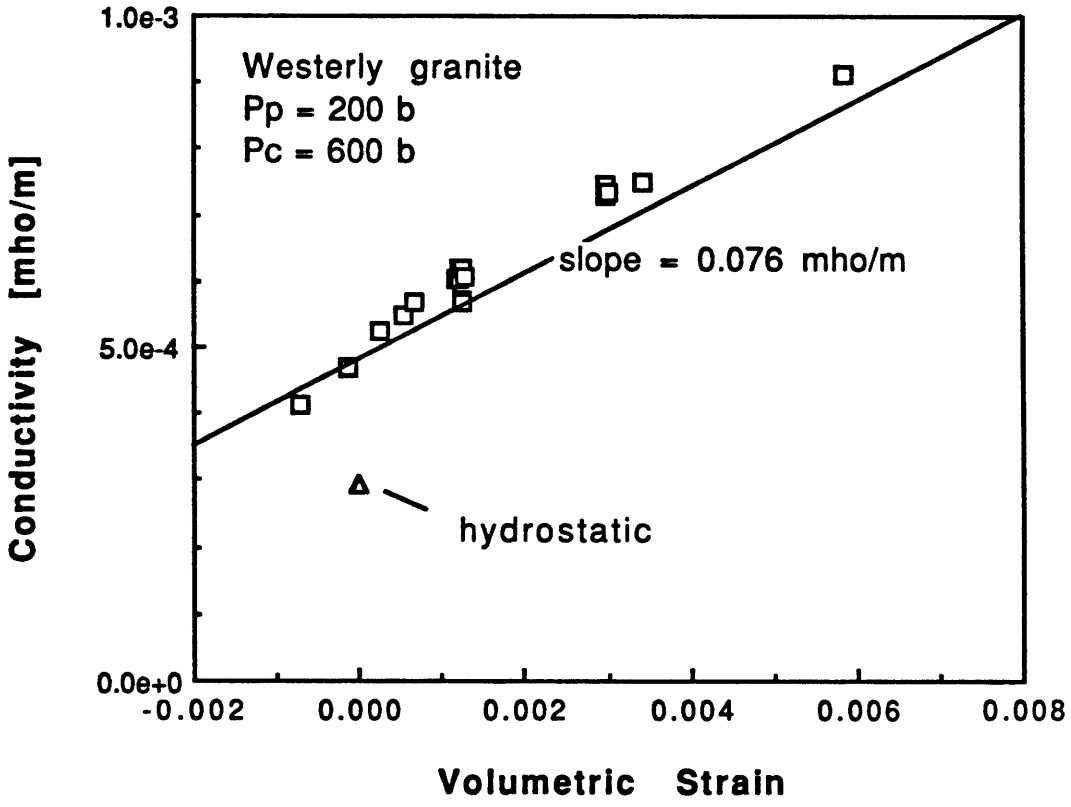
1.0e-3
5.0e-4
0.0e+0
Conductivity [mho/m]
Westerly granite
Pp = 200 b
Pc = 600 b
slope = 0.076 mho/m
hydrostatic
-0.002
0.000
0.002
0.004
0.006
0.008
Volumetric Strain

Figure 3.9

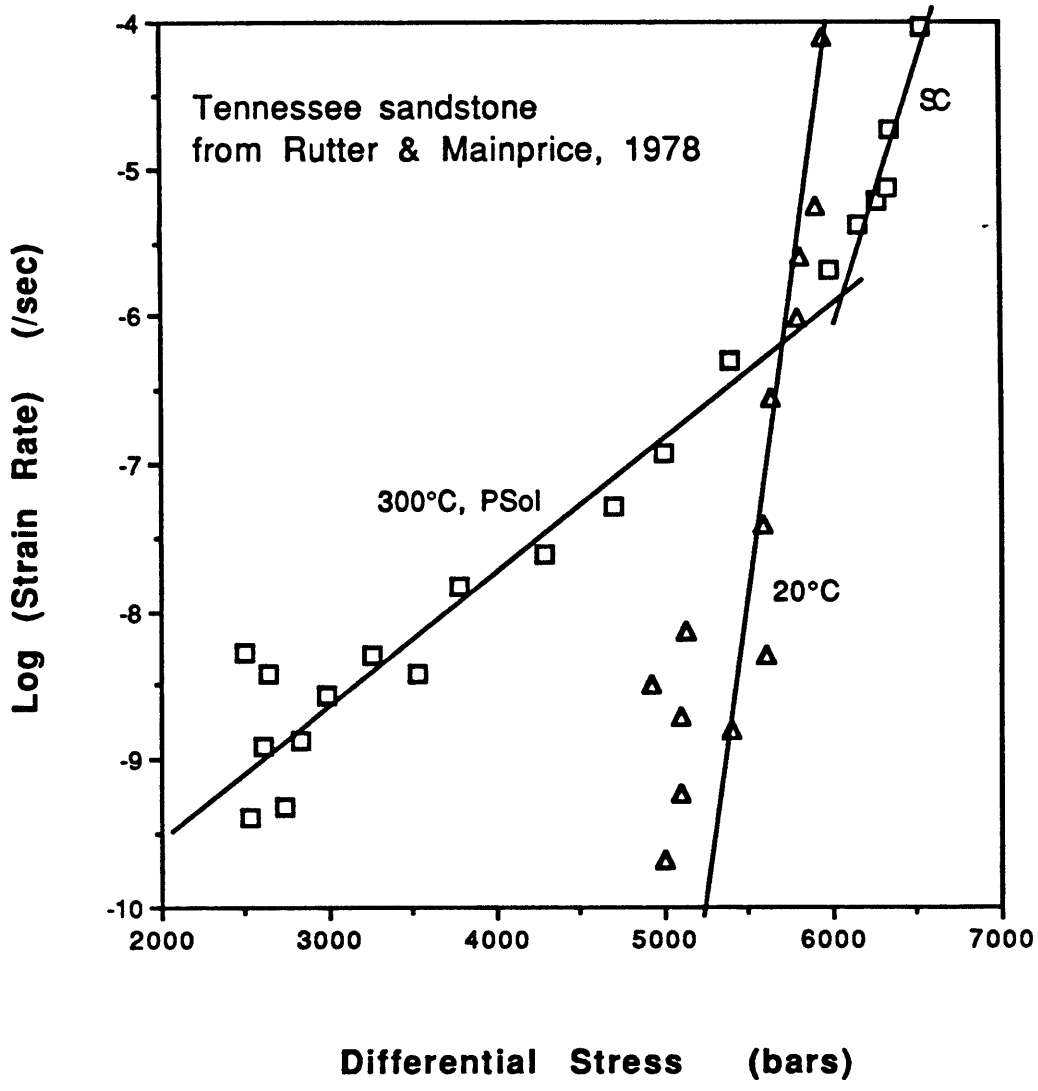
Tennessee sandstone
from Rutter & Mainprice, 1978
SC
300°C, PSol
20°C
-4
-5
-6
-7
-8
-9
-10
2000
3000
4000
5000
6000
7000
Log (Strain Rate) (/sec)
Differential Stress (bars)

Figure 3.10

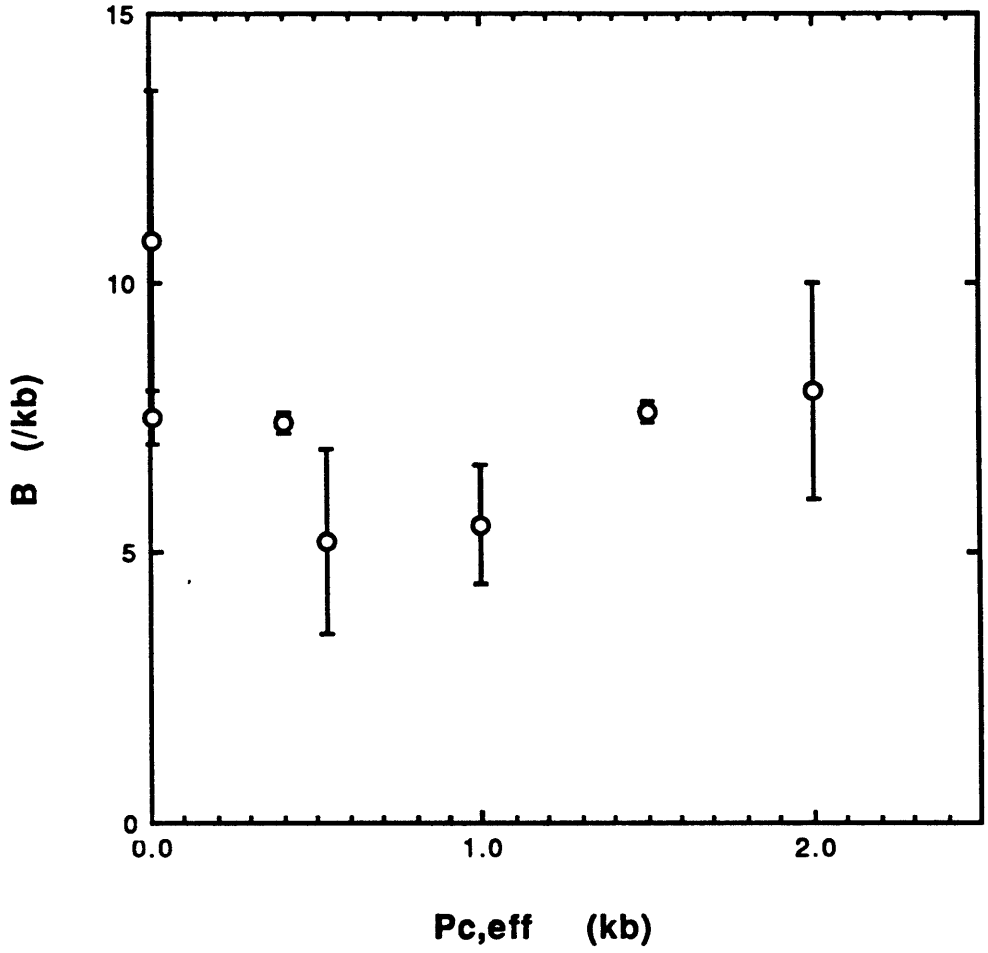

Figure 3.11

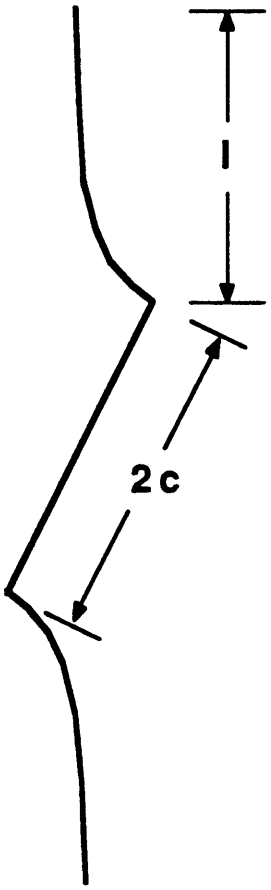

Figure 3.12

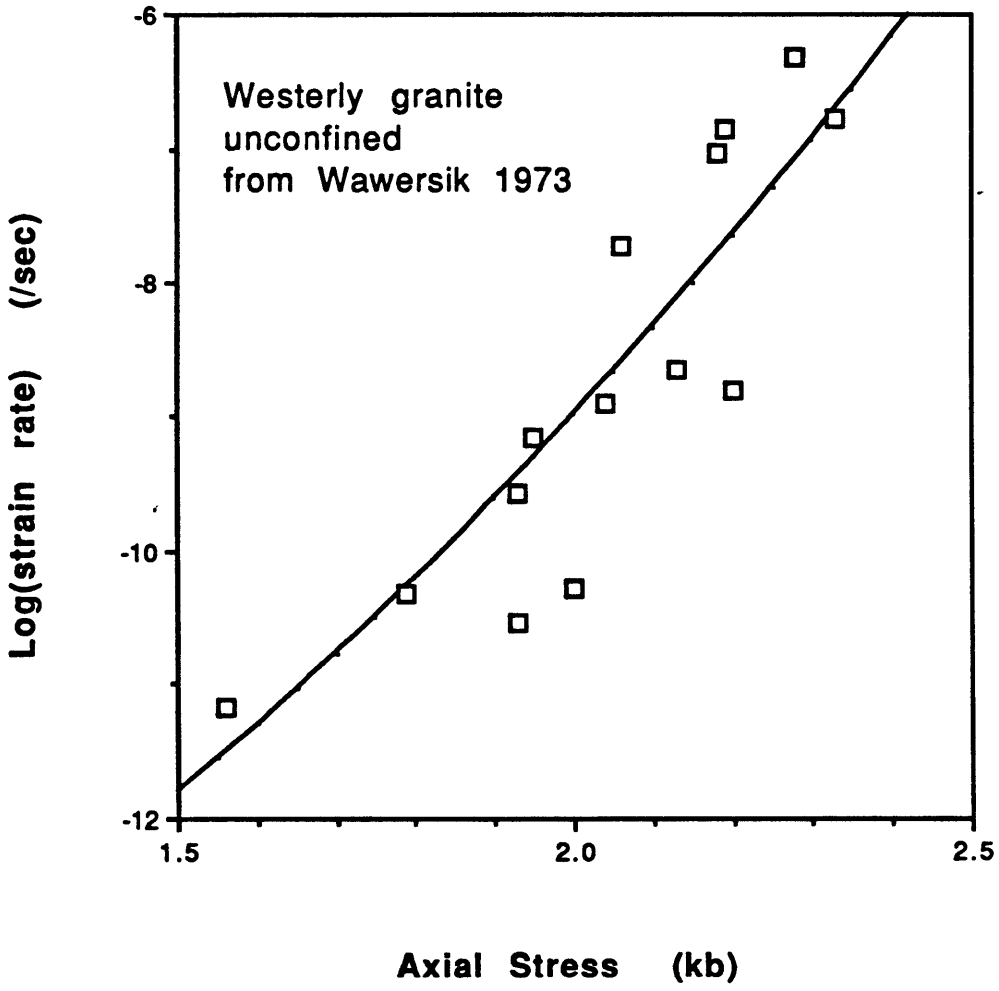
Westerly granite
unconfined
from Wawersik 1973
-6
-8
-10
-12
1.5
2.0
2.5
Log(strain rate) (/sec)
Axial Stress (kb)

Figure 3.13

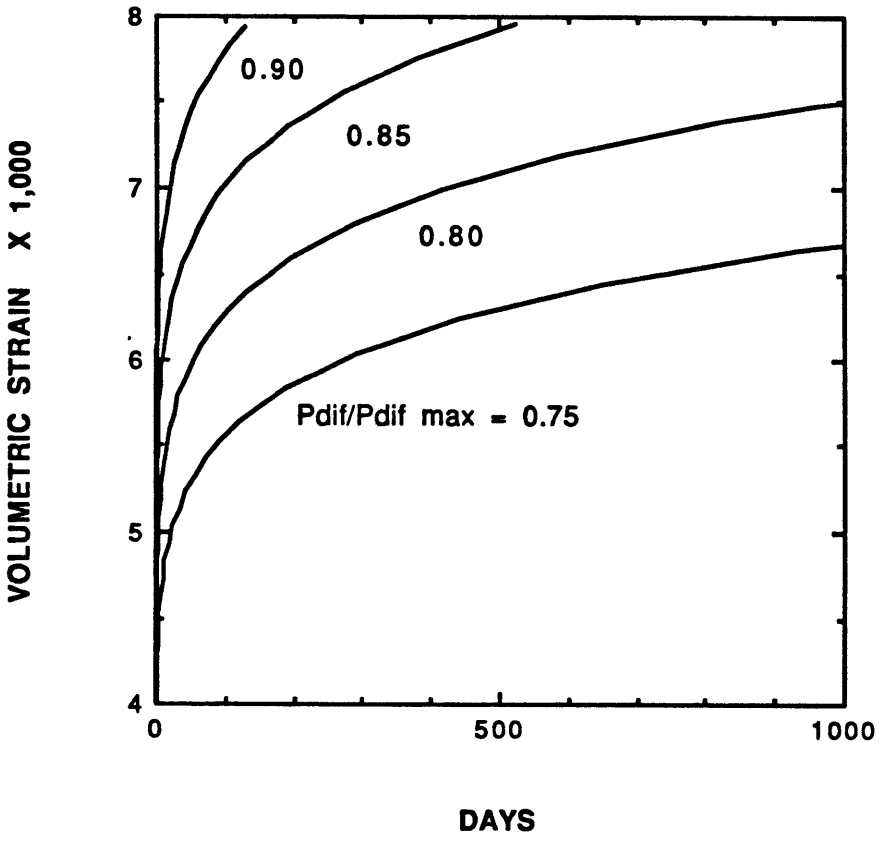
8
7
6
5
4
0.90
0.85
0.80
Pdif/Pdif max = 0.75
VOLUMETRIC STRAIN X 1,000
0
500
1000
DAYS

Figure 3.14

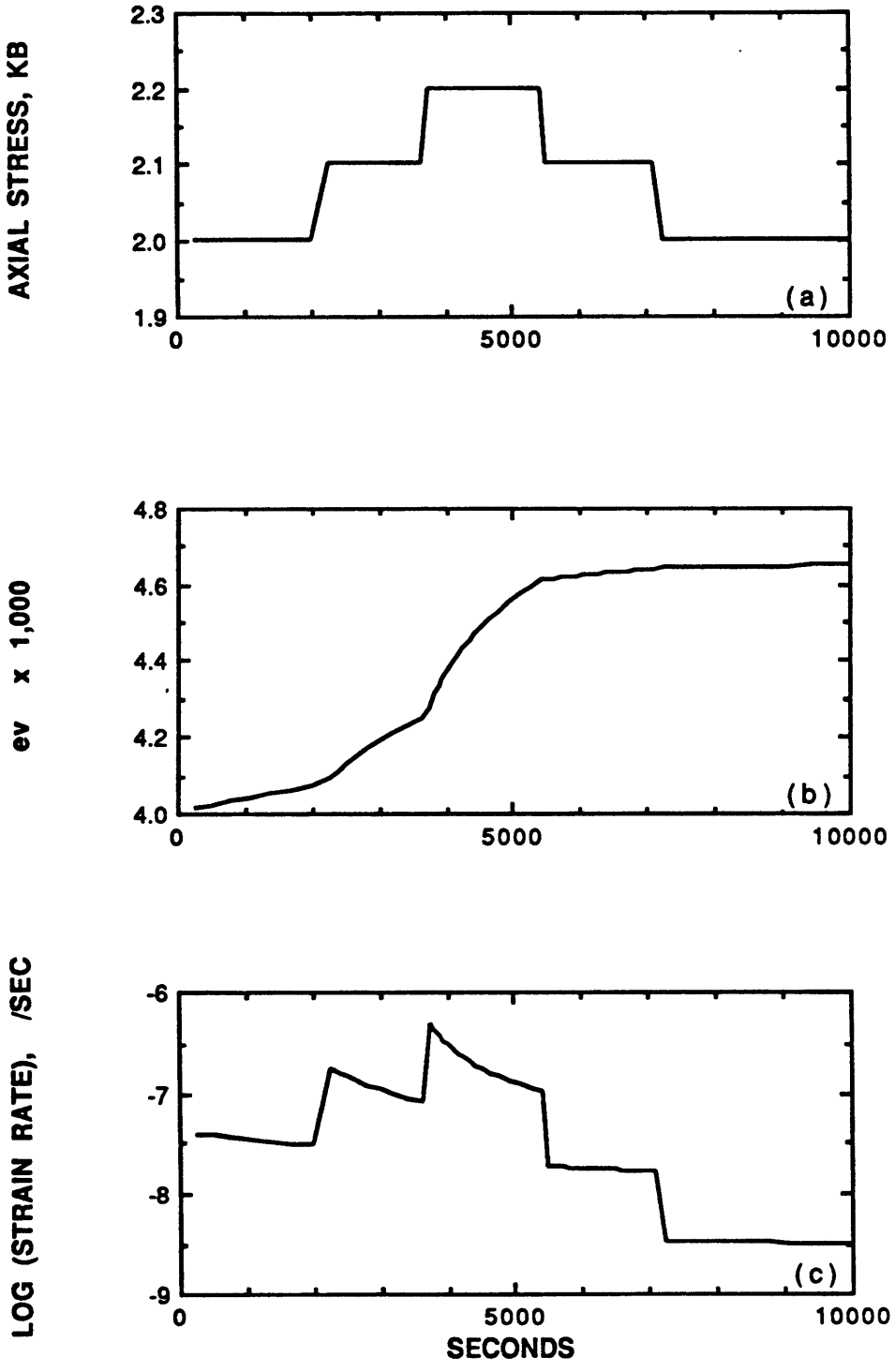
AXIAL STRESS, KB
2.3
2.2
2.1
2.0
1.9
0
5000
10000
(a)
ev x 1,000
4.8
4.6
4.4
4.2
4.0
0
5000
10000
(b)
LOG (STRAIN RATE), /SEC
-6
-7
-8
-9
0
5000
10000
(c)
SECONDS

Figure 3.15

CHAPTER 4

DEVELOPMENT OF ELECTRICAL RESISTIVITY ANISOTROPY DURING DEFORMATION OF GRANITE

abstract. Two triaxial deformation experiments have been conducted on brine-saturated (0.1 and 0.01 M_{aq} KCl) Westerly granite at effective pressures of 100 and 400 bars. Deformation histories included constant strain rate, constant stress and stress relaxation sequences. Complex resistivity, over the frequency range from 10^{-3} to 10^{5} Hz, was measured in both axial and transverse directions during the experiments. Low-frequency-limit resistivity ρ_{DC} increased with initial loading and then decreased steadily after the onset of dilatancy. The initial increase in ρ_{DC} was greatest in the transverse direction, in one experiment reaching a peak contrast $\rho_{DC\perp}/\rho_{DC\parallel} = 1.4$ at approximately 35% peak strength. With continued loading and the resultant opening of microcracks, the resistivity contrast decreased to approximately 0.8 by failure. In terms of the frequency dependence of resistivity, the general form of the real part of the resitivity varied little during deformation other than a uniform change in magnitude proportional to the changes in ρ_{DC}. Under initial hydrostatic stress, the phase angle between current and voltage ranged from 10 to 30 mrad over the frequency range 0.001 to 100 Hz. With the onset of dilatancy, notable changes occured in the phase spectra in the 0.001 to 10 Hz region. The changes differed in the axial and transverse directions and appeared to be the result of changing pore structure since they diminished upon removal of deviatoric stress. Although the variations in complex resistivity were subtle, their occurance in the Earth may be exploited as a means of identifying secular changes in stress or strain through induced polarization or magnetotelluric measurements.

Introduction

Remote measurements of electrical resistivity variations have provided information about the Earth that is not available from direct observation. For example, induced polarization (IP) has proved useful in prospecting for disseminated sulfides as well as other ore bodies (*Madden and Cantwell*, 1967; *Wong*, 1979; *Nelson and Van Voorhis*, 1983). In the field of earthquake prediction, resistivity studies have been used to search

for changes in stress and strain related to earthquakes (*Morrison*, 1978; *Rikitake and Yamazaki*, 1979; *Madden*, 1983; *Park and Lee*, 1988). Magnetotelluric measurements can sample lower crustal resitivity by taking advantage of the earth's naturally occuring electrical currents (*Hermance and Pedersen*, 1980). All of these techniques rely on either spacial or temporal variations in resistivity (for reviews see *Olhoeft*, 1980 and *Parkhomenko*, 1982). In addition, laboratory investigations have proven useful in determining how complex resistivity varies under controlled conditions. Such laboratory studies can provide information to assist in the interpretation of field observations (*Wong*, 1979; *Lockner and Byerlee*, 1986). Variations of ρ_{DC} as a function of confining pressure for a variety of wet rocks have been reported by *Brace et al.* (1965), *Brace and Orange* (1968a) and *Brace* (1971). These studies were extended to include the effects of stress (*Brace and Orange*, 1968b) as well as implications for coseismic changes (*Brace*, 1975). Other investigators (*e.g. Saint-Amant and Strangway*, 1970; *Shahidi et al.*, 1975; *Olhoeft*, 1980; *Lockner and Byerlee*, 1985a,b) have studied the frequency-dependent complex resistivity ρ^* for rock and other geological materials, primarily in connection with low-frequency IP phenomena.

The measurement of resistivity changes, before and during earthquakes, received much attention when *Barsukov* (1970) and *Sadovsky et al.* (1972) reported resistivity changes of more than 10% preceding earthquakes in the Garm region of the U.S.S.R. These findings were followed by reports of similar changes in resistivity before a magnitude 4 earthquake on the San Andreas fault in California (*Mazzella and Morrison*, 1974). However, calculations indicated that such variations should have been accompanied by easily observable uplifts and tilts. In studying resistivity changes related to earthquakes, both active dipole-dipole measurements (*Morrison and Fernandes*, 1986) and passive telluric current measurements (*Madden*, 1983; *Park and Lee*, 1988) have been used. We investigate in this paper the additional possibility of using standard IP techniques to identify temporal variations in stress or strain.

The generalized form of Ohm's law can be expressed as

$$E_i = \rho_{ik} J_k \qquad (4\text{-}1)$$

where E and J are, respectively, electric field intensity and current density. From (4-1) it is recognized that, similar to stress and strain, resistivity is a second rank tensor

quantity. In most field applications, resistivity is considered isotropic so that it can be represented by a scalar value:

$$\rho_{ik} = |\rho| \, \delta_{ik} \tag{4-2}$$

where δ_{ik} is the Kronecker delta. However, for rocks subjected to large deviatoric stress, the orientation of microcracks, which control the resistivity of wet rocks, is highly anisotropic (*Hadley*, 1975; *Tapponier and Brace*, 1976; *Kranz*, 1980). For triaxial experiments, in which $P_2 = P_3 = P_c$, we assume that resistivity can be represented by

$$\rho_{ik} = \rho_{\|} \begin{vmatrix} 1 & 0 & 0 \\ 0 & \beta & 0 \\ 0 & 0 & \beta \end{vmatrix} \tag{4-3}$$

where $\beta = \rho_{\perp}/\rho_{\|}$ represents the contrast in resistivity between directions transverse and parallel to the sample axis. Because of design difficulties, triaxial experiments have typically measured resistivity parallel to the sample axis and therefore the maximum compressive stress direction. From earlier studies under hydrostatic conditions (*Lockner and Byerlee,* 1985a) it was determined that a measureable IP response occured in Westerly granite at frequencies below 100 Hz which was apparently the result of microcrack-pore fluid interactions. It was decided that a comparison of IP response for parallel and transverse directions might provide differences that could be related to microcrack anisotropy. The results of these measurements are reported here.

Experimental

Two orthorhombic samples were prepared from a block of Westerly granite. Sample dimensions were 50.8 x 50.8 x 114 mm. The unusual square-cross-sectioned samples were chosen to simplify electric field shape as well as electrode geometry for the transverse measurements. However, in retrospect, the more common cylindrical sample geometry would probably have been a better choice. Axial and transverse foil strain gages were applied directly to the surface of the sample and coated with a silicone sealant to isolate them from the pore fluid (Fig. 4.1). Ag/AgCl electrodes were prepared by depositing AgCl on silver screens. Since complex resistivity measurements require a four electrode geometry, electrode assemblies in the transverse direction consisted of sample/electrode/frit/electrode/frit. Electrode assemblies in the axial direction consisted of sample/electrode/frit/electrode/fused silica. Frits were machined pieces of Coors AHP99 porous ceramic. This material is 99% Al_2O_3 bonded with a boro-silicate glass containing no Mg or Ca and has a porosity of 28%. It is strong enough to support the differential stresses applied to the sample column. To isolate the sample assembly from the silicone oil confining fluid, all external surfaces were covered with pieces of 3.2 mm-thick vinyl which were sealed with vinyl cement. This proved to be a difficult task and is not recommended for future experiments. All electrode and strain gage leads were brought out through the vinyl jacket and out of the pressure vessel by means of electrically insulated feed-throughs. For the first experiment (P_c = 200 bars), electrolyte contained 0.01 M_{aq} KCl, saturated with AgCl to prevent stripping of electrodes, to give an electrolyte resistivity of approximately 5 ohm-m. For the second experiment (P_c = 600 bars), electrolyte was 0.1 M_{aq} KCl, again saturated with AgCl, for a resistivity of 0.7 ohm-m. Due to the large thermal coefficient of the electrolyte resistivity, experiments were conducted in a controlled temperature chamber at 30.0 ± 0.1 °C. Constant confining pressure and pore pressure were maintained throughout each experiment by means of an automated computer control system. A small stainless steel pore fluid reservoir was connected to the bottom of the sample to reduce pore pressure variations which might result from rapid changes in sample pore volume during the experiments as well as to aid in flushing the sample of residual salts. Total axial displacement was monitored with an external DCDT displacement transducer attached

to the piston assembly. Axial force was measured in the first experiment with an external load cell and in the second experiment with an internal strain gage bridge. All pressures, displacements and strains were sampled once a second using a 16-bit A/D converter.

The system used to measure complex resistivity is described in *Lockner and Byerlee* (1985a). For frequencies above 100 Hz, a two electrode system was in which the inner electrode pair was connected, in sequence to a Hewlett Packard 4275A (10 kHz to 1 MHz) and a 4274A (100 Hz to 100 kHz) LCR meter. These instruments are designed to determine sample impedance at discrete frequencies (three samples per decade). At low frequency (10^{-3} to 10^{2} Hz), a four-electrode system was employed as shown in Fig. 4.2b. A 1-V peak-to-peak sine wave was used as an excitation signal (LCR meters were also set at this supply voltage). This resulted in a current density of order 10^{-3} amp/m^2. The voltage drop across the sample was sensed with a high input impedance (>3 x 10^{8} ohms) instrumentation amplifier. To determine current, a precision decade resistor was placed in series with the sample. Voltage drop across the resistor was also measured and, by knowing the resistance, was converted to current. By sampling voltage and current over a full cycle, both magnitude and phase of the sample impedance were determined.

To saturate the sample, the sample assembly was placed in the pressure vessel and evacuated for a minimum of 4 hr. Pore fluid was then forced into the sample at the desired run pressure (100 bars in the first experiment and 200 bars in the second). This was continued for at least 3 days, until fluid ceased to enter the sample. Once it was determined that the sample was satisfactorily saturated, the piston was advanced to make contact and the experiment was begun.

Precision of pore pressure, confining pressure and axial stress measurements were respectively 0.1, 0.1 and 0.2 bars. Precision of axial displacement was 0.3 μm. Sensitivity of strain gage measurements was 1 μstr, although due to temperature fluctuations, long-term resolution was approximately 10 μstr. In measuring sample impedance, cable effects were measured using a dummy sample and were then automatically corrected for. However, these correction were not complete, as can be seen by a small offset in phase angle where the high and low frequency systems overlap at 100 Hz. Since capacitive effects roll off as $1/\omega$, this error should be insignificant below about 10 Hz. Using the manufacturer's specifications for the LCR

meters and assuming 0.025% sampling error for the low-frequency measurements (12-bit A/D resolution) nominal errors in sample impedance determinations are as follows: for limpedancel, ± 0.3 to ± 3% (> 100 Hz) and ± 0.03 to ± 0.05% (< 100 Hz). Errors in measuring phase angle ϕ range from ± 1.0 to ± 18.0 mrad (> 100 Hz) and from ± 0.3 to ± 1.0 mrad (< 100 Hz). To convert sample impedance to resistivity, a correction factor due to the test geometry must be determined. For resistivity parallel to the sample axis, the geometric factor is known to approximately 0.3%. However, no correction is made due to sample deformation due to load. This results in axial resistivity being systematically underestimated by as much as 4%. Larger errors exist in converting transverse impedance to resistivity. In the case of the axial measurement, electric field lines are essentially parallel. However, because of electrode geometry, field lines in the transverse measurements diverge from one electrode and converge at the other. In addition, there is a small leakage current to the top end plug. To analyze these geometric effects, a 2D finite difference model of the sample was developed. Various value of $\beta = \rho_{\perp}/\rho_{\parallel}$ were used as input and the corresponding apparent sample resistance was determined. The resultant equi-potential lines for $\beta = 1$ are plotted in Fig. 4.3a. Notice the distortions of the eqi-potential lines near the top end plug due to the leakage current. For laminar current flow in the x-y plane, resistance R_X can be normalized by resistivity: $\mathbf{R_X} = R_X w/\rho$ where $\mathbf{R_X}$ is non-dimensional resistance and w is the sample width in the z-direction. β is plotted as a function of $\mathbf{R}_{\perp}$ in Fig. 4.3b, along with a quadratic fit (solid line). This results in the empirical relation:

$$\beta = -0.01 + 0.321\,(R_{\perp}w/\rho_{\parallel}) + 0.225\,(R_{\perp}w/\rho_{\parallel})^2\,. \qquad (4\text{-}4)$$

Then, $\rho_{\perp}$ is computed from β and $\rho_{\parallel}$. β and $\rho_{\perp}$ are known to approximately 5%.

The first experiment was run at P_p = 100 bars and P_c = 200 bars. Differential stress and axial displacement are plotted *vs* time in Fig. 4.4. P_{dif} was increased slowly to 2.3 kb and then held constant. After approximately 6,000 s of creep, strain rate was accelerating and the sample approaching failure. At this point, axial displacement was held constant and the stress was allowed to relax. When the differential stress had dropped to 2.05 kb, a through-going fault formed which intersected both transverse electrodes. This resulted in a sudden stress drop to 0.92 kb. Real resistivity at 10 Hz, which will be refered to as ρ_{DC} is plotted in Fig. 4.4b. Note that $\rho_{DC\perp}$ is somewhat greater than $\rho_{DC\parallel}$ during the creep portion of the experiment but quickly drops as the through-going fracture forms. This is expected since the fracture provided a low-resistance path between the transverse electrodes. As is common in low confining pressure experiments, the fracture formed at a steep angle and, in fact, intersected both end pieces. However, it is noteworthy that a large directional resistivity contrast developed well before the main stress drop, presumably in response to the development of a large scale dilatant zone. Following the stress drop, this resistivity contrast disappeared.

Time histories for the second experiment, which lasted 11 days, are shown in Fig. 4.4. This experiment was conducted at P_p = 200 bars and P_c = 600 bars. Following an initial loading phase, in which differential stress reached 3.32 kb, the sample was deformed at an axial displacement rate of 1.1 x 10^{-6} mm/s for a nominal strain rate of 1 x 10^{-8} s^{-1}. Since a significant fraction of this displacement was accomodated by elastic shortening of the piston, the true axial strain rate of the sample averaged 0.6 x 10^{-8} s^{-1}. The strain gage readings (Fig. 4.5b) show a gradual increase in volumetric strain rate over the course of the experiment, culminating in an abrupt acceleration in strain. The sample was unloaded and the experiment ended before a macroscopic fault was formed. The raw 10 Hz sample resistances, uncorrected for geometry, are plotted in Fig. 4.5c. The directional resistivity contrast β is plotted in Fig. 4.5d and the corresponding resistivity values are shown in Fig. 4.6. Resistivity is replotted as a function of differential stress in Fig. 4.7. In the initial loading stage of the experiment, both resistivity and β showed a rapid increase, peaking at approximately 35% failure

strength. $\rho_{DC\parallel}$ increased by approximately 50% which agrees well with results from *Brace and Orange* (1968b). The subsequent steady decrease in $\rho_{DC\parallel}$ to 38% of the peak resistivity by failure is less than the values reported by Brace and Orange (15 - 20%). However, their granite experiments were conducted at 2 to 4.5 kb confining pressure and showed a trend to greater resistivity changes at higher confining pressure. Since beginning crack populations are more completely closed at higher confining pressure, opening of cracks during the dilatant stage will lead to a relatively larger drop in resistivity at high confining pressure. This effect could explain the observed trend. In our experiment, the transverse resistivity increased more rapidly than axial resistivity during the initial loading. The peak contrast was $\beta = 1.4$. In the initial loading phase, cracks oriented normal to the loading axis are preferentially closed. These cracks are more important to conduction paths for transverse resistivity than for axial resistivity. Consequently, it is reasonable to expect their closure to have a greater effect on $\rho_{DC\perp}$ than on $\rho_{DC\parallel}$.

As shown in Fig. 4.5, the drop in resistivity corresponds to the onset of dilatancy. This is expected since the decrease in resistivity must be the result of new and/or more efficient pathways appearing in the rock. Since these new pathways have a preferred orientation parallel to the sample axis, we might expect them to contribute more effectively to axial conduction than to transverse conduction. However, this does not appear to be the case, since β rapidly drops to about 0.80. *Madden* (1976) considered the effect of anisotropy on conductivity of embedded networks. He pointed out that due to the strong interrelationship between flow paths in different directions, large anisotropies on a microscopic scale tend to result in much smaller anisotropy of bulk properties. This effect appears to play a significant role in the resistivities of the present samples. However, the fact that the anisotropy actually reverses sense with the growth of axial cracks requires some additional explanation. Both theoretical and laboratory studies of crack interactions (*e.g. Segall and Pollard*, 1980; *Horii and Nemat-Nasser*, 1985) indicate that until crack densities become large, axial cracks tend not to link up. Thus, new axial crack growth may not be effecient at increasing connectivity for flow in the axial direction. At the same time, these same cracks have finite width and are typically outgrowths of existing cracks. Thus they are guaranteed to contribute to lateral conduction. This could provide an explanation for the observed results. If it is correct, we could expect that in the very final stage of crack growth, in which crack density is

large enough to force cracks to interconnect, β should increase. If such a phenomenon occurs however, it is not observable in the present data (Fig. 4.6b).

Complex Resistivity

We next turn our attention to the full frequency-dependent complex resistivity measurements. The real component of the axial resistivity data ρ' is plotted as a function of frequency in Fig. 4.8a. The labels on individual curves correspond to the times indicated in Fig. 4.5. Phase angle $-\phi$ by which current leads voltage is plotted in Fig. 4.8b. The sharp roll off in ρ' and the corresponding increase in $-\phi$ above 1kHz are the result of relaxation mechanisms at the rock-water interfaces and represent a transition from resistive to dielectric behavior. Since the time constant for this relaxation is proportional to $R_{DC||}$, the transition shifts to higher frequency as $R_{DC||}$ decreases. The offset in phase angle at 100 Hz is the result of inadequate removal of cable effects for the high frequency measurements. Since the capacitive effects roll off as $1/\omega$, these errors should not be significant below about 10 Hz. In the low-frequency portion of the spectrum, the gradual decrease in ρ' with increasing frequency is the result of a broadly distributed set of relaxation mechanisms. This effect is also indicated by the relatively featureless but significant phase angle of about 10 mrad in the hydrostatic data (1 degree = 17.45 mrad). Since Westerly granite contains almost no minerals that can contribute to faradaic or surface exchange reactions, we attribute this low-level IP response to interactions of the microcrack surface double layers. Interpreted in this manner, the broad low-frequency distribution reflects a distribution in microcrack dimensions. The gradual decrease in ρ' with frequency is quantified by the IP parameter Percent Frequency Effect (PFE), defined as the percent decrease in ρ' per decade in frequency. The hydrostatic data give PFE = 1.4.

The transverse complex resistivity data is shown in Fig. 4.9. The real component of resistivity ρ' shows all of the same trends that were observed in $\rho'_{||}$. Notice that curve 'A' has increased above the hydrostatic resistivity, reflecting the trend in the early DC resistivity data. The phase plot (Fig. 4.9b) shows a phase content in the 0.01 to 100 Hz range that is not observed in the axial data. This is true even for the hydrostatic data, which, for an isotropic material, cannot occur. At this time, we have no explanation for this phase response, and must accept the possibility that it indicates a problem in the test

configuration. As a result, the transverse phase results cannot be treated with full confidence.

The most interesting feature in the complex resistivity data is the progressive variation in low-frequency phase angle during the experiment. This is shown in detail in Figs. 4.10 through 4.12. The initial loading of the sample is accompanied by a general loss in low-frequency phase content in both the axial and transverse directions (Fig. 4.10). In addition, the transverse phase shows the development of a peak at 0.4 Hz. This is followed (Fig. 4.11) by the development of a similar peak in the axial phase spectrum at 0.01 Hz. A similar, though less convincing peak, was observed in axial resistivity measurements for Westerly granite in creep (*Lockner and Byerlee*, 1986) and is reproduced in Fig. 4.13. In that experiment, a lower electrolyte salt concentration was used, resulting in an overall increased phase response. Since a decrease in electrolyte concentration has the effect of expanding the surface double layer width, the differences in the phase response in these two experiments suggest an intriguing area for future research. The newly-formed peaks in the phase spectra persist until failure (Fig. 4.12). When the sample was unloaded and returned to hydrostatic pressure (Fig. 4.12), the axial phase spectrum recovered its pre-stressed value above 0.1 Hz, although at lower frequencies, almost no recovery occured. This may reflect the partial closure of cracks to create short length scale restrictions in the current paths. In a similar fashion, the transverse phase spectrum recovered at frequencies above about 0.01 Hz. One interesting aspect of the phase response is that the modified spectra that developed during the dilatant stage of the experiment showed no additional change as the sample approached failure. In this sense, ρ' responded primarily to strain while phase angle responded mainly to stress. The emergence of a peak in the axial phase spectrum at 0.01 Hz is interperted as resulting from the development of a characteristic length in the network of conduction paths. If a diffusion mechanism were responsible for this peak, the diffusion length scale can be estimated by assuming a relation of the form $L^2 \approx 2Dt$. Then a diffusion coefficient of $D_{Cl^-} = 2 \times 10^{-5}$ cm^2/s and t = 50 s (one-half the period) suggests a characteristic length of approximately 0.4 mm. This is on the order of the mean grain size for Westerly granite. In a similar manner, the peak in the transverse phase spectrum at 0.4 Hz would yield a characteristic length scale of 0.07 mm. While additional information is required to have confidence in this interpretation, these values do suggest that measurement of the phase spectra is providing information about the

development of the microcrack structure in the rock. Although the variations in phase angle are on the order of only 10 mrad, they would be observable by high-quality IP field measurements. As a result, it may be possible to use this phenomenon to monitor secular changes in microcrack geometry as part of an earthquake prediction program. The technique may also have application as a well logging tool for inferring down-hole stress orientation.

References

Barsukov, O. M., Relationship between the electrical resistivity of rocks and tectonics processes, *Bull. (Isv) Acad. Sci. U.S.S.R., Earth Physics, 1,* 55, 1970.

Brace, W. F., Resistivity of saturated crustal rocks to 40 km based upon laboratory measurements, in *The Structure and Physical Properties of the Earth's Crust, Geophys. Monogr. Ser., 14,* edited by J. G. Heacock, 243-255, AGU, Washington, D. C., 1971.

Brace, W. F., Dilatancy related electrical restivity changes in rocks, *Pure Appl. Geophy., 113,* 207-217, 1975.

Brace, W. F., A. S. Orange and T. R. Madden, The effect of pressure on the electrical resistivity of water-saturated crystalline rocks, *J. Geophys. Res., 70,* 5669-5678, 1965.

Brace, W. F. and A. S. Orange, Electrical resistivity changes in saturated rocks during fracture and frictional sliding, *J. Geophys. Res., 73,* 1433-1445, 1968a.

Brace, W. F. and A. S. Orange, Further studies of the effects of pressure on electrical resistivity of rocks, *J. Geophys. Res., 73,* 5407-5420, 1968b.

Hadley, K., Dilatancy: further studies in crystalline rocks, Ph.D. Thesis, Mass. Inst. Tech., Cambridge, Ma, 1975.

Hermance, J. F. and J. Pedersen, Deep structure of the Rio Grande Rift: a magnetotelluric interpretation, *J. Geophys. Res., 85,* 3899-3912, 1980.

Horii, H. and S. Nemat-Nasser, Compression-induced microcrack growth in brittle solids: axial splitting and shear failure, *J. Geophys. Res., 90,* 3105-3125, 1985.

Kranz, R. L., The effects of confining pressure and stress difference on static fatigue of granite, *J. Geophys. Res., 85,* 1854-1866, 1980.

Lockner, D. A. and J. D. Byerlee, Complex resistivity measurements of confined rock, *J. Geophys. Res., 90,* 7837-7847, 1985a.

Lockner, D. A. and J. D. Byerlee, Complex resistivity of fault gouge and its significance for earthquake lights and induced polarization, *Geophys. Res. Lett., 12,* 211-214, 1985b.

Lockner, D. A. and J. D. Byerlee, Changes in complex resistivity during creep in granite, *Pure Appl. Geophys., 124,* 659-676, 1986.

Madden, T. R., Random networks and mixing laws, *Geophys., 41,* 1104-1125, 1976.

Madden, T. R., High sensitivity monitoring of resistivity and selfpotential variations in the Hollister and Palmdale areas for earthquake prediction studies, in*Summaries of Technical Reports,* vol. *17,* 355-358, *Open File Rep. 83-918,* National Earthquake Hazards Reduction Program, U.S. Geological Survey, Washington, D.C.,1983.

Madden, T. R. and R. Cantwell, Induced polarization, a review, *Min. Geophys., 2,* 373-400, 1967.

Mazzella, A. and H. F. Morrison, Electrical resistivity variations associated with earthquakes on the San Andreas fault, *Science, 185,* 855-857, 1974.

Morrison, H. F., The study of temporal resistivity variations on the San Andreas fault, in*Summaries of Technical Reports,* vol. *6,* 250-251, National Earthquake Hazards Reduction Program, U.S. Geological Survey, Washington, D.C.,1978.

Morrison, H. F. and R. Fernandes, Temporal variations in the electrical resistivity of the Earth's crust, *J. Geophys. Res., 91,* 11618-11628, 1986.

Nelson, P. and G. Van Voorhis, Estimation of sulfide content from induced polarization data, *Geophys., 48,* 62-75, 1983.

Olhoeft, G. R., Electrical properties of rocks, in *Physical Properties fo Rocks and Minerals,* edited by Y. S. Touloukian, W. R. Judd, and R. F. Roy, McGraw-Hill, New York, 1980.

Park, S. K. and T. C. Lee, Variations in electrical properties induced by stress along the San Andreas fault at Parkfield, California, in*Summaries of Technical Reports,* vol. *27,* 242-244, *Open File Rep. 88-673,* National Earthquake Hazards Reduction Program, U.S. Geological Survey, Washington, D.C.,1988.

Parkhomenko, E. I., Electrical resistivity of minerals and rocks at high temperature and pressure, *Rev. Geophys. Space Phys., 20,* 193-218, 1982.

Rikitake, T. and Y. Yamazaki, A resistivity precursor of the 1974 Izu-Hanto-Oki earthquake, *J. Phys. Earth, 27,* 1-6, 1979.

Sadovsky, M. A., I. L. Nersesov, S. K. Nigmatullaev, L. A. Latynina, A. A. Lukk, A. N. Semenov, I. G. Simbireva and V. I. Ulomov, The processes preceeding strong earthquakes in some regions of Middle Asia, *Tectonophysics, 14,* 295-307, 1972.

Saint-Amant, M. and D. W. Strangway, Dielectric properties of dry, geological materials, *Geophysics, 35,* 624-645, 1970.

Segall, P. and D. Pollard, Mechanics of discontinuous faults, *J. Geophys. Res., 85,* 4337-4350, 1980.

Shahidi, M., J. B. Hasted and A. K. Jonscher, Electrical properties of dry and humid sand, *Nature, 258,* 596-597, 1975.

Tapponnier, P. and W. F. Brace, Development of stress-induced microcracks in Westerly granite, *Int. J. Rock Mech. Min. Sci., 13,* 103-113, 1976.

Wong, J., An electrochemical model of the induced-polarization phenomenon in disseminated sulfide ores, *Geophysics, 44,* 1245-1265, 1979.

Figure Captions

Figure 4.1 Sample column assembly for complex resistivity measurements.

Figure 4.2 Schematic diagram of resistivity measurement system. Upper diagram is for high-frequency measurements (10^2 - 10^6 Hz) using two-electrode technique. Lower diagram is for low-frequency measurements (10^{-3} - 10^2 Hz) using four-electrode technique.

Figure 4.3 a) Eqi-potential surfaces for finite-difference model of sample geometry using a directional resistivity contrast $\beta = 1$. b) Relation between b and non-dimensional apparent sample resistance as determined by the difference model.

Figure 4.4 Time plot for experiment at $P_p = 100$ bars, $P_c = 200$ bars; a) differential stress and axial displacement b) axial and transverse resistivity at 10 Hz.

Figure 4.5 Time plot for experiment at $P_p = 200$ bars, $P_c = 600$ bars; a) differential stress and axial displacement b) strain gage outputs c) uncorrected axial and transverse sample resistances at 10 Hz d) computed directional resistivity contrast.

Figure 4.6 10 Hz resistivity plots for 600 bar confining pressure experiment.

Figure 4.7 10 Hz resistivity plotted as a function of differential stress for 600 bar confining pressure experiment.

Figure 4.8 Complex resistivity for 600 bar confining pressure experiment. Labels on curves refer to times shown in Fig. 4.5. a) Real component of axial resistivity b) phase angle.

Figure 4.9 Complex resistivity for 600 bar confining pressure experiment. Labels on curves refer to times shown in Fig. 4.4. a) Real component of transverse resistivity b) phase angle.

Figure 4.10 Low-frequency phase plots for 600 bar confining pressure experiment. Times are shown in Fig. 4.5.

Figure 4.11 Low-frequency phase plots for 600 bar confining pressure experiment. Times are shown in Fig. 4.5.

Figure 4.12 Low-frequency phase plots for 600 bar confining pressure experiment. Times are shown in Figs. 4.5 and 4.6.

Figure 4.13 Low-frequency phase plot for axial resistivity during initial stage of creep experiment on Westerly granite at P_c = 50 bars, P_p = 100 bars and P_{dif} = 1,600 bars (from *Lockner and Byerlee,* 1986).

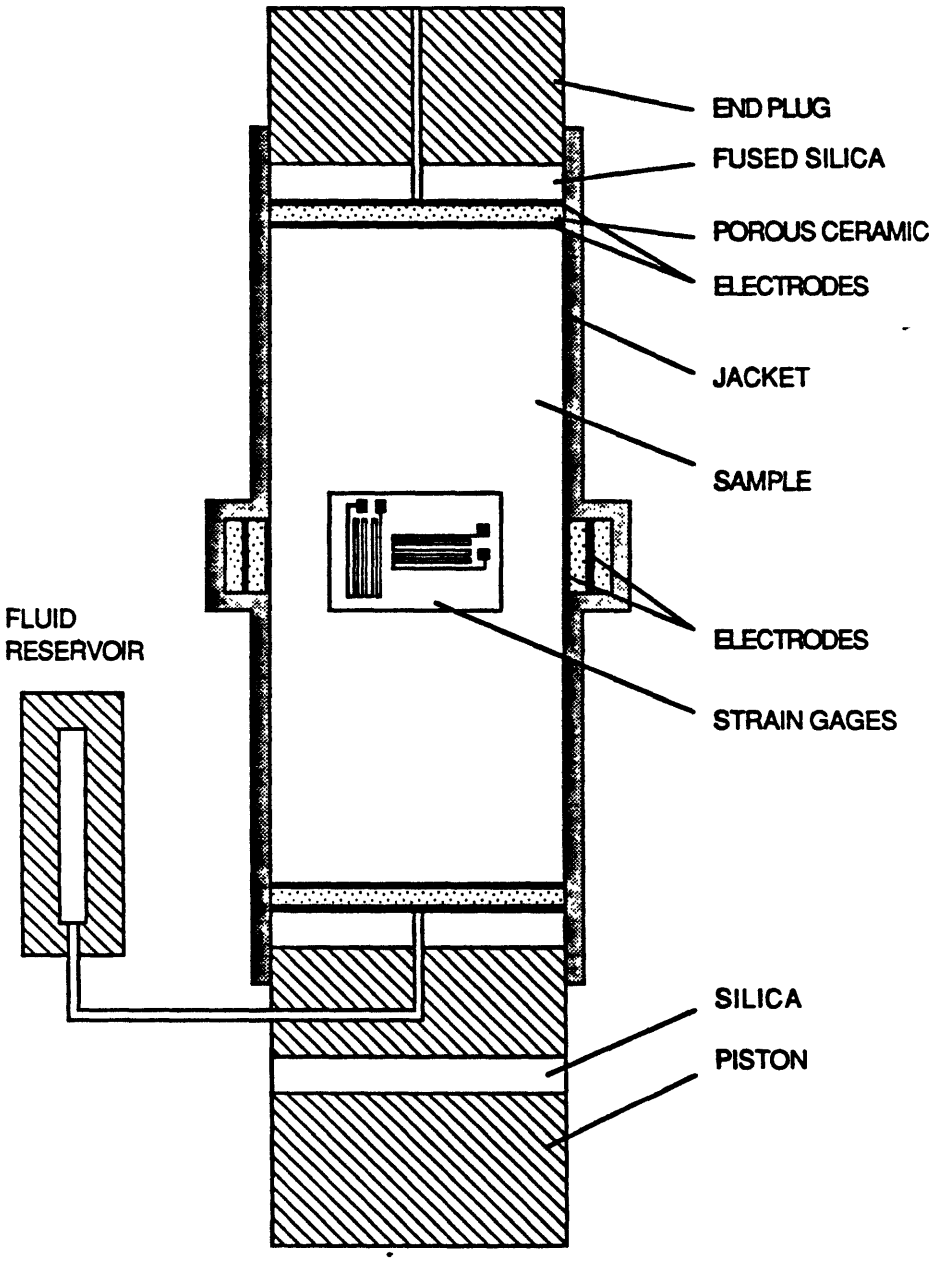
END PLUG
FUSED SILICA
POROUS CERAMIC
ELECTRODES
JACKET
SAMPLE
ELECTRODES
STRAIN GAGES
FLUID
RESERVOIR
SILICA
PISTON

Figure 4.1

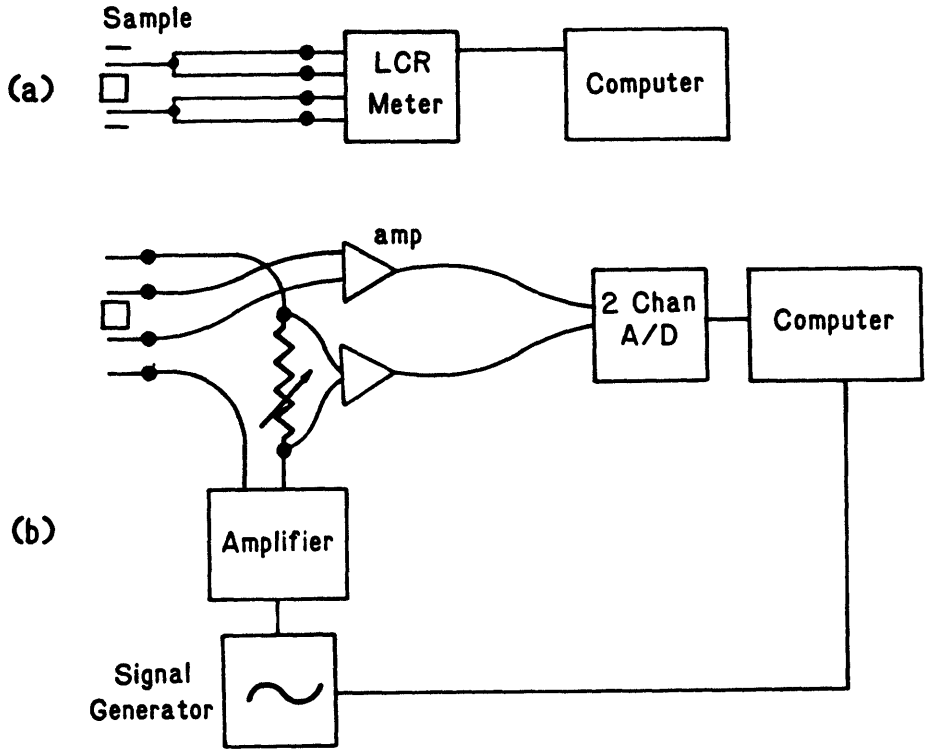
(a)
Sample
LCR
Meter
Computer
(b)
amp
2 Chan
A/D
Computer
Amplifier
Signal
Generator

Figure 4.2

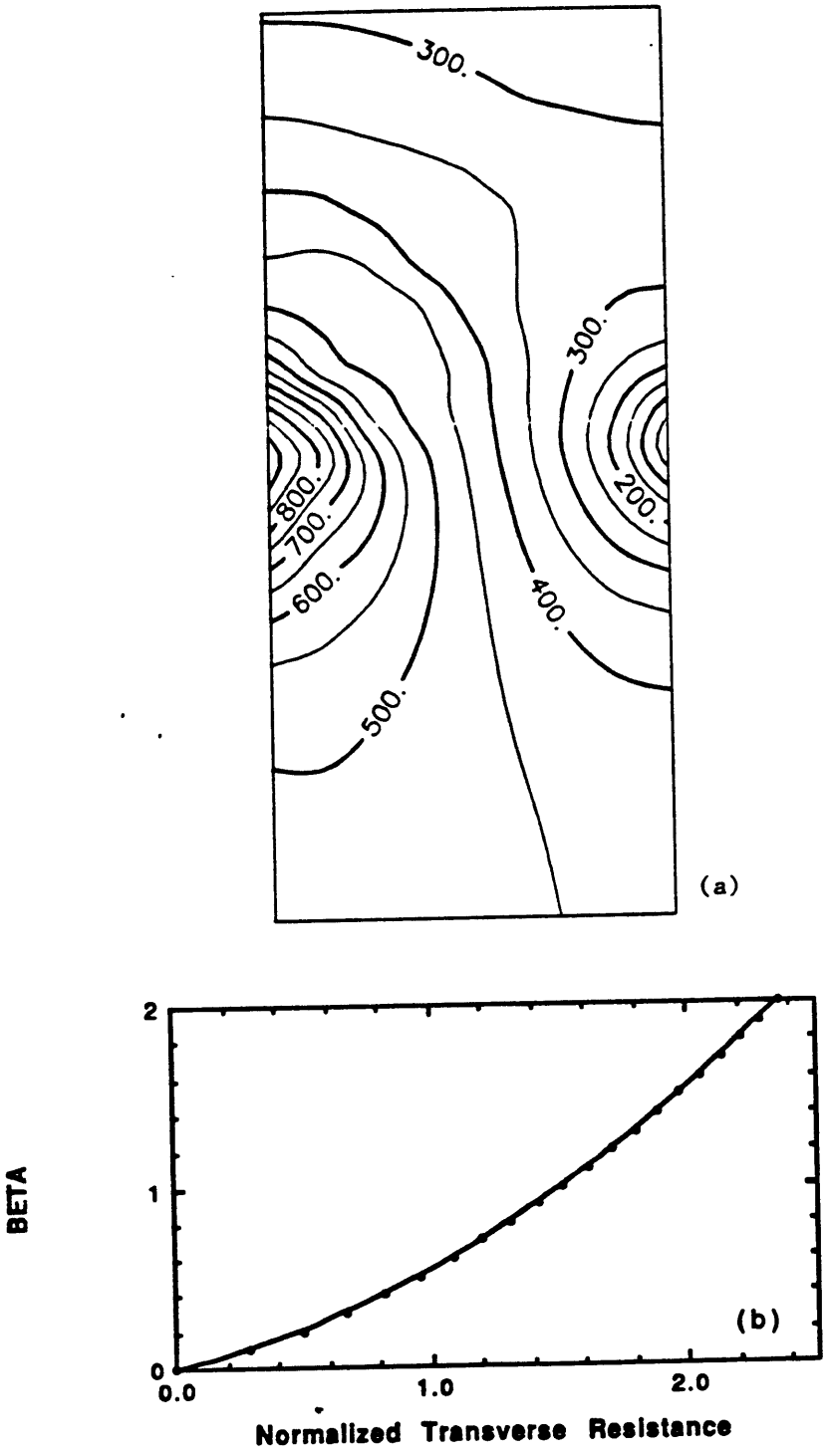
300.
300.
800.
700.
600.
500.
400.
200.
(a)
BETA
2
1
0
0.0
1.0
2.0
(b)
Normalized Transverse Resistance

Figure 4.3

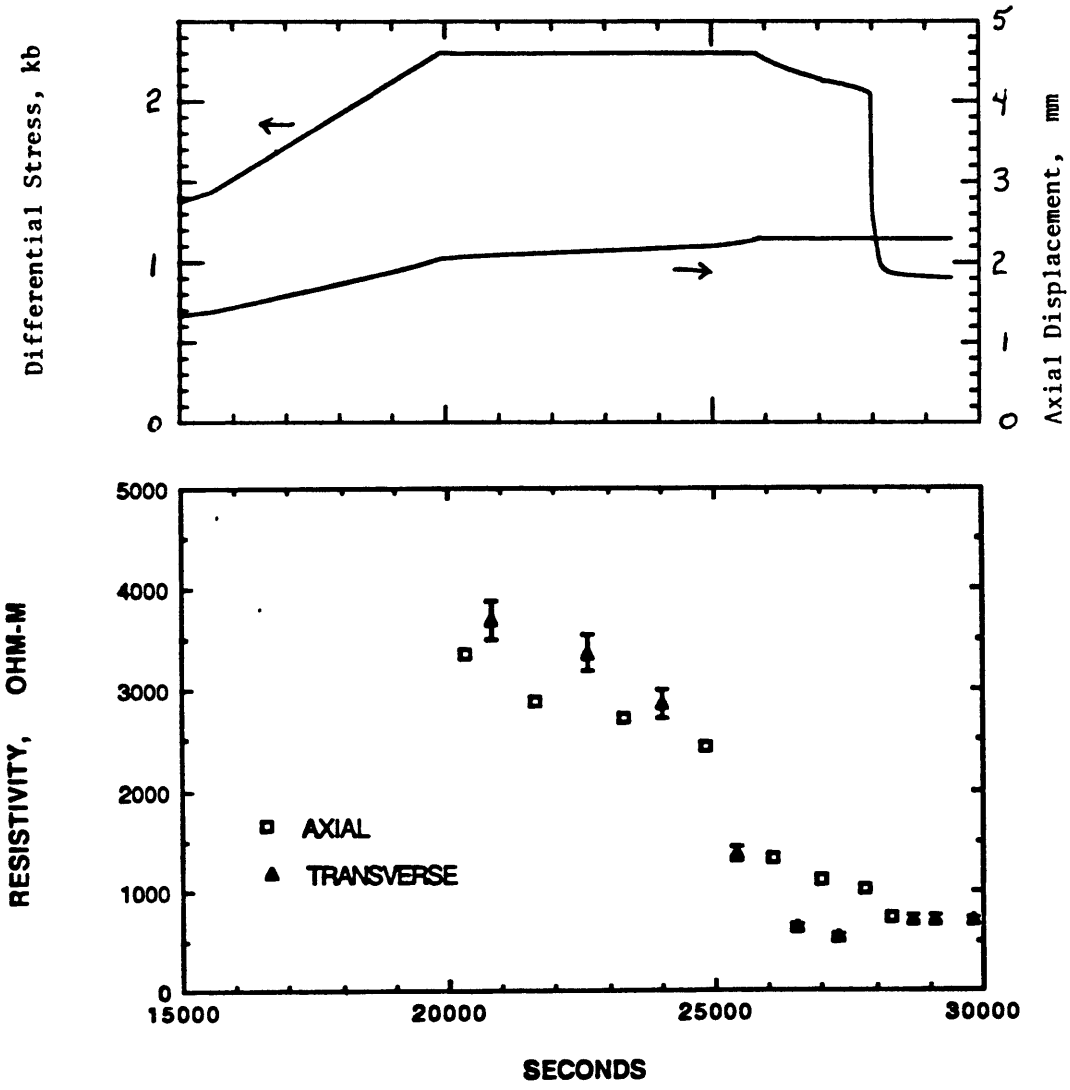
Differential Stress, kb
Axial Displacement, mm
RESISTIVITY, OHM-M
AXIAL
TRANSVERSE
SECONDS

Figure 4.4

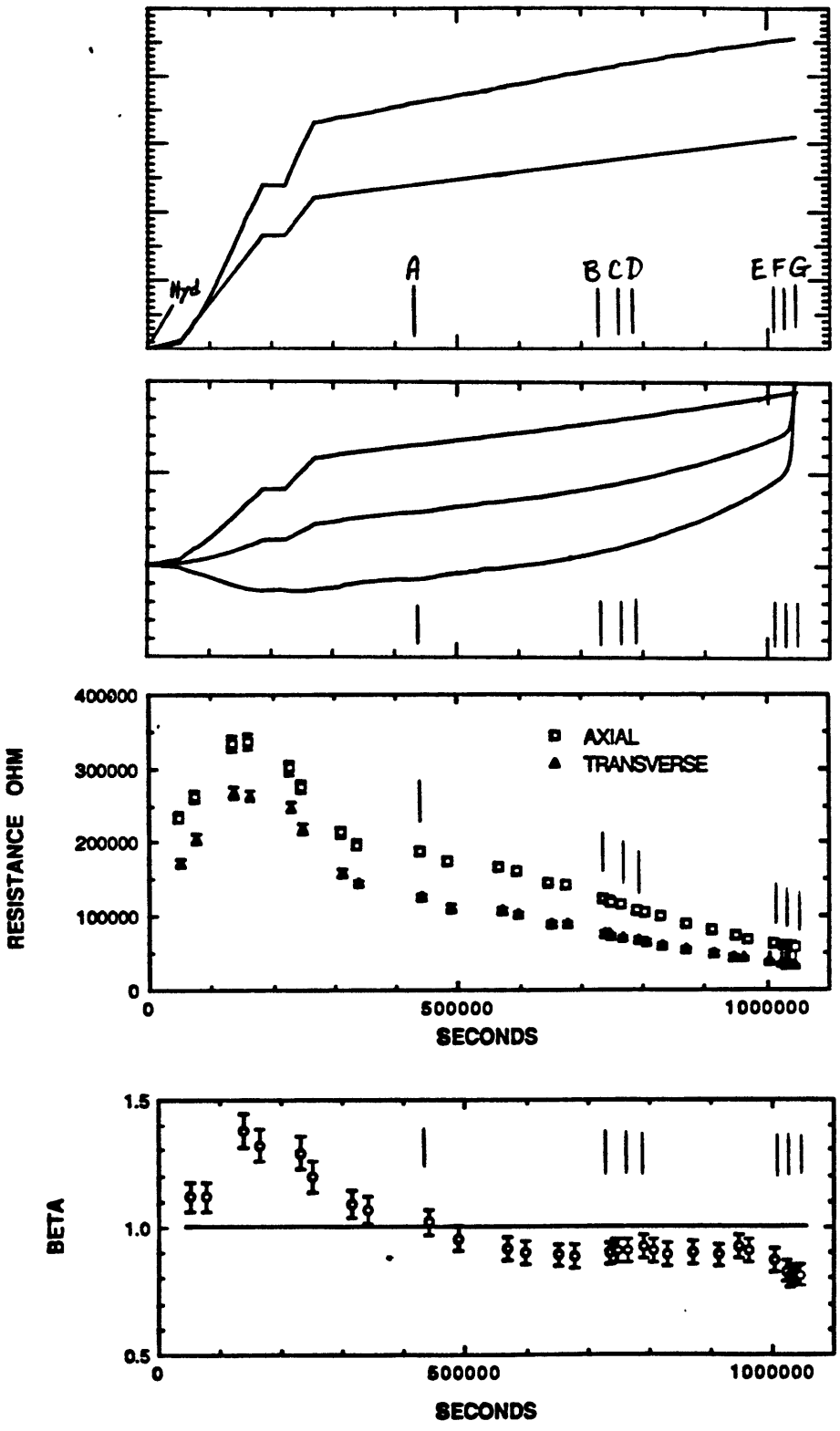
Hyd
A
B C D
E F G
RESISTANCE OHM
400000
300000
200000
100000
0
AXIAL
TRANSVERSE
0
500000
1000000
SECONDS
BETA
1.5
1.0
0.5
0
500000
1000000
SECONDS

Figure 4.5

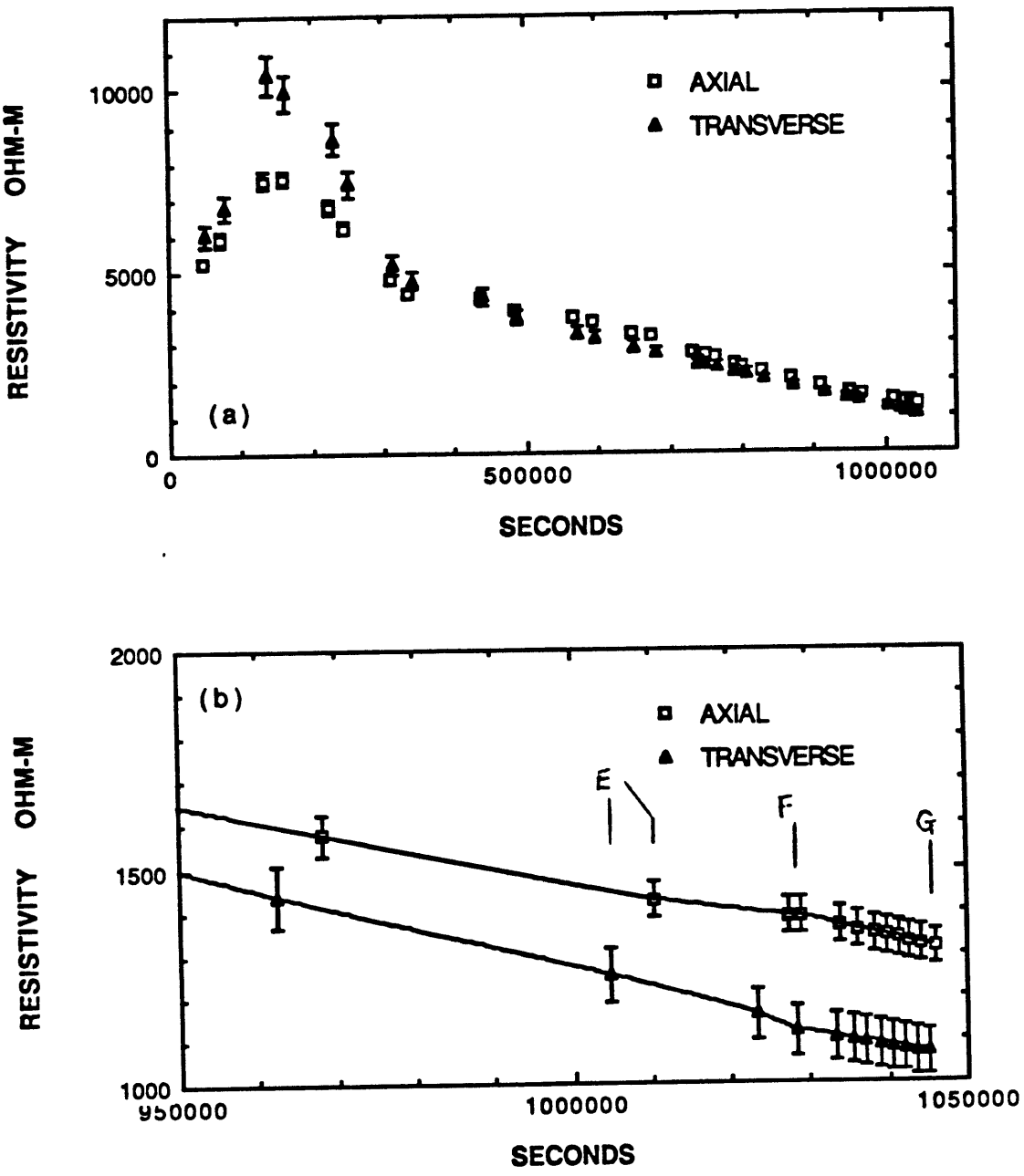
RESISTIVITY OHM-M
10000
5000
0
(a)
AXIAL
TRANSVERSE
0
500000
1000000
SECONDS
RESISTIVITY OHM-M
2000
1500
1000
(b)
AXIAL
TRANSVERSE
E
F
G
950000
1000000
1050000
SECONDS

Figure 4.6

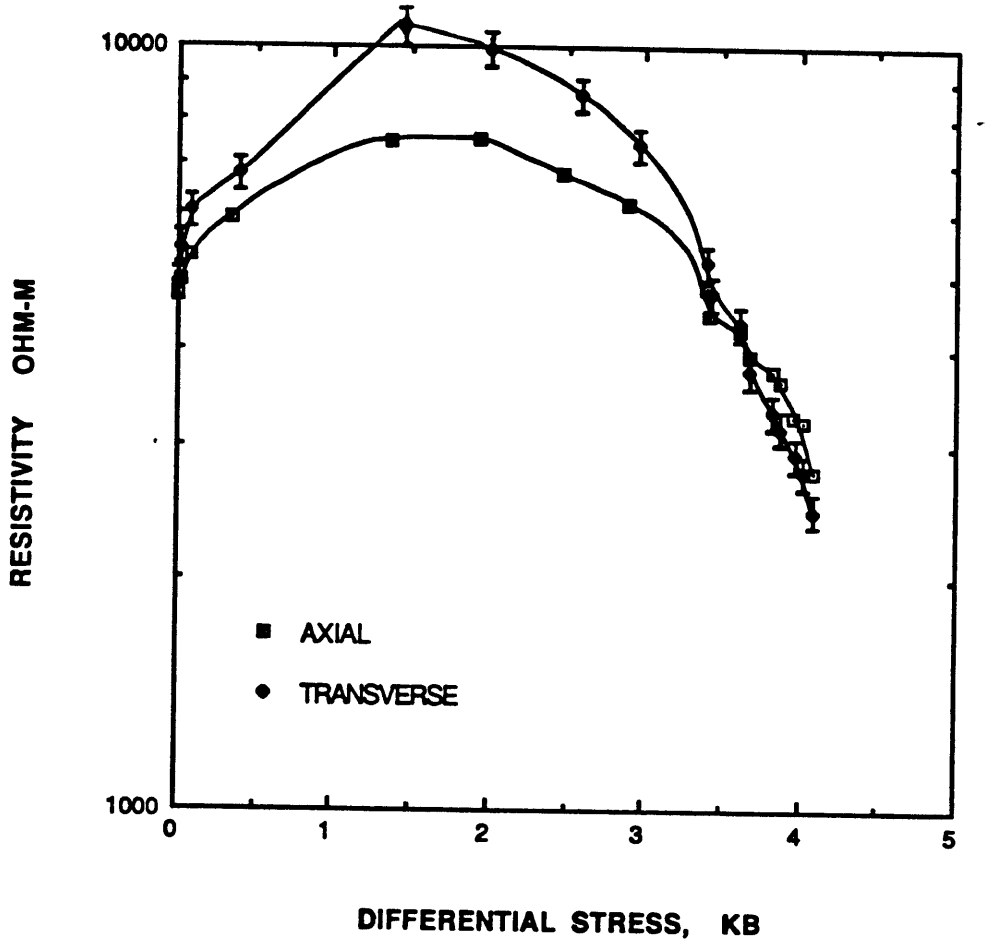
10000
1000
RESISTIVITY OHM-M
AXIAL
TRANSVERSE
0
1
2
3
4
5
DIFFERENTIAL STRESS, KB

Figure 4.7

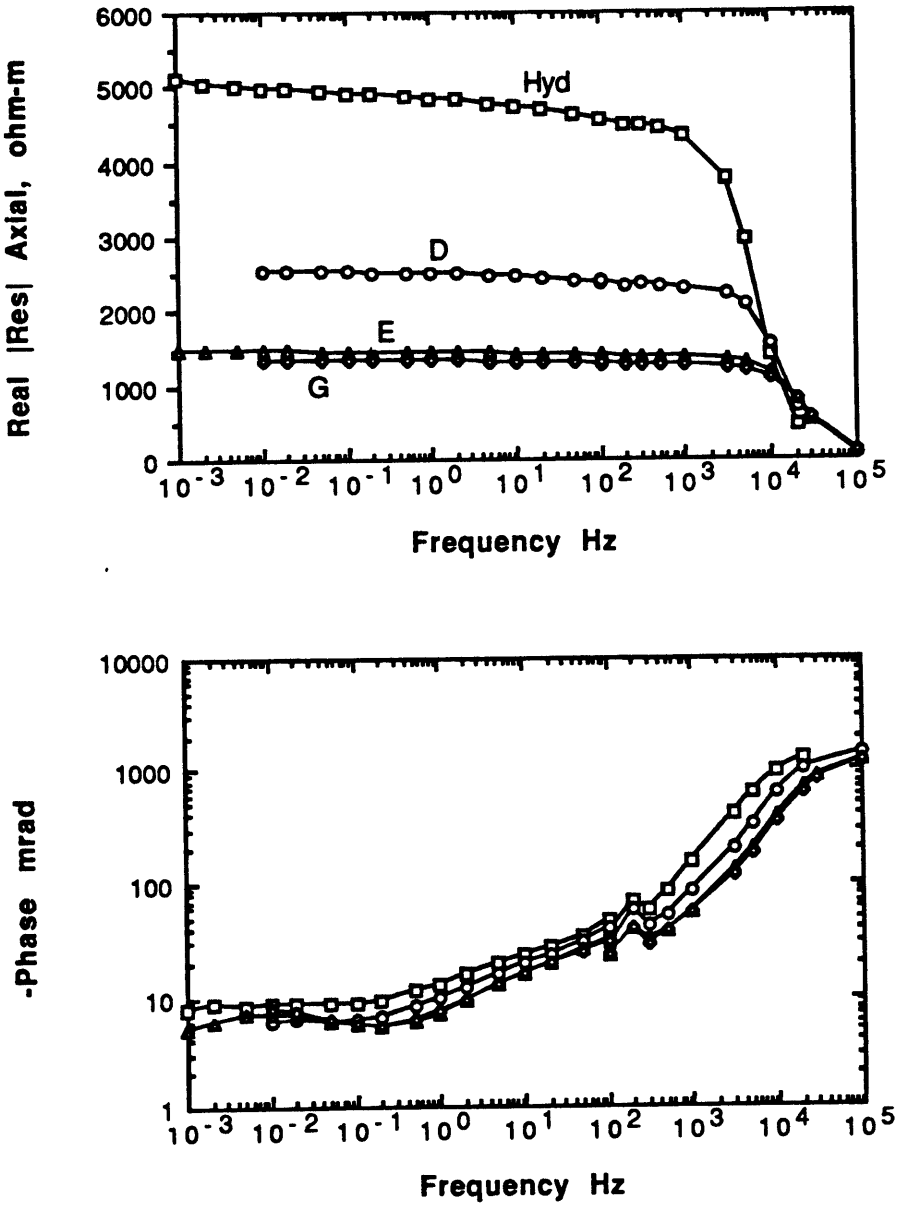
Real |Res| Axial, ohm-m
6000
5000
4000
3000
2000
1000
0
Hyd
D
E
G
10-3 10-2 10-1 100 101 102 103 104 105
Frequency Hz
-Phase mrad
10000
1000
100
10
1
10-3 10-2 10-1 100 101 102 103 104 105
Frequency Hz

Figure 4.8

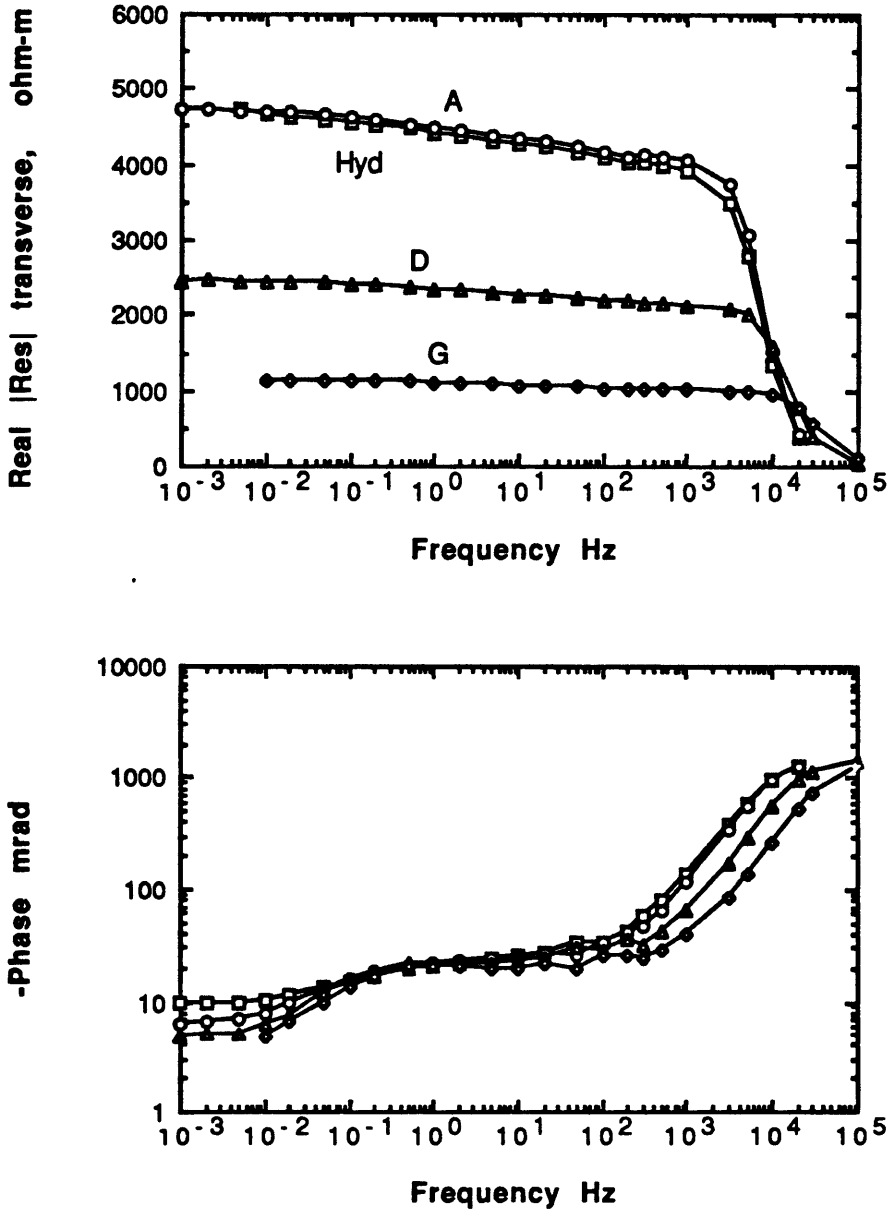
Real |Res| transverse, ohm-m
6000
5000
4000
3000
2000
1000
0
A
Hyd
D
G
10-3 10-2 10-1 100 101 102 103 104 105
Frequency Hz
-Phase mrad
10000
1000
100
10
1
10-3 10-2 10-1 100 101 102 103 104 105
Frequency Hz

Figure 4.9

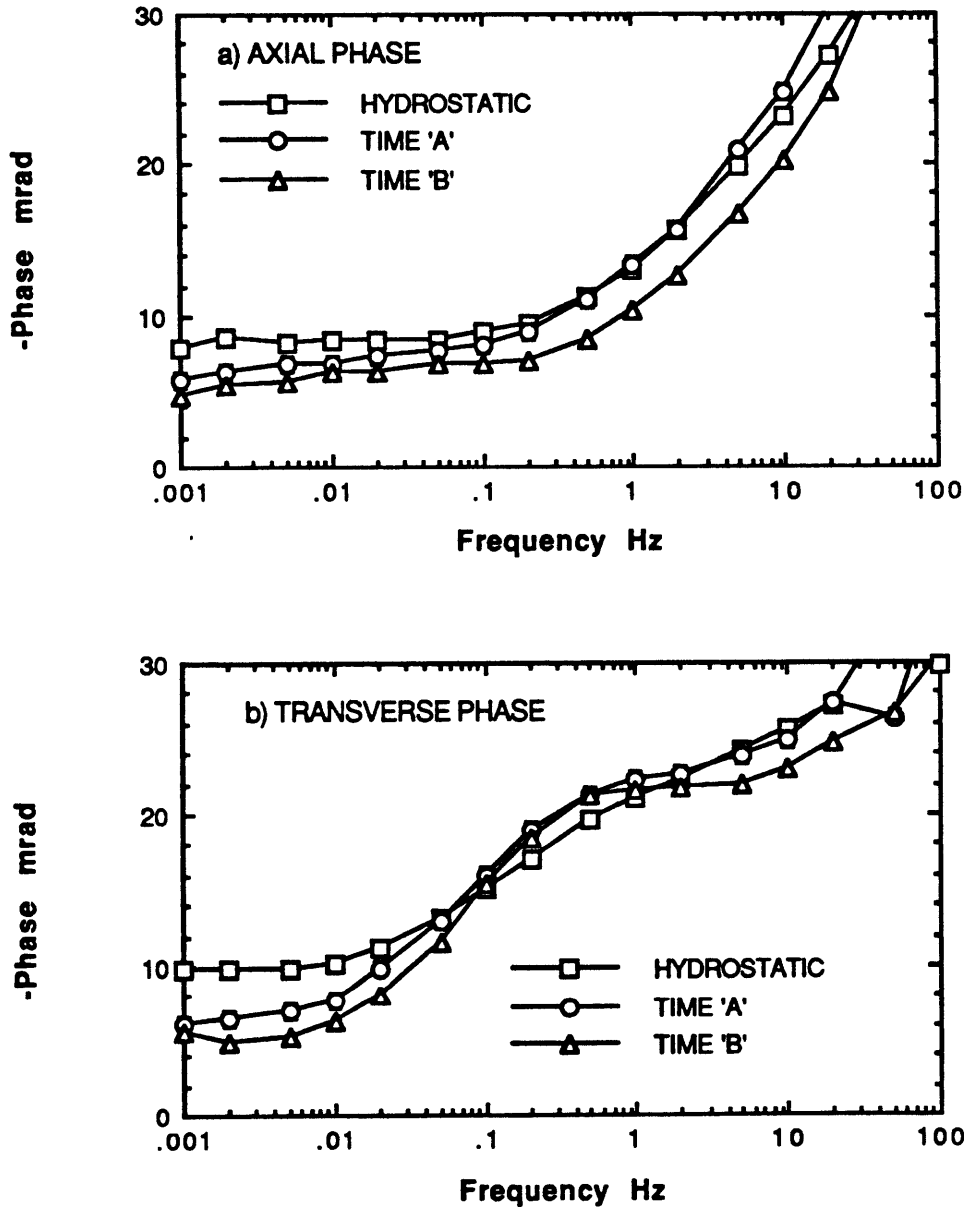
a) AXIAL PHASE
HYDROSTATIC
TIME 'A'
TIME 'B'
-Phase mrad
30
20
10
0
.001
.01
.1
1
10
100
Frequency Hz
b) TRANSVERSE PHASE
HYDROSTATIC
TIME 'A'
TIME 'B'
-Phase mrad
30
20
10
0
.001
.01
.1
1
10
100
Frequency Hz

Figure 4.10

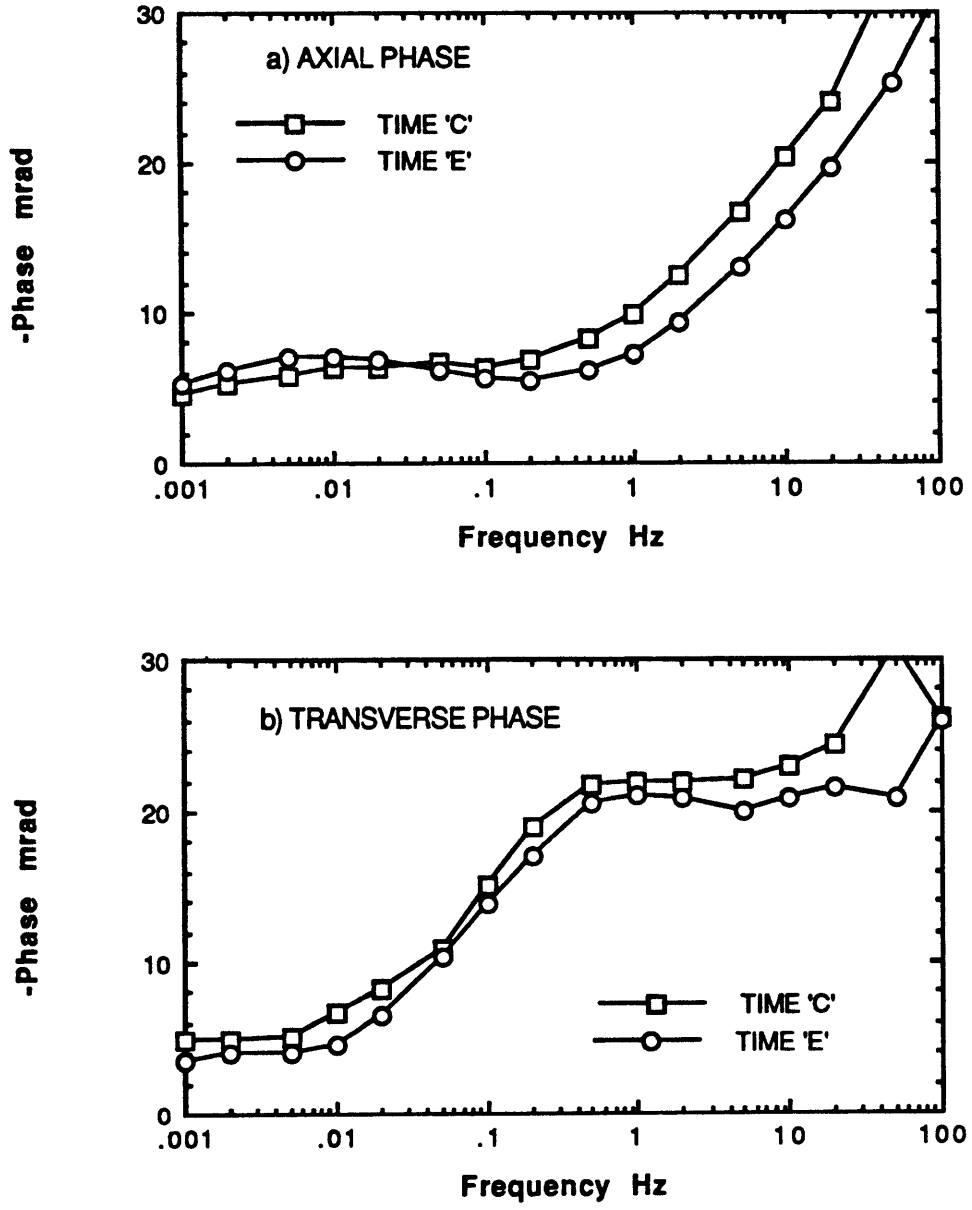
a) AXIAL PHASE
TIME 'C'
TIME 'E'
-Phase mrad
30
20
10
0
.001
.01
.1
1
10
100
Frequency Hz
b) TRANSVERSE PHASE
TIME 'C'
TIME 'E'
-Phase mrad
30
20
10
0
.001
.01
.1
1
10
100
Frequency Hz

Figure 4.11

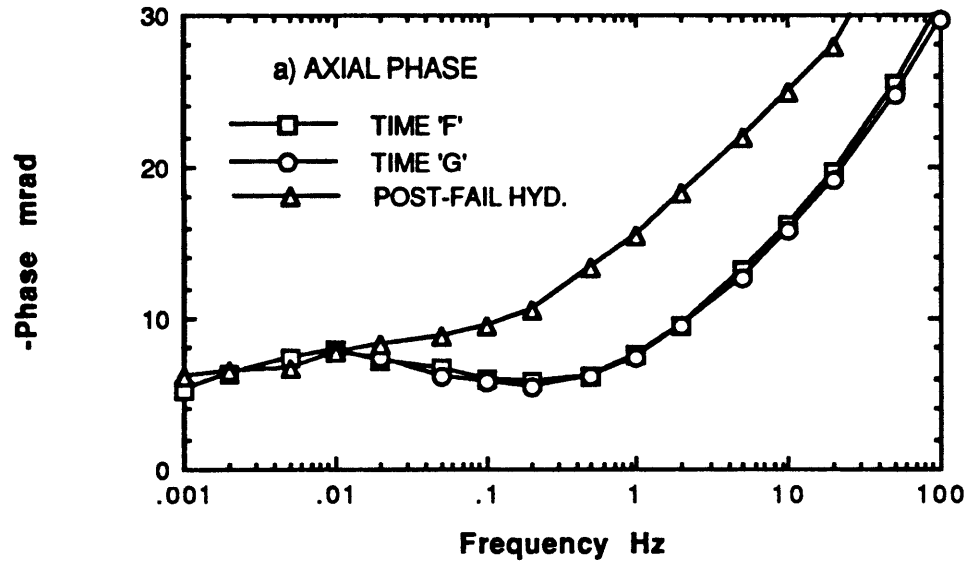
a) AXIAL PHASE
TIME 'F'
TIME 'G'
POST-FAIL HYD.
-Phase mrad
30
20
10
0
.001
.01
.1
1
10
100
Frequency Hz

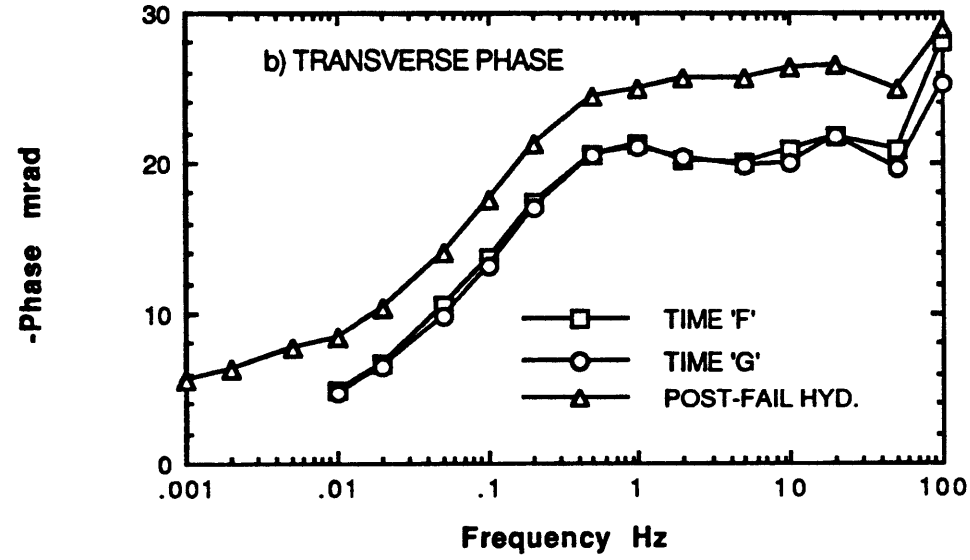
b) TRANSVERSE PHASE
TIME 'F'
TIME 'G'
POST-FAIL HYD.
-Phase mrad
30
20
10
0
.001
.01
.1
1
10
100
Frequency Hz

Figure 4.12

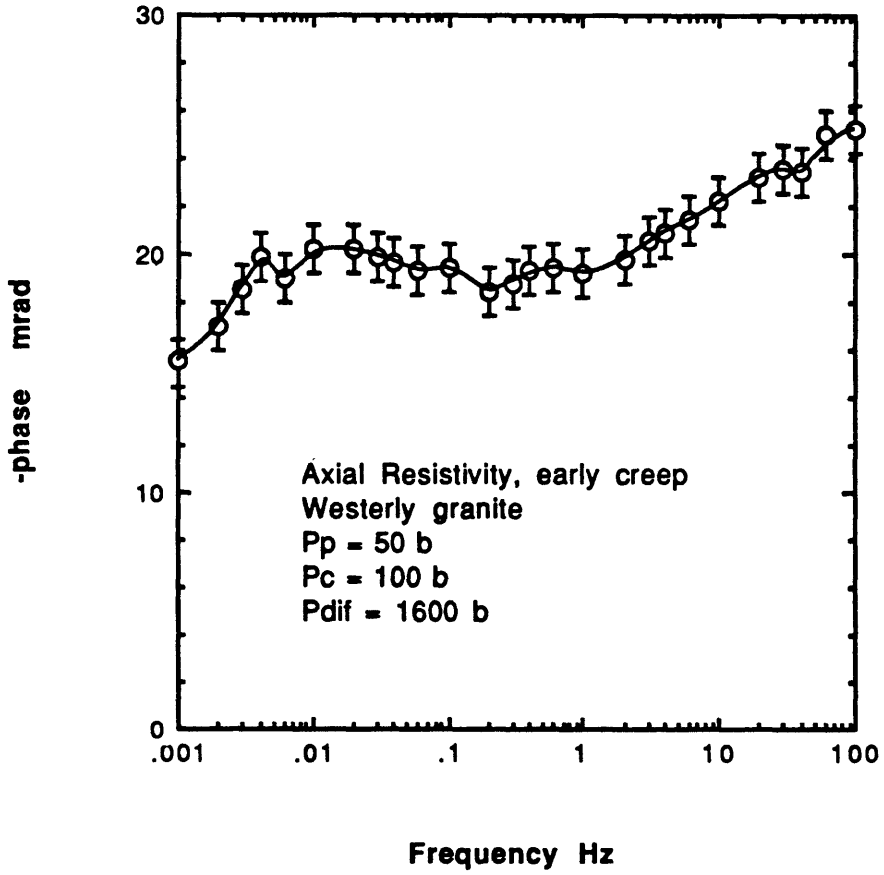
30
20
10
0
.001
.01
.1
1
10
100
-phase mrad
Frequency Hz
Axial Resistivity, early creep
Westerly granite
Pp = 50 b
Pc = 100 b
Pdif = 1600 b

Figure 4.13

CHAPTER 5

CHANGES IN CONDUCTIVITY DURING DENSIFICATION OF QUARTZ POWDERS

abstract. A series of high-temperature densification experiments have been performed in which strain and electrical resistivity were measured. Starting material was ultra-fine quartz powder (5-10 μm-diameter). Confining pressure ranged from 2,000 to 3,700 bars and pore pressure from 300 to 2,000 bars. All runs were conducted at 700°C and were saturated with distilled water. Initial porosity in all experiments was in excess of 40%. Experiments lasted from 10 hr to 8 days, with ending porosities from 19% to as little as 8 ± 1%. In all experiments, initial volumetric compaction rates were rapid (10^{-5} to 10^{-6} s^{-1}), decreasing quickly to rates in the range 10^{-7} to 10^{-8} s^{-1} after approximately 1 day. Electrical conductivity as well as porosity decreased monotonically during the experiments. Conductivity ranged from 10^{-2} to 10^{-4} mho/m. A model is presented in which decrease in conductivity is initially controlled by the loss of fluid filled pore volume, followed by a transition, at approximately 15% porosity, to a condition in which conductivity in controlled by constrictions in interconnecting channels.

Introduction

The experiments presented in this paper are intended to extend our understanding of the manner in which fluid filled pores may exist in the lower crust. A variety of studies have been conducted in which metallic oxides have been hot-pressed in the presence of water (*Kingery et al.*, 1976; *Brantley,* 1987; *Watson and Brenan,* 1987). One important question in these studies concerns the stability of fluid-filled pores and whether, under equilibrium conditions, they will remain connected by a network of channels, or become isolated from each other. This question has important consequences for the ability of a rock mass, under metamorphic conditions, to transport fluid. Water which is released in metamorphic reactions will tend to rise in response to bouyancy forces. If the pore structure remains connected, it will allow water to migrate at relatively low fluid pressures. If, on the other hand, pores tend to become isolated, fluid pressures could rise to near-lithostatic in order to maintain connected pathways. This will have an

important effect on the ease of transport of water and dissolved minerals.

In a related issue, properties of the lower crust are inferred primarily through remote sensing techniques based on measurements of seismic wave velocities and attenuation, gravity and electrical conductivity. Conductivity in the mantle is dominated by ionic conduction in the solid mineral phases, since temperatures are high enough to produce significant ionic mobility. However, for the lower temperatures present in the earth's crust, the dominant mineral phases become poor conductors, and conduction is determined primarily by the movement of ions dissolved in the pore fluids. Here again the interconnectedness of the pores will play an important role in determining conductivity. The present experiments were designed to address these issues. In one sense, the results reported here should be regarded as a progress report since the experiments have not yet been run to near-equilibrium pore geometries. At the same time, both the compaction rate and conductivity data are unique and are of interest in their own right.

Experimental

The starting material in all experiments was an ultra-fine quartz powder obtained from crushed Ottawa sand by means of air centrifuge separation. In all but one run, a 5-10 μm-diameter fraction was used. An additional run was performed using a >20 μm fraction to study the effect of grain size. The quartz powder is described more fully in *Brantley* (1987). With the exception of run 12, cylindrical samples were formed by cold pressing in a steel chamber. In this procedure, the quartz powder was compacted by a piston with an axial stress of 3.0 ± 0.6 kb. This resulted in an initial porosity ϕ, for the 5-10 μm powder, of 0.46 ± 0.02 (ϕ_{init} = 0.41 for the >20 μm powder). In run 12, quartz powder was placed directly into the copper jacketted sample assembly so that it underwent little precompaction. Sample diameter in all experiments was 19.1 mm and length was nominally 18 mm. The assembled sample column is shown in Fig. 5.1. The sample is sandwiched between aluminum oxide spacers, each containing a 1.5 mm-diameter axial hole. The top hole allows access of pore fluid (distilled, deionized water) and also contains a thermocouple to measure sample temperature. A porous ceramic frit, placed on the top of the sample prevents quartz powder from extruding past the thermocouple. The frit is machined from 28% porosity Coors AHP99. This material is 99% Al_2O_3 bonded with a boro-silicate glass containing no Mg or Ca. The lower spacer contains a 1.9 mm-diameter Ag wire electrode which is electrically insulated from the rest of the sample assembly and pressure vessel. The central electrode penetrates 10.0 ± 0.05 mm into the sample. The sample is separated from the Ar gas confining medium by a 0.51 mm-walled annealed Cu sleave which was silver plated to retard corrosion. Since these experiments are intended to run for many days, it is critical that the sample be strictly isolated from the confining fluid. In early runs, we found that Ar gas slowly diffused through the viton o-rings use to seal the sample assembly. Thus, a more complicated assembly, shown on the upper end plug in Fig. 5.1, was developed for these experiments. This assembly consists of two viton o-rings and an intermediate split steel ring. The split-ring is connected to atmospheric pressure through a small vent hole. Thus, any gas which leaks past the upper o-ring is trapped by the split-ring assemby and vented to the atmosphere. Since positive pore pressure is maintained in the sample at all times, argon can never enter the pore fluid system. A

similar result is achieved in the lower seal assembly by placing a stainless-steel screen at the top of the piston. This allows Ar to escape out through the hole in the piston that contains the central electrode wire. A Pt-wire resistance heater is placed around the sample assembly and is packed with thermally conductive boron nitride to minimize thermal gradients. This entire sample assembly is then placed in the pressure vessel and pressurized to the desired confining and pore pressures. Finally, temperature is raised to the desired run temperature. Confining pressure is measured with a manganin coil and pore pressure with a strain gague pressure transducer. A high-speed servo-control valve is used to advance a hydraulic ram against the piston, maintaining an axial stress on the sample which is equal to the confining pressure. Thus the sample is compacted in a virtually hydrostatic stress state. A DCDT displacement transducer, attached to the piston, provides a continuous record of axial shortening. This axial shortening is converted to volumetric strain e_v by assuming $\varepsilon_a = \varepsilon_\theta$ so that for finite strain, $\varepsilon_v = (1 + \varepsilon_a)^3 - 1$. All pressures are held constant by an automated computer control system. An independent measure of volumetric strain is achieved by measuring the volume of pore fluid, needed to maintain constant pressure, that is removed from the sample. This precision system is capable of resolving changes of 0.015 mm^3, or approximately $\partial\varepsilon_v = 3$ μstr. All experiments were run at a temperature of 700°C (β-quartz stability field). Confining pressure ranged from 2,000 to 3,700 bars (1 bar = 0.1 MPa), and pore pressure ranged from 300 to 2,000 bars. Pressures, temperature and displacement were recorded automatically once every second using a 16 bit multiplexed A/D converter.

Sample resistance was measured periodically during the course of each experiment by comparison to a precision decade resistor. The measurement circuit is shown in Fig. 5.2. A Wavetek model 142 signal generator was used to provide a 100 Hz sine-wave of nominal 1 volt peak-to-peak voltage. This excitation signal was connected to the sample in series with the decade resistor box. A high-input-impedance ($>3 \times 10^8\ \Omega$) instrumentation amplifier was then connected, successively, across the sample and the precision resistor, which was adjusted to match the sample resistance. Sample resistances typically ranged from 10^3 to 10^6 ohms.

Accuracies of confining pressure and pore pressure are, respectively, 10 and 5 bars. Precisions are 0.2 bars. Precision of axial displacement is 0.3 μm. During the experiments, samples typically neck by 1 - 2% due to the support of the Al_2O_3 spacers. Thus we estimate that final porosities are known to ± 1%. Final sample dimensions are

measured after removal from the pressure vessel and, based on starting weight and an assumed density of $\rho_{quartz} = 2.65$ g/cm^3, used to compute ending porosity. The final porosity is then combined with the axial shortening data to back-calculate the porosity during the run. Consequently, porosity values have larger uncertainties in the early stages of the experiments. The run temperature of 700° is for the center of the sample and is accurate to ± 10°. The temperature gradient was determined by moving a thermocouple up and down the axis of a dummy sample. Temperature at the ends of the sample was found to drop off by 15°.

Although sample resistance was determined to ± 0.5% accuracy, conversion to conductivity σ requires determination of a geometric scaling factor: $\sigma = 1/\alpha R$ where α has units of length. A radially symmetric finite difference model was developed to compute α. For the nominal sample dimensions, $\alpha = 0.0268 \pm 0.005$ m. However, the value of α will decrease as the sample densifies. This correction is not made in computing the conductivity data, resulting in a systematic error of up to 6%.

Run conditions, starting materials and ending porosities for the series of experiments are listed in Table 5.1. Most experiments were conducted at an effective pressure P_e of 1,700 bars ($P_e = P_c - P_p$, where P_c is confining pressure and P_p is pore pressure). Densification and conductivity curves are shown in Figs. 5.3 and 5.4. Note that all runs showed similar compaction histories, namely an initial period of rapid compaction, trailing off, after approximately 10 hr, to a much slower compaction rate. This can be seen more clearly in Fig. 5.5 where volumetric strain rate is plotted as a function of time. Runs 14 and 15, at P_p = 1,000 bars, had the fastest initial compaction rates shown in Fig. 5.5. Run 13 (P_p = 2,000 bars) actually had the fastest compaction rate. However, due to equipment problems, this sample had to be unloaded and restarted. Consequently, the initial rate is not shown. In all runs that lasted for more than 2 days, compaction rates decayed to approximately 2 - 3 x 10^{-8} s^{-1}. This represents about 0.2% porosity loss per day and indicates that little additional compaction can be expected for reasonably lengthed experiments. These runs were all at 300 bars pore pressure. However, the 2 kb pore pressure run was compacting 4 to 5 times faster and appeared capable of approaching an equilibrium density if it had continued for a few more days. The faster compaction rate is apparently the result of increased H_2O activity at high pore pressure.

The volume of pore fluid removed from the sample to maintain constant pore pressure is recorded during each experiment. This constitutes an independent measure of sample compaction and can be used to test the accuracy of the determination of porosity from axial shortening. Data from run 11 at P_p = 1,000 bars are shown in Fig. 5.6. In this figure, the change in volume of the room temperature pore pressure intensifier is plotted as a function of porosity (calculated from axial shortening data). Since fluid mass is conserved in the pore fluid system, the volume change in the sample can be related to the volume change in the intensifier by

$$\Delta V_2 = \rho_1/\rho_2 \, \Delta V_1 \qquad (5\text{-}1)$$

where ρ_1 is water density in the intensifier and ρ_2 is water density in the sample. A

least squares fit to the data requires a density ratio of 3.2 ± 0.2. The correct ratio of 3.55 predicts the line shown in Fig. 5.6. The most likely cause of the discrepancy is a calibration error in the load cell due to seal friction. This would imply that the axial stress was slightly lower than the confining pressure so that the sample compacted laterally more than it compacted axially. Since porosities are back-calculated from the ending sample dimensions, beginning porosities are systematically calculated too small. For example, in this run, a back-calculated porosity of 18% should in fact be 19.5%. This fluid pore volume measurement was only made for a few of the runs so we have not made this correction to any of the data.

Conductivity-porosity relations are summarized in Fig. 5.7. For a given porosity, a general increase in conductivity with increasing pore pressure is observed. This trend reflects an increase in fluid conductivity with pore pressure, primarily reflecting the increase in fluid density with pressure. One apparent inconsistancy in the conductivity data is run 12 which, although it has lower porosity than runs 9 and 10, has about the same conductivity. This is the only sample run a high effective pressure (3,700 bars) and in addition was not cold pressed as were all the other samples. As a result, its unusually high conductivity may reflect a difference in grain packing geometry. At this point, this explanation is only conjecture and needs to be verified by additional experiments. Another notable feature of Fig. 5.7 is the shallow slope and relatively high conductivity of run 11 (compared to runs 9 and 10). This is the only run in which the unsorted >20 μm powder was used. Once again, a possible explanation would be a difference in grain packing geometry for this experiment. This effect also needs further investigation.

The matrix conductivity was measured before the start of run 10 by pre-loading the sample, at temperature, while evacuated. In this manner, conductivity of the quartz matrix was determined to be 8×10^{-5} mho/m. Conductivity for single crystal quartz is highly anisotropic (*Kronenberg and Kirby,* 1987). Conductivity perpendicular to the c-axis is approxiately 10^{-5} mho/m at 700°C, although parallel to c, conductuctivity as high as 10^{-2} has been reported. Values that we have measured for the dry aggregate are approximately one-half the conductivity reported by *Olhoeft* (1981) for Westerly granite and a hornblende schist at the same temperature. The lower conductivity of the quartz powder is probably due to the inefficient conduction resulting from the open pore structure. One of the primary reasons for undertaking these experiments was to

determine whether the residual pore structure remained connected as the samples compacted. If the interconnecting passages pinch off so that pores become isolated, then the sample conductivity should drop to the value for matrix conduction at the residual porosity. If, on the other hand, pores remained connected, the slope of the conductivity-porosity plot should decrease before reaching the matrix conductivity. As shown in Fig. 5.7, we have come within one-half decade of the matrix conductivity without observing any decrease in slope. This indicates that in the experiments performed so far, interconnecting channels have continued to close. By the end of run 15, compaction rate was about 1% per day. Thus, we expect to be able to observe the final stages of channel closure in future experiments. If the trends in the data are extrapolated to the matrix conductivity, they indicate that the low pore pressure runs 9 and 10 would retain residual porosities of 8 to 10%. The high pore pressure experiments, run at the same effective pressure, would have residual porosities of 3 to 5%. One explanation for this would be that the increased fluid pressure allows material from the grain contacts to be transported farther into the open pores before being redeposited.

Archie's law is a well known empirical relation between conductivity and porosity which is used mainly for sedimentary rocks (*Timur et al.*, 1972), although its applicability has also been evaluated for crystalline rocks (*Brace et al.*, 1965; *Lockner and Byerlee*, 1986). The most common form of Archie's law is

$$\sigma_{fluid}/\sigma_{rock} = \phi^{-m} \qquad (5\text{-}2)$$

where σ_{fluid} and σ_{rock} are, respectively, conductivity of fluid and conductivity of saturated rock. m typically ranges from 1 to 2 and is near 1.7 for many sandstones (*Timur et al.*, 1972). Values of m for the present experiments are listed in Table 5.1. In most cases, the exponents are significantly larger than what is observed for sandstones as well as low porosity Westerly granite. It may be more appropriate to remove the residual porosity when fitting the present data to Archie's law since, as the connecting passages pinch off, the residual pore volume no longer plays a role in limiting conductivity. A similar approach was taken in *Brace et al.* (1965) were they made a distinction between crack and pore porosity. If this is done, the resulting values of m can be reduced to the range of values observed for sedimentary rocks. In this sense,

uncharacteristically large values of m may be indicative of rocks in which a significant residual porosity is nearly isolated. In the next section we take a different approach and attempt to model the conductivity data in terms of geometric changes in the pore structure during densification.

Conductivity-porosity Model

As a first step in modeling the conductivity-porosity data, we begin with a simple model based on the following assumptions:

Assumption 1) The starting aggregate consists of hexagonally close-packed spheres of equal size. This implies an initial porosity $\phi_i \sim 0.26$. We will first model the well sorted (5-10 μm) quartz powder. From the density determinations ($\phi = 0.46 \pm 0.02$) of the cold press procedure used to form the initial samples, we know that the starting material has a more open structure than efficiently packed spheres. Also, SEM studies show that the initial powder contains angular grains. However, the sharp corners of grains will be more reactive and grains will tend to become more rounded at temperature. Thus, it is not clear how severe the errors are that are introduced by this simplifying assumption.

Assumption 2) All current paths are from pores (high σ) to connecting channels (low σ) to neighboring pores, etc. The connecting channels are expected to dominate conductivity; especially as they approach closure.

Assumption 3) Porosity decreases, as connecting channels pinch off, towards a final porosity ϕ_f, that is indicated by asymptotes in the data. Connecting channels are approximated as shown in Fig. 5.8. The channel cross-section at the narrowest point is approximately triangular with sides 2c. The length of each channel is approximately 2a.

Assumption 4) Densification occurs by transport of material from grain contacts to pores. This process results in movement of grain centers toward each other and is measured by grain overlap = 2b. This geometry gives the following relations:

$$\begin{aligned} a &= r \sin \varphi \\ b &= r (1 - \cos \varphi) \\ c &= r \sin \theta \\ \varphi &= \cos^{-1}(1 - b/r) \\ 2\theta + 2\varphi &= \pi/3 \, . \end{aligned} \qquad (5\text{-}3)$$

Conductance of Channels and Pores

For a single channel,

$$Y_c = \sigma_{fluid} \text{ area/length} \approx \sigma_{fluid} \sqrt{3}c^2/2a \qquad (5\text{-}4)$$

where Y is conductance and σ_{fluid} is conductivity of fluid. Substituting (5-3) gives

$$Y_c = \sqrt{3}\, \sigma_{fluid}\, r \sin^2(\pi/6 - \varphi)/\sin \varphi\,. \qquad (5\text{-}5)$$

For hexagonal close packing, pores are approximately cubic in shape (Fig. 5.9), and are connected to neighboring pores by eight channels. Volume of a unit cell is

$$V_{uc} = 16\sqrt{2}\, \zeta\, r^3 \qquad (5\text{-}6)$$

where $\zeta = (1 - \phi_i)/(1 - \phi)$ is a measure of volumetric strain relative to the initial state. Then, pore volume of a unit cell is simply ϕV_{uc}. The radius of a pore of equivalent volume becomes

$$r_p = \{(3/4\pi)\, \phi\, V_{uc}\}^{1/3}\,. \qquad (5\text{-}7)$$

Pore conductance is approximated by

$$Y_p \approx \sigma_{fluid} \text{ area/length} \approx \sigma_{fluid}\, (\pi r_p^2)/(2r_p) = \pi\, \sigma_{fluid}\, r_p/2\,. \qquad (5\text{-}8)$$

While this includes a rather crude approximation to the true geometric factor contributing to pore conductivity, it will not be too far from the correct value, and as long as the pore geometry does not change significantly with compaction, the geometric factor will remain constant.

Each unit cell contains one pore connected to pores in neighboring cells. Macroscopic planar current flow in, for example, the x-direction (Fig. 5.9), involves parallel flow in two channels leaving a pore. These channels connect to two new channels, in series, which enter the next pore. Thus the equivalent unit cell conductance

(Fig. 5.10) is

$$Y_{uc} = \{1/Y_p + 1/Y_c\}^{-1} . \qquad (5\text{-}9)$$

Finally, conductivity for a unit cell, and therefore for the entire matrix, becomes

$$\sigma = Y_{uc} \text{ length/area} = \sqrt{2}/4 \{(1 - \phi)/(1 - \phi_i)\}^{1/3} Y_{uc}/r . \qquad (5\text{-}10)$$

Relating Porosity to Unit Cell Deformation

When the connecting channels have pinched off ($Y_c = 0$):

$$\begin{aligned} &\phi = \phi_f \\ &\theta = 0 \\ &\varphi_f = \pi/6 \\ &b_f = r (1 - \cos \varphi_f) = r (1 - \cos \pi/6) . \end{aligned} \qquad (5\text{-}11)$$

Assumption 5) b is linearly related to strain of the aggregate and therefore to porosity:

$$\phi = \phi_i - 3zb/r . \qquad (5\text{-}12)$$

Coefficient z depends on geometry; *e.g.* coordination of grains and amount of debris filling pores. Since $\phi_f = \phi_i - 3zb_f/r$, substitution of (5-11) and rearrangement gives

$$z = (\phi_i - \phi_f)/(3(1 - \cos \pi/6)) . \qquad (5\text{-}13)$$

For a given ϕ_i and ϕ_f, (5-13) is sufficient to fully specify the problem.

Representative plots of (5-10), using $\phi_f = 0.02$ and 0.04, are shown in Fig. 5.11 along with data from experimental run 13. Since the appropriate fluid conductivity is not known, the theoretical curve is shifted vertically to give the best fit and in fact is in good agreement with the data. Runs 14 and 15 are also fit reasonably well, although for the other data sets, at higher porosity, the model grossly over-estimates porosity

dependence of conductivity. Note that run 13 achieved the greatest densification of all the runs. Since the present model is dominated by the closure of the connecting channels, which should become increasingly important as densification progresses, the good agreement with run 13 is encouraging. The inability to fit the less dense conductivity data may indicate that pore conductivity is domimant in those runs. We next explore this possibility.

Modification for Initial Porosity

Equation (5-10) will generate a family of curves depending on the choice of ϕ_f. Since these curves all exhibit a gradual change in slope, fitting the individual data segments from the various runs is a severely underdetermined problem. We next make the assumption that the suite of runs, using the same starting material and conducted at the same effective pressure and temperature, all represent portions of a single densification curve. This curve can then be reconstructed by shifting conductivity data from the various runs vertically so that they overlap. Such a composite curve, using data from runs 9, 10, 13, 14, and 15, is presented in Fig. 5.12. Where the various data sets overlap in Fig. 5.12, their slopes generally agree with each other, providing some confidence that this procedure is valid. The relative shifts in the data sets are assumedto be the result of variations in fluid conductivity. Fluid conductivities, normalized by run 13, are predicted to be 0.04, 0.06, 0.7 and 0.7 for runs 9, 10, 14 and 15, respectively. Since runs 9 and 10 had the same run conditions, a discrepancy in their fluid conductivities probably indicates a problem in one or both of these runs. Experiment 10 had been run dry at temperature to measure matrix conductivity. It was then cooled, saturated and reheated. Consequently, it may have suffered damage due to thermal cracking, providing a possible explanation for its enhanced conductivity.

In the model developed so far, conductivity is dominated by the conductivity of the channels after as little as one percent compaction. Since the starting material is less dense that what would be expected for close-packed spheres, pores should be expected to be connected more efficiently in the early stages of densification than would be predicted by the model. To include this feature in the model, we assume that a cross-over porosity ϕ_{co} exists, above which pore conduction dominates, and below which channel conduction dominates. Then (5-9) is modified to

$$Y_{uc} = \{1/Y_p + 1/(QY_c)\}^{-1} \qquad (5\text{-}14)$$

with the condition that when $\phi = \phi_{co}$, $Y_p = QY_c$. Q can be interpreted to indicate the efficiency of the interconnecting channels relative to that predicted by the close-packed model. Expanding (5-10) to give the explicit porositiy dependence of conductivity results in

$$\sigma = \frac{\sigma_{fluid}}{\left(\frac{32}{3\pi^2}\right)^{1/3}\phi^{-1/3} + \left(\frac{2}{3}\right)^{1/2} Q\left(\frac{1-\phi_i}{1-\phi}\right)^{1/3}\left[\frac{1-\left(1-\frac{\phi_i-\phi}{3z}\right)^2}{4\left(1-\frac{\phi_i-\phi}{3z}\right)^2-1}\right]^{1/2}} \qquad (5\text{-}15)$$

The dependence due to pore conduction is given by the first term in the denominator. Two model curves, using $\phi_f = 0.02$ and 0.04 are shown in Fig. 5.12 along with the composite data. Both model curves use $\phi_i = 0.43$ and $\phi_{co} = 0.15$ to conform to the data. These models provide a good fit, suggesting that the aggregate is approaching a final porosity of 3 ± 1%. The model curves require values of Q of 43 ± 6, indicating that the initial model significantly underestimated the channel conductance in the early stages of compaction. Apparently, for the starting sample geometry, the pore structure is sufficiently open so that the pores form a connected network with no significant intervening channels. However, for the present run conditions, at approximately 15% porosity, a transition occurs where pores become sufficiently isolated that connecting channels begin to dominate electrical conduction. The residual porosity is better constrained for this composite data set than for most of the individual runs. If, as suggested in the last section, we remove the residual porosity and plot log σ *vs* log(ϕ - ϕ_f), the resulting slope is 1.7, which is precisely the porosity dependence observed for sandstones (*Timur et al.*, 1972).

TABLE 5.1 - Run Conditions

All runs at 700°C

Run	Grain Size [μm]	P_c [bars]	P_p [bars]	P_e [bars]	Ending ϕ (± 0.01)	m (Archie's law)
9	5 - 10	2,000	300	1,700	0.18	
10	5 - 10	2,000	300	1,700	0.19	2.9
11	>20	2,000	300	1,700	0.10	0.8
12	5 - 10	3,700	300	3,400	0.08	1.9
13	5 - 10	3,700	2,000	1,700	0.07 (±0.02)	2.8
14	5 - 10	2,700	1,000	1,700	0.11	2.8
15	5 - 10	2,700	1,000	1,700*	0.11	2.1

*Run 15 was pre-compacted at P_c = 3,700 b, P_p = 0, T = 18°C.

References

Brace, W. F., A. S. Orange and T. R. Madden, The effect of pressure on the electrical resistivity of water-saturated crystalline rocks, *J. Geophys. Res., 70,* 5669-5678, 1965.

Brantley, S. L., The chemistry and thermodynamics of natural brines and the kinetics of dissolution-precipitation reactions of quartz and water, Ph.D. Thesis, Princeton University, Princeton, N. J., 1987.

Kingery, W. D., H. K. Bowen and D. R. Uhlmann, *Introduction to Ceramics, 2nd. edition,* John Wiley and Sons, New York, 1032 pp., 1976.

Kronenberg, A. K. and S. H. Kirby, Ionic conductivity of quartz: DC time dependence and transition in charge carriers, *Amer. Mineralogist, 72,* 739-747, 1987.

Lockner, D. A. and J. D. Byerlee, Changes in complex resistivity during creep in granite, *Pure Appl. Geophys., 124,* 659-676, 1986.

Olhoeft, G. R., Electrical properties of granite with implications for the lower crust, *J. Geophys. Res., 86,* 931-936, 1981.

Timur, A., W. B. Hempkins and A. E. Worthington, Porosity and pressure dependence of formation resistivity factor for sandstones, in *Trans. Can. Well Logging Soc. Fourth Formation Evaluation Symposium,* 18 pp., 1972.

Watson, E. B. and J. M. Brenan, Fluids in the lithosphere, part 1: Experimentally-determined wetting characteristics of CO_2 - H_2O fluids and their implications for fluid transport, host-rock physical properties, and fluid inclusion formation, submitted to *Earth and Planetary Sci. Lett.,* 1987.

Figure Captions

Figure 5.1 Sample column assembly for hot press experiments.

Figure 5.2 Schematic diagram of sample resistance measurement circuit. Voltage drop across sample is balanced against voltage drop across precision decade resistor.

Figure 5.3 Summary of porosity and conductivity plotted as a function of time for runs 9 - 12.

Figure 5.4 Summary of porosity and conductivity plotted as a function of time for runs 13 - 15.

Figure 5.5 Log_{10}(volumetric strain rate) plotted *vs* time for all experiments.

Figure 5.6 Plot of porosity change as calculated from axial shortening *vs* pore fluid removed from sample to maintain constant pressure.

Figure 5.7 Log σ *vs* log ϕ for all experiments. Matrix conductivity was determined from evacuated sample. See Table A1 for values of exponent in power law fit.

Figure 5.8 Cross-sectional view of channel connecting pores in HCP model. Grain centers are assumed to approach each other as material at grain contacts (shown as overlapping regions) is removed and deposited in pores.

Figure 5.9 Cross-section of HCP geometry showing relation between grains, pores and connecting channels.

Figure 5.10 Equivalent circuit for current flow in x-direction (Fig. 5.9). Y_p is

conductance of pore and Y_c is conductance of connecting channel.

Figure 5.11 Comparison of run 13 data to model predictions (eq. 5-10) using residual porosity ϕ_f of 2 and 4%. Model curves have been shifted vertically for best fit.

Figure 5.12 Composite conductivity curve for all runs in which P_e = 1,700 b. Data sets are shifted vertically to overlap. Two curves for extended model (eq. 5-15) are plotted for residual porosities of 2 and 4%. A cross-over porosity of 15% is used. Above this value, pore conductivity dominates while below it, channel conductivity dominates.

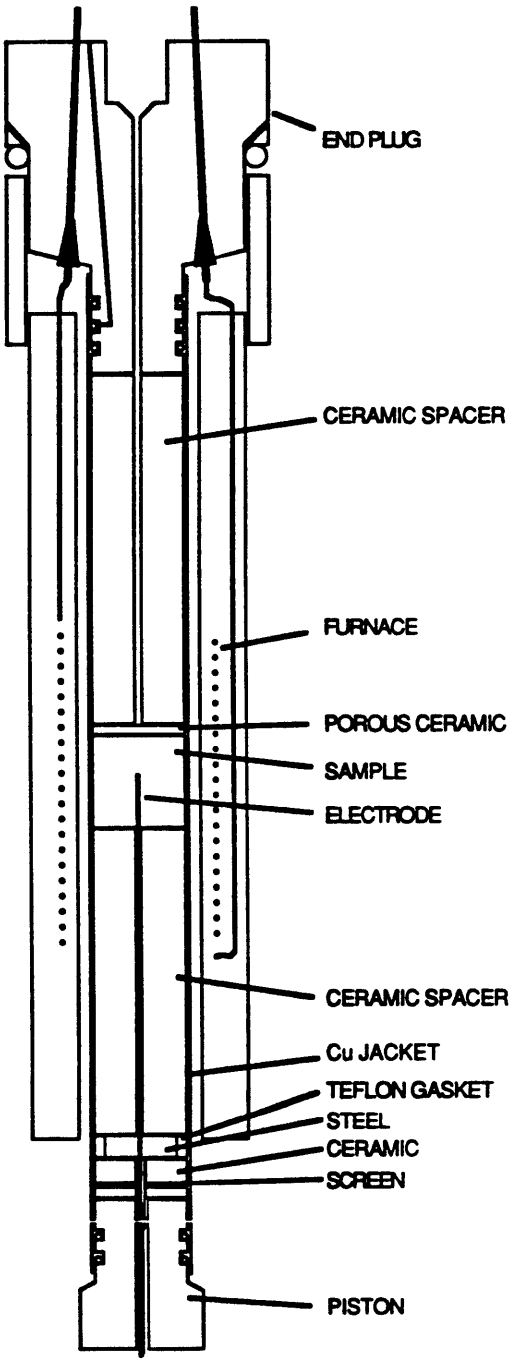
END PLUG
CERAMIC SPACER
FURNACE
POROUS CERAMIC
SAMPLE
ELECTRODE
CERAMIC SPACER
Cu JACKET
TEFLON GASKET
STEEL
CERAMIC
SCREEN
PISTON

Figure 5.1

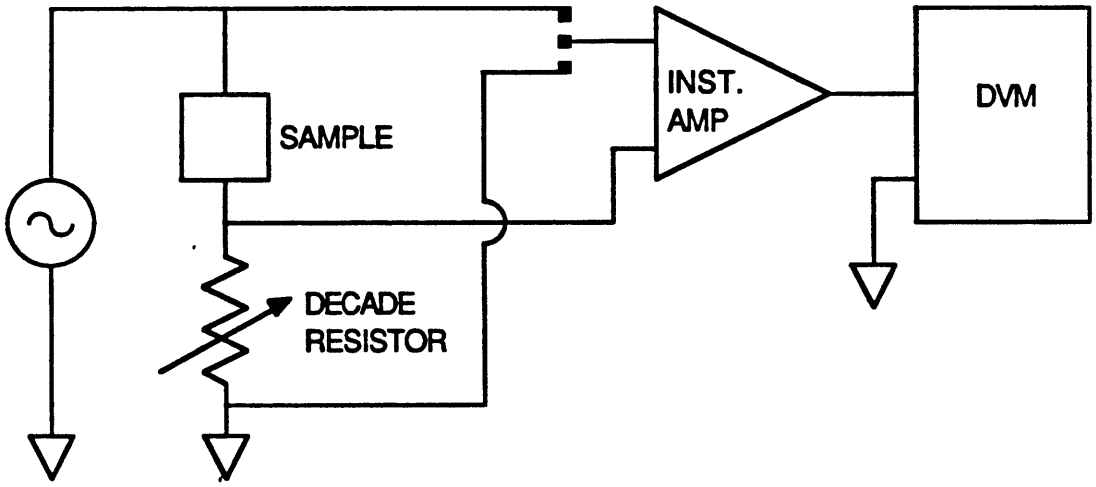

Figure 5.2

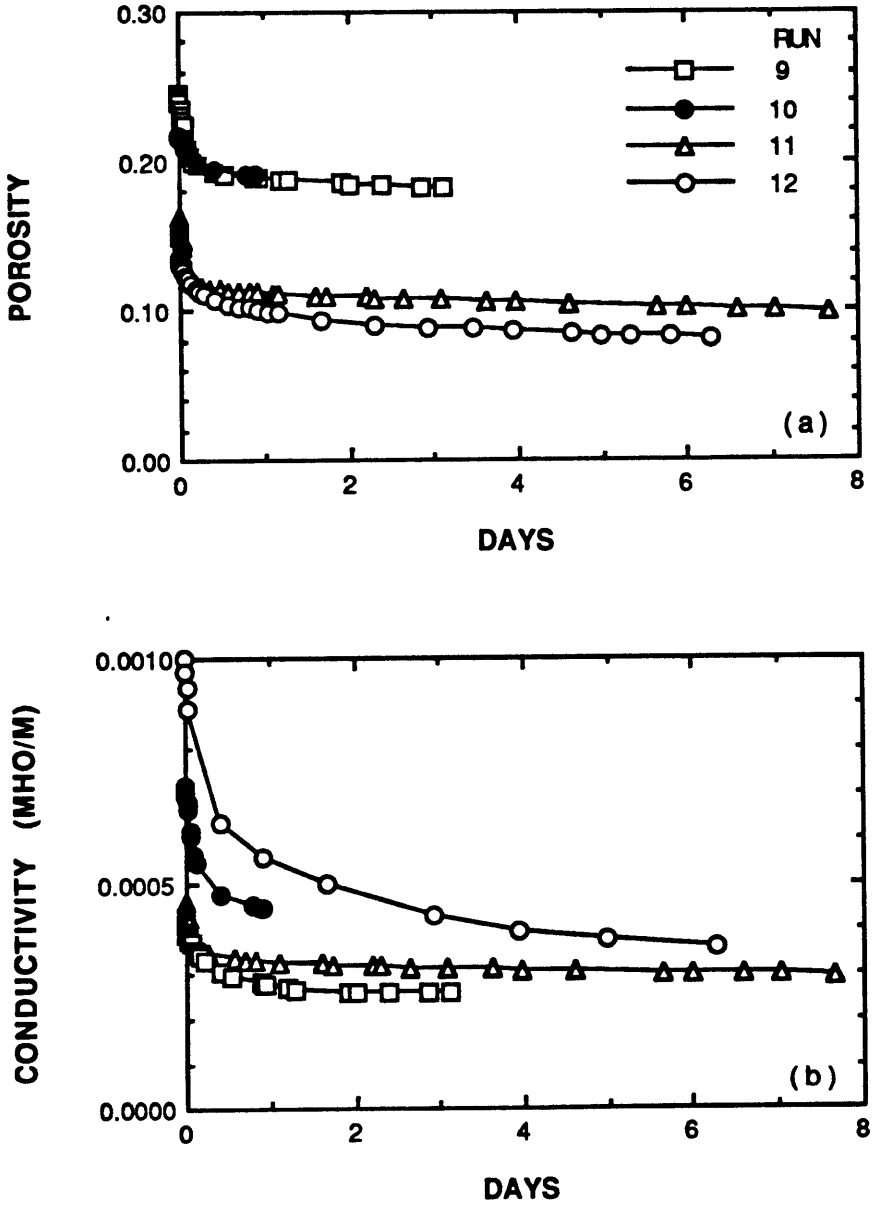
0.30
0.20
0.10
0.00
POROSITY
RUN
9
10
11
12
(a)
0
2
4
6
8
DAYS
0.0010
0.0005
0.0000
CONDUCTIVITY (MHO/M)
(b)
0
2
4
6
8
DAYS

Figure 5.3

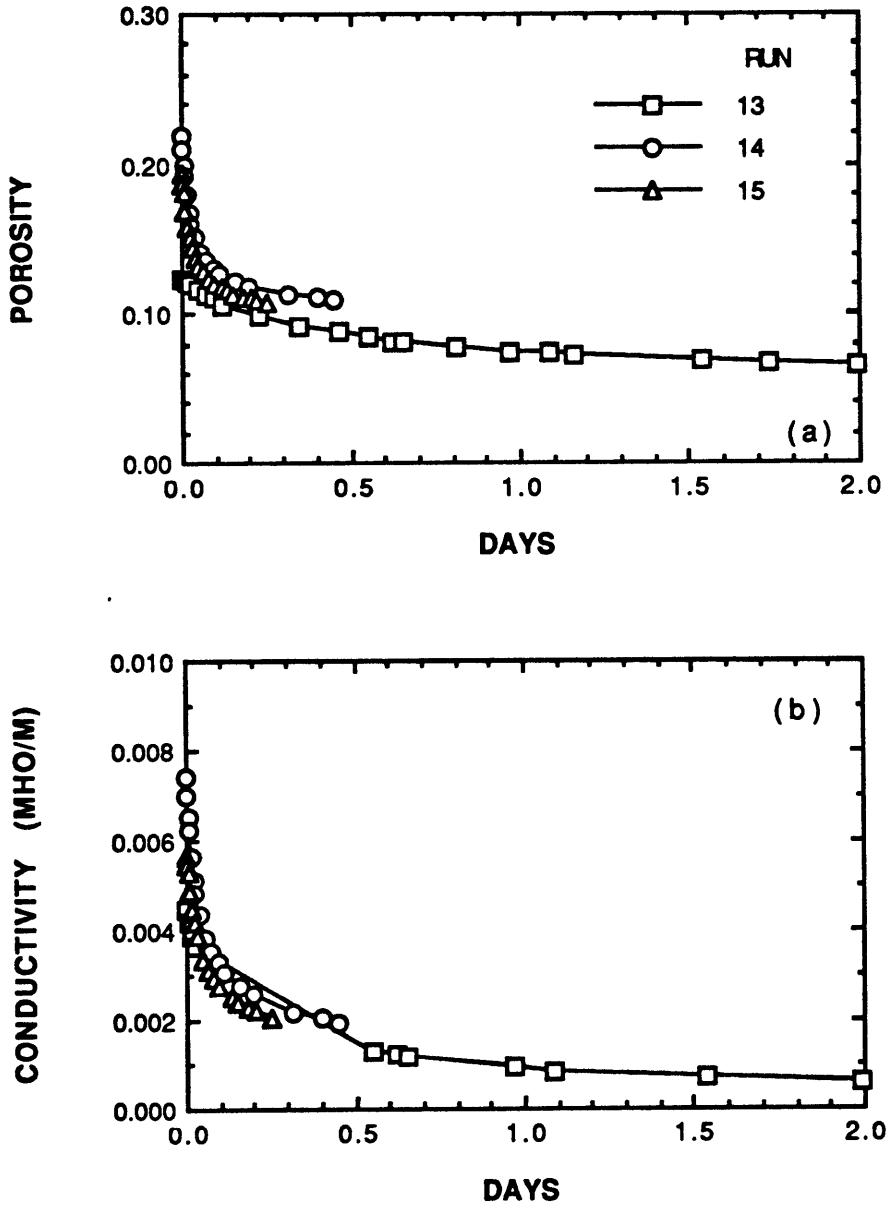
0.30
0.20
0.10
0.00
POROSITY
RUN
13
14
15
(a)
0.0
0.5
1.0
1.5
2.0
DAYS
0.010
0.008
0.006
0.004
0.002
0.000
CONDUCTIVITY (MHO/M)
(b)
0.0
0.5
1.0
1.5
2.0
DAYS

Figure 5.4

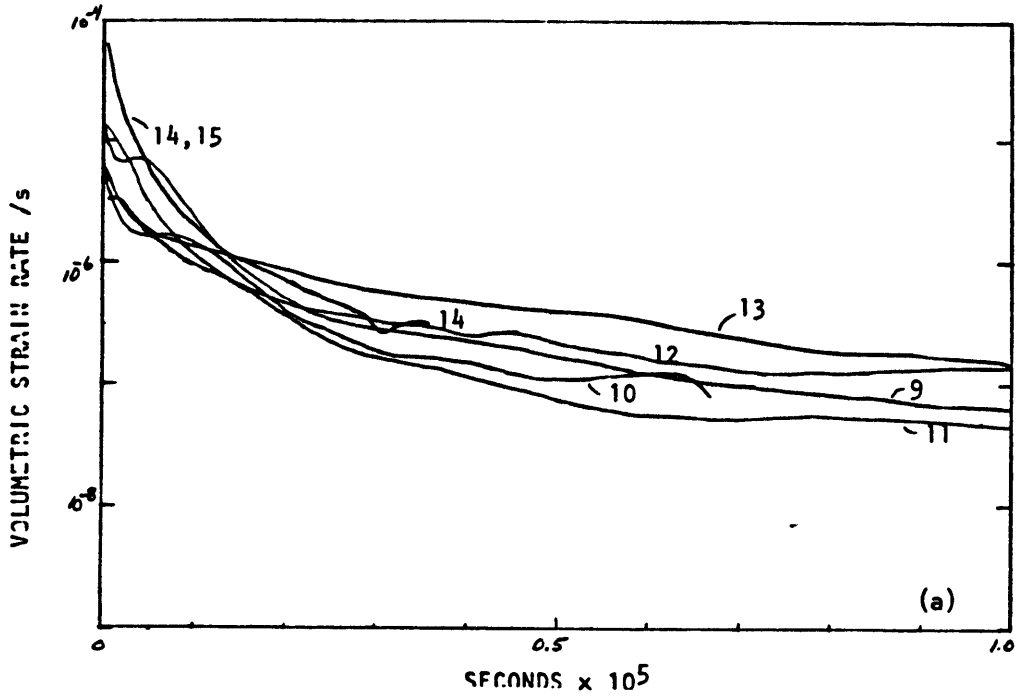
VOLUMETRIC STRAIN RATE /s
14,15
13
14
12
10
9
11
(a)
0
0.5
1.0
SECONDS x 10^5

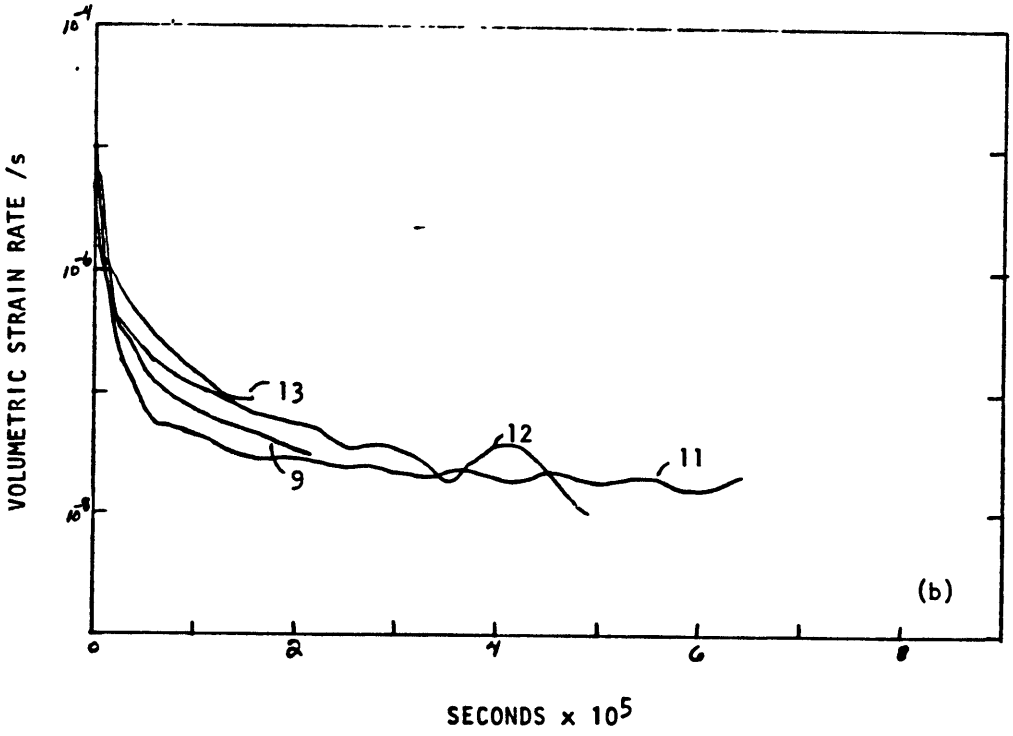
VOLUMETRIC STRAIN RATE /s
13
12
11
9
(b)
0
2
4
6
8
SECONDS x 10^5

Figure 5.5

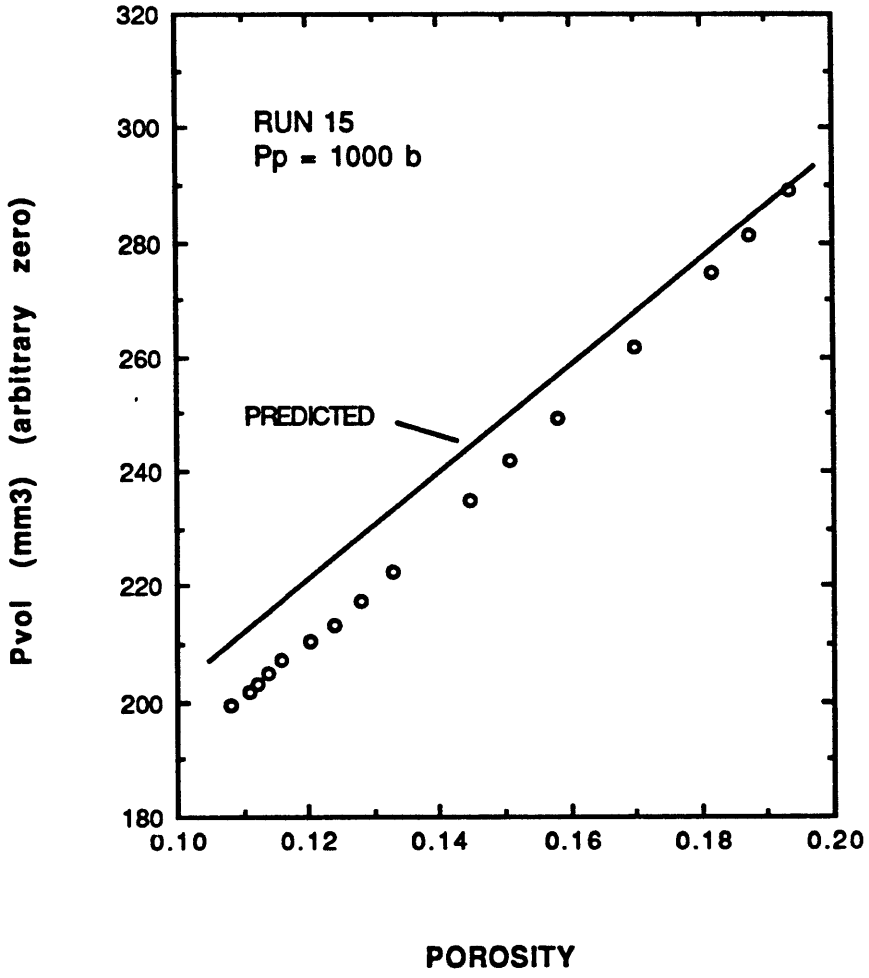
RUN 15
Pp = 1000 b
PREDICTED
Pvol (mm3) (arbitrary zero)
320
300
280
260
240
220
200
180
0.10
0.12
0.14
0.16
0.18
0.20
POROSITY

Figure 5.6

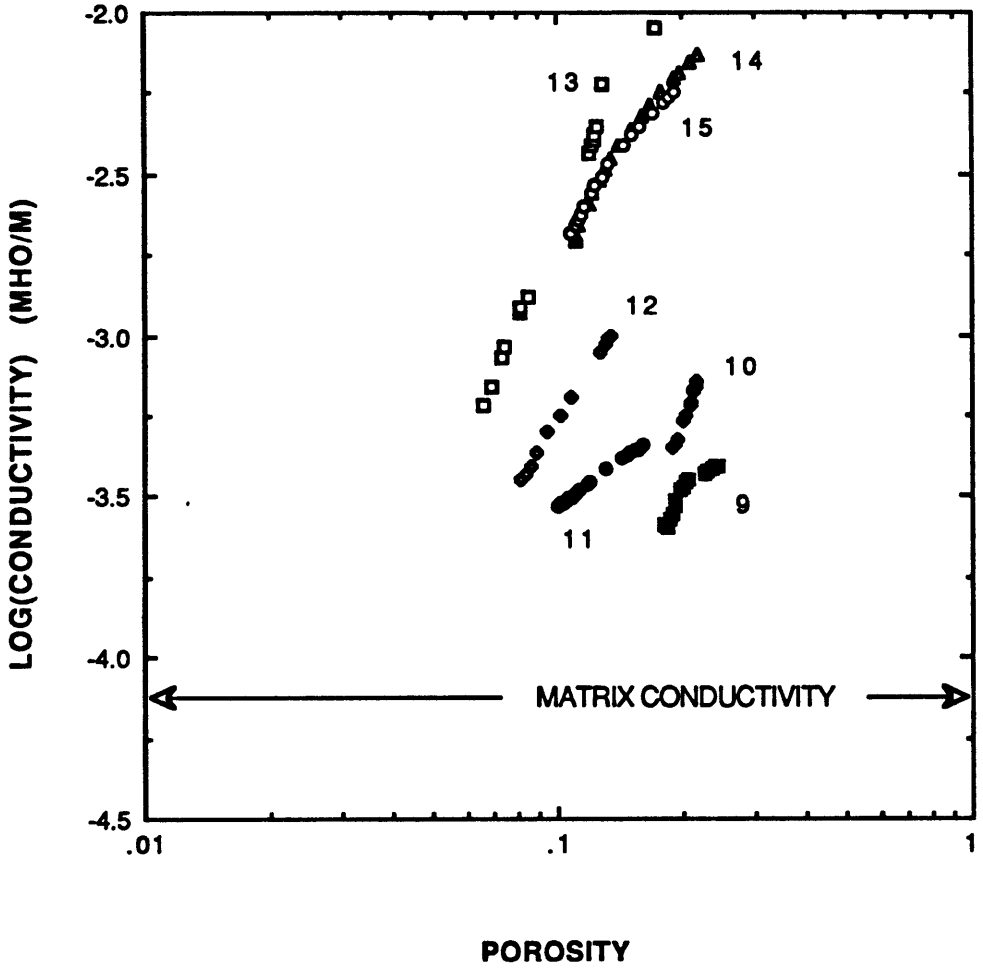
-2.0
-2.5
-3.0
-3.5
-4.0
-4.5
LOG(CONDUCTIVITY) (MHO/M)
.01
.1
1
POROSITY
MATRIX CONDUCTIVITY
13
14
15
12
10
9
11

Figure 5.7

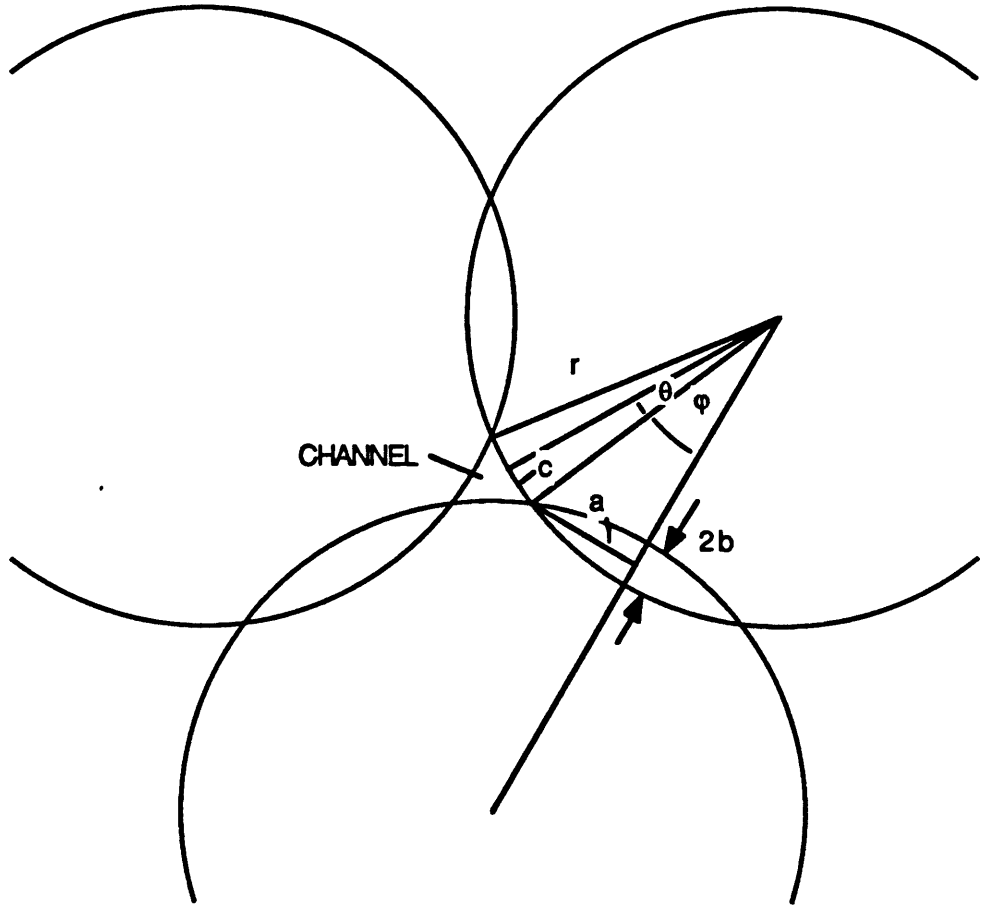

Figure 5.8

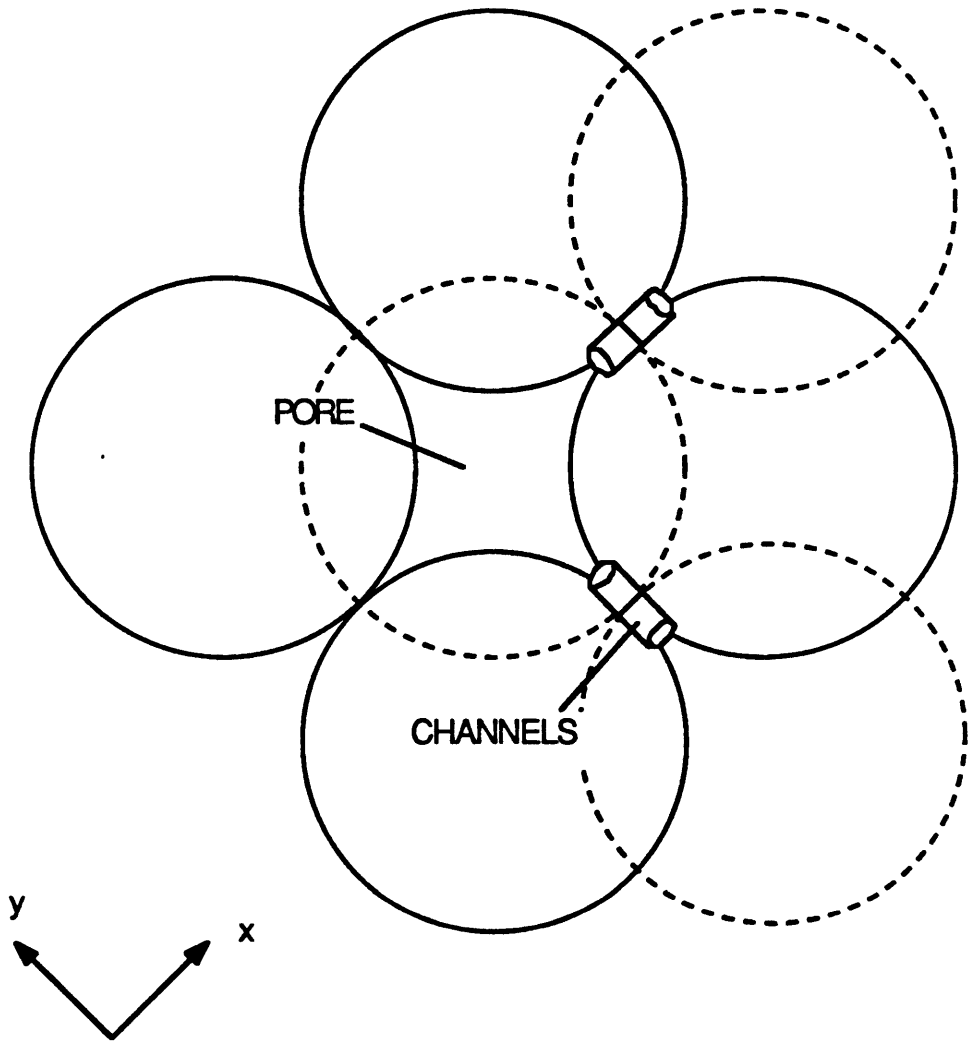

Figure 5.9

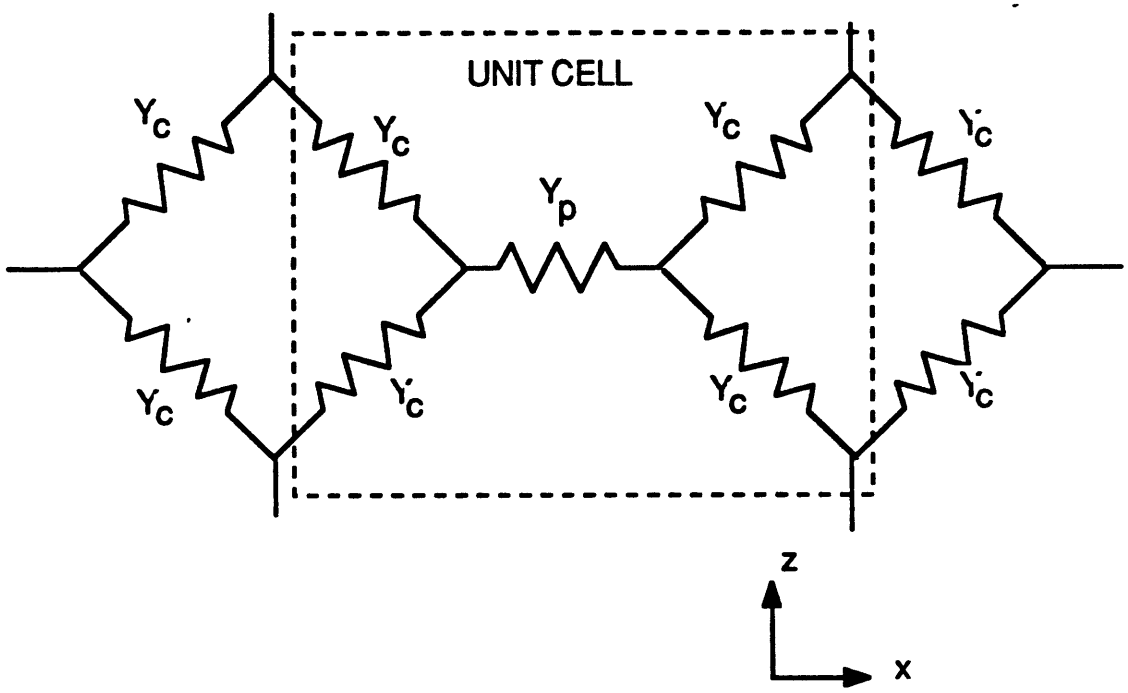

Figure 5.10

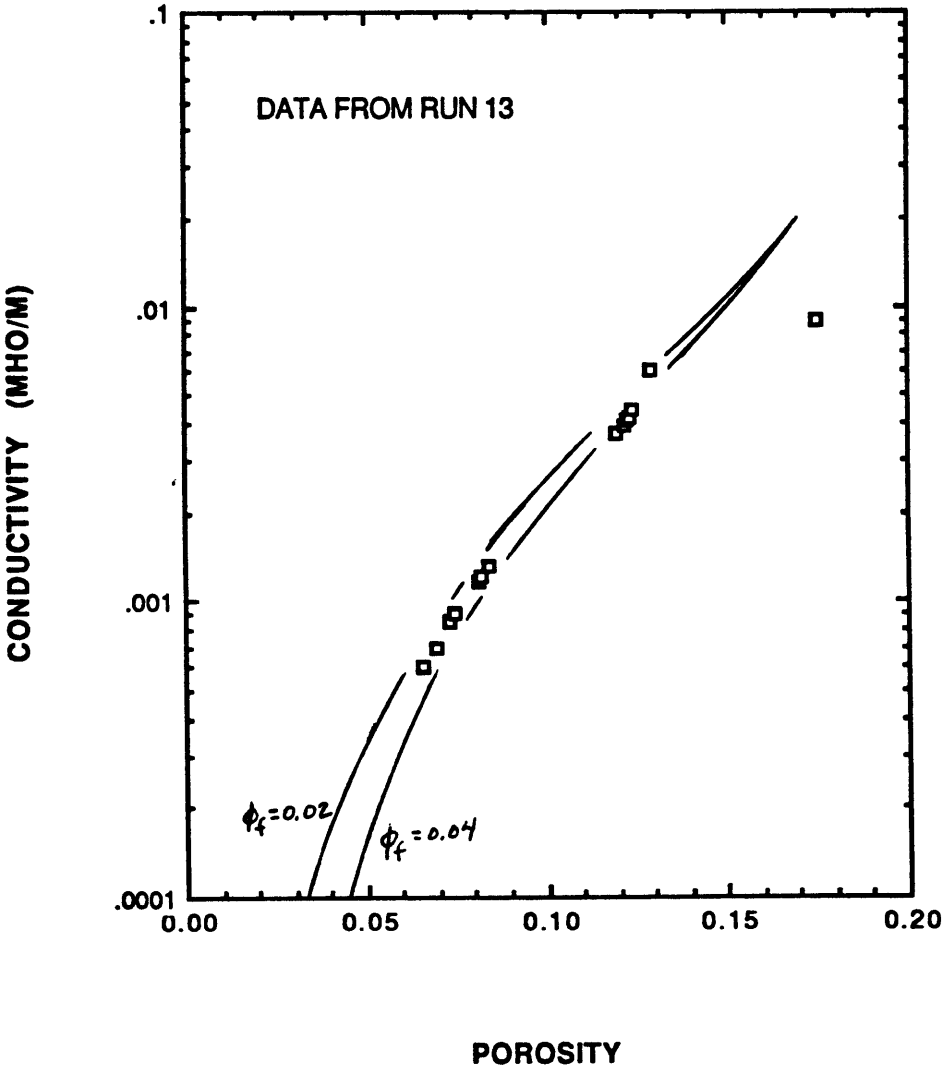
DATA FROM RUN 13
CONDUCTIVITY (MHO/M)
.1
.01
.001
.0001
0.00
0.05
0.10
0.15
0.20
POROSITY
$\phi_f = 0.02$
$\phi_f = 0.04$

Figure 5.11

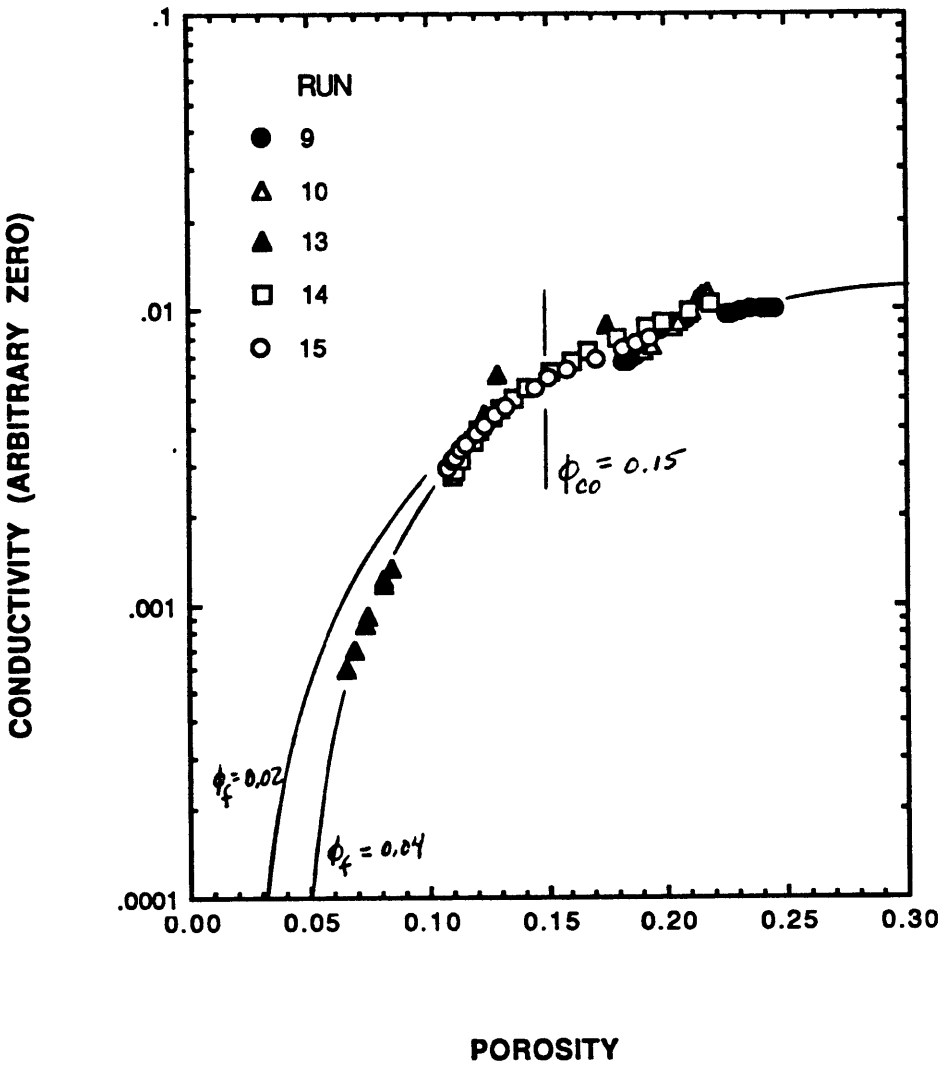
.1
.01
.001
.0001
RUN
9
10
13
14
15
$\phi_{co} = 0.15$
$\phi_f = 0.02$
$\phi_f = 0.04$
0.00
0.05
0.10
0.15
0.20
0.25
0.30
CONDUCTIVITY (ARBITRARY ZERO)
POROSITY

Figure 5.12

ACKNOWLEDGEMENTS

Writing this is the most enjoyable part of the thesis. Clearly, this work could not have been completed, especially considering the time frame, without the support of a number of people. Foremost at MIT have been my advisors and friends, Ted Madden and Brian Evans. They consistantly challenged me to extend beyond what I thought were my limitations. My conversations with them seemed always to leave me with an expanded point of view. The graduate students, especially those that haunted the fifth, sixth and seventh floors, were terrific and very supportive. I will miss them. Earle Williams was helpful with the modeling, especially in untangling some of my thinking about tensor properties.

I thank J. R. Rice for his thoughtful comments and suggestions.

At the USGS, I thank the OEVE Branch of Engineering Seismology and Geology for their generosity in providing computer time for the numerical modeling. Special thanks goes to L. M. Baker for his advice and time in dealing with the computational effort. In terms of the experimental sections of the thesis, all experiments were conducted in the Rock Deformation Laboratory of the OEVE Tectonophysics Branch. In that lab, R. Summers was most helpful in bringing me up to speed on the high-temperature deformation apparatus as well as numerous other high pressure techniques. I am especially appreciative of D. Bartz for his enthusiasm and support and for his unique talents as a machinist. If I needed it, he always managed to either find it or make it. D. Moore and C. Morrow have also been helpful, through the years, in making the Deformation Lab a stimulating and enjoyable place to work.

I thank the USGS Graduate School Education Program, the SEG Scholarship Program as well as MIT for the financial support that made it possible for me to return to school.

I also thank Dr. Mell for his encouragement and for, over the years, keeping alive in my mind the possibility of returning to school.

I thank my parents, Ruth and Avery, for all their support and for always being there. Also, thank you Tom and thank you Barbara.

My wife Robin has been unbelievable throughout this experience. Completing this degree has been a true test of her commitment and dedication. She has seen me through difficult times and I love her. My daughters Catherine and Christine have also been

terrific. They have managed to remind me that life isn't all that serious after all.

Finally, my deepest gratitude goes to my friend and mentor, Jim Byerlee. He has stood by me all these years and has taught me more than anyone about the true meaning of the scientific method. I dedicate this thesis to our friendship.